

# Synthetic Calcium Silicate Hydrates

THÈSE N° 7658 (2017)

PRÉSENTÉE LE 24 JUILLET 2017

À LA FACULTÉ DES SCIENCES ET TECHNIQUES DE L'INGÉNIEUR  
LABORATOIRE DE TECHNOLOGIE DES POUDRES  
PROGRAMME DOCTORAL EN SCIENCE ET GÉNIE DES MATÉRIAUX

ÉCOLE POLYTECHNIQUE FÉDÉRALE DE LAUSANNE

POUR L'OBTENTION DU GRADE DE DOCTEUR ÈS SCIENCES

PAR

**Abhishek KUMAR**

acceptée sur proposition du jury:

Prof. D. Damjanovic, président du jury  
Prof. P. Bowen, Prof. K. Scrivener, directeurs de thèse  
Dr A. Testino , rapporteur  
Dr B. Lothenbach, rapporteuse  
Prof. F. Stellacci , rapporteur



ÉCOLE POLYTECHNIQUE  
FÉDÉRALE DE LAUSANNE

Suisse  
2017





“काममय एवायं पुरुष इति।  
स यथाकामो भवति तत्क्रतुर्भवति।  
यत्क्रतुर्भवति तत्कर्म कुरुते।  
यत्कर्म कुरुते तदभिसंपद्यते॥”

“You are what your deep, driving desire is  
As your desire is, so is your will  
As your will is, so is your deed  
As your deed is, so is your destiny”

- Brihadaranyakopanishat 4.4.5



*Dedicated to my family...*



## Acknowledgement

Many people directly, indirectly played an influential role during this thesis work, without them, it would be an impossible task. I would like to sincerely apologise in case I miss out on someone.

Firstly, heartfelt thanks to my advisor, Guru – Professor Paul Bowen, who gave me this opportunity to indulge into this topic. With him comes a constant source of motivation and encouragement. The freedom to trials, experiments, working flexibility are only some of the many perks of working under his guidance. Not to forget his friendly approach to life, science, student, dance etc. allowed me to build up my confidence and stay put in the new tech field I touched upon during this thesis work. Secondly, I am very grateful to my Co-advisor, Professor Karen Scrivener for sharing her extensive experience in cement field, for inspiration and invaluable comments. Apart from being a formidable scientist, she is a role model in many other aspects. I would like to thank both of them for their trust in me and the scientific opportunity accorded to me.

I would also like to thank Prof. Heinrich Hofmann for useful discussions and for always being a motivating figure in LTP. Furthermore, I would like to thank Dr Barbara Lothenbach and Dr Dimitri Kulik for helping me with GEMS for the thermodynamic modelling. Sincere thanks to Prof. D. Macphee, Dr Virendra Parashar, Prof. M. Doherty, Prof. M. Mozzatti, Dr Patrick Juilland, Dr Stephane Gretzl and Prof. Robert Flatt for taking interest and dedicating their time and for their stimulating scientific discussions.

I am grateful to all my thesis collaborators, Prof. Bruno Humble, Prof. Lyndon Emsley, Prof. Aaron Rossini, Mr Danny Lambert, Dr Brennan Walder, Mr Albert Hoffstetter, Mr Mohammad Reza Andalibi and Dr Andreas Testino for their endless efforts and contributions towards my thesis work.

I would also like to thank my students I was working with, especially Bhuvanesh Srinivasan, whose scientific contributions can be found in the thesis articles. His master thesis provided much needed to be accelerated results and insights into the subject.

Special thanks to Jirawan Siramanont and Aslam M. Kuhni for in-valuable discussion and comments over my research work, to make it more fruitful and all the good time shared during conferences. Big thanks also goes to my other colleagues at LTP, past – Lionel Maurizi, Usawadee, Marie-Gabrielle, Abhishek Tewari, Aurelie, Nadia, Milica and LTP, present – Marijana, Azade, Weitian, Amarnath, David, Irena, Débora, João, Silvia for all their help and companionship and their constant encouragement that helped me bailing out during the rather tedious writing phase at the end. I would like to thank LTP administrative and laboratory staffs – Shawn koppenhoefer, Carlos, and Sophie for helping me out with my lab and office queries whenever I needed them. Especially thanks to Anne Remillet for her super-efficient working mode as LTP ex- secretary. I would also like to thank members of LMC past and present, especially Elise, Arnaud, Berta, Mathew Antoni, Pawel, Amelie, François, Lily, Julien, Ruben,

Alexandre, Mink, Xuerun, and Aurélie for always making me feel welcome and for interesting scientific suggestions.

The project was funded by the Swiss national foundation (SNF 153044), for which I thank them profoundly. The project was also the part of Nanocem network as partner project. Nanocem network was very helpful and made it easy to discuss with fellow PhD students as well as to get the industrial viewpoint, which was very enriching. I profited a lot from the travels to meet and discuss with a great number of proficient scientists and gain from their knowledge.

Life will be motionless without friends. During the four years of my thesis I had many amazing experiences and memories with friends, I would like to give my special thanks Mahsa, Raja, Teju, Rishikesh, Srini, Nice, Prasad, Deepti, Aamani, Govinda, for their ever ending enthusiasm towards me, helped me a lot in reviewing me after work hours. Thank you all and I am looking forward to the next reunion.

I would not be here without my family. At this point, I would like to thank my parents for unconditional love and support at every stage of my life. I would also like to thank my brother and cousins for being the best of companions and friends and for always helping me out whenever I needed. I still keep learning, even from the future generation of our family, my niece, and my nephews, thanks to them for making all my India trips memorable.

Lastly, I would like to thank all the member of the jury committee who kindly agreed to review my work and provided me with positive feedback.

Abhishek  
Lausanne, 2017

## Abstract

Cementitious materials make up about half of all the materials produced worldwide. They are the most affordable building materials with the lowest carbon footprint per kg when compared to any other in the category. Since its introduction over 200 years ago, its use has multiplied many fold to be currently at 3 billion tonnes per year, accounting for about 8% of worldwide carbon emission which is forecast to double within the next 30 years. Upon hydration of cementitious materials, the principle product formed is Calcium Silicate Hydrate (C-S-H) that binds all the aggregates together. Solutions to reduce this Carbon footprint depend on being able to improve the development of early age strength, which is controlled by the self-limiting growth of the C-S-H, particularly when using alternative supplementary cementitious materials (SCMs) to replace Portland cement. The greatest difficulty to overcome this limitation is the lack of knowledge on the growth and structure of C-S-H. It is poorly crystalline and cannot be characterised by classical crystal techniques. Moreover, in the Portland cement system, the effect of different elements on C-S-H growth is unclear. Furthermore, there is a lack of kinetic analysis on C-S-H growth.

This thesis work presents a synthetic method to produce uniform C-S-H phases with Ca:Si ratios from 1 to 2, with a ratio above 1.6 being achievable for the first time in any given synthetic system. Higher ratios are of particular importance when compared to a real system, where it exists around 1.75 (Avg.). This was achieved with a novel rapid precipitation method by controlling mixing and reaction chemistry. These synthetic C-S-H precipitates are chemically uniform at the nanoscale and allowed us to determine a better defined atomistic structure with the use of dynamic nuclear polarisation (DNP) NMR techniques and atomistic simulations. The discovered structures reveal the inclusion of a calcium site in the interlayer that bridges chain terminating silicate species. This site is associated with an environment of strong hydrogen bonding that stabilises the structure and, consequently, promotes high Ca:Si ratios in C-S-H. The major result is thus a clear relation between the atomic level defect structure and the high Ca:Si ratio in C-S-H. Further, the C-S-H phases were analysed by Raman micro-spectrometry and Fourier Transform Infrared spectroscopy (FTIR) and revealed a proximity to a defective tobermorite structure and the probability of a single solid solution model for the Ca:Si range from 1.25 to 2. A morphological transformation point is also reported to be near to pH~11, where C-S-H solid phases clearly change from nanoglobules (spherical) to nanofoils (platelets).

The key role of the thermodynamic conditions (speciation, pH, concentration etc.) was clearly observed in the formation of C-S-H phases with desirable morphology and Ca:Si ratios. A study of the effect of other divalent ions, commonly encountered in cementitious systems, on the formation of silicate hydrates were made in comparison with calcium. It was discovered that Calcium plays a special interaction role with different silicate species in the formation of C-S-H phases that is not shown by any other divalent ions. Hence revealing the importance and uniqueness of the C-S-H phases in the cementitious system.

The developed understanding of the thermodynamic conditions and its control in the formation of desired precipitated synthetic C-S-H phases was applied to the formation of C-S-H in the Portland cement system formed upon the hydration of Alite (an impure Tri-Calcium silicate main phase in cementitious materials). We could predict the calorimetric behaviour of the system based on the knowledge of the formation mechanism of synthetic C-S-H. Also, it allowed us to forecast desirable conditions to get a particular phase or response of the hydrating system. Kinetic data were collected from the synthetic precipitation experiments by following the Ca consumption from solution. Then with help of thermodynamics speciation modelling and Population Balance Modelling (PBM) an empirical growth model for C-S-H was developed.

Overall, all these results together have given a much clearer picture of the atomistic structure of C-S-H, in particular, the role of calcium in the interlayer and keys to modifying the reactivity and growth of this most ubiquitous substance that holds together the built environment and infrastructure.

## **Keywords**

Reactor, C-S-H,  $^{29}\text{Si}$  NMR,  $^1\text{H}$  NMR, DFT, Atomistic simulation, XRD, TEM, SEM, ICP, XRF, Raman, FTIR, pH, Availability, Mobility, species, surfaces, nucleation, growth, population balance modelling



## Resumé

Les matériaux cimentaires représentent environ la moitié de tous les matériaux produits dans le monde entier. Ils sont les matériaux de construction les plus abordables avec la plus faible empreinte carbone par kg par rapport à tout autre dans la catégorie. Depuis son introduction il y a plus de 200 ans, son utilisation s'est multipliée par plusieurs fois pour être actuellement de 3 milliards de tonnes par an, ce qui représente environ 8% des émissions mondiales de carbone qui devrait doubler au cours des 30 prochaines années. Lors de l'hydratation des matériaux cimentaires, le principe produit formé est le Silicate Hydrate de Calcium (C-S-H) qui lie tous les agrégats ensemble. Les solutions pour réduire cette empreinte carbone dépendent de l'amélioration du développement de la force de l'âge précoce, qui est contrôlée par la croissance autonome du C-S-H, en particulier lors de l'utilisation d'autres matériaux cimentaires complémentaires (SCM) pour remplacer le ciment Portland. La plus grande difficulté à surmonter cette limitation est le manque de connaissances sur la croissance et la structure de C-S-H. Il est peu cristallin et ne peut être caractérisé par des techniques de cristaux classiques. De plus, dans le système de ciment Portland, l'effet de différents éléments sur la croissance C-S-H n'est pas clair. En outre, il n'y a pas d'analyse cinétique sur la croissance C-S-H.

Ce travail de thèse présente une méthode synthétique pour produire des phases C-S-H uniformes avec des rapports Ca: Si de 1 à 2, avec un ratio supérieur à 1,6 pouvant être atteint pour la première fois dans un système synthétique donné. Des ratios plus élevés revêtent une importance particulière par rapport à un système réel, où il existe environ 1,75 (moyenne). Ceci a été réalisé avec une nouvelle méthode de précipitation rapide en contrôlant le mélange et la chimie de réaction. Ces précipités synthétiques C-S-H sont chimiquement uniformes à l'échelle nanométrique et nous ont permis de déterminer une structure atomique mieux définie avec l'utilisation de techniques de NMR à polarisation nucléaire dynamique (DNP) et de simulations atomiques. Les structures découvertes révèlent l'inclusion d'un site de calcium dans la couche intercalaire qui relie les espèces de silicate qui terminent la chaîne. Ce site est associé à un environnement de forte liaison hydrogène qui stabilise la structure et, par conséquent, favorise les rapports élevés Ca: Si en C-S-H. Le résultat principal est donc une relation claire entre la structure des défauts du niveau atomique et le rapport Ca: Si élevé en C-S-H. En outre, les phases CSH ont été analysées par micro-spectrométrie Raman et spectroscopie infrarouge à transformée de Fourier (FTIR) et ont révélé une proximité d'une structure de tobermorite défectueuse et la probabilité d'un seul modèle de solution solide pour la gamme Ca: Si de 1,25 à 2. A Le point de transformation morphologique est également proche du pH ~ 11, où les phases solides de CSH changent clairement de nanoglobules (sphériques) à nanofoils (plaquettes).

Le rôle clé des conditions thermodynamiques (spéciation, pH, concentration, etc.) a été clairement observé dans la formation de phases C-S-H avec une morphologie souhaitable et des rapports Ca: Si. Une étude de l'effet des ions divalents électrolytiques, couramment rencontrés dans les systèmes cimentaires, sur la formation d'hydrates de silicate a été faite par rapport au calcium. On a découvert que le calcium joue un rôle d'interaction spécial avec différentes

espèces de silicate dans la formation de phases C-S-H qui ne sont pas représentées par d'autres ions divalents. Il révèle donc l'importance et l'unicité des phases C-S-H dans le système cimentaire.

La compréhension développée des conditions thermodynamiques et son contrôle dans la formation des phases CSH synthétiques précipitées désirées a été appliquée à la formation de CSH dans le système de ciment Portland formé lors de l'hydratation d'Alite (une phase principale de silicate de Tri-Calcium impur dans des matériaux de ciment) . Nous pourrions prédire le comportement calorimétrique du système en fonction de la connaissance du mécanisme de formation du C-S-H synthétique. En outre, il nous a permis de prévoir des conditions souhaitables pour obtenir une phase particulière ou une réponse du système hydratant. Les données cinétiques ont été recueillies à partir des expériences de précipitation synthétique en suivant la consommation de Ca de la solution. Ensuite, avec l'aide de la modélisation de la spéciation thermodynamique et de la modélisation de la balance des populations (PBM), un modèle de croissance empirique pour C-S-H a été développé.

Dans l'ensemble, tous ces résultats ont donné une image beaucoup plus claire de la structure atomistique de CSH, en particulier, le rôle du calcium dans l'intercalaire et des clés pour modifier la réactivité et la croissance de cette substance la plus omniprésente qui maintient l'environnement bâti et l'infrastructure .

## **Mots clés**

Réacteur, C-S-H,  $^{29}\text{Si}$  NMR,  $^1\text{H}$  NMR, DFT, simulation atomique, XRD, TEM, SEM, ICP, XRF, Raman, FTIR, pH, Disponibilité, Mobilité, espèces, surfaces, nucléation, croissance, modélisation de l'équilibre de la population

# Contents

|  |           |
|--|-----------|
| <b>Acknowledgement .....</b>                                 | <b>1</b>  |
| <b>Abstract .....</b>  | <b>3</b>  |
| <b>Keywords .....</b>  | <b>4</b>  |
| <b>Resumé .....</b>  | <b>5</b>  |
| <b>Mots clés.....</b>  | <b>6</b>  |
| <b>Contents.....</b>   | <b>7</b>  |
| <b>List of figures.....</b>                                  | <b>9</b>  |
| <b>List of tables.....</b>                                   | <b>12</b> |
| <b>1 Introduction and Scope of thesis .....</b>              | <b>13</b> |
| 1.1 Significance .....                                       | 13        |
| 1.2 Dissertation scope and objectives .....                  | 14        |
| 1.3 Organisation of thesis.....                              | 16        |
| <b>2 Fundamentals.....</b>                                   | <b>17</b> |
| 2.1 Introduction .....                                       | 17        |
| 2.2 Portland cement system.....                              | 18        |
| 2.2.1 Cement .....   | 18        |
| 2.2.2 Cement hydration.....                                  | 19        |
| 2.2.3 Microstructure and strength development .....          | 21        |
| 2.2.4 C-S-H .....  | 24        |
| 2.3 Synthetic system.....                                    | 30        |
| 2.3.1 The tetrahedral silicates building block .....         | 30        |
| 2.3.2 Thermodynamics and kinetics of reactions .....         | 32        |
| 2.3.3 Precipitation of a solid .....                         | 33        |
| 2.3.4 Modelling of synthetic system .....                    | 36        |
| <b>3 Material and methods .....</b>                          | <b>38</b> |
| 3.1 Introduction .....                                       | 38        |
| 3.2 Controlled synthetic system and product recovery. ....   | 39        |
| 3.3 Sample characterization methods .....                    | 40        |
| 3.4 Doping Studies.....                                      | 40        |
| <b>4 Synthesis of calcium silicate hydrates .....</b>        | <b>42</b> |
| 4.1 Introduction.....  | 42        |
| 4.2 Manuscript.....  | 43        |
| <b>5 Atomic Structure of Calcium Silicate Hydrates .....</b> | <b>61</b> |
| 5.1 Introduction.....  | 61        |

|     |   |     |
|-----|---|-----|
| 5.2 | Manuscript.....   | 61  |
| 6   | Calcium silicate hydrate formation pathways and alite hydration.....  | 74  |
| 6.1 | Introduction .....  | 74  |
| 6.2 | Manuscript.....   | 74  |
| 7   | Doping effect of other divalent ions.....   | 88  |
| 7.1 | Introduction .....  | 88  |
| 7.2 | Manuscript.....   | 88  |
| 8   | Kinetic analysis of Calcium silicate hydrate formation.....   | 99  |
| 8.1 | Introduction .....  | 99  |
| 8.2 | Manuscript.....   | 99  |
| 9   | Summary of thesis and Quo Vadis .....   | 119 |
|     | Reference:.....   | 122 |
| 10  | Appendix .....  | 131 |
|     | SI A: Supplementary information for the article – The Atomic level information for cementitious Calcium silicate hydrates ..... | 131 |
|     | SI B: Supplementary information on thermodynamics modeling.....   | 131 |
|     | SI C: Supplementary information for the article – Kinetics analysis for Calcium silicate hydrate formation. ....                | 131 |
| 11  | CV.....   |     |

## List of figures

|  |    |
|--|----|
| FIGURE 1: INGREDIENTS OF CONCRETE AND PRICE/PRODUCTION OF DIFFERENT CONSTRUCTION MATERIALS -----   | 13 |
| FIGURE 2: BACKSCATTERED SEM IMAGE OF A MATURE CEMENT PASTE SHOWING THE MAIN MICROSTRUCTURAL FEATURES.-----   | 15 |
| FIGURE 3: A) PORTLAND CEMENT SYSTEM: COMPLEX C-S-H FORMATION B) STEPS TO DESIGNING A NEW SYNTHETIC SYSTEM TO UNDERSTAND UNIFORM C-S-H SYSTEM. -----  | 17 |
| FIGURE 4: GENERAL FLOW CHART OF CEMENT PRODUCTION, SCHEMATIC DIAGRAM OF ROTATORY KILN, FROM RAW MATERIAL TO CLINKER INSIDE ROTATORY KILN -----   | 18 |
| FIGURE 5: DISSOLUTION MODES - SLOWEST IS THE RATE-DETERMINING STEP (RDS) OF THE PROCESS <sup>18</sup> -----  | 19 |
| FIGURE 6: (1) PARTIAL DISSOLUTION OF C3S (2) THE GRAINS START TO AGGLOMERATE (3) C-S-H STARTS TO NUCLEATE HETEROGENEOUSLY ON THE C3S SURFACE (4) WHICH ENHANCES THE HARDENING OF THE CEMENT UNTIL THE C- S-H LAYER REACHES A CRITICAL THICKNESS WHEN THE HYDRATION IS LIMITED BY DIFFUSION OF WATER. (5) SCHEMATIC OF C3S HYDRATION VERSUS TIME. <sup>12,20</sup> -----  | 20 |
| FIGURE 7: RATE OF HEAT EVOLUTION DURING THE HYDRATION OF PORTLAND CEMENT. -----  | 21 |
| FIGURE 8: COMPRESSIVE STRENGTH DEVELOPMENT OVER TIME IN PASTES OF PURE CEMENT COMPOUNDS <sup>41</sup> -----  | 22 |
| FIGURE 9: MODEL OF A HYDRATED PORTLAND CEMENT PASTE -----  | 22 |
| FIGURE 10: A) DIMENSIONAL RANGE OF SOLIDS AND PORES IN A HYDRATED CEMENT PASTE. (B) IN FIG. 2-7A, THE DIMENSIONAL RANGE COVERS SEVEN ORDERS OF MAGNITUDE. TO ILLUSTRATE HOW WIDE THE RANGE IS, B) ILLUSTRATES A SIMILAR RANGE USING THE HEIGHT OF A HUMAN BEING AS A STARTING POINT AND PLANET MARS AS THE ENDING POINT. <sup>17</sup> -----   | 23 |
| FIGURE 11: RELATIONSHIP BETWEEN WATER/CEMENT RATIO AND POROSITY -----  | 24 |
| FIGURE 12: TOBERMORITE STRUCTURE AND SILICATE NOMENCLATURE -----   | 25 |
| FIGURE 13: A) FELDMAN -SEREDA MODEL <sup>57</sup> B) JENNINGS MODEL <sup>7</sup> -----   | 28 |
| FIGURE 14: ALITE HYDRATION CAPTURED BY ESEM <sup>63</sup> A) UN-HYDRATED C3S B) HYDRATED C3S AFTER 24 HOURS C) HYDRATED C3S AT 96 HOURS -----  | 29 |
| FIGURE 15: CALCULATED BENDING POTENTIAL FOR Si-O-Si (IN CIRCLE) AND Si-S-Si (IN SQUARE) UNITS, (ADAPTED FROM BURDETT, 1988) -----  | 31 |
| FIGURE 16: DISTRIBUTION OF AQUEOUS SILICATES SPECIES AT 25° C, IN TOTAL Si CONCENTRATION OF 0.1 M (LEFT) AND 10 <sup>-5</sup> M (RIGHT). -----   | 32 |
| FIGURE 17: KINETICS PROCESSES DURING PRECIPITATION -----   | 34 |
| FIGURE 18: A) CLASSICAL NUCLEATION AND GROWTH <sup>74,76</sup> B) RELATION BETWEEN NUCLEATION, GROWTH RATE AND CONCENTRATION OF SPECIES. <sup>77,76</sup> -----  | 34 |
| FIGURE 19: MECHANISMS OF NUCLEATION (MULLIN, 1993) <sup>73</sup> -----   | 35 |
| FIGURE 20: OSTWALD STEPS RULE - SHOWING THE DIFFERENT PATHWAYS TOWARDS THE FINAL PRECIPITATED PRODUCT. <sup>71</sup> -----   | 35 |
| FIGURE 21: GENERAL SCHEME OF THE SYNTHESIS AND CHARACTERIZATION -----  | 38 |
| FIGURE 22: (A) TOBERMORITE STRUCTURE AND STRUCTURAL NOMENCLATURE (B) DEFECTIVE TOBERMORITE STRUCTURE WITH MISSING BRIDGING TETRAHEDRA AND EXTRA INTERLAYER CALCIUM. -----  | 45 |
| FIGURE 23: SCHEMATIC OF THE REACTION VESSEL. -----   | 47 |
| FIGURE 24: A) NANOFOILS MORPHOLOGY FOR Ca:Si OF 2 (ALL Ca:Si RATIOS FROM 1.25 TO 2 SHOWED THE SAME MORPHOLOGY) B) FTIR C) TGA D) XRD -----   | 52 |
| FIGURE 25: NANOGLOBULES MORPHOLOGY FOR Ca:Si OF 1 B) FTIR C) TGA D) XRD -----  | 53 |
| FIGURE 26: RAMAN MICROSCOPIC ANALYSIS: A) SAMPLE PELLET PREPARATION, B) SPOT SIZE USED FOR ANALYSIS, C) INTENSITY PLOT COMPARING RAMAN SPECTRA OF ALL 30 SPOTS, D) STACKED PLOT COMPARING RAMAN SPECTRA OF ALL 30 SPOTS FOR A Ca:Si RATIO 2 SYNTHETIC C-S-H. -----   | 53 |
| FIGURE 27: STEM -EDX POINT ANALYSIS ON NANOFOILS B) Ca:Si RATIO COMPARISON -----   | 54 |
| FIGURE 28: MID-IR SPECTRA OF C-S-H SAMPLES WITH DIFFERENT Ca:Si RATIO -----  | 55 |
| FIGURE 29: RAMAN SPECTRA FOR THE PRECIPITATED C-S-H SAMPLE WITH VARYING Ca:Si RATIOS. -----  | 57 |
| FIGURE 30: COVER PAGE OF JPCC MANUSCRIPT -----   | 61 |
| FIGURE 31 STRUCTURAL ELEMENTS OF C-S-H. (A) HIGH-RESOLUTION TEM IMAGE OF PURE C-S-H WITH Ca:Si RATIO OF 2.00, SHOWING ITS “NANOFOIL” MORPHOLOGY. (B) FOURIER TRANSFORM IR SPECTROSCOPY SHOWED NO EVIDENCE OF PHASES OTHER THAN THE C-S-H, INCLUDING Ca(OH) <sub>2</sub> . (C) COMPARISON OF RAMAN SPECTRA OF Ca(OH) <sub>2</sub> (GREEN), CaCO <sub>3</sub> (BLUE), A SAMPLE OF C-S-H WITH Ca:Si = 2.0 AFTER 4 SCANS (LOWER BLACK), AND A SAMPLE OF C-S-H WITH Ca:Si = 2.0 AFTER 78 SCANS (UPPER BLACK). (C) |    |

|  |     |
|--|-----|
| CHAIN TOPOLOGY IN THE LAYERED 14 Å TOBERMORITE (Ca:Si = 0.83). (D) DEFECTIVE AND SHORT DREIERKETTEN CHAINS IN C-S-H, SHOWING TWO DIMERS ( $N = 0$ ) AND ONE PENTAMER ( $N = 1$ ).-----   | 65  |
| FIGURE 32: ONE- AND TWO- DIMENSIONAL DNP ENHANCED $^{29}\text{Si}$ CP MAS SPECTRA OF C-S-H SAMPLES FOR QUANTIFICATION OF SILICATE CHAIN DISTRIBUTIONS. (A) 1D SPECTRA ACROSS THE COMPOSITIONAL SERIES. (B) EXPERIMENTAL 2D REFOCUSSED INADEQUATE SPECTRA FOR THREE OF THE C-S-H COMPOSITIONS STUDIED (THE SPECTRA HAVE BEEN SHEARED TO PRODUCE A COSY-LIKE REPRESENTATION). CONTOURS ARE DRAWN IN 10% INTERVALS BEGINNING AT 5% OF THE MAXIMUM SIGNAL INTENSITY. -----   | 66  |
| FIGURE 33: DNP ENHANCED 2D $\{^1\text{H}\}^{29}\text{Si}$ HETCOR CORRELATING $^1\text{H}$ SPECTRA TO SPECIFIC Si SITES. (A) THE 2D CORRELATION SPECTRUM FOR THE Ca:Si = 1.50 COMPOSITION ACQUIRED WITH A 7 MS CP CONTACT TIME. (B) 1D CROSS SECTIONS PARALLEL TO THE $^1\text{H}$ DIMENSION EXTRACTED AT THE POSITION OF THE DASHED LINE IN THE 2D SPECTRUM, REPRESENTING $^1\text{H}$ SPECTRA CORRELATED TO $\text{Q}^{(1)}$ . (C) SIMULATED $^1\text{H}$ CHEMICAL SHIFT SPECTRA AGGREGATED OVER C-S-H SUBSTRUCTURES THAT EITHER POSSESS (BLUE) OR LACK (RED) THE BRIDGING CALCIUM SITE $\text{Ca}_\text{B}$ . THE INTENSITY OF THESE SPECTRA ARE NORMALIZED WITH RESPECT TO THE MAXIMUM OF THE $\text{Q}^{(1)}$ PEAK. THE REGION DOWNFIELD OF 10 PPM IS SHADED TO INDICATE THE DOMAIN OF STRONGLY HYDROGEN BONDED SPECIES. ----- | 68  |
| FIGURE 34 SCATTER PLOT SHOWING THE CORRELATION BETWEEN THE O–O DISTANCES AND THE CHEMICAL SHIFTS OF PROTONS PARTICIPATING IN THE DIFFERENT TYPES OF HYDROXYL-OXYGEN INTERACTIONS OCCURRING IN THE C-S-H SUBSTRUCTURES. -   | 70  |
| FIGURE 35: THE STRUCTURE DETERMINED HERE OF C-S-H FOR A Ca:Si RATIO OF 1.5, VIEWED ALONG THE [A] AXIS. THE RELATIVE PROPORTIONS OF DIMERS, PENTAMERS, OCTAMERS, UNDECAMERS, AND TETRADECAMERS ARE 81%, 14%, 3%, 1%, AND 1%, RESPECTIVELY. THE CHEMICAL COMPOSITION OF THIS STRUCTURE IS $\text{Ca}_{1.5}\text{SiO}_{3.35}(\text{OH})_{0.3} \cdot 2\text{H}_2\text{O}$ . THE RELATIVE POSITIONS OF HYDROXYLS AND WATER MOLECULES HAVE BEEN RELAXED KEEPING ALL OTHER ATOMS FROZEN FOR EASE OF VISUALIZATION.  | 71  |
| FIGURE 36: SILICATE SPECIES PREDICTED FROM GEMS MODELING IN CASE A (A) BEFORE MIXING OF CALCIUM (B) AFTER MIXING OF CALCIUM (THE @ REPRESENTS A WATER MOLECULE IN THE FULL CHEMICAL FORMULA)-----  | 78  |
| FIGURE 37: A) NANOFOILS MORPHOLOGY OF C-S-H B) LIQUID STATE NMR OF REACTING SILICATE SOLUTION AND FINAL SOLID STATE NMR OF THE C-S-H -----   | 79  |
| FIGURE 38: SILICATE SPECIES PREDICTED FROM GEMS MODELING IN CASE B (A) BEFORE MIXING OF CALCIUM (B) AFTER MIXING OF CALCIUM (THE @ REPRESENTS A WATER MOLECULE IN THE FULL CHEMICAL FORMULA):-----   | 80  |
| FIGURE 39: : SILICATE SPECIES PREDICTED FROM GEMS MODELING IN CASE C (A) BEFORE MIXING OF CALCIUM (B) AFTER MIXING OF CALCIUM (THE @ REPRESENTS A WATER MOLECULE IN THE FULL CHEMICAL FORMULA):-----   | 81  |
| FIGURE 40: XRD ANALYSIS A) NANOFOILS B) TAPERED NANOFOILS C) NANOGLOBULES -----  | 83  |
| FIGURE 41: THE DIFFERENT GROWTH MECHANISMS OF C-S-H; A) NANOFOILS: 2 B) NANONEEDLES: BLUE CIRCLE SHOWS C-S-H NANONEEDLES, RED CIRCLE SHOWS THE FORMATION OF CALCIUM HYDROXIDE. C) NANOGLOBULES -----   | 84  |
| FIGURE 42: ALITE HYDRATION: ALITE HYDRATION AT W/S 0.7, WHERE $Y_{\text{LEFT}}$ -AXIS SHOWS THE HEAT RELEASED PER GRAMS OF ALITE AND X-AXIS SHOWS THE TIME IN HOURS, $Y_{\text{RIGHT}}$ -AXIS SHOW THE pH CHANGES DURING THE HYDRATION. AROUND 2HR, THE ACCELERATION REGIME BEGINS WITH THE FORMATION OF NANONEEDLES. THE PEAK IS REACHED AROUND 10H. -----  | 85  |
| FIGURE 43: TEM IMAGING FOR CASE E (A) BEFORE HYDRATION (B) 2 MINUTES (C) 30 MINUTES OF HYDRATION-----  | 86  |
| FIGURE 44: ) CALORIMETRIC CURVES FOR ALITE HYDRATION AT W/S 250, WHERE Y-AXIS IS HEAT RELEASED AND X-AXIS IS TIME IN MINUTES. THE EXPERIMENT IS QUITE REPRODUCIBLE AS SHOWN BY THE TWO REPETITIONS (BLUE AND ORANGE DOTS) PRESENTED. THE INCREASE IN THE HEAT IS THE MANIPULATION AND PLACEMENT OF THE SAMPLES HOLDER INTO THE CALORIMETER, THE REAL HEAT RELEASE MEASUREMENT STARTS AT THE GREEN BLOCK AFTER 5 MINUTES. -----   | 87  |
| FIGURE 45: DIFFERENT C-S-H MORPHOLOGIES AS A FUNCTION OF PRECIPITATION CONDITIONS A) UNIFORM NANOGLOBULES B) UNIFORM NANOFOILS C) TAPERED NANOFOILS AND CALCIUM HYDROXIDE. -----   | 92  |
| FIGURE 46 A) BARIUM SILICATES DOPANTGLOBULES (B1) WITHOUT $\text{Ca}^{2+}$ B) MIXED MORPHOLOGY OF C-S-H NANOFOILS AND BA DOPANTGLOBULES (B2) -----   | 93  |
| FIGURE 47 A) MAGNESIUM SILICATE DOPANTGLOBULES (M1) WITHOUT $\text{Ca}^{2+}$ B) MIXED MORPHOLOGY OF C-S-H NANOFOILS AND MG DOPANTGLOBULES (M2)-----  | 93  |
| FIGURE 48: ZINC SILICATE DOPANTGLOBULES (Z1) WITHOUT $\text{Ca}^{2+}$ -----  | 94  |
| FIGURE 49: MIX MORPHOLOGY OF C-S-H NANONEEDLES AND DOPANT CONICAL PYRAMIDS (Z2) -----  | 94  |
| FIGURE 50: SILICATE SPECIATION AT 0.175MM BEFORE MIXING -----  | 96  |
| FIGURE 51: SPECIATION DISTRIBUTION WHEN MIXED WITH CALCIUM-----  | 96  |
| FIGURE 52: SPECIATION DISTRIBUTION WHEN MIXED WITH MAGNESIUM -----   | 97  |
| FIGURE 53: MORPHOLOGY MECHANISM (THE REPRESENTATION IS NOT SCALE TO ACTUAL SIZES); A) SILICATE IONS AT HIGH pH B) CALCIUM CONDENSATED NANOFOILS FORMATION C) CALCIUM CONDENSATED TAPERED FOILS AND FORMATION OF ION-HYDROXIDE. D) DOPANTGLOBULES FORMATION. -----  | 97  |
| FIGURE 54: EXPERIMENTAL CONDITIONS AND DATA RECORDING -----  | 102 |

|  |     |
|--|-----|
| FIGURE 55:PH AND MOLAL IONIC STRENGTHS (A-C) AND THE CORRESPONDING PORTLANDITE AND C-S-H SUPERSATURATION RATIOS (D-F) AS A FUNCTION OF $\text{Na}_2\text{SiO}_3+\text{NaOH}$ SOLUTION ADDED AT 2.00 (A, D), 0.5 (B, E), AND 0.11 (C, F) $\text{ML.MIN}^{-1}$ FLOW RATES CALCULATED BY OLI SOFTWARE (OPEN MARKERS) AND OUR SPECIATION CODE AQEQBRM (LINES) (LEGENDS COMMON FOR BOTH GRAPHS).----- | 107 |
| FIGURE 56:CONCENTRATION PROFILES FOR DIFFUSION- AND INTEGRATION-CONTROLLED GROWTH <sup>24</sup> -----  | 109 |
| FIGURE 57: COMPETING GROWTH MECHANISMS AS A FUNCTION OF SUPERSATURATION <sup>36</sup> -----  | 110 |
| FIGURE 58: NANOFOILS MORPHOLOGY FOR $\text{Ca:Si} = 2$ -----   | 111 |
| FIGURE 59:EXPERIMENTAL $\text{Ca}^{2+}$ MOLE AMOUNTS (OPEN CIRCLES) AND PREDICTED VALUES (LINES) BASED ON AQEQBRM, EQBRM, AND PBE MODELING FOR 2 (A), 0.50 (B), AND 0.11 $\text{ML.MIN}^{-1}$ (C) INLET FLOW RATES; LEGENDS ARE COMMON FOR ALL GRAPHS. -----   | 115 |
| FIGURE 60:SIMPLE SCHEMATIC REPRESENTATION O POSSIBLE PATHWAYS AND TYPE OF ASSOCIATED PARTICLES-----  | 115 |
| FIGURE 61: AMOUNT OF C-S-H PRECIPITATED FROM SOLUTION AND THE CORRESPONDING PH VALUES FOR 2 (A, D), 0.50 (B, E), AND 0.11 $\text{ML.MIN}^{-1}$ (C, F) INLET FLOW RATES. -----  | 116 |
| FIGURE 62: TEMPORAL EVOLUTION OF SUPERSATURATION WITH RESPECT TO C-S-H AND PORTLANDITE, AND THE CORRESPONDING C-S-H NUCLEATION EVENTS FOR 2 (A, D), 0.50 (B, E), AND 0.11 $\text{ML.MIN}^{-1}$ (C, F) INLET FLOW RATES; VERTICAL DASHED LINES IN SUPERSATURATION GRAPHS INDICATE THE PERIOD OVER WHICH NUCLEATION TAKES PLACE AS PLOTTED IN (D-F) -----  | 117 |
| FIGURE 63:OVERLAID PLOTS OF SUPERSATURATION WITH RESPECT TO C-S-H (A), LINEAR GROWTH RATE (B), PRIMARY NUCLEATION (C), AND SECONDARY NUCLEATION (D) FOR DIFFERENT INLET FLOW RATES AS A FUNCTION OF TIME NORMALIZED WITH $t_{\text{END}}$ (TIME AT THERE IS NO MORE NUCLEATION AND $G < 10^{-14} \text{ M.S}^{-1}$ )-----  | 117 |

## List of tables

|   |     |
|---|-----|
| TABLE 1: TYPICAL COMPOSITION OF OPC .....   | 19  |
| TABLE 2: COMPONENTS OF HYDRATED CEMENT PASTE .....  | 23  |
| TABLE 3: VARIOUS STRUCTURAL MODEL OF C-S-H .....  | 28  |
| TABLE 4: THERMODYNAMICS PARAMETERS DESCRIPTIONS .....   | 32  |
| TABLE 5: SATURATION INDEX AND STATE OF SYSTEM .....   | 33  |
| TABLE 6: LIST OF IONS DOPED IN C-S-H SYSTEM .....   | 41  |
| TABLE 7   AMOUNT OF NaOH AND pH CALCULATED BY THERMODYNAMIC MODELLING (GEMS )FOR THE<br>SYNTHESIS OF C-S-H WITH DIFFERENT Ca:Si RATIOS COMPARISON. .... | 48  |
| TABLE 8: EXPERIMENTAL VS. THERMODYNAMIC MODELLING – pH, Ca:Si. ....   | 51  |
| TABLE 9: IR BAND ASSIGNMENT .....   | 55  |
| TABLE 10: RAMAN BAND ASSIGNMENT .....   | 57  |
| TABLE 11: . DIMER MOLE FRACTION $x_0$ AND MEAN REPEAT INDEX FOR THE FOUR COMPOSITIONS ANALYZED. ....  | 69  |
| TABLE 12: C-S-H SYNTHESIS CONDITIONS.....   | 76  |
| TABLE 13: ALITE HYDRATION CONDITONS.....  | 77  |
| TABLE 14: Q SPECIATION AND MCL FOR HOMOGENEOUS PHASES OF C-S-H IN CASE A AND C. ....  | 82  |
| TABLE 15: OVERALL EXPERIMENTAL CONDITIONS.....  | 91  |
| TABLE 16: CONSIDERED SPECIES AND THEIR TJ ACTIVITY COEFFICIENT PARAMETERS .....   | 106 |
| TABLE 17: MASS ACTION EQUATIONS FOR MODEL C-S-H PRECIPITATION SYSTEM .....  | 106 |
| TABLE 18: BOUND FOR UNKNOWN KINETICS PARAMETERS .....   | 110 |
| TABLE 19: OPTIMIZED KINETIC PARAMETERS .....  | 114 |



# 1 Introduction and Scope of thesis

## 1.1 Significance

Concrete, seen as a global commodity, is a type of composite material, where cement acts as binder, sand, and stones as aggregates and iron or steel bars as reinforcement as presented in Figure 1. Cement in the presence of water hardens and act as glue to bind the other components. Cement hydration is a complex phenomenon. As presented in Figure 1, concrete is the most widely used material, so abundant that cement production is one of the leading industrial sources of greenhouse gases among all construction materials, contributing to about 8% of global emissions, despite the lowest emission per kg.<sup>1,2</sup> To get an idea, this value it is roughly three times higher than the CO<sub>2</sub> emission from air transportation (2.2%) and still higher than the release of the entire chemical (5.3%) and steel industry (5.2%).<sup>3</sup> In the past decade or so, with the faster urbanisation rate, the annual cement production almost doubled itself and is expected to reach up to four-fold by year 2050.<sup>4</sup>

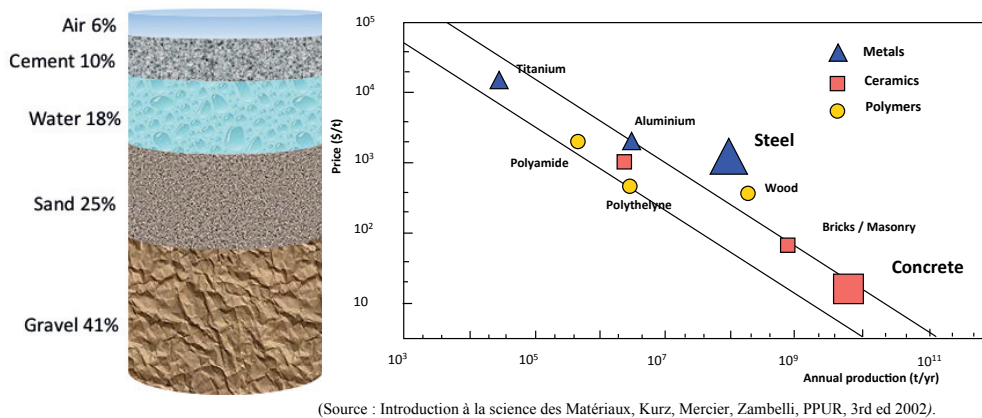


Figure 1: Ingredients of concrete and Price/production of different construction materials.

The world production of hydraulic cement was 3.36 gigatonnes with China (1800 t), India (220 t) and USA (63.5 t) being the top three producers by 2015<sup>5</sup>. About 40% of the CO<sub>2</sub> emissions originate from the combustion of fossil fuels used in operations while approximately 60% result from the transformation of limestone into calcium oxide ( $\text{CaCO}_3 \rightarrow \text{CaO} + \text{CO}_2$ ), leading to the formation of Alite ( $\text{Ca}_3\text{SiO}_5$ ) and Belite ( $\text{Ca}_2\text{SiO}_4$ ). The calcium silicate phases - Alite provides early age strength development (days to months) whereas Belite shows long-term strength development (months to years).

Due to rapid urbanisation, there is an increasing demand by the building sector for faster early age strength which has led to an increase in the Alite/Belite ratio. As a consequence, to transform some of the Belite that forms at 800 °C to Alite forming at 1400 °C, more burned lime must be used. Consequently, there are higher energy needs to produce cement with a

higher Alite/Belite ratio. Nearly 40% of the global energy consumed worldwide occurs in building and its operation and hence contributing to a huge global carbon footprint. Hence, using sustainable and affordable ways to produce concrete is a global priority, both on an environmental and economic front.

Despite the fact that Portland cement in its present form has existed for over a century, still, all its physical and chemical transformations are yet to be fully deciphered. Most of all, disagreement regarding the exact nature of the early hydration products still prevails. Besides the relatively simple principles of construction, the chemical mechanisms leading to strength development are not fully understood.<sup>4,6</sup>

One of the most widely accepted solutions is the use of supplementary cementitious materials (e.g. slag, fly-ash, metakaolin, and silica-fume, which have a lower carbon footprint) to replace part of the cement used to make concrete. The major limitation to this technology is low early age strength due to the modified rate of hydration.<sup>4</sup> A general lack of understanding of the hydration mechanisms that govern even the performance of ordinary Portland cement (OPC) impedes progress. This is due to the complexity of several minerals engaged in dissolution and precipitation reactions to form hydration products. The greatest difficulty is the lack of structural information on the formation of the main cement hydration product, calcium silicate hydrate (C-S-H),<sup>7,8</sup> which forms about 50-60% by volume of cement paste. This is linked to the fact that previously no method could synthesise C-S-H with Ca:Si ratios greater than 1.6, whereas in ordinary Portland cement this ratio is  $\geq 1.75$  at early ages.<sup>9-11</sup> As well as the very poor crystalline nature of C-S-H which prevents the structural elucidation by standard diffraction methods.<sup>7-9</sup>

The understanding of the hydration process is further complicated by additives/admixtures and external physical factors such as relative humidity etc.. Presently, no single characterization method exists that can follow the hydration process in its entirety. Therefore a multidisciplinary approach and a combination of methods are needed to elucidate the structure and growth mechanisms involved in hydration. Once achieved this will, in turn, allow a better control and use of sustainable materials in cement and concrete. This is the main goal of this thesis.

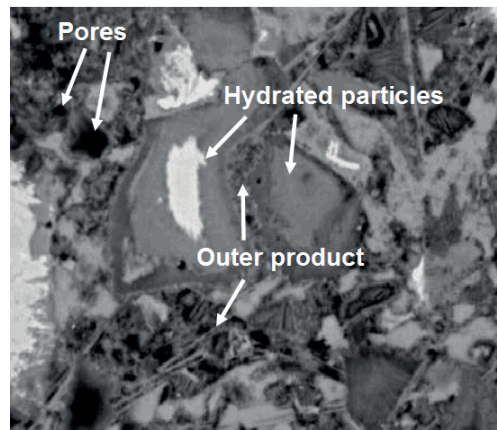
## 1.2 Dissertation scope and objectives

It is quite clear that to have a deep understanding of the early age hydration period, we need to have a more in-depth knowledge of the primary hydration product (i.e.) C-S-H and its process of nucleation and growth. Considering the hardened cement paste (HCP) micro-structure, it consists of variable pores and solids of different sizes. The microstructure of a mature cement paste can be seen in

Figure 2, which shows the major product as C-S-H, a highly disordered phase. Crystalline calcium hydroxide ( $\text{Ca(OH)}_2$ ), is the next major phase formed during hydration. Apart from C-S-H and  $\text{Ca(OH)}_2$ , there are traces of Ettringite and Monosulphate formed that also occurs in different morphologies and sizes. The rest of the volume can also consist of unhydrated cement particles. Moreover, there could be empty spaces or pores, left out deliberately or formed by

the improper consolidation of the paste or chemical shrinkage. The total pore volume is a function of the water/cement ratio, degree of hydration, and curing conditions .

With the above complexity of the real Portland cement system, it seems a difficult task to develop sufficiently advanced understanding regarding C-S-H. Thus, we need pure and homogeneous model systems to arrive at any sort of conclusive results. In this thesis, a synthetic system has been adopted with the aim of preparing C-S-H that is more representative of the Portland cement systems than previous synthetic approaches. Furthermore, the model system can be extended towards the more complex real system by doping with essential elements existing in the actual cement systems used in practice.



(Source: Image courtesy of Paul Stutzman, Concrete Microscopy Library, Illinois, USA)

Figure 2: Backscattered SEM image of a mature cement paste showing the main microstructural features.

The thesis was funded by the Swiss national foundation where my role in the project as an experimentalist can be divided into five parts.

- i) Develop a synthetic reactor system that can synthesise C-S-H with desired Ca:Si ratio, morphology and homogeneity.
- ii) Develop the characterization protocols for the synthetic C-S-H produced.
- iii) To elucidate C-S-H structural information by spectroscopic studies.
- iv) Shed light on the growth kinetics of the synthetic C-S-H.
- v) To approach the Portland cement system by doping the model synthetic system with elements known to be present in industrial cement.

During the process of understanding C-S-H, certain theories were developed that improves our understanding of cement hydration. In summary, the questions that needed to be answered at the outset of the thesis can be summarised as:

- Can we synthesise pure phase C-S-H, representative of the Portland cement at early ages?

- Can we elucidate the structure of C-S-H?
- What is the role of Calcium and its effect on silicate polymerization?
- Using kinetic analysis can an understanding the formation mechanism of C-S-H be found?
- What is the effect of doping on the pure C-S-H formation with other individual ions present in cement?

### 1.3 Organisation of thesis

The thesis is divided into two segments. Part one describes the general literature and current understanding of C-S-H, sets up the objectives and describes the materials and methods used. The second part consists of the results of the experimental studies and their analysis in the form of journal articles. In part 2, each chapter starts with a short introduction to the article presented and ends with the achieved results and outlook. Each article covers its own deep literature in the field of work presented for the article. The Supplementary material of each article can be found in the annexes at the end of the thesis.

**Chapter 1** – Is an introduction to the context of the thesis and sets up the overall objectives of the thesis work.

**Chapter 2** – Fundamentals and theoretical background of the topics touched on in the thesis work are briefly summarised.

**Chapter 3** – Materials and methods, developed or adopted for the experimental studies are described

**Chapter 4** – Synthetic system, synthesis & characterization, and structural evaluation via. FTIR and Raman: Article Kumar A, et.al; “*Controlled synthesis and characterization of homogeneous Calcium Silicate Hydrates phase with high Calcium to Silicate ratio*”, CCR, to be submitted

**Chapter 5** – Synthesis and characterization by DNP-NMR to evaluate the atomic structure of C-S-H: Kumar A, et.al; “*The Atomic-Level Structure of Cementitious Calcium Silicate Hydrate*”, JPCC, published on the cover page of JPCC.

**Chapter 6** – Application of thermodynamics control on real cement system. Article: Kumar A, et.al; “*Cementitious Calcium silicate hydrates formation pathways and insights into alite hydration control*”, CCR, to be submitted.

**Chapter 7** – Effect of the other divalent ions on the formation of C-S-H: Article: Kumar A, et.al; “*Initial observations: Effect of the presence of divalent ions ( $Ba^{2+}$ ,  $Mg^{2+}$ ,  $Zn^{2+}$ ) on the morphology of precipitating calcium silicate*”, Conference Article.

**Chapter 8** – Kinetic analysis of C-S-H growth by the use of population balance modelling Kumar A, et.al; “*Simplistic model for growth of Calcium Silicate Hydrates from solution*”, PCCP, to be submitted

**Chapter 9** – Summary of the thesis and *Quo Vadis*

**Annexure** – Supplementary Information

## 2 Fundamentals

### 2.1 Introduction

This chapter covers state of the art for the thesis work that can be divided into two categories. Firstly, understanding the Portland cement system, the origin of C-S-H and the constraints related to its studies in Portland cement system. It provides the basic introduction to the production of cement and the underlying chemistry. The hydration process leading to the formation of many phases, in particular, the main phase C-S-H. Secondly, to study C-S-H synthetically one needs a good understanding of C-S-H part (i.e.) silicate chemistry and its behaviour under different thermodynamics conditions. Precipitation being the chosen approach to synthesise C-S-H, the state of the art regarding precipitation processes is briefly presented. It is needed to work out a controlled synthetic system to produce industrially relevant uniform C-S-H phases and model its formation. Precipitation in principle combines particle formation (nucleation event) and its growth, is also very briefly presented. The simple schematic in Figure 3 shows all the fundamental aspects described split into three major section for this chapter.

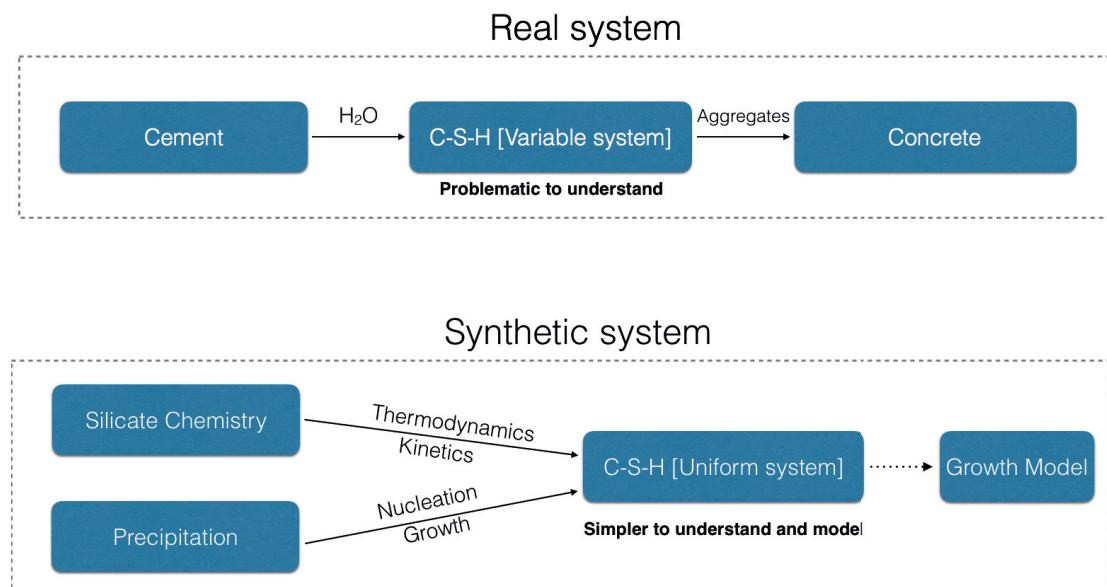


Figure 3: a) Portland cement system: Complex C-S-H formation b) Steps to designing a new synthetic system to understand uniform C-S-H system.

## 2.2 Portland cement system

### 2.2.1 Cement

Cement acts as the chemical adhesion between the aggregates, making up to 10% of the concrete by volume. In the past, the Roman's describe the masonry of crushed stones as aggregates and burned lime as glue, as opus caementicium, one of the first traces of currently used word "cement".<sup>12</sup> The Pantheon, constructed in about 125 AD, to date is the world largest unreinforced dome, is a superb example of cementitious material use. Fast forward to the present day cement consisting of  $\text{CaO}$ ,  $\text{SiO}_2$ ,  $\text{Al}_2\text{O}_3$  and  $\text{Fe}_2\text{O}_3$ <sup>12</sup>, was developed by Issac Charles Johnson in 1845, prepared at elevated temperature. However, the primary idea of such material was planted by William Aspidin in 1824. Ordinary Portland cement (OPC) is a mixture of compounds prepared by burning limestone and clay together at temperatures ranging from 1400 to 1600° C.<sup>13</sup> Figure 4, describes the manufacturing processes, starting from raw materials to final powdered cement.<sup>12</sup>

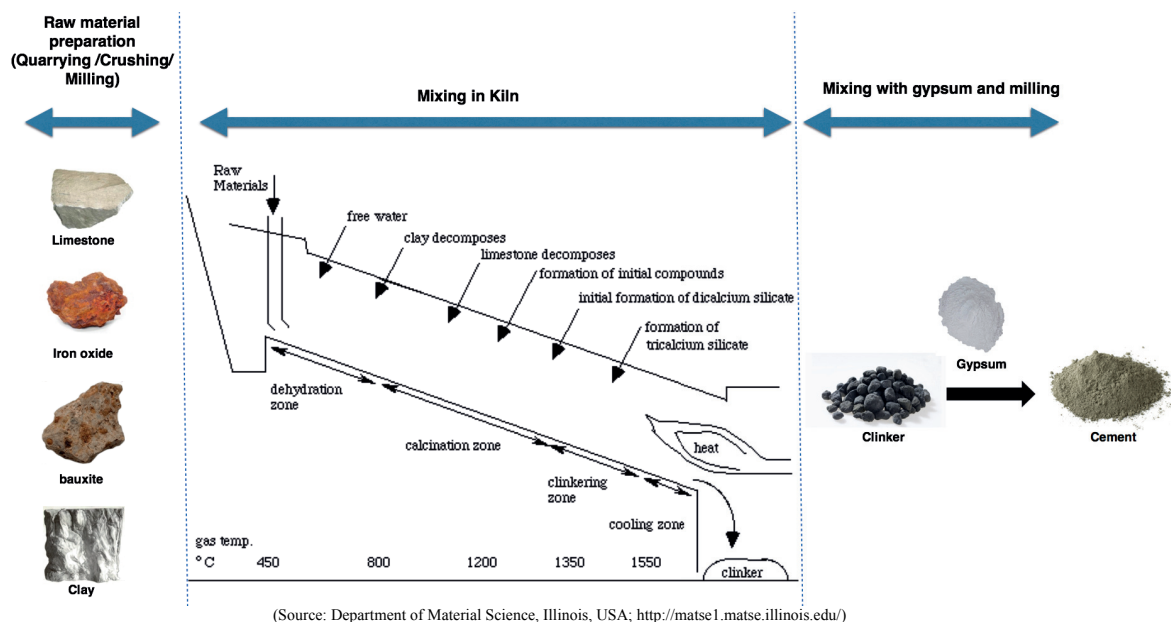


Figure 4: General flow chart of cement production, schematic diagram of rotatory Kiln, from raw material to clinker inside rotatory kiln

The mixture of raw materials is heated in inclined rotating steel cylinders that can be up to a hundred meters in length. This mix enters and moves down from the higher end, while heat is generated at the lower end of the kiln by the injected fuel. The burning fuel provides the necessary heat for materials to react and it can take up to hours to pass through the kiln. Usually, the reacting raw materials pass through four stages, evaporation, calcination - decomposition leading to loss of carbon dioxide and bound water, Clinkering - formation of calcium silicates and final stage is cooling.<sup>14,15</sup> After these four stages, "clinker" is formed. It is further cooled and ground to a certain size before mixing with gypsum and other additives to form the ordinary Portland cement. Ordinary Portland cement (OPC) consists of five major compounds and some minor. The typical composition is listed by weight percentage in OPC is given in



Table 1.<sup>16,17</sup>

| Cement Compound                                 | Weight Percentage | Chemical Formula   |
|---|-------------------|--|
| Tricalcium silicate (C <sub>3</sub> S) or Alite | 50 %              | Ca <sub>3</sub> SiO <sub>5</sub> or 3CaO·SiO <sub>2</sub>  |
| Dicalcium silicate (C <sub>2</sub> S) or Belite | 25 %              | Ca <sub>2</sub> SiO <sub>4</sub> or 2CaO·SiO <sub>2</sub>  |
| Tricalcium aluminate (AfT)                      | 10 %              | Ca <sub>3</sub> Al <sub>2</sub> O <sub>6</sub> or 3CaO·Al <sub>2</sub> O <sub>3</sub>  |
| Tetracalcium aluminoferrite (AFM)               | 10 %              | Ca <sub>4</sub> Al <sub>2</sub> Fe <sub>2</sub> O <sub>10</sub> or 4CaO·Al <sub>2</sub> O <sub>3</sub> ·Fe <sub>2</sub> O <sub>3</sub> |
| Gypsum  | 5 %               | CaSO <sub>4</sub> ·2H <sub>2</sub> O   |

Table 1: Typical composition of OPC

### 2.2.2 Cement hydration

The Portland cement consists of Alite (an impure form of tricalcium silicate), Belite (an impure form of dicalcium silicate), tricalcium aluminate, ferrite and added gypsum when in contact with water this leads to the formation of portlandite, C-S-H, hydrogarnet, ettringite, monosulfate and iron oxide. Upon the addition of water, tricalcium silicate rapidly reacts to release calcium ions, hydroxide ions, and a large amount of heat. This reaction step is called dissolution and the dissolved ions combine to form precipitates. Dissolution is the disassociation of solute particle from the solid surface and distribution in a solvent (water in our case) or foreign matter to gain entropy according to the 2<sup>nd</sup> law of thermodynamics. This occurs at the expense of bond breakage between the solute particles leading to the disintegration of the material, the opposite of the crystallisation process. In a simple sense, the whole process can be roughly summarised in two steps, firstly the escape of solute molecules or reaction rate at the surface and secondly, diffusion of these solute molecules into the bulk liquid phase. Hence the interfaces between the solute material and the solution play a very important role. The overall reaction rate is either limited by diffusion or by the interface reaction rate, as described schematically in figure 5, the slowest step in the sequence is the rate-determining step (RDS).<sup>18,19</sup>

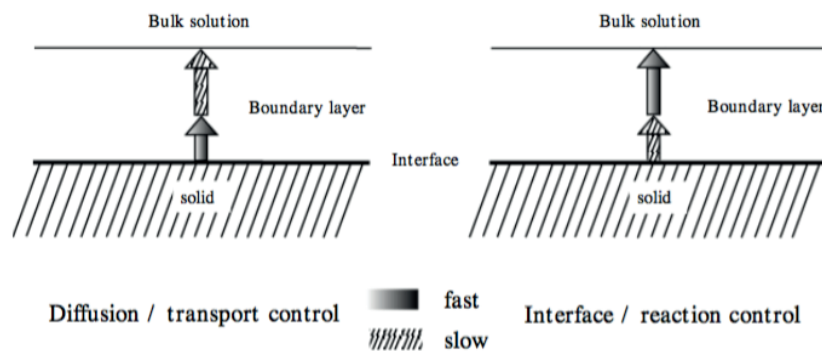


Figure 5: Dissolution modes - Slowest is the rate-determining step (RDS) of the process<sup>18</sup>

Several factors can affect the dissolution process, some of which can be inherent and some environmental. Inherent parameters such as interatomic forces, crystal structure and defects and polymorphism can all influence the dissolution of the solute material. A general elementary school rule “like dissolve like” (i.e.) non-polar solvent dissolve non-polar or non-ionized solute and vice-versa. The dissolution process can be influenced by environmental conditions such as

saturation state of the system expressed by a  $\Delta G$  function. With the limits  $\Delta G = 0$  equilibrium and  $\Delta G = \infty$  infinitive dilution (under saturation). Impurities in the system, pH and other parameters such as inhibition of mineral dissolution by the formation of a protective thin layer of precipitate that inhibits further dissolution of the minerals.<sup>17</sup> During Alite hydration, the pH rises sharply with the release of hydroxide ( $\text{OH}^-$ ) ions.<sup>11</sup> The reaction continues producing silicate, calcium and hydroxide ions until the system becomes saturated with respect to calcium hydroxide and C-S-H. Once this occurs, the calcium hydroxide starts to crystallise and simultaneously, calcium silicate hydrate begins to form. Ions precipitate out of solution accelerating the dissolution reaction of tricalcium silicate to calcium and hydroxide ions (Le Chatelier's principle). Furthermore, the existing calcium hydroxide and calcium silicate hydrate crystals provide a heterogeneous surface upon which more C-S-H or  $\text{Ca}(\text{OH})_2$  can form. As shown in Figure 6 (1-4), the C-S-H crystals grow thicker making it more difficult for water molecules to reach the unhydrated tricalcium silicate. The speed of the reaction is now controlled by the rate at which water molecules diffuse through the calcium silicate hydrate coating. This coating thickens over time causing the production of calcium silicate hydrate to become slower and slower.<sup>12,20</sup>

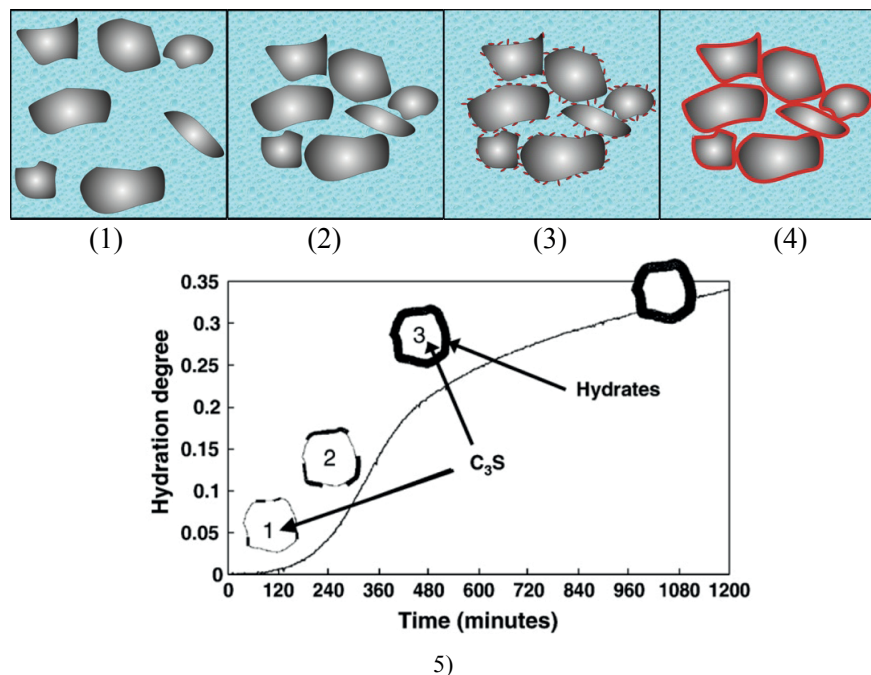
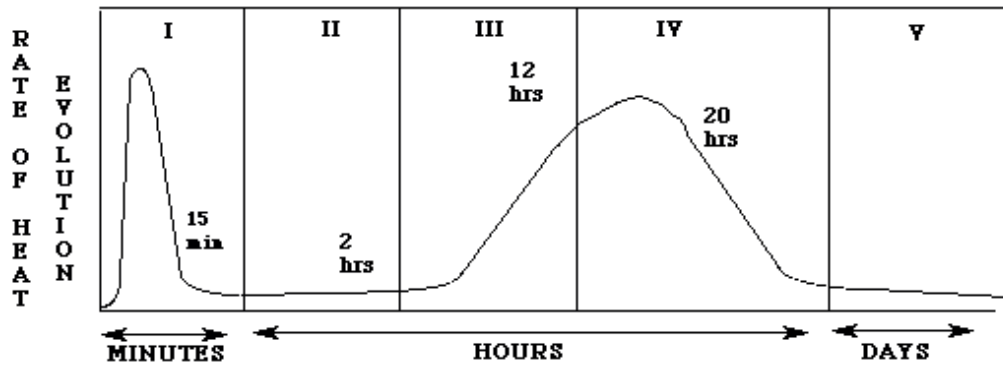


Figure 6: (1) Partial dissolution of C<sub>3</sub>S (2) the grains start to agglomerate (3) C-S-H starts to nucleate heterogeneously on the C<sub>3</sub>S surface (4) which enhances the hardening of the cement until the C-S-H layer reaches a critical thickness when the hydration is limited by diffusion of water. (5) Schematic of C<sub>3</sub>S hydration versus time.<sup>12,20</sup>

Different stages in hydration process are well charted by calorimetry studies. The heat generated is shown below as a function of time. It can be described in five stages presented in figure 7. In stage I, initial burst in the heat evolution is seen from the most reactive constituents of the cement compound that rapidly dissolve. Stage II is known as the induction period. The evolution of heat slows dramatically in this stage and can last from one to three hours. Physically the concrete is in a plastic state that allows easier workability. The initial setting starts by the end of this stage.





(Source: Department of Material Science, Illinois, USA; <http://matse1.matse.illinois.edu/>)

Figure 7: Rate of heat evolution during the hydration of Portland cement.

In stages III and IV, hydration of tricalcium silicates shows a peak in heat evolution and during the formation of C-S-H and  $\text{Ca(OH)}_2$ , eventually reaching a maximum and then descending. During these stages, concrete hardens. Stage V is reached after around 36 hours. The slow formation of hydrate products continues as long as water and unhydrated silicates are available. Typically, many theories have been proposed in past explaining the onset of the induction regime in stage II and corresponding termination. Some authors suggested it occurs due to formation of protective metastable layer over Alite grains considerably slowing down the dissolutions.<sup>21–26</sup> Formation of less soluble educts by surface protonation of Alite leading to reduced dissolution.<sup>27,28</sup> Pore solution composition in combination with lowering surface defects may also slow the dissolution process.<sup>4,29</sup> Formation of electric double layer with Si-rich surface and adsorption of  $\text{Ca}^{2+}$  ion on these surface leading to positive charges and hindering further dissolution, due to an initial incongruent dissolution of Alite.<sup>19,30</sup> the density of crystallographic defects have been correlated to the length of the induction period<sup>29,31,32</sup> and the presence of Aluminium leading to formation of Calcium aluminate silicate hydrates (C-A-S-H) phases are presented as reasons for the onset of the induction period.<sup>33</sup> Whereas the termination of the induction period has been related to rupture of the protective layer by osmotic pressure.<sup>30</sup> Formation of C-S-H from metastable C-S-H phases or ion composition in the pore solution leading to loss of protective layer.<sup>26,34</sup> Further growth of the C-S-H can lead to rapid dissolution of Alite phase.<sup>35–37</sup> Some authors related the termination of induction period to poisoning of  $\text{Ca(OH)}_2$  precipitation sites being eliminated by consumption of Si ion in formation of C-S-H,  $\text{Ca(OH)}_2$  precipitation revived, determining the rate of overall reaction.<sup>38,39</sup>

### 2.2.3 Microstructure and strength development

In general, in Portland cement the rates of hydration during the first few days ranked from fastest to slowest are **tricalcium aluminate ( $\text{C}_3\text{A}$ )** > **tricalcium silicate** > **tetracalcium aluminoferrite** > **di-calcium silicate**. The aluminate and sulphate phases begin to react and go into the solution and with rising saturation of these species, within a matter of minutes, needle-shaped crystals of calcium trisulfoaluminate hydrate, called ettringite appears. At later stages, ettringite may become unstable and will decompose to form monosulfoaluminate hydrate.<sup>40</sup> It is followed by hexagonal crystal formation of calcium hydroxide and fibrous

particles of calcium silicate hydrates filling up the spaces between the aggregates. Hence providing the early age strength. As seen in figure 8, the C-S-H formed from hydration of Tricalcium silicate ( $C_3S$ ) is responsible for most of the early strength (first 7 days). Di-calcium silicate ( $C_2S$ ), which reacts more slowly, contributes only to the strength at later times.

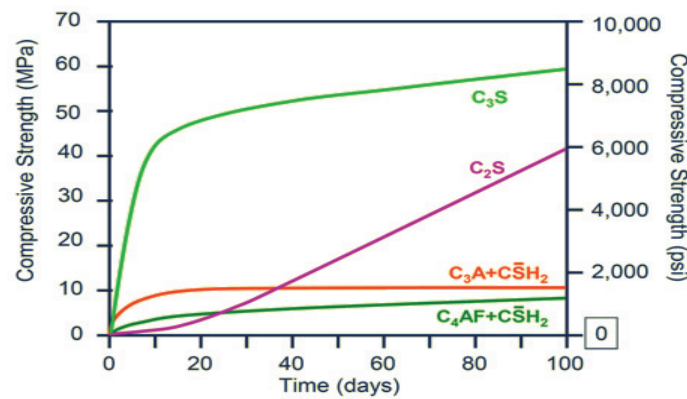
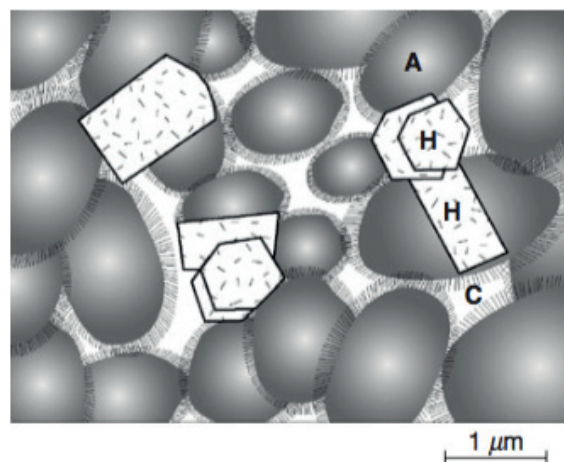


Figure 8: Compressive strength development over time in pastes of pure cement compounds <sup>41</sup>

From a microstructural point of view, the formed phases are not consistent in sizes or morphology. The inhomogeneity in the microstructure governs properties like strength and other mechanical properties. Rheological properties of freshly mixed cement paste also influence the microstructure of the hardened paste.<sup>17</sup> In figure 9, a model of well hydrated is presented (adopted from - Mehta, P. & Monteiro, P. J. M. *Concrete: Microstructure, Properties, and Materials*. 2006). “A” represents an aggregation of poorly crystalline C-S-H particles which have at least one colloidal dimension (1 to 100 nm). Inter-particle spacing within an aggregate is 0.5 to 3.0 nm (Avg. 1.5 nm). H represents hexagonal crystalline products such as  $Ca(OH)_2$ . They form large crystals, typically around 1  $\mu m$ . C represents capillary cavities or voids which exist when the spaces originally occupied by water do not get completely filled with the hydration products of cement. The size of capillary voids ranges from 10 nm to 1  $\mu m$ , but in well-hydrated pastes with a low water/cement ratio, they are less than 100 nm<sup>17</sup> as summarised in Table 2.



(Source: Mehta, P. & Monteiro, P. J. M. *Concrete: Microstructure, Properties, and Materials*. 2006)

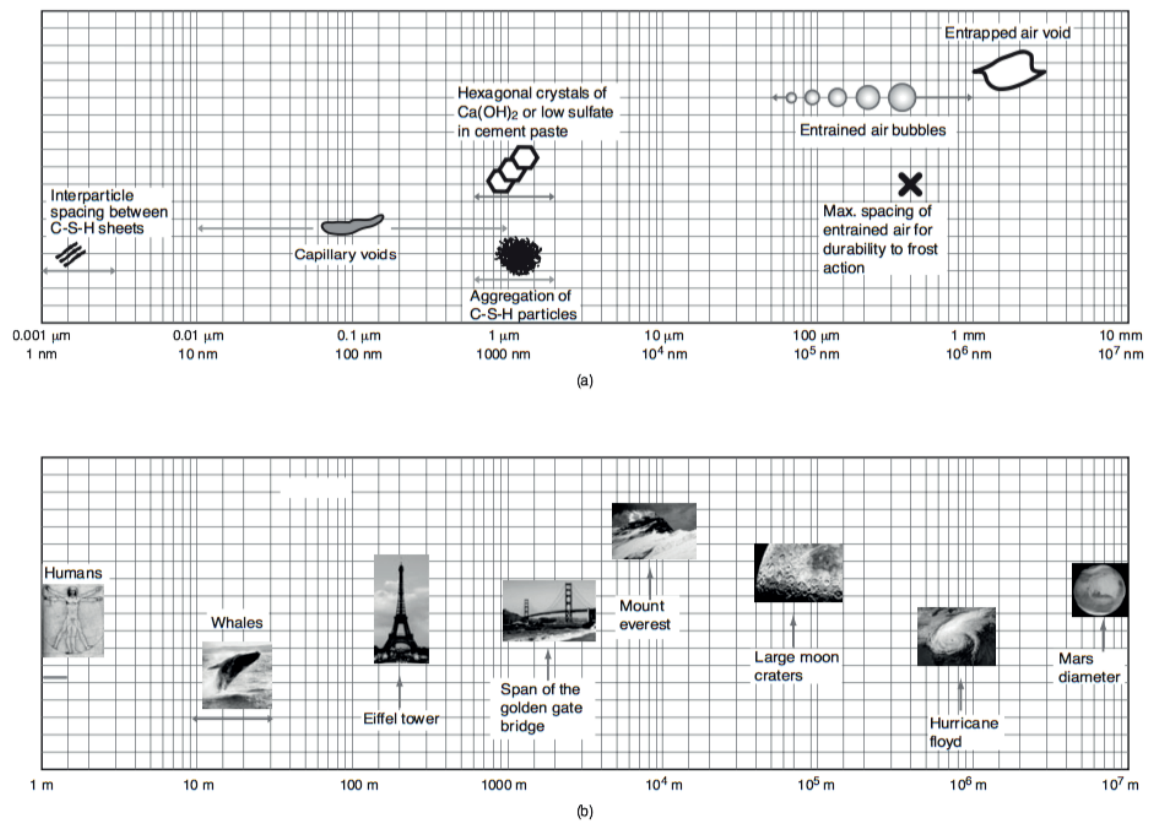
Figure 9: Model of a hydrated Portland cement paste

The microstructure can be classified into the following segments and their % occupancy by volume.

| Sl.no | Solids in the hydrated cement paste | Voids in hydrated cement paste | Water in cement paste  |
|-------|-------------------------------------|--------------------------------|------------------------|
| 1     | Calcium silicate hydrate: 50-60%    | Interlayer space in C-S-H      | Capillary water        |
| 2     | Calcium Hydroxide: 20-25 %          | Capillary Voids                | Adsorbed water         |
| 3     | Calcium Sulphoaluminate: 15-20%     | Air voids                      | Chemically bound water |
| 4     | Unreacted cement Grains: 1-15%      |                                | Interlayer water       |

Table 2: Components of hydrated cement paste

The variation of the size involved in the microstructure of the hydrated cement paste is presented schematically in Figure 10<sup>17</sup>, with comparison compared to real life examples.



(Source: Mehta, P. & Monteiro, P. J. M. *Concrete: Microstructure, Properties, and Materials*. 2006)

Figure 10: *a)* Dimensional range of solids and pores in a hydrated cement paste. *(b)* In Fig. 2-7a, the dimensional range covers seven orders of magnitude. To illustrate how wide the range is, *b)* illustrates a similar range using the height of a human being as a starting point and planet Mars as the ending point.<sup>17</sup>

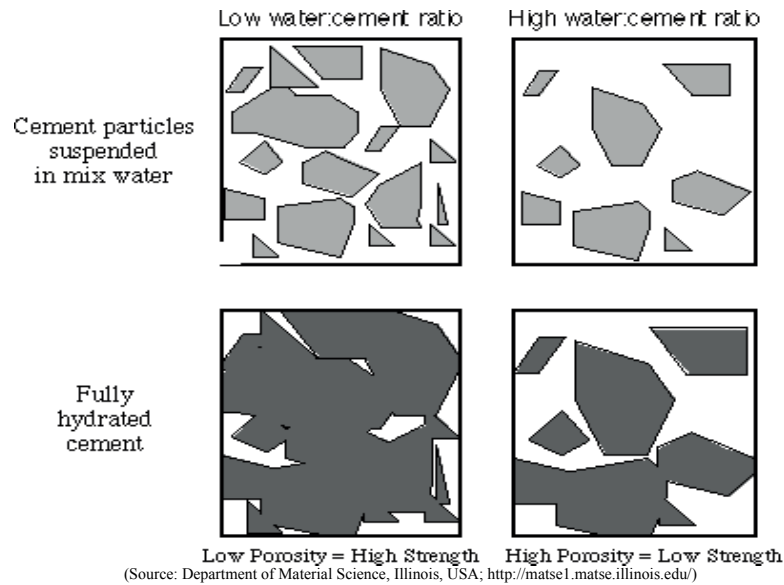


Figure 11: Relationship between water/cement ratio and porosity

The water content in the hydration process plays a crucial role that is responsible for the strength development. The hydration process uses up only some of the added water and the remaining provides the workability to concrete and remains in the pore spaces. The higher the quantity of these pores diminished the amount of strength-forming calcium silicate hydrate diminishes the mechanical properties of concrete. Consider the figure 11, with higher water content we have disconnected hydrated cement with high porosity and vice versa with low water content. Although the growth mechanism of these C-S-H is still debatable, by now it is quite clear that a better understanding of C-S-H formation in the real cementitious systems can allow us to manipulate the composition of cement towards more sustainable construction with higher durability.

## 2.2.4 C-S-H

It is a herculean task to understand C-S-H formation, growth and kinetics in a real system due to inhomogeneity within the C-S-H phase itself, let alone the complexity caused by numerous phases in the hydrated system. The fact that the term C-S-H is hyphenated signifies that C-S-H is not a well-defined compound, the Ca:Si ratio varies between 1.2 and 2.1 and the structural water content varies even more.<sup>42</sup> The structure of C-S-H can be looked at from three different ranges— atomic level, meso level, microstructure level.

### 2.2.4.1 Atomistic structure

C-S-H can be defined by its Ca:Si ratio, Si-OH content, Ca-OH content, and mean chain length. Any good model prediction towards the C-S-H structure should be able to explain the variations in these defining elements. C-S-H possess short range order.<sup>43</sup> With variable composition, it appears to have bimodal composition distribution and become more homogeneous with hydration over a year.<sup>42</sup> Chromatographic studies on the tri-methyl-silylation system for Si groups revealed for the first time, the existence of dimers at the early age of hydration and six

months beyond to longer chains such as pentamer, octamers etc.<sup>44</sup> In fact at much later stages the study reported the ratio of dimer to the polymer being 0.6.

With advances in NMR spectroscopy, more studies were made using  $^{29}\text{Si}$  NMR,<sup>45–49</sup> to understand the silicate environments in C-S-H structures that can distinguish between different silicate species ( $\text{Q}^0$  – monomer,  $\text{Q}^1$  – dimer etc. see Figure 12) and were found to be consistent with earlier studies, reporting dimer at early stages with no cross-linking indicating linear chains. With end member silicates ( $\text{Q}^1$ ) and middle members ( $\text{Q}^2$ ), the mean chain length (MCL) can be calculated<sup>50</sup> and reported to be around 2 for first few days of hydration. With some percentage ( $\sim 8\text{--}10\%$ ) of monomers still observed at 12 months of hydration and beyond (presumably from unreacted anhydrous silicates as shown by Pustovgar et al<sup>48</sup>). The MCL increases from 2 to 3.1 in OPC and 2 to 3.3 in Alite paste after one year of hydration and reportedly does not exceed 5 even after 26 years.<sup>50</sup> It was assumed that the dimeric silicate is somewhat connected by the bridging silicate in the “dreierketten” structure as observed in naturally occurring mineral “tobermorite”, as shown in Figure 12. The layered structure of tobermorite is composed of a calcium plane (sky-blue sphere) bordered by two silicate chains (tetrahedral) via oxygen atoms (in red) and separated by the interlayer space containing water molecules (transparent sphere), hydroxyl groups and some calcium ions. The details of the tobermorite structure is explained by Bonaccorsi et.al<sup>51</sup> where the distance between the two layers is  $14 \text{ \AA}$

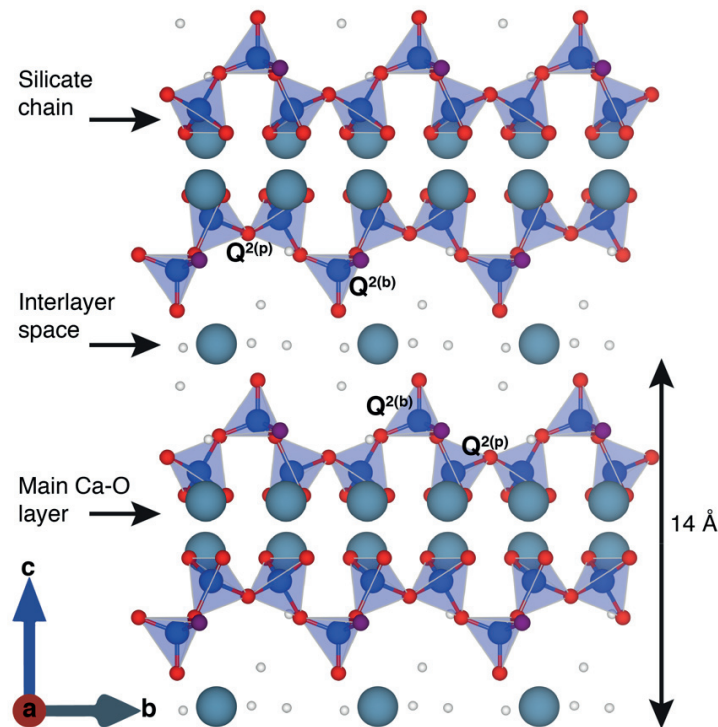


Figure 12: Tobermorite structure and Silicate nomenclature

Other advanced NMR studies<sup>45</sup> on C-S-H's with Ca:Si ratios of 0.7, 0.9, 1.5 prepared by mixing  $\text{SiO}_2$  with  $\text{CaO}$  in a water suspension with a water to solid ratio of 50, reported the ratio between the paring silicate in the plane ( $\text{Q}^{2p}$ ) and bridging ( $\text{Q}^{2b}$ ) silicates, close to two conforming to a “deirerketten” structure. They also observe some  $\text{Q}^3$ - $\text{Q}^3$  cross-linking between Si chains decreasing with higher Ca:Si ratio, whereas the absence of  $\text{Q}^1$ - $\text{Q}^1$  single indicating  $\text{Q}^1$ , the signal coming from end chain  $\text{Q}^1$ , increasing with higher Ca:Si ratios. Also, with increasing Ca:Si, they infer the presence of Ca-OH in the interlayer and reported to interact with bridging tetrahedral at lower ratios. Whereas Ca-OH interacts with all Si at higher ratios indicating its presence in the calcium layer itself or a reduction in the interlayer distance. Klur et.al<sup>47</sup> reported by NMR relaxometry studies, the presence of two distinct proton environment in C-S-H (Ca: Si - 1.05), interacting with Si. This is an indication of two different phases in the sample or two different environments in the same phase. With Raman spectroscopic studies<sup>52</sup> on C-S-H with Ca:Si between 0.2 to 1.5, the mean Si- O- Si angle was found to be  $139.7^\circ$ - $140.7^\circ$ , similar to  $14 \text{ \AA}$  tobermorite  $138.55^\circ$ . All these experimental data's over the year has led to many structural models<sup>50,53-55</sup> based on  $14 \text{ \AA}$  tobermorite due to great similarities in the findings. Another form of tobermorite also exists with  $11 \text{ \AA}$  distance between the layers. The problem with these tobermorite based structural model is the composition of Ca:Si ratio in the structure of tobermorite is 0.83, whereas the compositional ratios in cementitious materials are varying between 0.7 to 2.1. In order to explain the Portland cementitious system from these models, there are various ways to increase the Ca:Si ratio. This is the point where different models start to diverge. However, there are three noted ways to increase the ratio,<sup>50</sup> described below.

- Eliminating the bridging tetrahedrons originally in the tobermorite structure, forming dimers and polymers distribution of  $3n-1$ , n being an integer. Similar observations were made for polymer distribution by state of the art experimental studies.[reference needed]
- Deprotonating the Si tetrahedrons forming  $\text{Si-O}^-$  groups to be charge balanced by  $\text{Ca}^{2+}$  ions, also consistent with the observation of Calcium in the interlayer from prior experiments.
- Fully depolymerised (no bridging Si tetrahedrons) and fully deprotonated structure of tobermorite still has maximum Ca:Si ratio of 1.5, much lower than the average observed in early age Portland cement systems with a Ca:Si ratio of 1.75

From spectroscopic studies the Si-O-H bonding still exists in the structure even at higher Ca:Si ratio of 1.5, meaning that in addition to the above-mentioned methods there has to be an additional defective mechanism to introduce more Calcium in the structure, leading to use of the term “*Defective tobermorite*” structure. Based on this piece of information different authors have proposed categorically following three ways to model the cementitious system from tobermorite structure. Firstly<sup>53</sup>, tobermorite-portlandite model: deprotonation of Si-O-H is charge compensated by Ca-O-H instead of  $0.5\text{Ca}^{2+}$ , this extra calcium being accommodated in the interlayer. Secondly<sup>43</sup>, charge compensation of deprotonated Si-O-H by a layer of portlandite intermixed with tobermorite layers, (i.e.) presence of Ca-O-H as intra-layer than being in the interlayer. Lastly,<sup>56</sup> intermixed tobermorite and Jennite. Jennite is another naturally



occurring mineral with infinite sheets of dreierketten structure like tobermorite but the Calcium layer is not linear instead they are corrugated. Although with jennite the Ca:Si ratio is 1.5, it can be raised by deprotonation and de-polymerization process similar to tobermorite.

#### 2.2.4.2 Mesoscale structure

Although the exact mesostructure of C-S-H is still debatable, several models have been proposed to explain the properties of the materials. The Feldman-Sereda model,<sup>57</sup> based on the experimental observations, visualises the C-S-H structure as being composed of an irregular or kinked array of layers which are randomly arranged to create interlayer spaces of different shapes and sizes (5 to 25 Å). It was based on the fact that C-S-H being tobermorite like structure, combined with observation of hysteresis effects and irreversible behavior upon drying and rewetting. With drying or removal of water bring the layers closer leading to formation of permanent crystalline bonds between the layer, explaining irreversibility. Hysteresis was concluded to be occurring due to the way water leave the layer from the edges, meaning the distance between the layer at the edges will be smaller than the core region until complete drying of the interlayer. Upon rewetting, water enters from the edges towards the slowly shrinking core region with smaller interlayer distance at the edges. The authors developed a microstructural model composed of relatively long crystalline sheets which in some regions are connected and form nano-crystalline regions which consist of a few sheets as seen in the figure 13(a). A similar model<sup>58,59</sup> based soft X-ray microscopy of hydrating silica particles in a solution saturated with respect to portlandite, has also been proposed. The model considered two types of region, one defect free linear region and other being highly defective regions leading to curvature of the C-S-H sheets. This also explains the formation of “sheaf-of-wheat” morphology formation of C-S-H from silicate particles in supersaturated solution of portlandite. The authors explain the linear region of sheets allows near sheets to nucleate on top of each other with limited growth in perpendicular region, whereas with defective region (curves) would allow the new sheet to grow independently. Thus longer the chain gets, more are the defective regions, more are the nucleation sites for growth of “sheaf –of-wheat” like morphology.

Based on specific surface area measurement, Jennings et.al proposed a different microstructural model where he considers spherical building blocks aggregating to form “globules”. These globules can pack themselves to form high density(HD) C-S-H or loosely to form low density (LD) C-S-H. This is relevant to the two density areas observed in the morphology of C-S-H in the cementitious system (outer and inner product<sup>48</sup>). Considering this model, the size of building blocks could be estimated (~ 1.2 nm or if adjustments are made due to the underlying layer structure of C-S-H: ~ 2.5 x 5 nm) and their density to be 2.6 g/cm<sup>3</sup> and their approximate chemical formula: (CaO)<sub>1.7</sub> (SiO<sub>2</sub>)<sub>1.8</sub> (H<sub>2</sub>O)<sub>1.8</sub>. The model is presented in the figure 13b.

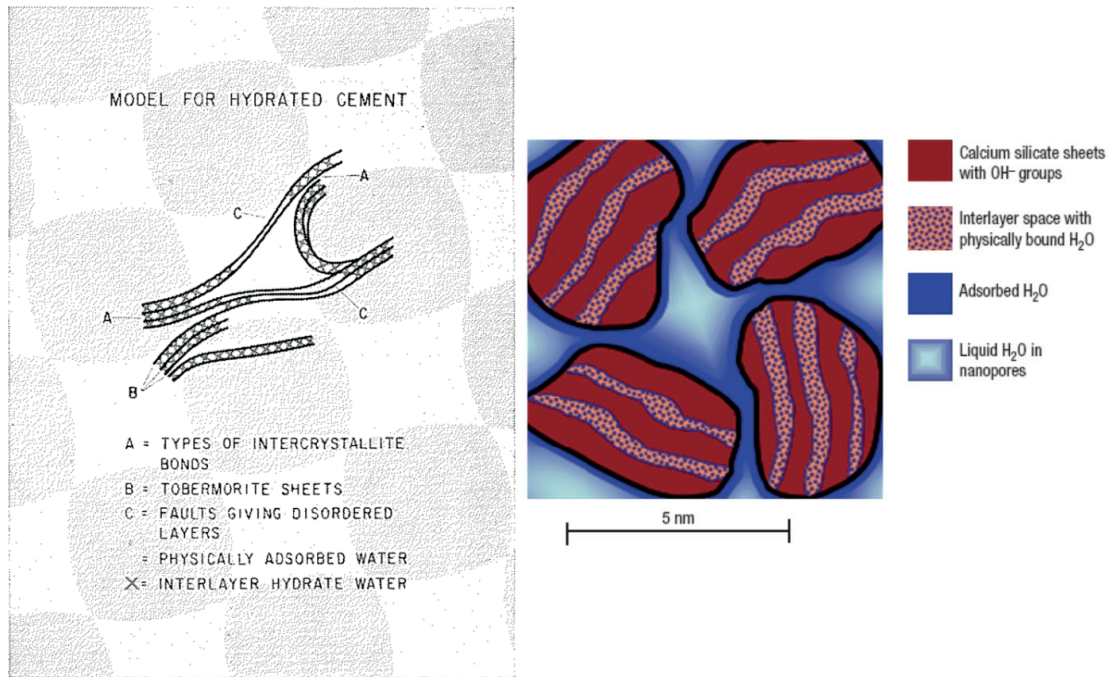


Figure 13: a) Feldman -Sereda model<sup>57</sup> b) Jennings Model<sup>7</sup>

All the authors seem to agree upon the fact that C-S-H has very high specific interface area with a large quantity of nanometric pores. These should be taken into account for modelling as they will influence the final microstructural model and properties. In table 3 a summary of some other models proposed in the literature and the experimental methods from which they based their models.

| Name of the model | Experiment     | Type of C-S-H Model               | Characterization Method                                |
|-------------------|----------------|-----------------------------------|--|
| Powers            | Water sorption | Colloids                          | All products gels, particle size 5 nm, gel pore volume |
| Taylor            | X-ray /TGA     | Imperfect tobermorite and jennite | Atomic structure of C-S-H                              |
| Braunauer         | Water sorption | 2-3 Layers                        | Structure changes upon drying                          |
| Wittmann          | Modulus vs. RH | Colloids                          | Structure not defined                                  |

Table 3: Various structural model of C-S-H

#### 2.2.4.3 Microstructure/Morphology

Due to their nanoscale dimensions, agglomeration tendency, instability under electron beams, C-S-H phases have only been imaged with limited resolution. In general, there are two types of C-S-H morphologies. One being observed in early ages of hydration in the pores spaces around the un-hydrated structures and other being observed at the later stages of hydration within the original hydrated volume. They are referred as outer C-S-H or low density (LD) and inner C-S-H or high density (HD) respectively.<sup>50,60-62</sup> Outer C-S-H has more defined texture,



and reported in Alite hydration with water to solid ratio of 0.3 grew up to 1.5 microns in 600 days of hydration. Inner product C-S-H is much more homogeneous, composed of more globular particles with diameters of  $\sim 4\text{-}6\text{ nm}$ .<sup>50</sup> The pores in inner product C-S-H are much smaller than in outer product C-S-H (up to about 10 nm). The morphology of inner product C-S-H seems to be unaffected by the changing Ca:Si ratio, where outer product C-S-H seems to change depending on the Ca:Si (starting chemical conditions). The addition of alkali (KOH, NaOH) also effects the structural order in C-S-H.<sup>60,62</sup> Consider the Figure 14, it shows the different steps of Alite hydration leading to C-S-H formation as seen from the environmental SEM (ESEM).<sup>63</sup> Firstly, the unhydrated grains of Alite with smooth surfaces lead to the formation of fibrous C-S-H and some unreacted grains after 24h. After 96h, one can clearly see the two different phases of C-S-H, namely high density or inner C-S-H formed at later stages of hydration and low density or outer C-S-H formed at early ages of hydration.

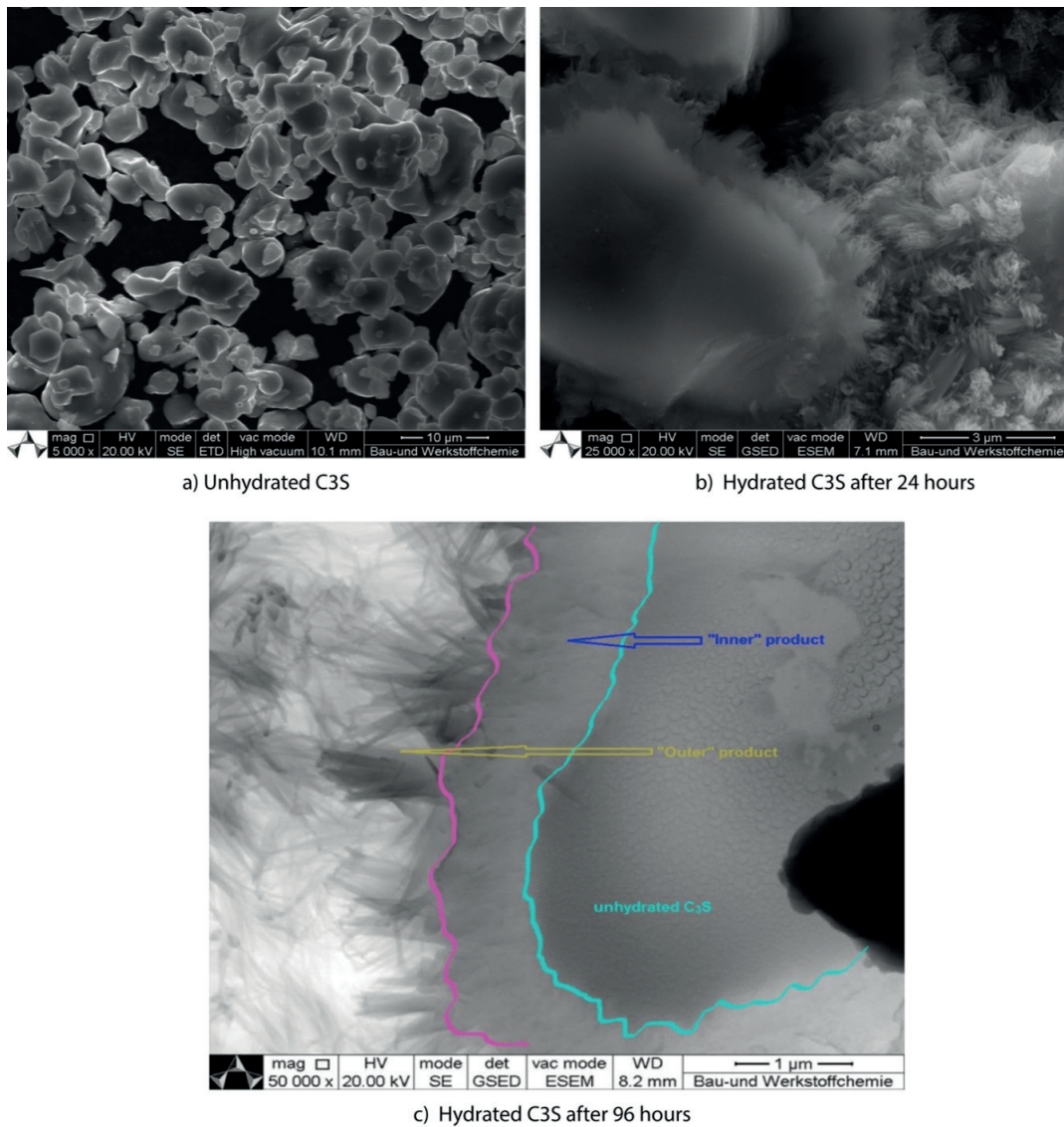


Figure 14: Alite hydration captured by ESEM<sup>63</sup> a) Un-hydrated C3S b) Hydrated C3S after 24 hours c) Hydrated C3S at 96 hours

## 2.3 Synthetic system

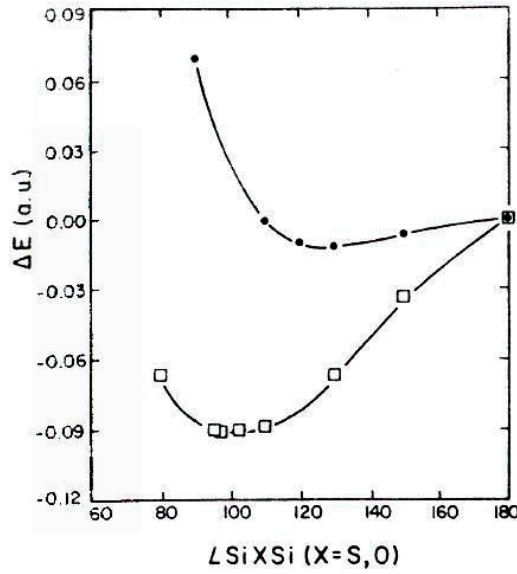
Considering all the constraints to understand the formation of C-S-H in the real Portland cement systems, a controllable synthetic system seems to be the way forward. With that being said, it comes with its own set of challenges. Over past 30 years of synthetic approaches to study C-S-H systems earned a great deal of data on the thermodynamics of C-S-H formation but some vital information is still absent, especially for C-S-H that is representative of early age C-S-H existing in Portland cement systems. This is the bottle neck in synthetics studies (i.e.) to be able to synthesise C-S-H with the desired composition ( $\text{Ca/Si} \geq 1.5$ ) & morphology in a controlled fashion needs to be overcome. Moreover, the lack of morphological and kinetic data is also limiting the understanding of the main phase of cementitious systems. Hence there is scope for developing a novel synthetic system or route to produce these missing data. In fact, it is a kind of pre-requisite for any further progress in understanding C-S-H.

For new results we need a novel approach too, understanding the silicate chemistry seems to be one way to determining the best-suited thermodynamic conditions for desired results. Furthermore, we need to control the physical conditions to manage thereafter the kinetics of the system. In the following sections, we touch upon all the important aspects needed for creating a new synthetic route – from silicate chemistry, the principle of thermodynamics and kinetics, precipitation – basics of particle formation, reactor engineering and finally the modelling of these processes.

### 2.3.1 The tetrahedral silicates building block

Silicon belongs to non-transition elements family (IV-A) usually occurring in four-fold coordination with tetrahedral geometry. The most common occurrence being the  $\text{SiO}_4^{4-}$  ion - the building block for most silicate materials. In 1929 Pauling<sup>64</sup> proposed that Si-O bonding contains equivalently both ionic and covalent character. Although still debatable<sup>65</sup> the non-directional ionic bonding allows more variation in bond angles for Si-O-Si linkages with bending at oxygen atoms. In Figure 15, Burdett<sup>66</sup> reported that less energy is required to distort the geometry from the energy minimum at the oxygen-centred bending angle, compared to a less electronegative element such as Sulphur.

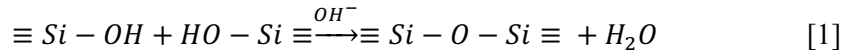
This flexibility of Si-O-Si linkage allows numerous possibility of connectivity of  $\text{SiO}_4^{4-}$  as building blocks. Conventionally, these building blocks are represented in the form of “ $\text{Q}_x$ ” notation, where x is the number of nearest neighbouring silicon's attached to the tetrahedral corner. For example,  $\text{Q}_0$ ,  $\text{Q}_1$  represent none, one apical oxygen sharing between two tetrahedra forming a dimer. It can also lead to 3D frameworks such as quartz. Silicate structures can accommodate a wide variety of cations to balance the charge of the fundamental structural unit, as well as the possible substitution of silicon atoms in the structure (for example, by aluminium).



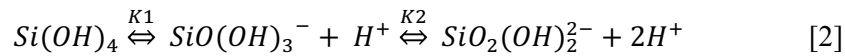
(Source: Burdett; Perspective in structural chemistry, 1988)

Figure 15: Calculated bending potential for Si-O-Si (in circle) and Si-S-Si (in Square) units, (adapted from Burdett, 1988)

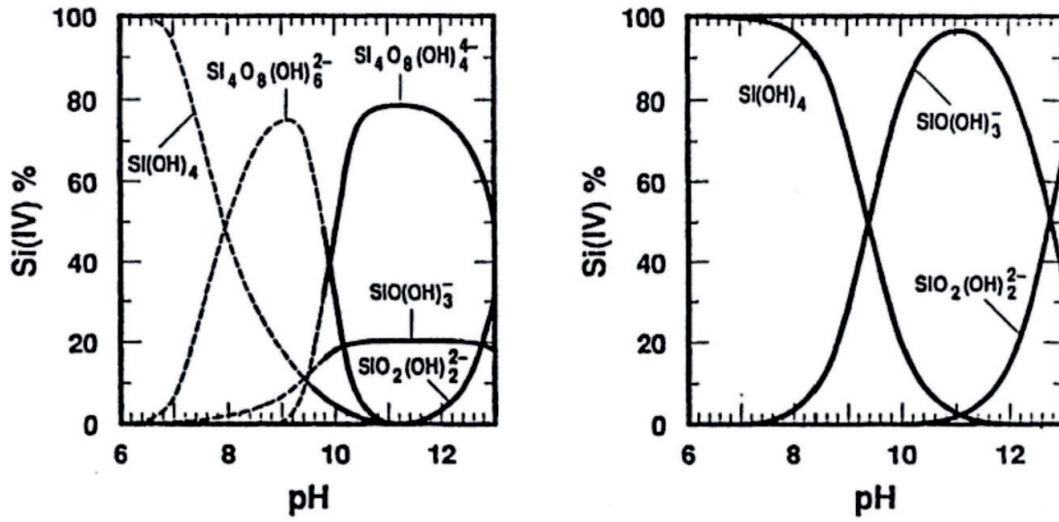
During silicate formation, these linkage frameworks between the silicates are highly governed by the pH conditions, ionic strength and cationic species<sup>67-69</sup>. Another peculiarity of silicate solutions is their ability to undergo condensation reactions *via* polymerization. Below pH 2, these reactions are catalysed by  $H^+$  whereas above pH 2,  $OH^-$  is catalysing by generating anionic species. The reaction can be described in equation [1]:



This condensation reaction of monomers forms dimers, trimers etc. According to Iler<sup>70</sup> it is only the first step of the polymerization process. It is followed by the nucleation of colloidal particles (step 2) and the growth of these particles (step 3). Silicon predominately exists as the neutral  $Si(OH)_4$  below pH 7. Above this pH, silicate tends to transform into single charged silicate species. The corresponding equilibria of only monomeric silic acid can be formally written as:



Where  $SiO(OH)_3^-$ , is the predominant monomolecular species above approximately pH 9. With  $SiO(OH)_3^-$  being a very weak acid,  $SiO_2(OH)_2^{2-}$  is observed in appreciable quantities only above pH 12, as shown in equation [2]. The silicate species in dissolution and precipitation of C-S-H, mentioned in other sections is formally written as  $H_2SiO_4^{2-}$ . Moreover, the possibility of condensation reactions and hence the occurrence of diverse soluble oligomeric species has to be taken into account. A silicate solution at high pH, however, are stabilized by electrostatic repulsion between the anionic silicate species.<sup>12,71</sup> Consider the pH vs. Silicate species presented in the figure 16, at two different concentration regimes, at concentrations of 0.1M and  $10^{-5}$  M respectively.

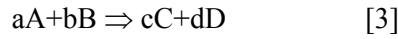


(Source: Brinker & Scherer; Sol-gel Science, 1990)

Figure 16: Distribution of Aqueous silicates species at 25° C, in total Si concentration of 0.1 M (Left) and 10<sup>-5</sup> M (right).

### 2.3.2 Thermodynamics and kinetics of reactions

It is interesting to understand cement hydration from the thermodynamic and kinetic points of view. Consider the simplistic chemical reaction:



This reaction continues in the forward direction until an equilibrium between reactant and product is achieved. Thermodynamics (time independent) describes hereby only the states of reaction whereas kinetics deals with the fate of the reaction partners during the reaction period (time dependent). The driving force for this reaction is the difference in the Gibbs free energy of the system  $\Delta G$ .<sup>18</sup>

$$\Delta G = \Delta G^\circ + RT \ln \left( \frac{a_C^c \cdot a_D^d}{a_A^a \cdot a_B^b} \right) \quad [4]$$

|  |  |
|--|--|
| $\Delta G^\circ$   | Standard difference in free energy of the system                 |
| T  | Absolute temperature   |
| R  | Molar gas constant (R=8.314 J/mol.k)                             |
| $Q = \left( \frac{a_C^c \cdot a_D^d}{a_A^a \cdot a_B^b} \right)$ | Reaction coefficient expressed in terms of activities of species |
| $a_i, \gamma_i, c_i$   | Ion activity, activity coefficient, concentration of species i   |

Table 4: Thermodynamics parameters descriptions

At equilibrium, the driving force (i.e.)  $\Delta G$  tends to zero. Hence from equation [4], we get:

$$\Delta G_r^\circ = -RT \ln \left( \frac{a_C^c \cdot a_D^d}{a_A^a \cdot a_B^b} \right) = -RT \ln (Q) \text{ or } \Delta G_r^\circ = -RT \ln (K_{sp}) \quad [5]$$

Where  $Q$  is referred to as  $K_{sp}$  at equilibrium, if we combine derivation of  $\Delta G^\circ$  and  $\Delta G$ , we arrive at the following equation. From equations [4] and [5]

$$\Delta G = -RT \ln(K_{sp}) + RT \ln(Q) = RT \ln\left(\frac{Q}{K_{sp}}\right) \quad [6]$$

Ion activity product (IAP) is the concentration of ions at a particular time in a precipitation system when  $IAP > K_{sp}$  we have a non-equilibrium system and formation of the product will take place until  $IAP = K_{sp}$ , combining with equation [6] we get:

$$\Delta G = RT \ln\left(\frac{IAP}{K_{sp}}\right) = RT \ln(W) = RT(SI) \quad [7]$$

Where  $IAP/K_{sp}$  is referred as  $W$  and  $SI$  are the saturation index defined as  $\log(W)$ . This implies that the driving force for a chemical reaction in aqueous solution is directly proportional to the saturation of the solid product in the solution. Whereby the following cases are distinguished:

|          |                          |
|----------|--------------------------|
| $SI < 0$ | System is undersaturated |
| $SI = 0$ | System is in equilibrium |
| $SI > 0$ | System is supersaturated |

Table 5: Saturation Index and state of system

The driving force for precipitation is the difference between the species  $IAP$  and the  $K_{sp}$ . A reaction is the stabilisation response the non-equilibrium caused by having an excess of certain species in solution to move back towards a thermodynamics equilibrium. The pathways or the route to arrive at the equilibrium is dealt in reaction kinetics. Reaction kinetics is a temperature dependent phenomenon. There is a minimum amount of energy (activation energy  $E_a$ ) needed to initiate the chemical reactions.

### 2.3.3 Precipitation of a solid

Precipitation can be regarded as rapid crystallisation with high supersaturation levels obtained by mixing two solutions that subsequently give a solution that is supersaturated. Nucleation rates are very high due to high supersaturation levels, and the particle size is small compared with conventional crystallisation from low supersaturation solutions. Kinetic parameters are used to describe the events of growth (growth rate), birth and death (nucleation rate, agglomeration and disruption kernel) of a precipitation process. The interplay of these parameters and their dependence on supersaturation, hydrodynamics and mixing determine the crystal size distribution as shown in Figure 17.

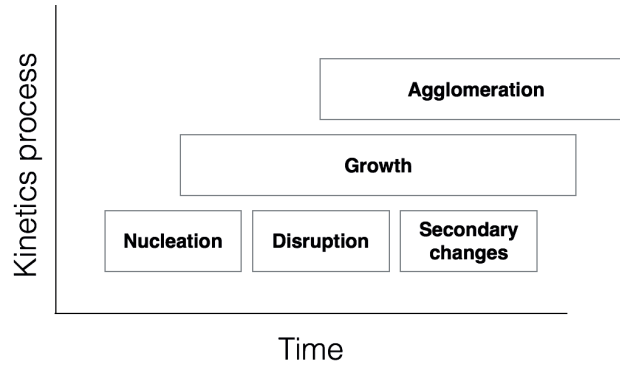


Figure 17: Kinetics processes during precipitation

From classical nucleation theory (CNT) the nucleation does not occur until the supersaturation reaches certain value ( $C_{\min}$ ) that correspond to the energy barrier for nucleation, figure 18(a), irrespective of crossing the equilibrium solubility ( $C_s$ ).<sup>72-76</sup> Once the nucleation event occurs the supersaturation of the growth species decreases and once the concentration drops below a certain value, no more nucleation will occur. Growth, however, continues until the concentration drops to the equilibrium value. Figure 18(b), shows a different view of solid formation, once the concentration passes equilibrium value ( $C_s$ ) embryos are formed and growth rate is already non-zero. Once reaching the critical value they assemble or convert to a nucleus. At this point, the nucleation rate is above zero and increases rapidly with concentration. In this region the nucleation and growth rates are inseparable but occur at a different pace.

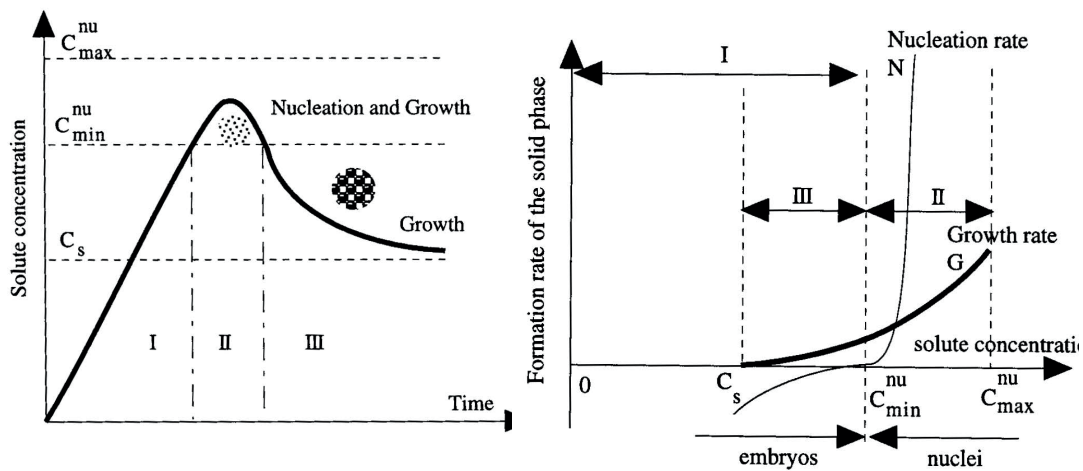


Figure 18: a) Classical nucleation and growth<sup>74,76</sup> b) Relation between nucleation, growth rate and concentration of species.<sup>77,76</sup>

The nucleation event can be divided into two processes. As shown in figure 19, primary nucleation and secondary nucleation. Primary nucleation event is the classical way to describe particle formation, where nuclei are generated in a supersaturated solution following the Gibbs-Thomson relationship. Although the formation of the nuclei can be purely from the solution referred as homogeneous primary nucleation or aided by any foreign species or surface present in the solution, referred to as heterogeneous nucleation. Nucleation plays a significant role in



lowering supersaturation conditions. In secondary nucleation, the nuclei formation is induced by the crystal of the same phase already present in the solution and affected by hydrodynamic conditions.

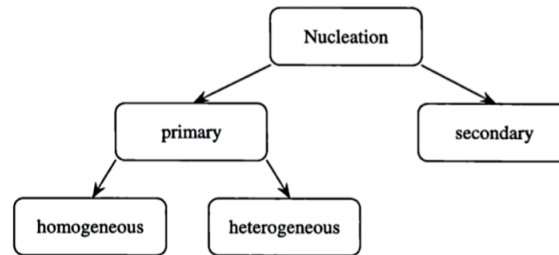


Figure 19: Mechanisms of Nucleation (Mullin, 1993)<sup>73</sup>

Final particle size distributions (PSD) of the particles formed are dependent on the growth processes. Broadly growth processes can be described to be governed by two phenomena. Firstly, the availability of growth species that includes – generation, the supply of the species to the growth sites by diffusion. Secondly incorporation phenomena at the growth surface. Depending on which is the slower of these steps one will serve as the rate determining factor as explained in section 2.1.2. As presented by various authors<sup>73,75</sup>, diffusion limited process favours uniform PSD, whereas surface controlled does not with the increasing growth time (t).  $\delta r$  represents the difference in the radii of the nuclei.

Secondary changes such **Ostwald ripening** can also occur in some precipitating systems, where small crystals tend to dissolve and aid in the formation of larger crystals. A kinetically controlled nucleation and growth mechanism are different from that of thermodynamically controlled by virtue of activation energy barrier as explained by Ostwald steps rule. The nucleation and crystal formation can start with a thermodynamically unstable phase and later transform into more stable polymorphs .<sup>78</sup>

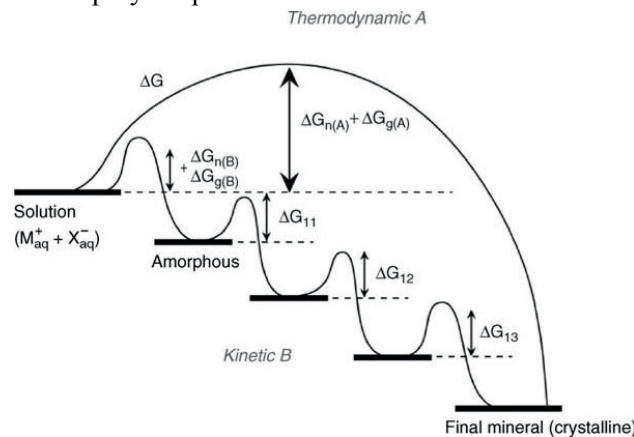


Figure 20: Ostwald steps rule - showing the different pathways towards the final precipitated product.<sup>71</sup>

In order to form C-S-H phases, the nucleation event can be controlled in a way to occur for very short duration, hence all nuclei's are formed in similar conditions. Practically it can be achieved if the growth species is identified and produced (concentration) abruptly by extremely

high supersaturation and brought down quickly below a critical concentration. This was why we need to first identify the species needed for the product we desire and the next question is how can we now control the supersaturation for a uniform formation of the product.

### 2.3.4 Modelling of synthetic system

#### 2.3.4.1 Population balance growth modelling (PBM)

In order to understand the kinetic growth mechanism of the C-S-H, we have adopted a population balance modelling (PBM) method in this thesis. The details of the PBM is presented in chapter 08 with experimental validation and parameterization. It is an powerful tool to understand the growth mechanism in precipitation processes. During the course of precipitation, individual particles may nucleate, grow, agglomerate or break and even leave the precipitation reactor in the continuous mode of operation. The mathematical framework used to describe the conservation of mass during this process of moving from a supersaturated solution to a suspension of precipitated particles is called the population balance. The concept of population balances for agglomerative processes was introduced by Hulbert and Katz (1964).<sup>79</sup> They derived their mathematical model from statistical mechanics and applied it to processes involving both growth and agglomeration. In general, the population balance of a system is derived from a number- continuity equation as illustrated in equation 8.

$$\text{Accumulation} = \text{Input} - \text{Output} + \text{Net generation.} \quad [8]$$

The population balance equation basically accounts for various ways in which particles of a specific state can either form or disappear from the system. When particle states are continuous, then processes, which cause their smooth variation with time, must contribute to the rates of formation and disappearance of specific particle types. It describes the evolution of the size distribution of an ensemble of particles simultaneously undergoing nucleation, growth, coalescence, and disruption. For a well-mixed suspension of constant volume, the population balance of the system can be written as follow:

$$\frac{\partial n(L,t)}{\partial t} + \frac{\partial}{\partial L}[G(L,t) n(L,t)] = B(n) - D(n) \quad [9]$$

where  $n(L,t)$  is the number density of particles at time  $t$  in the size range  $L$  to  $L + dL$  (for spheres with radius  $R$ , it is  $L = 2R$ ),  $G$  is the isotropic growth rate, and  $B$  and  $D$  are the rates of birth and death, respectively. If there are  $dN$  particles per unit volume, the density function is given by  $dN/dL$ . More case specific details to C-S-H kinetics and growth is presented in chapter 8.

#### 2.3.4.2 Thermodynamic modelling

In order to understand the thermodynamic constraints/controls in the synthetic system, we needed assistance from thermodynamic modelling. Commercially available software does not



take into account of variability in the formation of C-S-H system in the cementitious system. The Gibbs free energy minimization program GEM-Selector developed at PSI, Viligen and EMPA, Dubendorf was employed for thermodynamics modelling.<sup>80</sup> It is a geochemical modelling code which computes equilibrium speciation of the dissolved species as well as the kind and number of solids in equilibrium with the solution. Chemical interactions involving solids, solid solutions, aqueous electrolyte and gas phase are considered simultaneously. The thermodynamic data for aqueous species as well as for many solids were taken from the PSI-Nagra thermodynamic database,<sup>81</sup> while the solubility products for cement minerals were taken from the cemdata07 database<sup>81,82</sup> updated with the recent solubility products of calcium aluminate hydrates and hydro garnets. To model C-S-H, the CSHQ model was introduced that uses four different end-member C-S-H compositions ( $C_{1.5} S_{0.67} H_{2.5}$ ,  $C_{1.33} S H_{2.17}$ ,  $C_{0.83} S_{0.67} H_{1.83}$  and  $C_{0.67} S H_{1.5}$ ) to cover the complete range of Ca:Si ratios observed in C-S-H formation in real Portland cement systems. To compensate for the higher ratios of Ca:Si, it considers i) the coupled replacement of the bridging tetrahedral ( $SiO_2$ ) and two  $2H^+$  in the adjacent interlayer space by  $H_2O$  and  $Ca^{2+}$  and ii) the replacement of vacant interstitial sites by  $Ca(OH)_2$ . The CSHQ model is able to reproduce the changes in silicate chain length and in the aqueous concentrations with changing Ca:Si ratio in the solid C-S-H and is based on a sub lattice concept that describes the different structural units in C-S-H and their possible variations.

## 3 Material and methods

### 3.1 Introduction

Although each experimental chapter in Part II, covers all the methods and materials used, this chapter describes the general chemical and physical conditions adopted for synthesis and characterization. Specialised characterization techniques are also described individually in chapters 4 to 8. A synthetic system was designed to overcome the limitations previously encountered in synthetic systems, according to chemical engineering and particle engineering principles not always previously considered. We first describe the schematic sequence of processes (Fig. 22), then we describe all the characterization methods adopted to understand the product. Ending with a section on approach towards Portland cement system by doping pure phase C-S-H synthesis with elements and putting the developed understanding and theory to test.

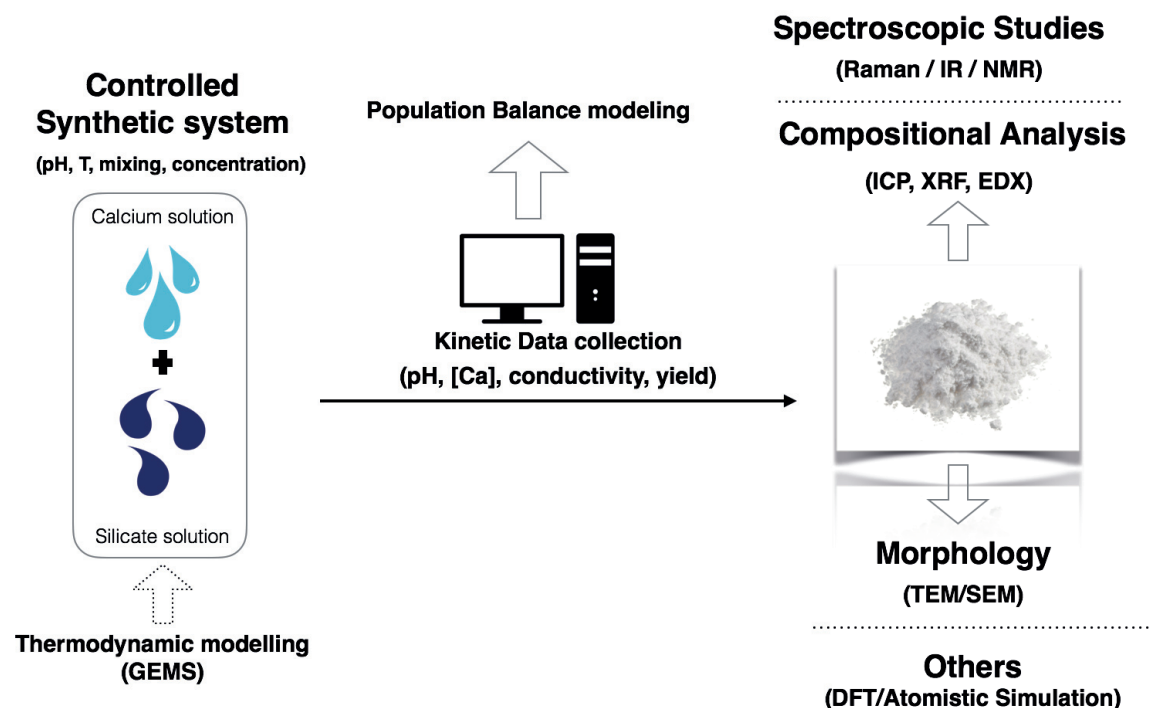


Figure 21: General scheme of the synthesis and characterization

### 3.2 Controlled synthetic system and product recovery.

A special micro-mixing, PMMA (Polymethyl methacrylate) based reactor system was fabricated in-house for the synthesis of C-S-H that shows excellent resistant to Acidic/Basic conditions. More detailed descriptions and functions are discussed in chapter 04 and Annexure. The reaction time is kept at 3 hours and 24 hours (for kinetic experiments). The reactor is equipped with a micromixer system mounted on the top, with 3 entries at mixing angles of 60°. Also to ensure efficient mixing, the reacting mixing length is fitted with a spiral static mixer (0.5 cm diameter, 4 segments/cm). All the experiments were carried out under a Nitrogen environment to avoid any carbonation effect with a steady flow rate between 0.1 ml/min to 5 ml/min. Aqueous solutions of calcium nitrate tetra hydrate (Fluka Chemicals) and sodium metasilicate (Sigma-Aldrich) were used for precipitation of C-S-H in 2:1 ratio concentrations of 0.2 mol/l and 0.1 mol/l respectively. These concentrations ensure high supersaturation wr.t. C-S-H (i.e.) the precipitating C-S-H does not affect the concentration of the solution species. High supersaturation also reduces the effect of heterogeneous nucleation. The sample was prepared in de-carbonized water by boiling de-mineralized ultra-pure (MilliQ) for 1 hour and cooled in ice bath. The solution was immediately prepared after cooling. The chemicals used for solution preparation were measured with  $\pm 0.01$  mg accuracy. All measuring electrodes were calibrated twice before each synthesis. To avoid dust and any kind of surface contamination, which might affect nucleation and growth, all chemical glassware used in solution preparation were washed and dried under laminar flow clean bench conditions (Scan AG.).

Two aspects are important in the synthetic system – Physical conditions/control and Chemical control. Physical control simply means mixing condition of reactants, the size of vessel and rate of reactant addition. In our case, we make it independent by ensuring reaction time is always larger than mixing time, (i.e.) faster mixing times. This way the system is chemical constrained and governs the product formation. It is provided by microstructure static mixers and the magnetic stirring. Flowrates are optimised accordingly to be suited to the reactor volume and mixing. Experiments done in carbon free environment helps to avoid carbonation that complicated the results in many previous synthetic systems. On the chemical control side, high supersaturation ensures that there are enough reacting species in the solution available for reaction, irrespective of the amount of material precipitating and leaving the solution at any given time. Hence we get uniformity in the sample. Desirable Ca:Si ratio is governed by thermodynamics, which is calculated using GEMS software. To have uniformity in the sample it is necessary to ensure that supersaturation is developed for very short periods of time for nucleation of growth species, and allowed to grow under similar conditions. This can be done by managing the mixing methods of the reactants. Three ways of reactant mixing are practised throughout the thesis termed as “Dropwise”, “Reverse-dropwise” and “micro-mixing” modes. In the dropwise mode, calcium is added to the silicate solution at a controlled flow rate with calculated drop volume into the calcium solution on magnetic stirring to ensure very short mixing times (sub millisecond), For the reverse-dropwise method, silicate solution is added to the calcium nitrate solution. In the micro-mixing mode, both reactants are mixed first in micromixer fitted with the reactor system and later allowed to age under magnetic stirring. Again flow rate and mixing length is controlled. In all of these methods, pH adjusting agents are always added on the silicate side and any doping or foreign elements (doping experiments)

are added on the calcium side. The amount of pH adjusting agent is calculated theoretically by GEMS. After the reaction, the precipitates were separated from mother liquor using vacuum filtration over 200 nm organic filter and later washed with Ethanol/water system to remove salts and unwanted ions from the surfaces of C-S-H.

### 3.3 Sample characterization methods

Morphological analysis was performed with a high-resolution Transmission electron microscope (TEM) and Scanning electron microscope (SEM). For the first time in SEM, samples were Osmium coated. A metallization coating is not just to reduce or eliminate charging, it is also helpful to impart to the image enhanced contrast. Osmium coating is done in gas phase allowing a better coating on the curved sheets of C-S-H and with smaller grain sizes of Osmium, the resolution is not lost by coating. Compositional analysis was performed with inductively coupled plasma (ICP), X-ray Florescence (XRF), Thermogravimetric analysis (TGA), Energy-dispersive X-ray spectroscopy (EDX), X-ray powder diffraction (XRD). The Spectroscopic analysis – with IR, Raman, being complimentary analysis to each other are well suited for material like C-S-H with short range order. Whereas, Dynamic nuclear polarisation (DNP) NMR was adopted for C-S-H system possessing high surface area and uniformity in the sample. Details of the methods presented are discussed in detail in chapter 4 to 8, wherever used.

Additionally, we also performed some supportive analysis for verification purposes only, such as Particle size distribution of C-S-H samples were measured on a Malvern Mastersizer S, a laser diffraction instrument. To have representative results three sets of measurement were taken and result presented later in the thesis is the average of the three. The sample was re-dispersed with 1% Poly-acrylic Acid (PAA). The solution was ultra-sonicated for 15 minutes. The measurements were made over 3 runs using a pump speed of 2000 rpm. Calculations were based on material properties of a reflective index 1.5 and absorption of 0.1 on Malvern Mastersizer 2000 software v5.1. Samples were analysed, once directly after the precipitation step and once after being filtered and dried. The Specific surface area (SSA) was determined on a Micromeritics Gemini 1330 by the 5-point BET method of determining of Specific Surface Area using Nitrogen Adsorption.. From the SSA analysis, an equivalent spherical diameter for the estimation of primary particle sizes can be calculated ( $D_{bet} = 6/\text{density} \times \text{SSA}$ ). The ratio of the  $D_{v50}$  measured by laser diffraction and the  $D_{bet}$  gives an indication of the degree of agglomeration. Two sets of BET were performed once the sample was dried in presence of air at 60°C for 3 hours and other batch dried in nitrogen at 50 °C for 30 hours with two repetitions of each.

### 3.4 Doping Studies

To approach the Portland cement system, certain elements were introduced in the model synthetic C-S-H system and were compared to the pure system. Elements were chosen from ions found in Portland cementitious systems as well as ions with a variation of their ionic sizes and charges. This was also to test certain hypotheses and to give a predictive capacity from our understanding of the C-S-H formation mechanism. In most cases, only single ions were added to the basic precipitation system to make the comparison easier. Below Table 6, is a list of all

the added elements that were investigated with general chemical pH conditions used. Cation 1 and Anion 1 are the tested dopants in the C-S-H phase produced from conventional reactant 1 and reactant 2. All the cation 1 are used in their nitrate forms in the experiments.

| <b>Cation 1</b>        | <b>Reactant 1</b>                 | <b>Reactant 2</b>                | <b>pH</b> |
|------------------------|-----------------------------------|----------------------------------|-----------|
| <b>Na<sup>+</sup></b>  | Ca(NO <sub>3</sub> ) <sub>2</sub> | Na <sub>2</sub> SiO <sub>3</sub> | 9-13.5    |
| <b>Na<sup>+</sup></b>  | Ca(NO <sub>3</sub> ) <sub>2</sub> | Na <sub>2</sub> SiO <sub>3</sub> | 13.3      |
| <b>K<sup>+</sup></b>   | Ca(NO <sub>3</sub> ) <sub>2</sub> | Na <sub>2</sub> SiO <sub>3</sub> | 13.3      |
| <b>Mg<sup>2+</sup></b> | Ca(NO <sub>3</sub> ) <sub>2</sub> | Na <sub>2</sub> SiO <sub>3</sub> | 10.5/13.3 |
| <b>Al<sup>3+</sup></b> | Ca(NO <sub>3</sub> ) <sub>2</sub> | Na <sub>2</sub> SiO <sub>3</sub> | 13.3      |
| <b>Fe<sup>2+</sup></b> | Ca(NO <sub>3</sub> ) <sub>2</sub> | Na <sub>2</sub> SiO <sub>3</sub> | 13.3      |
| <b>Zn<sup>2+</sup></b> | Ca(NO <sub>3</sub> ) <sub>2</sub> | Na <sub>2</sub> SiO <sub>3</sub> | 13.3      |
| <b>Ba<sup>2+</sup></b> | Ca(NO <sub>3</sub> ) <sub>2</sub> | Na <sub>2</sub> SiO <sub>3</sub> | 13.3      |
| -                      | -                                 | Na <sub>2</sub> SiO <sub>3</sub> | 13.3      |
| -                      | -                                 | Na <sub>2</sub> SiO <sub>3</sub> | 13.3      |

Table 6: List of ions doped in C-S-H system

## 4 Synthesis of calcium silicate hydrates

### 4.1 Introduction.

This chapter covers two important issues relating to Cement hydration. One being, can we really understand early age hydration period and the formation of C-S-H in a synthetic system? Is it possible to synthesise pure phase C-S-H that are representable of the one formed in a Portland cement system? Answering these questions also somewhat sheds light on – why none of the prior synthetic attempts were successful in doing so. Do we need a multidisciplinary approach or what is the missing elements in those studies? Secondly, can we combine different spectroscopic studies and atomistic simulation together to elucidate of the structure of C-S-H? If yes, how? This will help in a better understanding of the possible kinetics in nucleation and growth pathways of C-S-H.

Both the aspect – to **synthesise the desired C-S-H** and to **elucidate its characteristics** is a difficult task and involved different approaches and understanding from various fields. This chapter demonstrates that we have achieved both feats written in a manuscript and presented in section 4.2. The supplementary information of the article can be found in Annexure.

As the first author of the manuscript my contribution was to design a controlled reactor system, that could deliver the best thermodynamic conditions for synthesis of C-S-H calculated from the thermodynamic modeling. Further I contributed in the sample characterization with developed protocols to get insights into the precipitated C-S-H. The sample were provided to external collaborator for Raman, IR and XRF analysis. Remaining analysis presented in the manuscript is performed in-house by me.

## 4.2 Manuscript

### **Controlled synthesis and characterization of homogeneous Calcium Silicate Hydrates phase with high Calcium to Silicate ratio.**

Abhishek Kumar<sup>1</sup>, Bhuvanesh Srinivasan<sup>1,2</sup>, Aslam K Mohamed<sup>1</sup>, Danny Lambert<sup>3</sup>,  
Geneviève Massonnet<sup>3</sup>, Karen Scrivener<sup>4</sup>, Paul Bowen<sup>1</sup>

<sup>1</sup>Powder Technology Laboratory, Institute des Matériaux, École Polytechnique Fédérale de Lausanne EPFL, CH-1015, Switzerland

<sup>2</sup>Department of Earth & Environmental Sciences, Ludwig Maximilian University, D-80333, Munich, Germany

<sup>3</sup>School of Criminal Justice, University of Lausanne, CH-1015, Switzerland

<sup>4</sup>Construction Material Laboratory, Institute des Matériaux, École Polytechnique Fédérale de Lausanne EPFL, CH-1015, Switzerland

#### **Abstract**

The complex environment of hydrating Portland cement has made it difficult to fully understand the formation of the main hydration product Calcium Silicate Hydrate (C-S-H). To provide a better understanding of the formation a series of synthetic C-S-Hs have been synthesised by precipitation and fully characterized with Ca:Si ratios ranging from 1 to 2. The stoichiometry can be predicted by the use of thermodynamic modelling. No formation of any other secondary phases such as Portlandite are observed from FTIR, Raman, TGA analysis and electron microscopy. The powders are shown to be chemically uniform down to 3nm using Scanning transmission electron microscope – Energy Dispersive X-ray analysis. Raman and FTIR analysis indicate that C-S-H with Ca:Si ratios from 1.25 - 2 are part of one structural family. The synthetic method clarifies the factors affecting the formation of C-S-H and sheds some light on the different C-S-H morphologies and how their formation can be controlled.

**Keywords:** Synthetic C-S-H, Mid-IR spectroscopy, STEM - EDX, Raman microspectroscopy, Tobermorite

#### **Introduction**

Calcium Silicate Hydrate (C-S-H) contributes to about 55-60% volume of the total hydration products of Portland cement. It is highly variable in terms of Ca:Si ratio and morphology and hence the hyphens in the formula <sup>6</sup>. These C-S-H phases are poorly crystalline in nature with no long range order making it difficult to characterise their structure. This difficulty is compounded by the presence of numerous other phases in the real hydrated cementitious system <sup>4</sup>. For these reasons, many researchers have studied synthetic C-S-Hs to help elucidate both its structure and formation pathway <sup>10,53,83,84</sup>. The mesoscale structure and morphology are well studied but the atomic structure of the C-S-H is still an ongoing debate.

The most popular methods for synthesis of C-S-H has been by dissolution-precipitation<sup>10,84</sup> and by direct precipitation<sup>83</sup>. The batch dissolution /re-precipitation route uses calcium oxide, ultrafine silica and sometimes alkali hydroxides (NaOH or KOH) to modify pH. This route, which although it mimics the process in cement may lead to certain degree of inhomogeneity in chemistry at the sub-200nm level. The method is also very slow where reaching an equilibrium can take from 28 days up to 6 months<sup>10,84,85</sup>. The results however show very interesting overall characteristics of such synthetic C-S-H in particular with respect to their XRD, NMR and Raman characteristics. Most data can be well described using a defective tobermorite structure<sup>10,84</sup>. For the direct precipitation approach different reactants may be used i.e. solutions may be made from silica and CaOH<sub>2</sub> or by using sodium silicate and calcium nitrate solutions<sup>83</sup>. The results from both methods have been used to augment the thermodynamic modeling for C-S-H<sup>81</sup>. One of the main drawbacks of the synthetic C-S-Hs is that none of the previously reported methods have managed to produce C-S-Hs with Ca:Si ratios > 1.6. Early hydration products normally have Ca:Si ratios around 1.8<sup>42,86,87</sup> and thus some doubts about the suitability of synthetic C-S-H to represent early hydration products have been expressed.

For highly disordered structures like C-S-H spectroscopic methods such as NMR<sup>48,54,88–95</sup>, FTIR<sup>96–98</sup> and Raman<sup>52,99,100</sup> have been of great help deciphering some of the basic structural features. Neutron scattering and X-ray absorption on synthetic C-S-H phases combined with atomistic simulation have improved our understanding of C-S-H formation in recent years<sup>48,50,53,83,101</sup>. From these spectroscopic studies it is somewhat accepted that the structure of C-S-H can be based on the different tobermorite structures<sup>10,84,102</sup> which, in its so-called 14Å polymorph, has the approximate chemical composition Ca<sub>4</sub>(Si<sub>6</sub>O<sub>18</sub>H<sub>2</sub>). Ca.4H<sub>2</sub>O (i.e. a Ca:Si ratio of 0.83)<sup>8,50,102,103</sup>. The 14Å tobermorite structure shown in Figure 22 (a), contains layers of sevenfold coordinated (mono capped trigonal prisms) of Ca<sup>2+</sup> ions linked on both sides to linear silicate chains of the ‘dreierketten’ form in such a way as to repeat a kinked pattern after every three silicate tetrahedra<sup>102,104</sup>. Two of the three tetrahedra, named paired tetrahedra, are linked together and share O–O edges with the central Ca–O part of the layer. The third tetrahedron, named bridging tetrahedron, shares an oxygen atom at the pyramidal apex of a Ca polyhedron and connects the dimers of paired tetrahedra. In Q<sup>n</sup> notation, the superscript n denotes the number of surrounding Si to the central silica. Different silicate species (Q<sup>0</sup> – monomer, Q<sup>1</sup> – dimer etc.) and were identified using NMR studies, reporting dimer at early stages with no cross-linking indicating linear chains. With end member silicates (Q<sup>1</sup>) and middle members (Q<sup>2</sup>), the mean chain length (MCL) can be calculated<sup>50</sup> and is reported to be 2 for first few days of hydration. With some percentage (~ 8-10%) of monomers still observed at 12 months of hydration and beyond (presumably from unreacted anhydrous silicates as shown by Pustovgar et al<sup>48</sup>). The MCL increases from 2 to 3.1 in OPC and 2 to 3.3 in alite paste after one year of hydration and reportedly does not exceed 5 even after 26 years<sup>50</sup>. The calcium-silicate layers have a net negative layer charge which is compensated by Ca atoms in the interlayer region, which also contains water or other molecules<sup>97,105,106</sup>. Ca<sub>A</sub>, Ca<sub>B</sub>, Ca<sub>I</sub> are the additional, bridging and interlayer calcium introduced in the tobermorite interlayer as recently identified by NMR and atomistic simulation.<sup>107</sup>



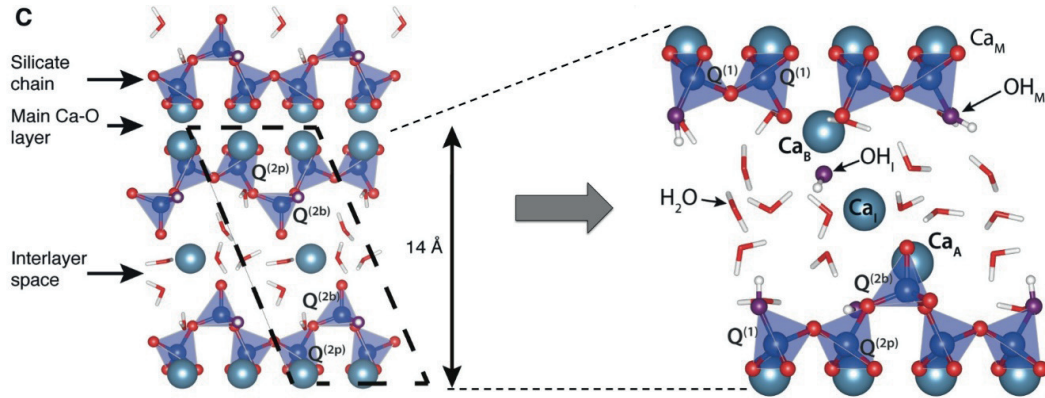


Figure 22: (a) Tobermorite structure and structural nomenclature (b) defective tobermorite structure with missing bridging tetrahedra and extra interlayer calcium.

In the pure tobermorite models the Ca/Si ratios are  $< 1$ , much lower than early age C-S-H in OPC (around 1.8). In the tobermorite models (Ca/Si ratios  $< 1$ ), the Ca:Si ratio can increase by removing some bridging tetrahedra (decrease of the Si content) and deprotonation of silanol groups with consequent addition of Ca ions and hydroxyl ions for charge compensation in the interlayer as shown in Figure 22 (b). The inclusions of these defects in the basic tobermorite structure along with possible second phases (jennite and calcium hydroxide)<sup>102</sup> has been the basis for several different structural models for C-S-H which are very briefly outlined in the flowing section.

Broadly, C-S-H has been identified as falling into two classes based on Ca:Si ratios, named C-S-H(I) and C-S-H(II), where Ca:Si ratio is low (below 1.0) and high (above 1.0), respectively<sup>53,97,106,108</sup>. Taylor et.al<sup>56,109</sup> correlated C-S-H(I) and C-S-H(II) to a tobermorite model and jennite model respectively, with jennite being another naturally occurring Calcium silicate mineral with high Ca:Si ratio of 1.75. Nonat et.al<sup>53,108</sup> presented a new nomenclature based on solution equilibria data with the existence of three different phases:  $\alpha$ -C-S-H ( $0.66 \leq \text{Ca:Si} \leq 1.0$ ),  $\beta$ -C-S-H ( $1.0 \leq \text{Ca:Si} \leq 1.5$ ) and  $\gamma$ -C-S-H ( $1.5 \leq \text{Ca:Si} \leq 2.0$ ) [12–14]. Both Fujii & Kondo<sup>110</sup> and Cong & Kirkpatrick<sup>54</sup> consider C-S-H as a structure between tobermorite and portlandite ( $\text{Ca}(\text{OH})_2$ ), the so-called defective-tobermorite model, while Richardson & Groves<sup>42,86</sup> proposed a model based on isolated silicate chains of variable length and OH content, intergrown with  $\text{Ca}(\text{OH})_2$ . Kirkpatrick et.al by Raman analysis reported jennite like regions, whereas in similar studies Garbev et.al.<sup>52</sup> demonstrated using Stade and Wiekert's model<sup>111</sup>, a C-S-H(I) phase with a Ca:Si ratio of 0.67 must consist of infinite silicate chains attached to a calcium polyhedral layer to give “tobermorite slabs.” A comprehensive review by Richardson<sup>8</sup>, summarises the different structural models proposed by a number of authors over the last fifty years.

The key questions yet to be fully resolved are –i) is there a need of invoking secondary phases to go beyond Ca:Si ratio 1.5 to compensate for excess calcium in the structure? ii) do C-S-H phases beyond 1.5, have different structural family or it can be still described by defective tobermorite structure? Lastly, in order to have more calcium in the structure, which of the mechanism is favoured first or all do all three mechanisms happens simultaneously? In order

to assess these question, synthetic C-S-H system seems to be a viable option where effecting factors can be compartmentalised and understood.

Many synthetic studies<sup>6,8,53,58,59,83,97,101,106,108,112–115</sup> of precipitating C-S-H is being carried out over past decade with two major road blocks, firstly to produce uniform phases of C-S-H over Ca:Si ratio 1.6 consistently without the presence of secondary phases such as portlandite. Secondly, to control the same synthetic system to predict and produce different Ca:Si ratio. Under the experimental conditions used to produce synthetic C-S-H to date thermodynamic modelling predicts the coexistence of C-S-H and portlandite at starting compositions with Ca:Si ratios  $> 1.6$ . This coexistence of the two phases limits the C-S-H ratio to 1.6 even if higher Ca contents are used. This has led to the idea that the existence of portlandite is inevitable at these high ratios and is the reason why synthetic C-S-H of Ca/Si ratios  $< 1.6$  have not been produced. This is somewhat of a conundrum as in Portland cements C-S-H with ratios of 1.8 are seen in the presence of large portlandite crystals and C-S-H occurs in different morphologies in the real system. Hence, there is some missing thermodynamic/kinetic link in all those previous studies. Thus, results obtained from most synthetic C-S-H studies are not directly useful for understanding the C-S-H formation in Portland cement systems where Ca:Si ratios  $> 1.5$  i.e. particularly for early ages.

In the current work, we synthesise C-S-H phases over a range of Ca:Si ratios from 1 to 2 under controlled conditions. The synthetic C-S-H's were obtained with a novel reactive crystallisation (precipitation) system producing high Ca:Si ratios  $\geq 1.6$ . This opens the door for better understanding of C-S-H atomic structure and its growth mechanism.

## Material and methods

### *Designed reactor system*

A reaction system was fabricated in-house for the synthesis of C-S-H. The vessel was made from poly(methyl methacrylate), which is chemically stable under acidic or basic conditions. Figure 23 shows a schematic of the reactor. It has four main parts – base, cylindrical wall, lid and micromixer unit. Electrodes for the measurement of pH, conductivity and calcium ions are inserted into the lid for real-time monitoring of the reaction conditions. There are also channels that allow for a purging flow of nitrogen gas across the main reaction chamber and an opening used for withdrawing small amounts of sample for analysis. A micromixer system is mounted on top of the vessel, consisting of three channels converging to a central vertical column. The length of the column is fitted with a spiral static mixer to combine the reactant solutions prior to admission into the reaction chamber. A low pulsation piston pump was used to feed the reactants into the channels A, B, and C at rates between 0.01 mL/min to 5 mL/min. The off-axis reactant channels join the mixing column at an angle of  $60^\circ$ . The stirring rate was 700-800 rpm. Nitrogen gas flowing at a rate of 20 mL/min was used to purge the chamber over the course of the reactions. Data from the different electrodes were recorded on a PC using LabX software (Mettler-Toledo) to ensure reproducibility but was not used here for kinetic analysis.

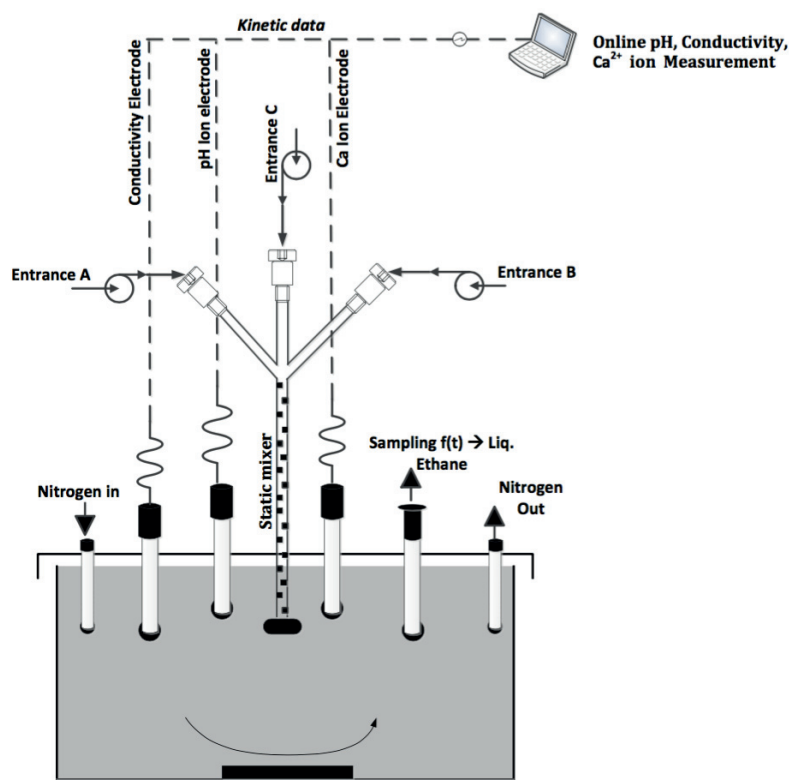


Figure 23: Schematic of the reaction vessel.

### *Thermodynamic Modelling*

Thermodynamic modelling was carried out using the Gibbs free energy minimization program GEM-Selektor (GEMS)<sup>116,117</sup>. GEMS is geochemical modelling code that can calculate equilibrium speciation of the solution and stable solid phases. C-S-H is modelled using CSHQ solid solution model<sup>81</sup>. Thermodynamic data for GEMS were taken from PSI-Nagra thermodynamic database. For cementitious systems, the solubility products of the minerals were provided in the latest database, Cemdata 07<sup>118,119</sup>

### *Synthesis and precipitate recovery*

Solutions of calcium nitrate and sodium silicate were prepared in decarbonized water by boiling demineralized ultra-pure water (milliQ) for one hour and cooling in an ice bath. Solutions were immediately prepared after cooling. Measuring electrodes were calibrated twice before each synthesis. To avoid premature nucleation, all chemical glassware was washed and dried under laminar flow hood (Skanair<sup>®</sup>, Scan AG). In a series of preliminary precipitation experiments calcium nitrate solutions (*Fluka Chemicals*, 21197) and sodium metasilicate (*Sigma-Aldrich*, 307815) solutions were pumped (at 20ml/min) via the micromixer into the reactor. Sodium hydroxide (*Acros-organics*, 134070025) was used to vary the pH of the final reaction mixture in addition of the sodium silicate solution. The Ca:Si ratio obtained in the solid phase, for these preliminary tests, after washing and drying (details below) was found to depend on the pH of the reaction mixture. Thermodynamic modelling using GEMS<sup>80,81</sup> showed

that that Ca:Si ratios above 1.5 could only be predicted to form under high pH conditions and when the calcium hydroxide was excluded. Thus a series of experiments were designed to precipitate different calcium to silicon ratios. We began by setting a 2:1 ratio of calcium to silicon in the starting solutions using equal volumes (100 ml) of 0.2 M and 0.1 M calcium nitrate tetrahydrate to sodium metasilicate. In this series of experiments, the calcium nitrate solution was added *dropwise* into the sodium metasilicate/sodium hydroxide solution at different flow rates. This dropwise method produced similar products to the preliminary micromixing method but gives more flexibility for the collection of kinetic data (to be carried out in the future). Thermodynamic modelling (GEMS<sup>80,81</sup>) was used to calculate the pH required to give different Ca:Si ratios, and this pH was achieved during synthesis by adding an appropriate amount of concentrated NaOH to the sodium silicate solution, (Table 7). We aimed to produce five different C-S-H powders with nominal Ca:Si ratios of 1.0, 1.25, 1.5, 1.75 and 2.0.

| Target Ca:Si (GEMS) | NaOH (GEMS) 10M | pH predicted (GEMS) |
|---------------------|-----------------|---------------------|
| 1.0                 | 0.05 mL         | 10.87               |
| 1.25                | 5.16 mL         | 11.47               |
| 1.5                 | 10.58 mL        | 12.05               |
| 1.75                | 16.62 mL        | 12.55               |
| 2                   | 20.00 mL        | 12.81               |

Table 7 | Amount of NaOH and pH calculated by thermodynamic modelling (GEMS) for the synthesis of C-S-H with different Ca:Si ratios comparison.

The C-S-H precipitates were collected after a duration of 3 hours and again after 24 hours. The precipitated solids were recovered by washing and vacuum filtration. For each 200 mL aliquot, an equal amount of ultra-pure water mixed with ethanol (50:50 v:v), followed by pure ethanol, was used for the wash. Vacuum filtration was done on 20 nm filter paper (Whatman<sup>TM</sup>, GE healthcare, ø 50 mm) to recover the washed C-S-H. The precipitated gel was carefully taken off the filter paper and stored in an airtight container. All other characterizations were carried out on the samples without further preparation.

### *Characterization techniques*

#### *Raman Analysis*

Raman analysis was carried out at ambient temperature (air conditioned at 22 °C) in backscattering geometry, using a *Renishaw Raman inVia Reflex* spectrometer. The excitation source was a diode NIR laser at 785nm (in order to minimise fluorescence effect on spectra), with a power of 8.2mW on the sample in order to avoid any sample damage. The detector was a charge-coupled device (CCD) air-cooled. The laser was focused onto the sample through a Leica microscope with x50 magnification. The laser spot size was about 88µm<sup>2</sup> (2.6 x 34µm, line focus mode). The scattered light was collected through the same objective, in an 180° geometry, and filtered with a dielectric edge Rayleigh rejection filter before being dispersed by a movable grating (1200l/mm). The spectra were acquired in the range of 200-1300 cm<sup>-1</sup> (Raman shift), with the following settings: 3 accumulations, 10s exposure time. The spectra

were all corrected for cosmic rays, smoothed and baseline corrected using a polynomial fit. They were also normalised to unity in the intensity range. To study the compositional uniformity on a pellet of C-S-H with a smoothed surface. The spot analysis with reduced spot size ( $4\ \mu\text{m}^2$ ), analysed more than 30 points on the particle surface. At depths of  $4\ \mu\text{m}$  and  $8\ \mu\text{m}$ , the characteristic peaks positions in the C-S-H were carried out.

#### *FTIR analysis*

The measurements for various Ca:Si ratios were performed on a Perkin-Elmer Spectrometer equipped with multiple detectors (DTGS and MCT) and an attenuated total reflectance (ATR) unit. It comes with a resolution of  $0.5\ \text{cm}^{-1}$  to  $64\ \text{cm}^{-1}$ . Wavelength accuracy was about  $0.1\ \text{cm}^{-1}$  at  $1600\ \text{cm}^{-1}$ . The ATR unit included the diamond crystal ( $1.8\ \text{mm}$  diameter) and a clamp for pressing solid materials onto the crystal with the constant pressure of 10,141 psi pressure. Data were recorded and processed using Spectrum One software. Diamond was used as Internal Reflection Element (IRE) since it has a high refractive index of (2.41) and excellent chemical and mechanical resistance. This makes it suitable for measurements of alkaline C-S-H samples. To obtain relative peak intensities that are similar to those obtained by transmission FTIR, the attenuated total reflectance (ATR) spectrum is multiplied by the wave number. This correction is usually included in the spectrometer control software. To obtain a high-quality ATR spectrum, the contact between the IRE and the sample is vital, as the evanescent wave decays rapidly from the IRE surface. However, our powder samples were fine enough, the reproducibility is sufficient to produce different ATR spectra. No other sample preparation steps are involved prior to measurement. The transmittance results of 256 scans were recorded between  $4000$  and  $450\ \text{cm}^{-1}$ , with individual measurements taken every  $2\ \text{cm}^{-1}$ . For the samples, air was used as the background.

#### Thermogravimetric analysis

The weight loss of samples was measured in a Mettler Toledo AG (TGA/SDTA851e) at a heating rate of at  $10\ ^\circ\text{C}/\text{min}$  from  $30\ ^\circ\text{C}$  to  $1000\ ^\circ\text{C}$  in flowing air. The total water in our C-S-H was estimated from the total water loss (as the saturation state before measurement had some uncertainty) between  $30$  and  $250\ ^\circ\text{C}$ . The amount of portlandite is quantified from the water loss around of the peak in the range from  $400 - 480\ ^\circ\text{C}$  and calcium carbonate was around  $630 - 710\ ^\circ\text{C}$ . No prior sample preparation involved, that is to say the wet slurry after washing and storage was used, such that the water content will only be an estimate.

#### Electron microscopy – imaging and chemical analysis

High resolution scanning electron microscopy (HR- SEM) micrographs were obtained by coating the samples with  $6\ \text{nm}$  of osmium (gas phase coating). The metallization reduces charging and provides enhanced image contrast. The analysis was carried out in a Zeiss Merlin, equipped with the GEMINI II column which combines ultra-fast analytics with high resolution imaging using advanced detection modes. The samples were analyzed with an acceleration voltage of  $1\ \text{kV}$  with probing current of  $300\ \text{nA}$ . On-axis in-lens secondary electron detection mode was employed for imaging. The instrument also provides up to  $0.6\ \text{nm}$  resolution in

scanning transmission microscopy (STEM) mode. In TEM, the samples were imaged at room temperature using a Tecnai F20 (FEI) operating at an acceleration voltage of 100kV from a LaB<sub>6</sub> gun with a line resolution of 0.34 nm. Images were recorded on a high sensitivity 4k x 4k pixel CCD camera. For SEM and TEM analysis, 50 mg of sample was dispersed in 40 mL of isopropanol. A drop of the suspended liquid was allowed to dry on a copper grid (200 mesh grids). The copper grids were glow discharged prior to sample deposition. The uniformity of the C-S-H was investigated by *Scanning transmission electron microscopy - Energy Dispersive X-ray analysis (STEM EDX)* in the FEI Tecnai Osiris analytical TEM instrument. The four windowless Super-X SDD EDX detectors integrated into the pole piece allow detection of 200,000 X-ray counts/s over a 0.9 sr solid angle. A high brightness XFEG gun allows EDX maps to be acquired in seconds to minutes. It operates with 200 kV high brightness XFEG with a point resolution of 0.24 nm and a probe current of 2 nA for EDX studies. The samples were prepared as for the SEM and TEM above. The major constituents of our C-S-H system were defined for elemental identification. The maps are binned after defining the evaluation methods. Once STEM micrographs are obtained, post-processing is performed using Bruker Esprit 1.8 software to obtain the corresponding chemical maps for the samples. The exported STEM image is processed for several parameters like detector effect corrections, Bremsstrahlung background, and Cliff-Lorimer quantification. Each spot corresponds to one pixel whose size is 2.34 nm x 2.34 nm. The signal obtained from each spot is processed to arrive at the final Ca:Si ratio at these points. A large background contribution to the signal is removed throughout the signal range spectra deconvolution is to be performed to address overlapped lines in the spectrum. The final quantification results of Ca:Si for each of these spots are recorded.

#### *X-ray Diffraction*

X-ray diffraction data was collected with a Bruker D8 Discover X-Ray diffractometer using double bounced monochromatic CuK alpha radiation ( $\lambda=1.54 \text{ \AA}$ ) with a fixed divergence slit size  $0.5^\circ$  and rotating sample stage. The C-S-H collected after washing with a water-ethanol solution followed by vacuum filtration was placed onto the sample stage and XRD patterns were recorded.

#### *Inductively coupled plasma – optical emission spectroscopy*

The over chemical compositions of the samples were analysed using Inductively Coupled Plasma in the Optical Emission Spectroscopy mode (ICP-OES). 0.25g of the sample is dissolved in 7 mL of 65% HNO<sub>3</sub> and then re-dissolved completely in 5 mL of fuming 100% ultra-pure HNO<sub>3</sub>. It was performed on ICPE-9000 series which is manufactured by Shimadzu and is a multitype ICP emission spectrometer with the ability to detect high ppb level of 5 to 6 broad digit analysis concentration ranges and batch analysis of various elements. Each analysis consisted of, verification at three dilutions levels 10, 100 and 1000 times. Each analysis was also repeated 3 times for greater consistency.



### *X-ray fluorescent*

In order to cross check, the ICP results the samples were analysed by X-Ray Fluorescent Spectroscopy (Optim'X 9900 Ceram XRF model). 20g of hydrated samples were dried at 105°C for 24 hours and ignited at 950°C for 1 hour. 7.7 g of Lithium Tetraborate ( $\text{Li}_2\text{B}_4\text{O}_7$ ) was added to 0.7 g of the calcined sample to make a fused bead.

## **Results and discussion**

### *Bulk compositions of the precipitated solid.*

The experimental conditions for the desired Ca:Si (theoretical) ratio in the precipitated solid were derived from thermodynamic modelling (GEMS). Experimentally achieved Ca:Si ratio from ICP-OES and XRF are shown in

Table 8, and show very good agreement with the theoretical values. The pH calculated according to GEMS agrees with the experimentally measured pH.

| Ca:Si<br>(GEMS) | pH predicted<br>(GEMS) | pH<br>(Experiment) | Ca:Si<br>(ICP) | Ca:Si<br>(XRF) |
|-----------------|------------------------|--------------------|----------------|----------------|
| 1.00            | 10.87                  | 11.1±0.03          | 1.10 ± 0.04    | 1.04           |
| 1.25            | 11.47                  | 12.5±0.03          | 1.26 ± 0.03    | 1.21           |
| 1.50            | 12.05                  | 12.6±0.03          | 1.50 ± 0.02    | 1.51           |
| 1.75            | 12.55                  | 12.7±0.03          | 1.80 ± 0.06    | 1.77           |
| 2.00            | 12.81                  | 12.8±0.03          | 1.98 ± 0.04    | 1.94           |

Table 8: Experimental vs. thermodynamic modelling – pH, Ca:Si.

These results shows that we are able to control the synthesis of bulk Ca:Si ratio in the precipitate but it is not clear that the Ca:Si ratio can be attributed to only C-S-H (as suggested from the GEMS modelling) or is there a possible contribution from other phases. This is investigated in detail in the next sections with experimental observations by electron microscopy, FTIR, TGA, XRD and Raman spectroscopy.

### **Morphology of C-S-H phases**

When the pH of the reacting solution was greater than 10.8,  $\text{Ca:Si} \geq 1.25$ , the morphology of the C-S-H particles were found to exist as *nanofolds* Figure 3 (a)s, The “*nanofolds*” had diameters between 200 and 300 nm and thicknesses around 6-10 nm (Figure 24 (a))No other phases were observed visually in the images. Figure 24 also shows FTIR, TGA and XRD for the precipitated C-S-H with a Ca:Si ratio of 2, none of them indicate the presence of CH in the sample.

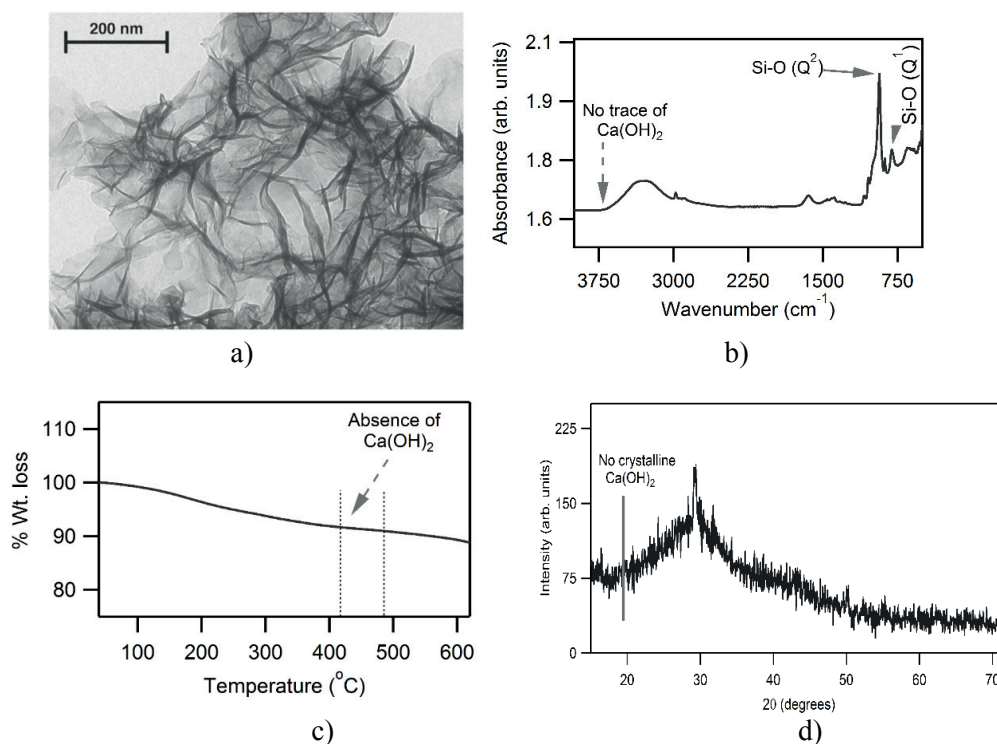
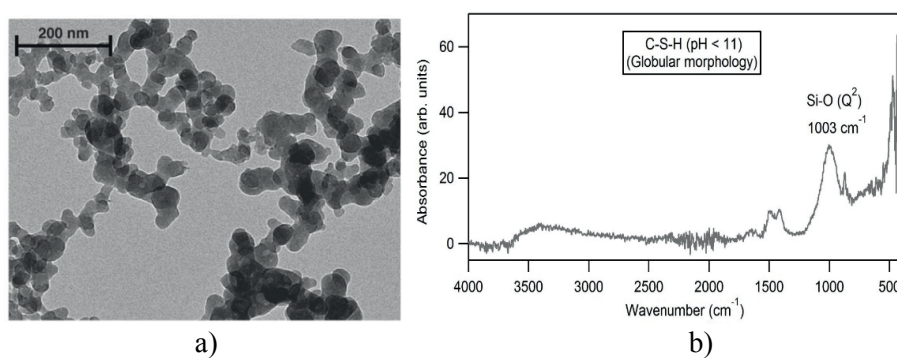


Figure 24: a) Nanofoils morphology for Ca:Si of 2 (All Ca:Si ratios from 1.25 to 2 showed the same morphology) b) FTIR c) TGA d) XRD

When the pH was below 10.9, C-S-H forms a “*nanoglobule*” morphology with a Ca:Si ratio of  $\leq 1.25$  (Figure 25a). The change in morphology may be related to the change in speciation of silicates with pH conditions, which currently under investigation but is beyond the scope of the current study.





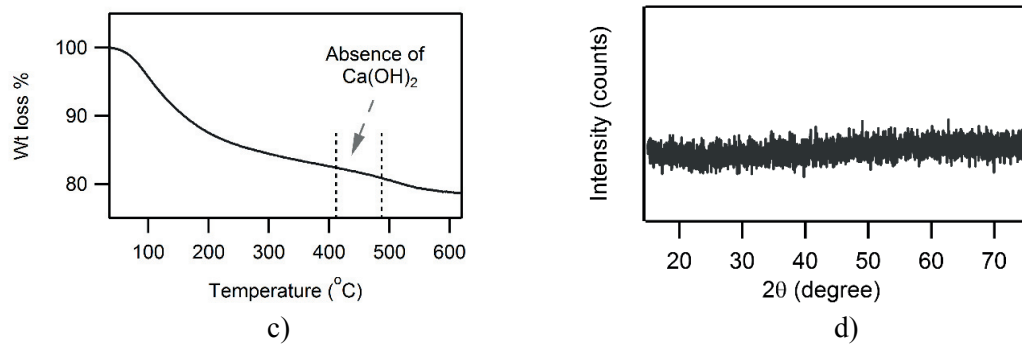


Figure 25: Nanoglobules morphology for Ca:Si of 1 b) FTIR c) TGA d) XRD

### Uniformity in the nanofoils

We will focus on the higher Ca:Si ratio C-S-H phases,  $\text{Ca:Si} > 1.25$  that are more representative of early age OPC systems. A schematic of the Raman point analysis sample area and scanning points ( $4 \mu\text{m}^2$ ) of the sample at the surface and at depths of  $4 \mu\text{m}$  and  $8 \mu\text{m}$  are shown in Figure 26 (a). The characteristic peaks do not change position indicating the chemical environment is similar at the micron scale, Figure 26(c)– shows a top view and Figure 26(d) the 2D spectra of all 30 points put together. This is true for all samples investigated with Ca:Si ratios  $\geq 1.25$ , showing very high uniformity at the micron scale.

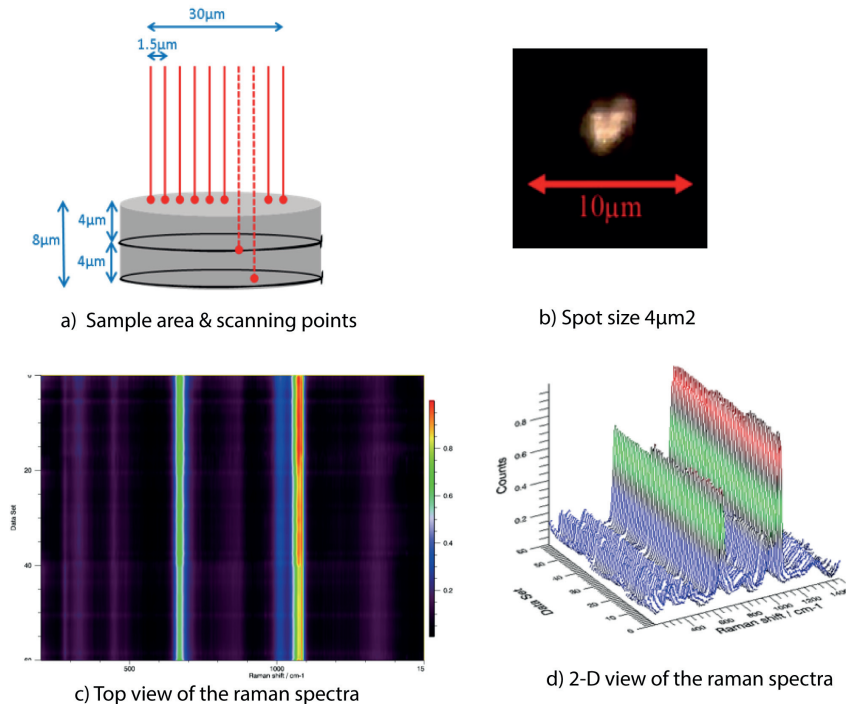
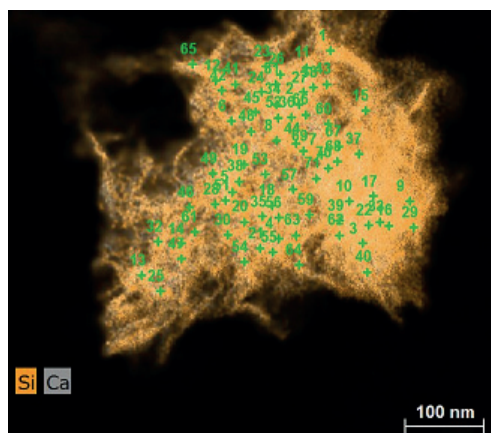


Figure 26: Raman microscopic analysis: a) Sample pellet preparation, b) Spot size used for analysis, c) intensity plot comparing Raman spectra of all 30 spots, d) stacked plot comparing Raman spectra of all 30 spots for a Ca:Si ratio 2 synthetic C-S-H.

In order to investigate the uniformity and consistency of the C-S-H samples to an even greater degree of spatial resolution, EDX in STEM mode was carried out. About 50 – 60 points were analysed individually from the chemical maps as shown in Figure 27(a) For each sample, the

standard deviation of the Ca:Si ratios measurements is less than 1%. EDX analysis shows an excellent uniformity of the Ca:Si ratio within the structure but due to the difficulty of accurately calibrating the instrument the actual Ca:Si determined ratio is systematically less than that obtained from the XRF and ICP methods.



a)

| Ca:Si<br>(Experimental) | Ca/ Si<br>(EDX)  |
|-------------------------|------------------|
| 1.00                    | $0.82 \pm 0.01$  |
| 1.25                    | $1.23 \pm 0.04$  |
| 1.50                    | $1.23 \pm 0.06$  |
| 1.75                    | $1.45 \pm 0.045$ |
| 2.00                    | $1.85 \pm 0.04$  |

b)

Figure 27: STEM -EDX point analysis on nanofoils b) Ca:Si ratio comparison

### Structural analysis from FTIR/Raman: one solid solution $1.25 \leq \text{Ca: Si} \leq 2$

The C-S-H samples were also investigated by Fourier transform infrared spectroscopy (FTIR) and Raman micro-spectroscopy.

#### FTIR

In Figure 28, the FTIR results presented are the average of all scans made over the samples. All samples have a complex group of bands in the range of  $800\text{--}1100\text{ cm}^{-1}$ , corresponding to the asymmetric and symmetric stretching (U) vibrations of Si–O bonds. The weak bands in the range of  $1400\text{--}1500\text{ cm}^{-1}$  correspond to the asymmetric stretching of  $\text{CO}_3^{2-}$ , and the small shoulder at  $875\text{ cm}^{-1}$  is due to the out-of-plane bending of  $\text{CO}_3^{2-}$ . It was not possible to collect spectra under an inert atmosphere and prevent incorporation of  $\text{CO}_2$ , which occurred when exposed to air, even for a very short time. The band at  $1640\text{ cm}^{-1}$  is due to H–O–H bending vibration of molecular  $\text{H}_2\text{O}$ . The broader band at  $3000\text{--}3700\text{ cm}^{-1}$  is due to stretching vibrations of O–H groups in  $\text{H}_2\text{O}$  or hydroxyls with a wide range of hydrogen-bond strengths. These assignments were made from references of minerals and other solids listed in Table 9.

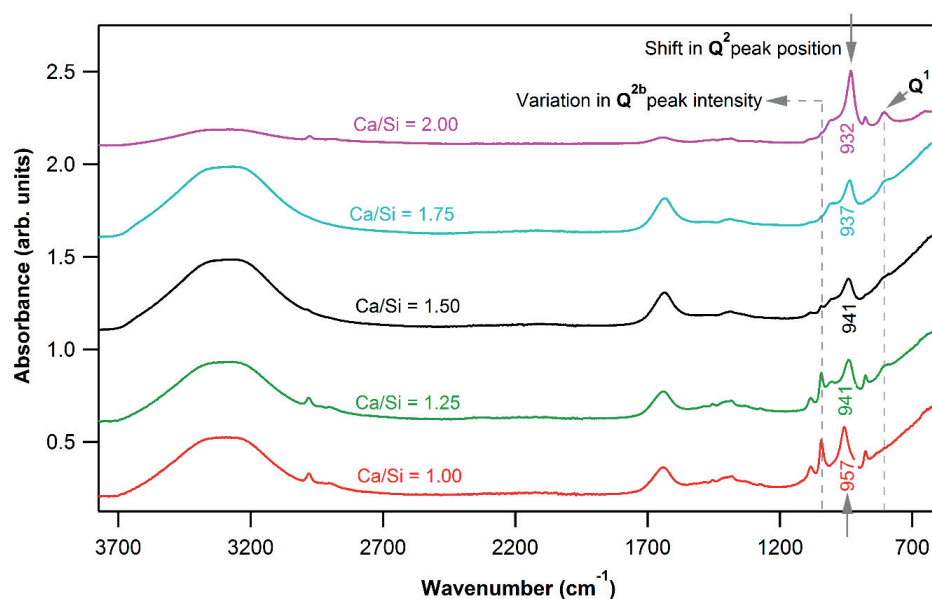


Figure 28: MID-IR spectra of C-S-H samples with different Ca:Si ratio

| Wavenumber (cm <sup>-1</sup> ) | Assignment   | References              |
|--------------------------------|--|-------------------------|
| <b>3400 - 3200</b>             | U O-H (H <sub>2</sub> O)                           | 96,104,120,121          |
| <b>2980</b>                    | U C-H (Ethanol)                                    | 122,123,124             |
| <b>1639</b>                    | δ O-H (H <sub>2</sub> O)                           | 104,120,125,126         |
| <b>1453</b>                    | U <sub>3</sub> CO (CO <sub>3</sub> <sup>2-</sup> ) | 120,121                 |
| <b>1386</b>                    | δ C-H (Ethanol)                                    | 123                     |
| <b>1084</b>                    | U <sub>3</sub> Si-O (Silica gel)                   | 96,121,126              |
| <b>1044</b>                    | U Si-O (C-S-H) Q <sup>2b</sup>                     | Our studies             |
| <b>957 – 932</b>               | U <sub>3</sub> Si-O (C-S-H) Q <sup>2</sup>         | Our studies, 96,104,121 |
| <b>876</b>                     | U <sub>2</sub> CO (CO <sub>3</sub> <sup>2-</sup> ) | 120,121                 |
| <b>805</b>                     | U Si-O (C-S-H) Q <sup>1</sup>                      | Our studies, 104,121    |

Table 9: IR band assignment

One key finding from the spectra is that there is no trace of a peak/hump in the region of 3645 cm<sup>-1</sup> which is a characteristic peak position for O-H stretching of Ca(OH)<sub>2</sub><sup>120</sup>, indicating the absence of crystalline calcium hydroxide in the system. The spectrum also includes the contribution of ethanol (used for washing), with features at 2980 cm<sup>-1</sup> and 1386 cm<sup>-1</sup> assigned to stretching (U) and bending modes (δ) of C-H, respectively. The strong band at around 957 – 932 cm<sup>-1</sup> for C-S-H is due to Si-O asymmetric (U<sub>3</sub>) stretching, previously identified as a Q<sup>2</sup> peak.<sup>96,104,121</sup> This characteristic Q<sup>2</sup> peak of C-S-H shifts towards lower wavenumbers with increasing Ca:Si ratio due to decreasing silicate polymerization.

This is in agreement with previous crystal models<sup>8,53,102</sup>, recent atomistic simulations<sup>127</sup> and our own NMR studies<sup>107</sup> that predict the structural mechanism for accommodating higher Ca:Si by depolymerization alongside deprotonation of silanol groups and incorporation of interlayer Ca. All three structural mechanisms are occurring simultaneously instead of one

being favoured over other, indicating the structure may belong to the single family especially for Ca:Si ratio above 1.25. This has never been shown clearly before for Ca:Si ratios  $\geq 1.6$  because of the inability to produce synthetic C-S-H in this stoichiometric domain. The band at  $805\text{ cm}^{-1}$  increases in intensity with Ca:Si ratio (in fact distinctly seen as a peak only for Ca:Si = 2) is assigned to Si-O symmetric stretching of  $Q^1$  tetrahedra. Another interesting feature is the presence of the band at  $1044\text{ cm}^{-1}$ , is designated to Si-O ( $Q^{2b}$ ) bridging tetrahedra. Yu<sup>104</sup> predicted that this regime of IR is expected to correspond to that of a  $Q^{2b}$  site. The peak intensities of this  $Q^{2b}$  indicates that bridging decreases with an increase in Ca:Si ratio. This data supports the general postulation (from NMR data)<sup>54,98</sup> that the Ca:Si ratio in C-S-H increases with the loss/omission of bridging tetrahedra that depolymerise the structure and with the simultaneous increase in the relative concentration of terminal  $Q^1$  sites. These results correspond to a defective tobermorite structure,<sup>10,50,53</sup> while no clear evidence of jennite-like structure is observed (i.e.) absence of principle absorption peak at  $1000\text{ cm}^{-1}$ . It appears that in our samples, de-bridging, depolymerization of silica tetrahedra and incorporation of Ca(-OH) in the interlayer is a simultaneous process, gradually taking place with an increasing Ca:Si ratio. This suggests that a single structural unit can describe the structure of C-S-H samples at Ca:Si > 1.25.

### Raman

The Raman spectra of our C-S-H samples presented in Figure 29. exhibit very high uniformity with better band resolution compared to previously reported synthetic work in the literature.<sup>10,52,88,96,128</sup> Relatively sharp bands indicate that the sample analysed has a uniform silicate structure, i.e. the Ca:Si ratio is spatially homogeneous within a given sample in agreement with the high chemical uniformity demonstrated in the STEM-EDX results above. Assignment of bands in our spectra are indicated in Table 10.

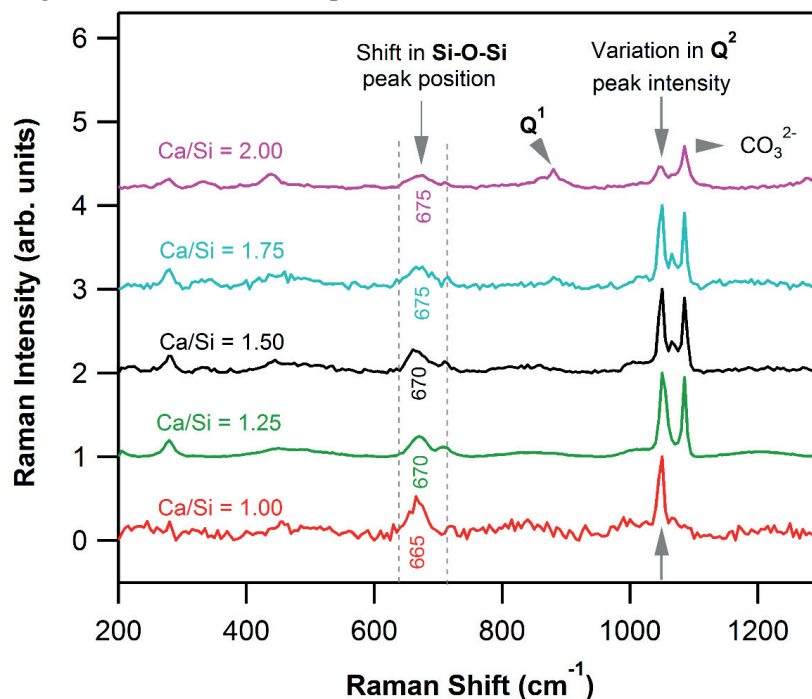


Figure 29: Raman Spectra for the precipitated C-S-H sample with varying Ca:Si ratios.

| Raman Shift (cm <sup>-1</sup> ) | Assignment  | References                    |
|---------------------------------|---|-------------------------------|
| 1080                            | U <sub>1</sub> CO <sub>3</sub>  |                               |
| 1050                            | U Si-O (C-S-H) Q <sup>2</sup>   |                               |
| 882-896                         | U <sub>1</sub> (SiO <sub>4</sub> ) Symmetric stretching of Q <sup>1</sup> |                               |
| 668-676                         | Symmetric Bending Si-O-Si   | 10,52,99,129, Own measurement |
| 445                             | U <sub>2</sub> (SiO <sub>4</sub> ), O <sub>nb</sub> -Si-O <sub>nb</sub>   |                               |
| 319-333                         | Lattice vibrations Ca-O   |                               |
| 280                             | CO (CO <sub>3</sub> <sup>2-</sup> )                                       |                               |

Table 10: Raman band assignment

The vibration observed at 1080 cm<sup>-1</sup> can be attributed to two modes of vibration: the symmetric stretching Si-O[Q<sup>3</sup>] mode or asymmetrical C-O stretching mode. The Si-O[Q<sup>3</sup>] has previously been generally observed for Ca:Si ratio  $\leq 1.25$ <sup>10,52,99</sup>, showing broad band of vibrations and disappearing with increasing Ca:Si. Therefore, we attribute this sharp band at 1080 cm<sup>-1</sup> to the symmetrical C-O stretching mode of the carbonate group. The high scattering cross-section of the symmetrical stretching [CO<sub>3</sub>] mode, means that even minor carbonation (as detected by FTIR above) of our samples yields to a relatively intense band in our Raman spectra near 1080 cm<sup>-1</sup>. Bands in the region 320–350 cm<sup>-1</sup> are assigned to Ca-O lattice vibrations (LV). This band is quite weak at lower Ca:Si ratios, while it sharpens and slightly shifts to higher frequencies at higher ratios. These changes presumably indicate a systematic strengthening of the Ca-O bonding with increasing Ca:Si ratio<sup>52</sup>. The band at 445 cm<sup>-1</sup> increases in intensity with increasing Ca:Si ratio, i.e. with increasing calcium content, could be attributed to O<sub>nb</sub>-Si-O<sub>nb</sub> bending vibrations. We assume that non-bridging oxygen atoms (O<sub>nb</sub>) attached to silicon are the main contributor to this vibration, thus explaining the observed increase in intensity with increasing Ca:Si ratio (the higher the Ca:Si, the higher the proportion of O<sub>nb</sub>). The peak in the spectra around 670 cm<sup>-1</sup> is assigned to Si-O-Si symmetrical bending (SB) vibrations. As shown in figure 8, the frequency of Si-O-Si bending bands is known to decrease either with increasing silicate polymerization or with increasing Si-O-Si angle.<sup>52,130</sup> We observe such a systematic gradual shift towards higher frequency from 665 to 675 cm<sup>-1</sup> with increasing Ca:Si ratio. The latter peaks (at higher Ca:Si ratio) are due to the higher degree of coupling of single silicon—bridging-oxygen (Si-O<sub>br</sub>) stretching vibrations.<sup>52,130</sup> The observation is coherent with our previous studies with NMR, showing the inclusion of Calcium in the interlayer.

With increasing Ca:Si ratio, the number of protons attached to O<sub>nb</sub> shared by silicon and calcium decreases. Consequently, the behaviour of the Raman scattering in the region 1040–1200 cm<sup>-1</sup> is consistent with deprotonation on the Si-O<sub>nb</sub> symmetric stretching (SS) vibration of Q<sup>2</sup> species. In our spectra (Figure 29) the Q<sup>2</sup> SS band at 1050 cm<sup>-1</sup> changes its intensity with increasing Ca:Si ratio with the minimal intensity for ratio 2. This was proposed by Garbev et.al<sup>52</sup> but not demonstrated since their synthetic technique could only produce C-S-H with Ca:Si ratio up to 1.50. According to Garbev et.al<sup>52</sup>, changes in the intensity of the SS Q<sup>2</sup> vibrations in this region could, therefore, be regarded as the result of two competitive processes that occur with increasing Ca:Si ratio: (i) an increasing number of Si-O-Ca linkages and (ii) a decreasing number of Q<sup>2</sup> species. The frequency shift of the Q<sup>2</sup> SS band as a function of Ca:Si

ratio may not depend solely on the degree of silicate polymerization, but may also reflect changes in calcium-coordination or the Ca–O<sub>nb</sub><sup>♦</sup> bond length in Si–O–Ca linkages. Another interesting aspect is shown by Wu et al.<sup>129</sup> is that Raman scattering in the range 1040–1100 cm<sup>-1</sup> are assigned to anti-symmetrical stretching of Q<sup>2</sup> stating that it cannot be neglected because its contribution is the greatest of all of the Q<sup>i</sup> configurations. It corresponds to the fact that depolymerization of the silicate structure should simultaneously lead to a decrease in the anti-symmetric stretching frequency and an increase in the symmetrical one as we observe in Figure 29.

Furthermore, we observe a weak intensity peak at 890 cm<sup>-1</sup> for Ca:Si >1.5, showing that the silicate anion structure consists of dimers (Si<sub>2</sub>O<sub>7</sub>) that are protonated, but there are only two OH groups per formula unit (p.f.u.) compared with four OH p.f.u. that's present in the phase with Ca: Si=0.67.<sup>52</sup> Bands in the 880–900 cm<sup>-1</sup> interval may be assigned to symmetric stretching of Q<sup>1</sup> silicate units (dimers). For our samples with Ca:Si =1 to 1.5, this band at 882 cm<sup>-1</sup> is barely distinguishable from the noise. Kirkpatrick et.al<sup>99</sup> described the enhancement of this band with increasing Ca:Si, but did not report a shift, whereas Garbev et.al<sup>52</sup> described the enhancement and slight shifting, but could not experimentally demonstrate the distinct sharp peak of Q<sup>1</sup> for Ca:Si ratio >1.5. We attribute the band at 882 cm<sup>-1</sup> to Q<sup>1</sup> chain end units and the band at 889 cm<sup>-1</sup> to silicate dimers. This again confirms that with increasing Ca:Si ratio, the “infinitely” long chains of the parent tobermorite minerals are no longer the dominant structural unit because depolymerization leads to shorter chains to finally form dimers.<sup>10,52</sup> Stronger band signals also indicate greater chemical uniformity of the samples used in this study. Kirkpatrick et.al.<sup>99</sup> in Raman analysis observed a broadband at 970 cm<sup>-1</sup> in the spectrum of a jennite standard, and attributed it to Q<sup>2</sup> silicate units therein, but we do not observe this or any of the other jennite characteristic bands at 655, 490, and 325 cm<sup>-1</sup>, even at higher Ca:Si ratio. In particular, we do not observe a significant shift of the Si–O–Si bending band towards 655 cm<sup>-1</sup> with increasing Ca:Si ratio. But on the contrary, we see a shift in the opposite direction. So there is no evidence for the general similarity of the analysed C-S-H structures to any local jennite-like structures or jennite like domains previously speculated.

Garbev et.al.<sup>52,131,132</sup> by Raman analysis demonstrated using Stade and Wieker's model<sup>111</sup>, a C–S–H(I) phase with a Ca:Si ratio of 0.67 must consist of infinite silicate chains attached to a calcium polyhedral layer to give “tobermorite slabs.” At this Ca:Si ratio, no additional calcium is needed in the interlayer as all silanol groups and bridging Si are intact. Thus, the interlayer consists solely of H<sub>2</sub>O molecules, which plays an essential role in holding together two “tobermorite slabs” consisting of infinite silicate chains. Moreover, assuming that the model of Stade and Wieker's holds, the upper limit for Ca:Si ratio must be 1.25, with the resultant formula Ca<sub>5</sub>[HSi<sub>2</sub>O<sub>7</sub>]<sub>2</sub>.nH<sub>2</sub>O, from which it becomes clear that at a Ca:Si ratio of 1.25 (in our sample C-S-H), there is an additional calcium atom in the interlayer. Beyond this ratio, the inclusion of more calcium atoms in the interlayer will result in higher Ca:Si ratios. These Raman results indicate that the structure of our synthetic C-S-H's are closer to tobermorite, with high end Ca:Si ratios appearing similar to that of a defective tobermorite structure.

---

<sup>♦</sup> nb: non bonded



There is a morphological point around pH 11, for Ca:Si between 1 and 1.25. Hence, there is a change in the structural family i.e. there are 2 solid solutions needed to describe C-S-H but there is no need for a third solid solution or new phase ( $\gamma$ -C-S-H). Then progressive changes in the spectra from 1.25 to 2. Suggesting that from  $>1$  to 2 one defective tobermorite structure can represent the different C-S-H's i.e. no need to invoke a new phase or solid solution above Ca:Si ratios of 1.6

## Discussion

We have shown that synthetic C-S-H with Ca:Si ratios  $\geq 1.6$  can be produced by well controlled precipitation techniques. From the series of preliminary experiments we showed that the experimental results (Ca:Si ratio) were consistent with thermodynamic modelling carried out with GEMS for Ca:Si  $\leq 1.6$  and for Ca:Si  $\geq 1.6$ , if portlandite precipitation was excluded. The absence of portlandite was confirmed experimentally. Although XRD is not very sensitive to small percentages or very poorly ordered nanocrystalline CH, FTIR is very sensitive and shows no signal at all in the expected region. This is backed up by the Raman spectroscopy and the lack of any significant weight loss in the TGA thermograms in the region between 400 and 500°C. The reason for the lack of portlandite is probably because of kinetics of nucleation and growth it is nominally (i.e. equilibrium thermodynamic calculation using GEMS) supersaturated with respect to CH. We left the precipitated C-S-H in the mother solution for up to 11 months in sealed vessels and saw no evolution of the phases in the sample, i.e. no formation of portlandite, suggesting that once formed the C-S-H of a particular stoichiometry is in equilibrium with its mother solution. The mother solution after 3hrs has very low calcium concentrations below  $10^{-7}$  M (ICP measurements). The question of the kinetics warrants further investigation and such a study is underway using the reactor described in this paper. Kinetic data is being collected for the change in the Ca ion activity via the reverse dropwise precipitation technique and data analysis will be made with a population balance modelling approach<sup>133</sup>. Since we dealt in general with wet slurries we did see carbonation on exposure to air, in both XRD, FTIR and Raman. This increase in carbonation products was particularly well seen in the FTIR/Raman results where calcium carbonate signals were seen to increase with exposure time, more detailed results are presented in<sup>107</sup>. All the carbonation products are probably from C-S-H decomposition which was previously suggested in the literature.<sup>96,121</sup>

The morphological point observed for pH's around 10.8 suggests that as in previous studies synthetic C-S-H can be grouped into 2 families. Previous studies separated on a solubility product basis but here we show that there is also a significant and easily recognisable morphological change. From this point, our Raman, FTIR and recent NMR studies<sup>107,117</sup> suggest our synthetic C-S-H's with Ca:Si ratios  $\geq 1.25$  all the way to 2 can be represented by one solid solution and not 2 or more as proposed previously<sup>6,53,81,134</sup>. Recently Kulik et.al<sup>135,136</sup> with their thermodynamics modelling seems to be heading in the same direction.

These uniform synthesis C-S-H can help in better understanding of the atomistic structure and possible growth mechanisms or pathways. The system can allow us to study the influence of other ions present in Portland cement or blended cement systems – maybe at lower concentrations to approach kinetics closer to those seen in Portland cement are necessary here. The system can provide the base for the understanding the influence of heterogeneous substrates on the nucleation, growth and precipitation pathway. Such uniform systems should also be useful in understanding the sorption/or effect of additives on C-S-H nucleation and growth.

## Conclusions

We have developed a synthetic precipitation system which allows the controlled synthesis of C-S-H with Ca:Si ratio from 1 to 2 without the presence of any secondary phases. The lack of secondary phases (in particular calcium hydroxide) was shown from FTIR, XRD, TGA, Raman or electron microscopy analysis. Also a synthetic C-S-H of desired stoichiometry can be predicted using thermodynamic modelling by controlling the pH and excluding the formation of Calcium hydroxide in the high concentration conditions investigated (0.2 M Ca). High-resolution STEM-EDX analysis showed that the 5 synthetic C-S-Hs produced in the current study were very uniform in chemical composition with deviations of Ca:Si ratios of less than 1 % at a 3nm scale. Analysis with FTIR and Raman of these chemically uniform C-S-H precipitates ranging from 1.25 to 2 resolved some key structural features not previously seen or reported. FTIR and Raman spectroscopic data for C-S-H samples confirms the close proximity of the structure of C-S-H with a defective tobermorite. Besides mutual agreement between the two spectroscopic results, the work indicates that one type of structure is sufficient to describe the synthetic C-S-H system for Ca:Si 1.25 to 2. Whereas, we clearly observe the for Ca:Si  $\leq 1.25$ , the change in morphology and change in the IR and Raman spectra appear to belong to another structural family. The current work now opens the door to investigating the formation pathway of C-S-H in more detail.

## Author information

Corresponding author: abhishek.kumar@epfl.ch

The Authors declare no competing financial interest

## Acknowledgment

We would like to thank Dr Dimitri Kulik and Dr Barbara Lothenbach for useful discussion and guidance. Authors would like to thank Swiss national foundation for financing this project (Grants No. SNF\_153044)



## 5 Atomic Structure of Calcium Silicate Hydrates

### 5.1 Introduction.

This chapter covers deals with the all-important debate over the atomic level information on the high Ca:Si ratio C-S-H. The next section is the accepted manuscript and the Supplementary information of the draft is presented in Annexure. As the first author in the manuscript, my role being an experimentalist is to provide the synthetic pure C-S-H for NMR studies that has a well characterized composition and morphology. Further, I contributed in understanding and interpretation of of NMR data and development of constraints for atomistic simulated structure from DFT calculations. The experimental evidence allows us to stand tall on our interpretation rather than just speculative modeling work made on average results from many different experimental set ups to produce C-S-H with probably significant variation in compositions and morphology.

### 5.2 Manuscript

The article was accepted in June 2017, as the cover page article for the Journal of Physical Chemistry C, with the following cover image.

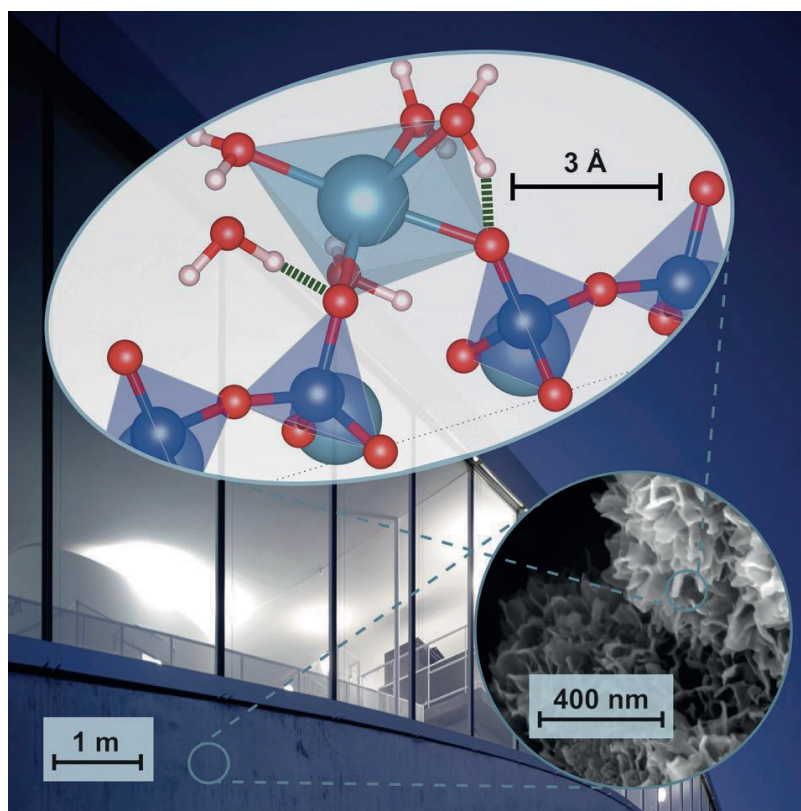


Figure 30: Cover page of JPCC manuscript

# Atomic-Level Structure of Cementitious Calcium Silicate Hydrate

Abhishek Kumar,<sup>1</sup> Brennan J. Walder,<sup>2</sup> Aslam Kunhi Mohamed,<sup>1</sup> Albert Hofstetter,<sup>2</sup> Bhuvanesh Srinivasan,<sup>1,3</sup> Aaron J. Rossini,<sup>4</sup> Karen Scrivener,<sup>5</sup> Lyndon Emsley<sup>\*2</sup> and Paul Bowen<sup>\*1</sup>

<sup>1</sup>Powder Technology Laboratory, Institut des Matériaux, Ecole Polytechnique Fédérale de Lausanne (EPFL), CH-1015 Lausanne, Switzerland

<sup>2</sup>Institut des Sciences et Ingénierie Chimiques, Ecole Polytechnique Fédérale de Lausanne (EPFL), CH-1015 Lausanne, Switzerland

<sup>3</sup>Department of Earth & Environmental Sciences, Ludwig-Maximilian University, D-80333, Munich, Germany

<sup>4</sup>Department of Chemistry, Iowa State University, Ames, IA 50011-3020, USA

<sup>5</sup>Construction Material Laboratory, Institut des Matériaux, Ecole Polytechnique Fédérale de Lausanne (EPFL), CH-1015 Lausanne, Switzerland

---

**ABSTRACT:** Efforts to tune the bulk physical properties of concrete are hindered by a lack of knowledge related to the atomic-level structure and growth of calcium silicate hydrate phases, which form about 50-60% by volume of cement paste. Here we describe the first synthesis of compositionally uniform calcium silicate hydrate phases with Ca:Si ratios tunable between 1.0 and 2.0. The calcium silicate hydrate synthesized here does not contain a secondary Ca(OH)<sub>2</sub> phase, even in samples with Ca:Si ratios above 1.6, which is unprecedented for synthetic calcium silicate hydrate systems. We then solve the atomic-level three-dimensional structure of these materials using dynamic nuclear polarization enhanced <sup>1</sup>H and <sup>29</sup>Si nuclear magnetic resonance experiments in combination with atomistic simulations and density functional theory chemical shift calculations. We discover that bridging interlayer calcium ions are the defining structural characteristic of single-phase cementitious calcium silicate hydrate, inducing the strong hydrogen bonding that is responsible for stabilizing the structure at high Ca:Si ratios.

---

## Introduction

Calcium silicate hydrate (C-S-H) is the primary binding component of concrete, forming about 50-60% by volume of hardened cement paste and making it one of the most common substances of the modern world. Because of its ubiquity, it is surprising that a complete description of its atomic-level structure remains the subject of debate<sup>137,138</sup>, and consequently its structure-property relationships are not well known. This makes it difficult to engineer C-S-H not only for its primary uses in construction, in which high reactivity and strength at low carbon footprints are desirable, but also for emerging applications such as dental filling and bone repair,<sup>139,140</sup> which require biocompatibility; waste water treatment,<sup>141,142</sup> which requires high specific surface areas; and encasement of nuclear waste,<sup>143</sup> which requires high structural integrity in the presence of significant radionuclide concentrations.

For Portland cements the precipitation of C-S-H occurs in conjunction with the precipitation of other material phases such as crystalline Ca(OH)<sub>2</sub>, ettringite, and CaCO<sub>3</sub>.<sup>144,145</sup> The C-S-H phases are known to be rich in calcium, with Ca:Si ratios exceeding 1.75 at early stages of hardening.<sup>146</sup> In contrast, synthetic C-S-H with Ca:Si ratios above ~1.5 are often observed in coexistence with a Ca(OH)<sub>2</sub> phase. Because of an inability to synthesize pure C-S-H with Ca:Si ratios above 1.5, many researchers believe that Ca-rich C-S-H systems are intrinsically a binary mixture of a chemically disordered single phase C-S-H material. In such a case, one phase consists of a “proper” C-S-H phase, with a layered silicate chain structure related to that of the naturally occurring calcium silicate hydrate mineral tobermorite and limited to Ca:Si ratios around 1.6. The other phase consists of nanocrystalline Ca(OH)<sub>2</sub>, which is thought to occur in bulk form occupying pores in the proper

C-S-H phase or as chemically distinct ribbons or sheets interwoven within the C-S-H structure itself.<sup>103,131,132,147,148</sup> This interpretation has the support of thermodynamic and solubility data analyzing a multitude of C-S-H systems.<sup>149</sup> Furthermore, in spite of a vast amount of experimental data yielding partial characterization, the positions of the calcium atoms in the interlayer, which are the essential aspects of high Ca:Si ratios in C-S-H, remain undefined. Thermodynamic modeling and crystal chemical reasoning have been applied to propose complete C-S-H structural models at Ca:Si ratios greater than 1.5,<sup>103</sup> but for these compositions the focus has been on the binary C-S-H/Ca(OH)<sub>2</sub> representation, for which experimental validation is ongoing.<sup>150</sup>

Here we introduce a method which achieves the synthesis of C-S-H possessing Ca:Si ratios between 1.0 and 2.0, maintaining a single phase composition even for C-S-H whose Ca:Si ratio exceeds 1.6. Aqueous calcium nitrate and sodium silicate solutions are reacted under conditions of high supersaturation and constant pH, the latter of which is set by the addition of a predetermined amount of alkali hydroxide. The production of a single phase composition at such Ca:Si ratios has not been achieved using conventional methods for C-S-H synthesis<sup>11,114,151–153</sup> relying on combinations of dissolution and direct precipitation<sup>6,83,97</sup> reactions that operate at either lower supersaturation or uncontrolled pH conditions. We also use  $\{^1\text{H}\}^{29}\text{Si}$  cross-polarization (CP) MAS NMR to measure populations of Q species, the connectivity between those species, and correlations between  $^{29}\text{Si}$  and  $^1\text{H}$  chemical shifts of the single-phase C-S-H produced using our rapid precipitation method. The greatest drawback of  $^{29}\text{Si}$  solid-state NMR is its low sensitivity, which we circumvent by using modern dynamic nuclear polarization (DNP) strategies<sup>154–156</sup> that have been recently used to study the hydration of cementitious systems with

tremendous success.<sup>94</sup> The Q species information allows us to quantify the extent of silicate polymerization in the structure. Finally, we use atomistic modeling to establish a connection between the measured  $^1\text{H}$  chemical shifts and the atomic-level position of calcium atoms in the interlayer, allowing us to solve the three-dimensional atomic-level structure of synthetic cementitious C-S-H.

## Methods

*Synthesis:* pH governs the type of silicates species available for precipitation of C-S-H. The Ca:Si ratio attained in the solid phase was found to depend on the pH of the solution. Thermodynamic modeling<sup>80,81</sup> also predicts that Ca:Si ratios above 1.5 can only be produced under high pH conditions, as occurs in the hydration of real Portland cement systems, in order to ensure that the electrostatically stable monomeric  $\text{SiO}_2(\text{OH})_2^{2-}$  species remains in abundance at high supersaturation and rapid precipitation conditions.

To maintain the desired supersaturation, pH, and mixing conditions, and to avoid carbonation, we developed a synthetic apparatus for controlling the reaction conditions to the degree of precision required, aided by real-time acquisition of kinetic data such as  $\text{Ca}^{2+}$  ion concentration, pH and conductivity. Details regarding its construction are given in the Supporting Information section II.

All reaction solutions were prepared in decarbonized, demineralized ultrapure water. The reaction chamber was kept under an inert nitrogen atmosphere in order to prevent carbonation. C-S-H precipitates were collected after a duration of 3 hours and again after 24 hours. The products were separated from mother liquor using vacuum filtration over a 20 nm organic filter and later washed with ethanol and water to remove salts and unwanted ions from the surfaces of C-S-H. We produced five different C-

S-H powders with nominal Ca:Si ratios of 1.0, 1.25, 1.5, 1.75 and 2.0. The precise experimental conditions for the precipitation of the different stoichiometry of the C-S-H were determined using thermodynamic modelling,<sup>81,157</sup> with the exclusion of calcium hydroxide, as there was no experimental evidence for its formation. Additional details are given in Section IV of the SI.

*Dynamic nuclear polarization:* DNP solid-state NMR experiments were carried out on the aqueous suspensions of freshly prepared C-S-H nanoparticles with added impregnation agent and were not dried. The impregnation agent used was 22 mM AMUPol in 65:35 v:v d<sub>8</sub>-glycerol:D<sub>2</sub>O, which was purged of dissolved oxygen by bubbling with N<sub>2</sub> gas for roughly five minutes. The addition of the radical polarizing agent further dilutes the samples by about 20%, but simple drying steps to increase the concentration of C-S-H led to sample deterioration (SI section VI). About 25 mg of the impregnated gels were worked into a 3.2 mm OD sapphire rotor and plugged with a PTFE insert. The drive caps were zirconia. The DNP enhanced NMR experiments were carried out at a nominal field strength of 9.4 T using a commercial Bruker AV I 400 MHz/263 GHz DNP NMR spectrometer.<sup>158</sup> The samples were rapidly transferred into the stator of the NMR probe which was pre-cooled to 100 K to promote glass formation. Proton DNP enhancements were found to exceed 35 for all samples.

*High resolution electron microscopy:* HRSEM micrographs were obtained by coating the samples with 6 nm of osmium (gas phase coating). The metallization reduces charging and provides enhanced image contrast. High resolution SEM analysis was performed on a Zeiss Merlin, equipped with the GEMINI II column which combines ultra-fast analytics with high resolution imaging using advanced detection modes. Osmium coated samples were analyzed with acceleration voltage of 1 kV with

probing current of 300 nA. On-axis in-lens secondary electron detection mode was employed for imaging. The instrument provides up to 0.6 nm resolution in STEM mode. In TEM mode, the samples were imaged at room temperature using a Tecnai F20 (FEI, The Netherlands) operating at an acceleration voltage of 100kV LaB<sub>6</sub> gun with a line resolution of 0.34 nm, with images being recorded on a high sensitivity 4k x 4k pixel CCD camera. For SEM and TEM analysis, 50 mg of sample was dispersed in 40 mL of isopropanol. A drop of the suspended liquid was allowed to dry on a copper grid (200 mesh grids). The copper grids were glow discharged prior to sample disposition.

*FTIR:* Freshly prepared samples were analyzed with a PerkinElmer FT-IR spectrometer, with a resolution of 0.5 cm<sup>-1</sup> to 64 cm<sup>-1</sup>. Wavelength accuracy was about 0.1 cm<sup>-1</sup> at 1600 cm<sup>-1</sup>. FTIR measurements were performed with an attenuated total reflectance (ATR) unit and data was recoded and processed using Spectrum One software. The ATR unit included a diamond crystal and a clamp for pressing solid materials onto the crystal with constant pressure. The transmittance results of 256 scans were recorded between 4000 and 450 cm<sup>-1</sup>, with individual measurements taken every 2 cm<sup>-1</sup>. For the solid gels, air was used as the background.

*Raman:* Non-invasive Raman microscopy was carried out using a Renishaw inVia Reflex spectrometer equipped with a 785 nm diode laser. The power delivered to the sample was 164 mW at a full power specification. The grating size was 1200 lines/mm with an edge filter for Rayleigh rejection. Ca(OH)<sub>2</sub> and CaCO<sub>3</sub> standards were measured at 5% power with a single 10 s accumulation period. Freshly prepared C-S-H was measured with multiple accumulation periods, each of 13 s exposure.

*MD:* Classical molecular dynamics simulation with force field potentials were used to test the structural stability of the proposed structures. The force field parameters used are known to



describe well cementitious material systems.<sup>159</sup> Simulations were done in a constant pressure ensemble at 300 K and a time step of 0.7 fs using Velocity Verlet integration algorithms

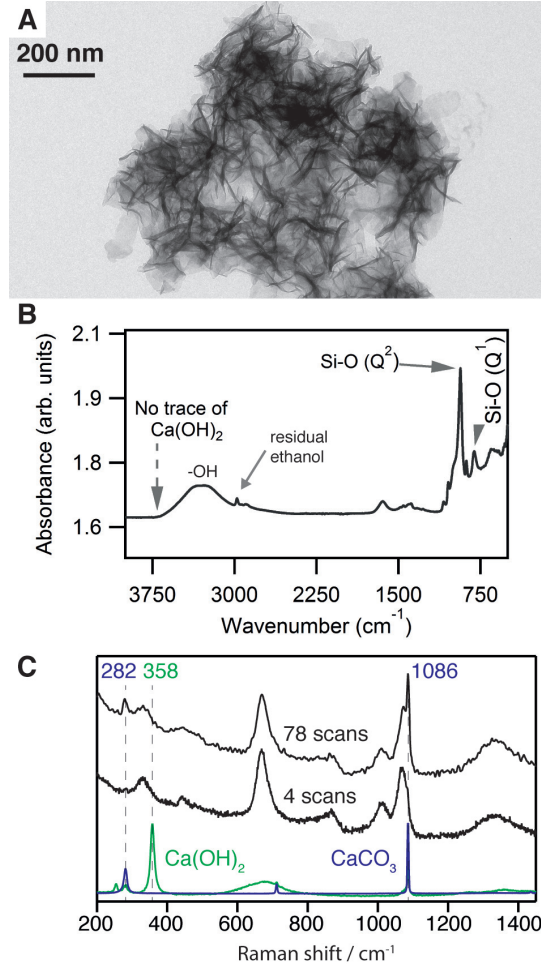
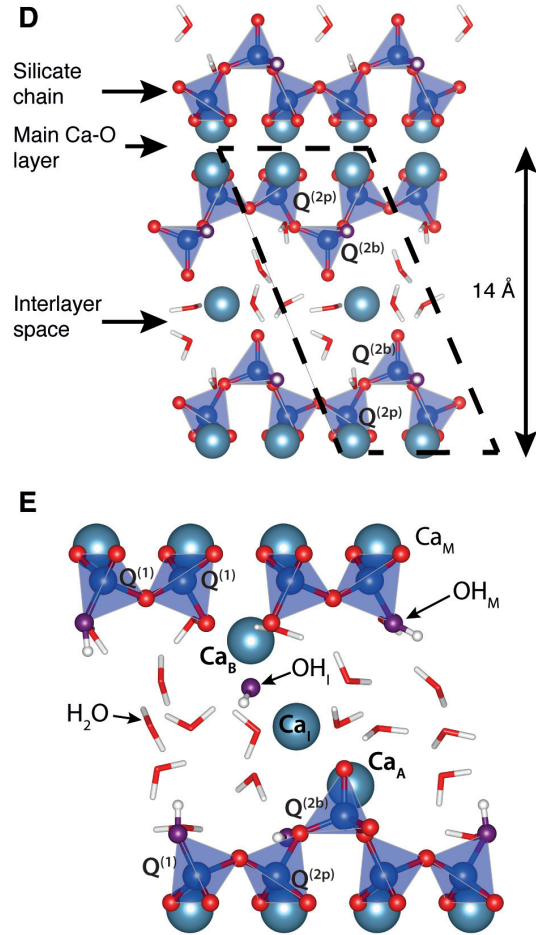


Figure 31 Structural elements of C-S-H. (A) High-resolution TEM image of pure C-S-H with Ca:Si ratio of 2.00, showing its “nanofoil” morphology. (B) Fourier transform IR spectroscopy showed no evidence of phases other than the C-S-H, including Ca(OH)<sub>2</sub>. (C) Comparison of Raman spectra of Ca(OH)<sub>2</sub> (green), CaCO<sub>3</sub> (blue), a sample of C-S-H with Ca:Si = 2.0 after 4 scans (lower black), and a sample of C-S-H with Ca:Si = 2.0 after 78 scans (upper black). (D) Chain topology in the layered 14 Å tobermorite (Ca:Si = 0.83). (E) Defective and short dreierketten chains in C-S-H, showing two dimers ( $n = 0$ ) and one pentamer ( $n = 1$ ).

**NMR shift calculations:** Atomic positions and unit cell parameters were optimized as described in the SI section XII. The chemical shielding  $\sigma_{calc}$  was calculated using the generalized gradient approximation (GGA) functional PBE<sup>161</sup> within the Quantum Espresso code<sup>162</sup> and the GIPAW method.<sup>163</sup> In every calculation a plane-wave maximum cutoff energy of 80 Ry,

implemented in DLPOLY.<sup>160</sup> Ewald summation was used to take into account the long range forces above a cutoff distance of 8.5 Å.



and a Monkhorst-Pack grid of  $k$ -points<sup>164</sup> corresponding to  $0.03 \text{ \AA}^{-1} - 0.04 \text{ \AA}^{-1}$  in reciprocal space was employed. The chemical shielding was converted into calculated chemical shifts  $\delta_{calc}$  by the relation  $\delta_{calc} = \sigma_{ref} - \sigma_{calc}$ , with the value of  $\sigma_{ref}$  determined by a linear regression between the calculated and experimental values for the calcium hydroxide structure (<sup>1</sup>H chemical shifts) and the

unperturbed tobermorite structure<sup>165</sup> (<sup>29</sup>Si chemical shifts).

## Results and Discussion

### Morphology

Two typical morphologies were seen by electron microscopy: “nanoglobules”, for the Ca:Si ratio of 1.00; and “nanofolds”, for Ca:Si ratios  $\geq 1.25$ , which is the morphology shown in Figure 31A. The foil morphology is very similar to morphologies for C-S-H seen in Portland cement systems with high alkaline contents.<sup>157,166</sup> Thicknesses of the foil-like structures are generally between 6 nm and 10 nm. The pure phase C-S-H systems were all shown by high-resolution analytical transmission electron microscopy (TEM) to be uniform for Ca:Si ratios

between 1.0 and 2.0 at less than a 9 nm<sup>2</sup> pixel size. This is also supported by X-ray diffraction (XRD) and scanning TEM with energy dispersive X-ray analysis (STEM-EDX), as described in the SI section V. No secondary phases such as Ca(OH)<sub>2</sub> were detected by IR or thermogravimetric analysis (TGA), as shown in Figure 31B; however, long exposure of C-S-H sample to open air (for example in TGA or XRD analysis) does eventually lead to the formation of CaCO<sub>3</sub>. This phenomenon manifests well in the Raman spectra of Figure 31C, showing that CaCO<sub>3</sub> forms during prolonged measurements in air, whereas the signature of Ca(OH)<sub>2</sub> is never observed regardless of measurement duration.  $\zeta$ -potential measurements on the samples

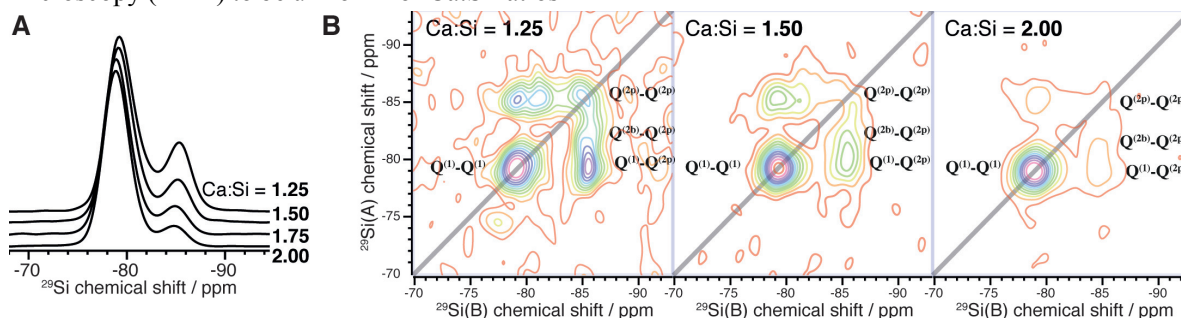


Figure 32.: One- and two- dimensional NMR enhanced <sup>29</sup>Si CP MAS spectra of C-S-H samples for quantification of silicate chain distributions. (A) 1D spectra across the compositional series. (B) Experimental 2D refocused INADEQUATE spectra for three of the C-S-H compositions studied (the spectra have been sheared to produce a COSY-like representation). Contours are drawn in 10% intervals beginning at 5% of the maximum signal intensity.

show negative potential surfaces indicating that calcium does not reside at the surface but is incorporated into the particles.

### Characterization by DNP NMR

C-S-H is a poorly ordered material, making atomic level structural determination using conventional X-ray and neutron diffraction methods challenging, especially for non-dried samples. Solid-state magic-angle spinning (MAS) NMR is a powerful method for studying disordered systems, and has been extensively

used to study the molecular structure of C-S-H and related mineral phases.<sup>100</sup> Previous <sup>29</sup>Si MAS NMR<sup>45,54,165,167–169</sup> and diffraction studies, often on dried materials, have established that the silicate chains in C-S-H are arranged according to the “dreierketten” model,<sup>45,54,170,17154</sup> which specifies a repeating unit for the chains comprised of a bridging-type Q<sup>(2b)</sup> silicate tetrahedron flanked by pairing-type Q<sup>(2p)</sup> silicate tetrahedrons, highlighted in the tobermorite structure shown in Figure 31D. The silicate chains are flanked by a calcium oxide layer and a hydrous interlayer. Each silicate tetrahedron shares two O atoms with other silicate

tetrahedrons and on this basis are both classified as  $Q^{(2)}$  species. The pairing-type  $Q^{(2p)}$  species direct the other two O atoms toward the main calcium layer whereas the bridging-type  $Q^{(2b)}$  species direct them toward the hydrous interlayer. Defects occur through the removal of a  $Q^{(2b)}$   $SiO_2$  unit, breaking up the idealized infinite silicate chains of tobermorite into finite segments consisting of  $(3n+2)$  silicate tetrahedrons, as illustrated in Figure 31E. The segments are terminated by  $Q^{(1)}$  silicate species. The interlayer calcium and water present in the original 14 Å tobermorite are  $Ca_I$  and  $H_2O$  respectively whereas the  $Ca_B$ ,  $Ca_A$  and  $OH_I$  are only present in the defective structures.  $Ca_B$  sites replace bridging silicate tetrahedrons,  $Ca_A$  sites are additional calcium atoms in the interlayer, and  $OH_I$  are additional hydroxyl groups in the interlayer to charge compensate the additional Ca ions needed to reach high Ca:Si ratios. Silicate dimers ( $n = 0$ ) have been observed by  $\{^{29}Si\}^{29}Si$  correlation NMR experiments to be the dominant species for systems with Ca:Si  $\sim 1.5$ , both for synthetic C-S-H systems and during the initial formation of C-S-H in hydrating tricalcium silicate.<sup>45,172</sup>

To overcome the low sensitivity of  $^{29}Si$  MAS NMR at natural isotopic abundance we use modern DNP strategies.<sup>154–156</sup> DNP is based on the transfer of large unpaired electron spin polarization to nearby protons by saturation of the electron spin transitions with microwaves, followed by CP transfer of the enhanced polarization to the  $^{29}Si$  nuclei. The electron polarization is provided here by the organic biradical AMUPol<sup>173</sup> that is added to the wet C-S-H as a minimal amount of  $d_8$ -glycerol/ $D_2O$  solution before the NMR sample is rapidly cooled to 100 K for the experiments.<sup>156,174–176</sup> The cryogenic temperatures are required to maximize the sensitivity enhancements by DNP, but are also important here to quench proton exchange and prevent the C-S-H from degrading during the experiments. Efficient DNP occurs

only for those parts of the sample that have successfully passed through the glass transition. We also note that pore water is susceptible to glass formation when rapidly inserted into the pre-cooled NMR probe even without the addition of a glassing agent such as glycerol.<sup>177</sup> We therefore do not expect the C-S-H structure to be disrupted by our experimental conditions; furthermore, even if pore water does crystallize in parts of the sample, inefficient DNP will suppress the NMR signal from these regions.

The polarizing agent contains labile deuterons, which can lead to the formation of calcium silicate deuterate through isotope exchange. At most, 40 mol% of labile hydrogen in the impregnated C-S-H gels (C-S-H hydrogen,  $D_2O$ , and the -OD groups of the  $d_8$ -glycerol) are deuterons given our DNP sample formulation and estimated C-S-H composition. If a reasonable allowance for excess pore and adsorbed water is made, this falls to about 25%. In fact, this upper limit is almost certainly never reached. Small-angle neutron scattering studies have shown that deuteron exchange into the gel is a diffusion driven process providing full isotope exchange on the time scale of tens of hours.<sup>178</sup> Since the impregnated sample never spent more than 1.25 h, and usually just 0.25 h, at room temperature prior to experiments, we expect the highest degree of partial deuteration to be surface based and the NMR signal should be representative of fully protonated bulk C-S-H. Moreover, there is little in the way of evidence in the small-angle neutron scattering literature to suggest that isotope exchange modifies C-S-H in any structurally significant way.

One-dimensional  $\{^1H\}^{29}Si$  DNP CP echo spectra for the five compositions are shown in Figure 32A. With the exception of the Ca:Si = 1.00 composition, good fits to the line shapes are obtained by modeling each of the constituent Q sites as a Gaussian function, whose amplitudes are used to determine the relative populations of the Q species. Relative

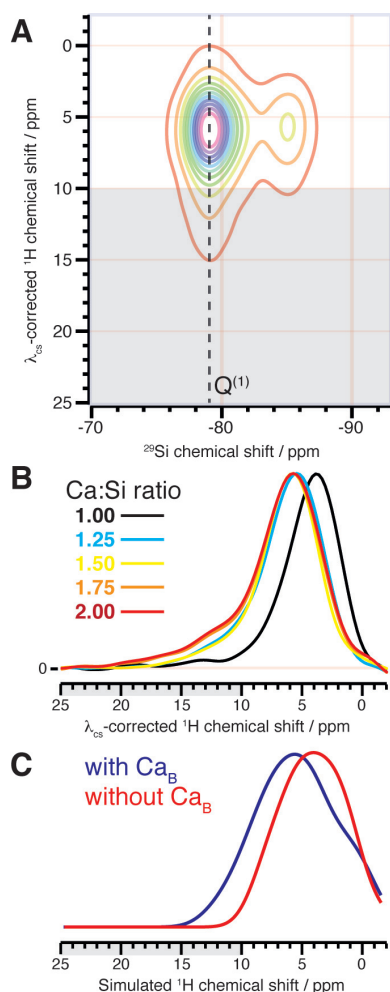


Figure 33: DNP enhanced 2D  $\{^1\text{H}\}\text{-}^{29}\text{Si}$  HETCOR correlating  $^1\text{H}$  spectra to specific Si sites. (A) The 2D correlation spectrum for the Ca:Si = 1.50 composition acquired with a 7 ms CP contact time. (B) 1D cross sections parallel to the  $^1\text{H}$  dimension extracted at the position of the dashed line in the 2D spectrum, representing  $^1\text{H}$  spectra correlated to  $\text{Q}^{(1)}$ . (C) Simulated  $^1\text{H}$  chemical shift spectra aggregated over C-S-H substructures that either possess (blue) or lack (red) the bridging calcium site  $\text{Ca}_\text{B}$ . The intensity of these spectra are normalized with respect to the maximum of the  $\text{Q}^{(1)}$  peak. The region downfield of 10 ppm is shaded to indicate the domain of strongly hydrogen bonded species.

signal intensities in DNP enhanced CP MAS experiments are not usually in proportion to the relative populations of the nuclei generating the signal as they often are in experiments using direct excitation without hyperpolarization unless we assume that 1) the length scale of hyperpolarization non-uniformity is larger than

the unit cell of the particle, and 2) cross-polarization kinetics can be measured and used to adjust the signal intensities appropriately.

The size of the C-S-H particles are sufficiently small and have a proton density sufficient for nearly uniform polarization of the particles over the recycle period. To the second point, we performed cross-polarization measurements for different values of the cross-polarization contact time. This data was fit to a simple  $IS$  model of CP kinetics for each site<sup>179</sup>. A detailed description of the fitting procedure and the  $Q$  populations determined by this method are given in the SI section VIII. We note here that the failure of the Ca:Si = 1.00 composition to fit well to the three-Gaussian model suggests a different molecular structure.

The  $\{^{29}\text{Si}\}\text{-}^{29}\text{Si}$  connectivity is measured using 2D refocused INADEQUATE experiments,<sup>180</sup> whose application to cementitious systems has hitherto not been feasible without isotopic enrichment.<sup>45,172</sup> In the  $\{^{29}\text{Si}\}\text{-}^{29}\text{Si}$  INADEQUATE spectrum only signals from covalently bonded  $^{29}\text{Si} - \text{O} - ^{29}\text{Si}$  pairs are retained. For linear silicate chains at natural isotopic abundance, these constitute at most 0.5% of all Si – O – Si pairs. The improvement in NMR sensitivity provided by DNP makes it possible to obtain such spectra,<sup>181</sup> as shown in Figure 32B. Autocorrelation peaks corresponding to  $\text{Q}^{(1)}\text{-Q}^{(1)}$  dimer and  $\text{Q}^{(2p)}\text{-Q}^{(2p)}$  extender units are observed, but peaks corresponding to  $\text{Q}^{(2b)}\text{-Q}^{(2b)}$  are always absent, consistent with the dreierketten model. Remarkably, the usually dominant  $\text{Q}^{(1)}\text{-Q}^{(1)}$  autocorrelation peak is entirely absent for the

Ca:Si = 1.00 composition (SI section IX), suggesting that this composition does not contain silicate dimers. Cross peaks from all three  $Q$  sites to  $\text{Q}^{(2p)}$  are also observed. Using the chemical shift constraints from the deconvolution of the 1D CP echo spectra, the INADEQUATE spectra are decomposed using 2D Gaussian line shapes to model each of the six



possible correlation peaks. This line shape generates reasonably good fits (SI section IX), suggesting that the chemical disorder is very local. The 2D peak intensities are fit simultaneously across the four compositions for a conditional probability  $P(A|B)$  that Q site A is connected to Q site B.

2D  $\{^1\text{H}\}^{29}\text{Si}$  HETCOR experiments were used to correlate  $^1\text{H}$  chemical shifts with the  $^{29}\text{Si}$  chemical shifts. Measurements were made using CP contact times of 0.7 ms and 7 ms for each sample. The use of a short contact time biases the contribution to the NMR signal from those protons that are close to the correlating  $^{29}\text{Si}$  nuclei, as compared to longer range correlations observed in the long contact time experiment, which samples proton environments out to  $\sim 1$  nm.

The line shape in the 2D  $\{^1\text{H}\}^{29}\text{Si}$  HETCOR spectrum shown in Figure 33A is dominated by inhomogeneous broadening resulting from chemical disorder, which prevents an accurate line shape deconvolution on the basis of proton site. Cross sections of these spectra yield  $^1\text{H}$  chemical shift spectra correlated to specific Q sites, as shown in Figure 33B for the  $Q^{(1)}$  correlation and in the SI section X for the others. We find that the intensity of the of the  $Q^{(1)}$  site relative to the  $Q^{(2)}$  sites is greater at shorter contact time, implying that  $Q^{(1)}$  species are located in a relatively hydrogen rich environment. We also see that the  $^1\text{H}$  chemical shift profiles for the  $\text{Ca}:\text{Si} \geq 1.25$  ratios possess a significant contribution above 10 ppm, indicative of strong hydrogen bonding.<sup>182</sup> A comparison to HETCOR spectra taken at short contact time (SI section X) reveals that the prominence of the downfield region for the  $Q^{(1)}$  correlated cross sections increases significantly at short contact time, a feature which is not shared by the  $Q^{(2b)}$  and  $Q^{(2p)}$  cross sections. This suggests that the strong hydrogen bonding occurs primarily in association with  $Q^{(1)}$  sites. We note

that the signature of strong hydrogen bonding is almost entirely absent from the HETCOR spectrum of the  $\text{Ca}:\text{Si} = 1.00$  composition, once again producing a spectrum

| Sample       | $x_0$ | $\sum_{n=0} x_n n$ |
|--------------|-------|--------------------|
| Ca:Si = 1.25 | 0.751 | 0.450              |
| Ca:Si = 1.50 | 0.816 | 0.285              |
| Ca:Si = 1.75 | 0.873 | 0.185              |
| Ca:Si = 2.00 | 0.900 | 0.136              |

Table 11: . Dimer mole fraction  $x_0$  and mean repeat index for the four compositions analyzed. Deviating substantially from its relatively calcium rich counterparts.

The line shapes lack any significant features near 2 ppm, where basic hydroxide protons would be prominent, suggesting any secondary amorphous or crystalline  $\text{Ca}(\text{OH})_2$  phase, if present, is not intimately mixed with the C-S-H structure. Such a signal was previously reported for C-S-H compositions with  $\text{Ca}:\text{Si}$  ratios up to 1.5.<sup>45,172</sup> It may be that the C-S-H/ $\text{Ca}(\text{OH})_2$  nanocomposite results from excessive drying and aging of the sample. Indeed, a recent high energy X-ray study lending support for a secondary phase of  $\text{Ca}(\text{OH})_2$  nanosheets interwoven into the C-S-H interlayer suggests that the  $\text{Ca}(\text{OH})_2$  phase grows as C-S-H ages.<sup>150</sup>

## Structural determination

It is known that C-S-H resembles a defective tobermorite.<sup>54,102</sup> In contrast to previous structural modeling studies for C-S-H, which consider random defects in tobermorite systems containing hundreds of atoms,<sup>51,54</sup> we adopt a methodology that focuses on the systematic creation of structurally well-defined defects. The defective substructures are then used as building blocks to represent C-S-H at higher  $\text{Ca}:\text{Si}$  ratios. A suitable base structure is required to begin. Tobermorite structures are generally named after

their characteristic interlayer distances; namely, 9 Å, 11 Å, or 14 Å tobermorite.<sup>183–185</sup> The choice of base structure for modeling depends the Ca:Si ratio<sup>186</sup> and drying conditions.<sup>138,187</sup> A dataset compiled by Richardson<sup>138</sup> shows that the interlayer distance in C-S-H decreases from ~13–14 Å at Ca:Si = 0.8 to ~10 Å at Ca:Si = 1.5. Recently, Roosz *et al.*<sup>188</sup> have shown that sample preparation and relative humidity significantly affect the interlayer distance measurement. The interlayer distance measured for a C-S-H of Ca:Si = 1.2 using XRD in dry and fully hydrated states were 9.5 and 12.3 Å, respectively. Since our samples are hydrated, we choose 14 Å tobermorite (Figure 31D) as the base motif for constructing our atomic-level model of C-S-H.

A defect is introduced by the removal of an SiO<sub>2</sub> unit from a Q<sup>(2b)</sup> unit. The extent to which we need to create defects is determined by the distribution of silicate chain lengths. With the Q species populations and connectivities we can determine the distribution of chain lengths for each composition,

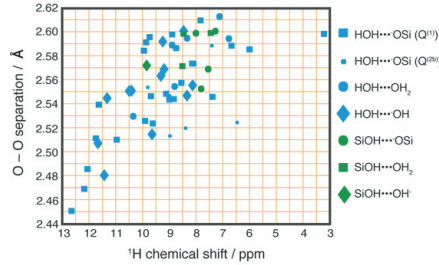


Figure 34 Scatter plot showing the correlation between the O–O distances and the chemical shifts of protons participating in the different types of hydroxyl-oxygen interactions occurring in the C-S-H substructures.

as described in the SI section IX and given in Table 11, to find

$$\sum_{n=0} x_n n = \frac{P(Q^{(2p)})}{P(Q^{(1)})}, \quad (1)$$

where  $x_n$  is the mole fraction of dreierketten chain species with repeat index  $n$ , and

$$x_0 = P(Q^{(1)}|Q^{(1)}), \quad (2)$$

as the mole fraction of dimers. The quantitative NMR results thereby provide three independent

constraints for calculating the distribution of silicate chains for each C-S-H composition. Using these constraints, we adopt a Monte Carlo method to predict the mole fraction distribution for chains up to  $n = 10$ , which we report in the SI section XI for each composition. Defect creation transforms the silicate tetrahedrons adjacent to the removed Q<sup>(2b)</sup> site into Q<sup>(1)</sup> sites, requiring the addition of H<sup>+</sup> and CaOH<sup>+</sup> to satisfy requirements of local charge balance. Additional molecular units of H<sub>2</sub>O and Ca(OH)<sub>2</sub> can also be incorporated into the structure. The defective motif is deemed acceptable if correct atomic bond distances, coordination numbers, and local charge balance remain satisfied after structural relaxation using density functional theory (DFT), leading to a series of substructures which are classified on the basis of defect geometry. Reduced unit cells are constructed by connecting the defect units through an aqueous interlayer or an aqueous interlayer with a Ca<sub>I</sub> and additional OH<sup>-</sup> for charge balance. In order to study medium range effects, we also consider different ways to combine the reduced unit cells, resulting in chain, dimer, and pentamer motifs. We study the effect of these different defect structures on the <sup>1</sup>H chemical shifts. A set of reduced unit cells are chosen to ensure a wide variety of different local defect environments as represented by the defect classification scheme described in the SI section XI. In Figure 33C, we show two calculated <sup>1</sup>H chemical shift spectra composed by summing over substructures that either possess or lack Ca<sub>B</sub>. In comparison with the experimental <sup>1</sup>H spectra in Figure 33B, these

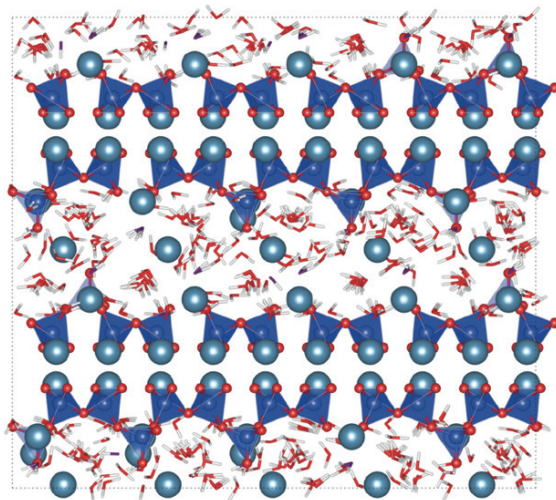


Figure 35: The structure determined here of C-S-H for a Ca:Si ratio of 1.5, viewed along the [A] axis. The relative proportions of dimers, pentamers, octamers, undecamers, and tetradecamers are 81%, 14%, 3%, 1%, and 1%, respectively. The chemical composition of this structure is  $\text{Ca}_{1.5}\text{SiO}_{3.35}(\text{OH})_{0.3} \cdot 2\text{H}_2\text{O}$ . The relative positions of hydroxyls and water molecules have been relaxed keeping all other atoms frozen for ease of visualization.

calculated spectra suggest that  $\text{Ca}_B$  is responsible for generating  $^1\text{H}$  NMR signals downfield of 10 ppm. Furthermore, the association between downfield shifted protons and hydrogen bonding leads us to infer that bridging calcium holds terminating chains together by coordinating to the defect site and promoting the formation of strong hydrogen bonds. On this basis we might also conjecture that bridging calcium is preferentially associated with silicate dimers, as suggested by the fact that both strong hydrogen bonds and dimers are lost when crossing under to the Ca:Si = 1.00 composition, though without further evidence this remains speculative.

The proton chemical shift calculations provide additional structural insight regarding the nature of the hydrogen bonding interactions. As Figure 34 shows, there is a linear correlation between the calculated  $^1\text{H}$  chemical shift and the O – O separation of the species engaged in electrostatic hydrogen-oxygen interactions, a well-established trend for inorganic oxide systems.<sup>182</sup> In particular, we observe that interlayer water protons that interact with interlayer hydroxide ions and the oxygen atoms of  $\text{Q}^{(1)}$  sites dominate in their contribution to the  $^1\text{H}$  chemical shift signal above 10 ppm. The key observation here is that each of these types of protons are located within 3 to 4 Å of  $\text{Ca}_B$ . Furthermore, we may consider that the protons involved in hydrogen bonding between interlayer water and a  $\text{Q}^{(1)}$  oxygen atom are less than a 3 Å from the  $\text{Q}^{(1)}$  silicon atom and are therefore favored in the HETCOR experiments at short contact time. For only two of the substructures analyzed, one of which lacks  $\text{Ca}_B$  entirely, the proton from the strongest  $\text{OH}_2\text{--OH}^-$  group is located greater than 5 Å away from a  $\text{Q}^{(1)}$ . We infer that it is these types of protons which explains the prominence of the region downfield of 10 ppm in the  $\text{Q}^{(1)}$

correlated proton spectrum, and that their association with bridging calcium in the structures that we have analyzed strengthens the confidence of our association.

Construction of structures that are representative of C-S-H proceeds by drawing from these defective substructures and the defect-free motif and tessellating them in a way that satisfies both the constraints of stoichiometry and the chain distribution determined by the  $^{29}\text{Si}$  NMR results. High Ca:Si ratios are obtained by deprotonation of a  $\text{Q}^{(2b)}$  silanol and adding  $\text{CaOH}^+$  and  $\text{Ca(OH)}_2$  in the form of  $\text{Ca}_A$  to the interlayer (Figure 31E). Our representative C-S-H unit cell is a tessellation of sixty such substructures coming to roughly 3 nm on each side, consistent with the degree of uniformity found by high-resolution analytical TEM. One such bulk C-S-H structure permitted by the ensemble of experimental NMR constraints determined for the Ca:Si ratio of 1.50 is shown in

Figure 35. A 2 ns MD simulation at constant pressure and temperature (300 K) shows that the resulting structures are stable, with realistic bond lengths and coordination geometries predicted. The C-S-H structures we propose for each the four compositions are given in the SI section XII. Unlike previously proposed structures based upon defective tobermorite,<sup>54,103,189,190</sup> our computational methodology specifies unambiguously the positions and coordination of calcium in the interlayer, rather than leaving them undefined or relegating its existence to a second phase, as in the tobermorite/ $\text{Ca(OH)}_2$  model. We do not claim that these structures represent the most energetically stable configurations; rather, we locate a viable, locally minimized configuration satisfying the NMR constraints. The proposed bulk structures are representative of a series of similar structures with similar defect concentrations and slightly different atomic arrangements. This should not change the average properties, but does explain why there is very little structural order seen in X-ray powder diffraction of non-dried C-S-H.

## Conclusions

We introduce a new synthetic method for C-S-H which controls pH throughout the process, and we produced uniform C-S-H with controlled Ca:Si ratios up to 2.0 for the first time. High sensitivity DNP solid-state NMR techniques have been used to characterize unique highly

uniform synthetic C-S-H particles with high Ca:Si ratios. In conjunction with atomistic scale modeling, atomic-level structures of defective tobermorite coherent over Ca:Si ratios from 1.25 to 2.00 have been determined without invoking secondary phases or glassy structures as confirmed by the clear absence of a signal from basic Ca-OH units in the 2D  $\{^1\text{H}\}^{29}\text{Si}$  HETCOR experiments. To interpret this data, we developed a computational approach which explores defective tobermorite substructural candidates, combining them in a manner satisfying our experimental constraints in order to build a full 3D structure which provides an accurate representation of structural and chemical environments in C-S-H for Ca:Si ratios up to 2.0. An essential aspect of these structures is the inclusion of a calcium site in the interlayer which bridges chain terminating silicate  $\text{Q}^{(1)}$  sites. This site is associated with an environment of strong hydrogen bonding which stabilizes the structure and, consequently, promotes high Ca:Si ratios in C-S-H. This thus establishes a clear relation between the atomic-level defect structure and the high Ca:Si ratio in C-S-H. This knowledge of the defect structure is a prerequisite for overcoming the self-limiting growth of C-S-H and to better understand growth mechanisms and kinetics. Such knowledge can further help formulate new classes of sustainable cements capable of exhibiting strong chain-bridging hydrogen bonding features while ensuring the early age strength development of the material.

## ASSOCIATED CONTENT

Supporting Information

Supplementary text and figures (.pdf)

Coordinate files for substructures and bulk representations

The Supporting Information is available free of charge on the ACS Publications website.

## AUTHOR INFORMATION

Corresponding Authors

\* Email: lyndon.emsley@epfl.ch, paul.bowen@epfl.ch

Author Contributions

All authors have given approval to the final version of the manuscript.

## ACKNOWLEDGMENT

The authors would like to acknowledge funding from the Swiss National Foundation (Grants No. 153044 and 200021\_160112) and ERC Advanced Grant No. 320860. We would also like to thank Dr. Sandra Galmarini, Dr. V.K. Parashar, Dr. B. Lothenbach, Dr. T. La Grange, and Dr. D. Demurtas for fruitful discussions. Dr. D. Lambert and Prof. G. Massonnet are thanked for their assistance with collecting the Raman data. The authors declare no competing financial interests.

## 6 Calcium silicate hydrate formation pathways and alite hydration.

### 6.1 Introduction

In this chapter we explore the formation pathways of C-S-H and extending it to gain some insight of the alite hydration that eventually provides the speciation for precipitation of C-S-H in real cementitious systems. As the first author in the manuscript, my role has been both as theoretician and experimentalist. Two main experimental systems are investigated and understood with the use of this unifying precipitation theory, namely, alite hydration (Portland cement system) and C-S-H formation (synthetic precipitation).

### 6.2 Manuscript

#### Cementitious Calcium silicate hydrates formation pathways and insights into alite hydration control

Abhishek Kumar<sup>\*1</sup>, Aslam. Kunhi Mohamed<sup>1</sup>, Bhuvanesh Srinivasan<sup>1,3</sup>, Danny Lambert<sup>2</sup>, Geneviève Massonnet<sup>2</sup>, Karen Scrivener<sup>4</sup>, Paul Bowen<sup>1</sup>

<sup>1</sup>Powder Technology Laboratory, École Polytechnique Fédérale de Lausanne EPFL, Switzerland

<sup>2</sup>School of Criminal Justice, University of Lausanne, Switzerland

<sup>3</sup>Department of Earth & Environmental Sciences, Ludwig-Maximilian University, D-80333, Munich, Germany

<sup>4</sup>Construction Material Laboratory, École Polytechnique Fédérale de Lausanne EPFL, Switzerland

#### Abstract

C-S-H grows uniformly in the presence of abundant reacting silicates species that is governed by the pH of the reaction solution. Higher  $\text{pH} \geq 13$  tends to form nanofoils like morphology whereas at lower  $\text{pH} \leq 11$  tend to form nanoglobules. Heterogeneous products are formed when the concentration of silicate species is limited leading to the formation of the secondary phases (i.e.) Calcium hydroxide (CH), at high pH conditions ( $\geq 13$ ). In cementitious system, hydration of anhydrous tri-calcium silicate (alite) serves as a source of reacting species in the pore solution that leads to the precipitation of Calcium Silicate Hydrate (C-S-H). Considering congruent dissolution with excess calcium at supersaturated concentration in the pore solution with evolving  $\text{pH} \geq 12.5$  leads to rapid dissolution of alite, forming C-S-H and CH similar to observe in direct precipitation of C-S-H and hence forming the acceleration regime. Moreover, hydration of alite at high pH conditions from start shows no acceleration regime.

#### Introduction

Calcium Silicate Hydrate (C-S-H) is the main phase that precipitates in the process of alite hydration, mainly responsible for mechanical properties of cement<sup>152</sup>. The complexity of cement based materials, which comes from the heterogeneous nature of the hydration products of ordinary Portland cement (OPC) often makes mechanistic pathways during hydration difficult to unravel. Alite, or its pure chemical phase tricalcium silicate ( $3\text{CaO} \cdot \text{SiO}_2$ , or, in



cement chemistry notation,  $C_3S$ ), is a major component of OPC and is frequently used to model the hydration of OPC<sup>33,191</sup>. However, even when modeling a simple system such as pure  $C_3S$ , the dissolution, diffusion and precipitation processes involved in the hydration process remain unclear. Despite significant recent progress<sup>29,152,166,192–194</sup> the simultaneous dissolution and precipitation lead to complications to extract accurate kinetic data on the dissolution,/ hydration reaction pathway. One issue with alite hydration is the apparent inconsistency between the low dissolution rate of  $C_3S$  that is observed during the hydration of cement and the theoretically high solubility of this phase calculated from the free enthalpy of formation of its constituting oxides<sup>29,61,152</sup>. With a dedicated set-up allowing the study of dissolution in conditions that avoid precipitation of hydrates, the true experimental solubility has been recently reported [6,10]. The results showed that the solubility product of  $C_3S$  is consistent with the solubility products of  $C_2S$  (alite) and  $CaO$  and its determination has revealed the importance of the surface hydroxylation of the silicate monomers and the free oxygen atoms present in these phases. Other species which interact with the surface through physical or chemical adsorption, also lead to an additional stabilization of the surface<sup>48</sup>. The presence of sulfate and aluminate ions, which are relevant species in cement pore solution, significantly reduces the dissolution rate of  $C_3S$  due to physical and chemical bonding with the surface<sup>11,152</sup>. The solubility of the surface, lower than expected from the simple calculation of the bulk solubility from the free enthalpies of formation<sup>21</sup>, leads to the conclusion that the composition of the pore solution during the cement hydration is very close to the solubility equilibrium of alite. Thus, the alite has to dissolve rather slowly from the very first minutes of hydration. In the case of a low interfacial dissolution rate controlled by near-equilibrium conditions, any topographical features affecting the surface of dissolution can significantly change the overall dissolution rate. The formation of etch pits is prominent during the dissolution of most minerals<sup>170</sup>. Many theoretical models have been proposed to describe the formation of etch pits<sup>29</sup> which appear at the surface defects. One of these defects, often believed to be dominant especially in conditions close to equilibrium<sup>152</sup>, is the screw dislocation. The difficulty lies in the challenge posed by the fast precipitation of low-soluble hydrates that perturb the investigations on pure dissolution regimes. A better understanding of the dissolution processes in cement could shed light on additional points related to hydration, including the so-called “dormant” period<sup>29</sup> and the factors limiting the cement hydration kinetics. Pustovgar et al<sup>48</sup> investigated tricalcium silicate ( $C_3S$ ) hydration by using in-situ NMR measurement and isothermal calorimetry.<sup>29</sup> Si-enriched  $C_3S$  was synthesized and the evolution of C-S-H monitored. This research revealed the degree of hydroxylation of the  $C_3S$  surface prior to any C-S-H precipitation was significant and was linked to the hydration rate.

Most of the previous studies have been directed towards understanding the dissolution part of alite hydration and its resulting pore solution analysis. If we term this as top to bottom approach. In this study we do bottom to top approach, where we first investigate the formation of C-S-H to understand the driving force for its precipitation from solution. The reaction pathway for C-S-H precipitation is then used to better understand the hydration of the alite phase. To study the C-S-H formation we will use our recently developed synthetic C-S-H precipitation system where we demonstrated that we can synthesize C-S-H of desired Ca:Si stoichiometry and excellent chemical uniformity<sup>107</sup> (Chapter 04). We will use this reactor to

precipitate C-S-H under different conditions to investigate the reaction pathway or growth mechanism. We then design experiments with alite samples to demonstrate how the understanding gained from the synthetic C-S-H allows us to control and gain insight into early alite hydration.

## Material and methods

### *Synthesis of C-S-H*

The C-S-H synthesis was carried out using aqueous solutions of Calcium Nitrate Tetrahydrate (*Fluka Chemicals*, 21197) and Sodium Metasilicate (*Sigma-Aldrich*, 307815) mixed in a closed batch reactor in a nitrogen environment, which has been described in detail elsewhere<sup>107</sup>. In all cases pH control was made using NaOH and the different concentration regimes and pHs studied are given in Table 12.

| Cases                    | Reactant A<br>(.4H <sub>2</sub> O) | Concentration<br>A | Reactant B<br>(.5H <sub>2</sub> O) | Concentration<br>B | pH         |
|--------------------------|------------------------------------|--------------------|------------------------------------|--------------------|------------|
| <b>A (T2 in Chp.6)</b>   | Ca(NO <sub>3</sub> ) <sub>2</sub>  | 0.2 M              | Na <sub>2</sub> SiO <sub>3</sub>   | 0.1M               | 13.3 ± 0.1 |
| <b>B (T3 in Chp 6)</b>   | Ca(NO <sub>3</sub> ) <sub>2</sub>  | 0.2M               | Na <sub>2</sub> SiO <sub>3</sub>   | 175µM              | 13.3 ± 0.1 |
| <b>C (T1 in Chp.. 6)</b> | Ca(NO <sub>3</sub> ) <sub>2</sub>  | 0.2 M              | Na <sub>2</sub> SiO <sub>3</sub>   | 0.1 M              | 10.8 ± 0.1 |

Table 12: C-S-H synthesis conditions

### Alite hydration and Isothermal calorimetry

A batch of alite (impure C<sub>3</sub>S, monoclinic) was synthesized in the laboratory by mixing 81.4 wt.% calcium carbonate (precipitated GR for analysis, Merck), 16.6 wt.% silica (highly dispersed extra pure, Merck), 1.3 wt.% magnesium oxide (GR for analysis, Merck) and 0.6 wt.% aluminium oxide (anhydrous, Merck). Powders were homogenized for 24 hours in a ball mill with deionized water and the blend was dried at 90°C for 24 hours. The dried mass was pressed into pellets and heat treated at 1500°C for 8 hours. The pellets were quenched in air, ground using a ring grinder and sieved at 100µm. Particle size distribution (D<sub>v</sub>50) of about 15µm was measured by laser diffraction<sup>196</sup>. Alite hydration is an exothermic process and can be followed using isothermal calorimetry. The resulting heat is the sum of the contributions of each individual reactions happening in the system. The heat release was recorded with an isothermal calorimeter (TAM Air, Thermometrics). This technique records the heat released by the exothermic reactions of cement hydration and compares it to a reference sample. The reference sample should have a constant heat capacity similar to the measured sample. For this study the reference sample is deionized water. The amount required is determined as  $Water_{ref} = \frac{C_{p\ water} \times m_{paste}}{C_{p\ water}}$ . Where  $C_p$  is the mass heat capacity of the material ( $C_{p\ water} = 4.18\ J \cdot g^{-1} \cdot K^{-1}$ ). The heat release at early ages can provide information about the dissolution of each anhydrous phase and the overall heat flow provides information about the degree of hydration of the system. 10 grams of paste were placed in glass vessel and then into the calorimeter. The ambient temperature was 20°C to ensure the



stability of the baseline. The measurements were carried out for 24 hours and 4 hours in the two cases studied.

| Cases    | Reactant A | Reactant B                     | Time<br>(Calorimetry<br>experiment) | W/S | Initial pH     |
|----------|------------|--------------------------------|-------------------------------------|-----|----------------|
| <b>D</b> | Alite      | Demineralized<br>Water         | 24h                                 | 0.7 | $7 \pm 0.1$    |
| <b>E</b> | Alite      | Saturated<br>$\text{Ca(OH)}_2$ | 4h                                  | 250 | $12.5 \pm 0.1$ |

Table 13: Alite hydration conditons

## Characterization of the alite and C-S-H

*Dynamic nuclear polarization (DNP) NMR:* DNP solid-state NMR experiments were carried out on the aqueous suspensions of freshly prepared C-S-H nanoparticles with added impregnation agent and were not dried. A detailed description can be found in <sup>107</sup>.

### *Electron microscopy*

High resolution scanning electronic microscopy (HRSEM) micrographs were obtained by coating the samples with 6 nm of osmium (gas phase coating). The detailed of sample preparation can be found elsewhere <sup>107</sup>. In Transmission electron microscopy (TEM), the samples were imaged at room temperature using a Tecnai F20 (FEI, The Netherlands) operating at an acceleration voltage of 100kV LaB<sub>6</sub> gun with a line resolution of 0.34 nm, with images being recorded on a high sensitivity 4k x 4k pixel CCD camera. Samples were first dispersed in isopropanol and allowed to dry on nthe sample holder in ambient air, for more details see<sup>107</sup>.

## Results and Discussion

### *Synthesis of C-S-H, characterization and reaction pathway hypothesis*

Here we will discuss the three different cases of C-S-H synthesis (A, B, C Table 1) under well controlled and designed conditions. These are used to illustrate the effects of different experimental conditions on the probable reaction pathway of C-S-H by varying either, pH or silicate concentration.

From our previous results, <sup>107</sup> that show a very uniform chemistry (< 3nm spot size in STEM-EDX) for our synthetic C-S-Hs we hypothesis that to form such a uniform C-S-H phase there is a single dominating chemical reaction with one major reacting species to form C-S-H. We designed the experiments to make the reacting system independent of any other physical factors such as mixing, diffusion, addition rates, seeding or heterogeneous surfaces. Silicates in solution can exist in numerous forms, so we fix the operating pH condition such that a single silicate species is dominant. For example at pH greater than 13, silicates tend to exist in aqueous solution as mainly  $\text{H}_2\text{SiO}_4^{2-}$ <sup>67,68,70,197,198</sup>. The other major reacting species (i.e.) calcium exists as  $\text{Ca}^{2+}/\text{CaOH}^+$ , at a ratio of around 5:1. To be able to neglect any effect from mixing, the reaction system is operated at 800 – 1000 rpm, giving mixing times of the reactants in the

microsecond domain. To ensure this mixing is sufficiently maintained in the stated domain the calcium solution needs to be added to the silicate solution dropwise at regulated flow rates. Details of the mixing considerations are provided in Annexe. In aqueous precipitation systems, the diffusion rate of the species under high mixing does not develop any diffusion limited constraints.

**Case A:** The concentration of calcium nitrate and sodium silicate solution are chosen as 0.2 and 0.1 M respectively to keep the supersaturation high. This means that the reacting species are readily available everywhere due to these high concentrations. Another advantage of keeping high supersaturation (high nucleation rate  $\sim$  fine particle formation) is that the initial amount of solid precipitating out of the solution is small and hence does not alter the precipitation reaction during the early nucleation process which should promote uniformity. The pH was maintained above 13, the species in solution from thermodynamic modelling before mixing is presented in Figure 36(a) and after 3hrs of reaction are shown in Figure 36(b), with the  $\text{CaSiO}_3 \cdot \text{H}_2\text{O}$  (or  $\text{CaSiO}_2(\text{OH})_2$ ) neutral complex in dominance.

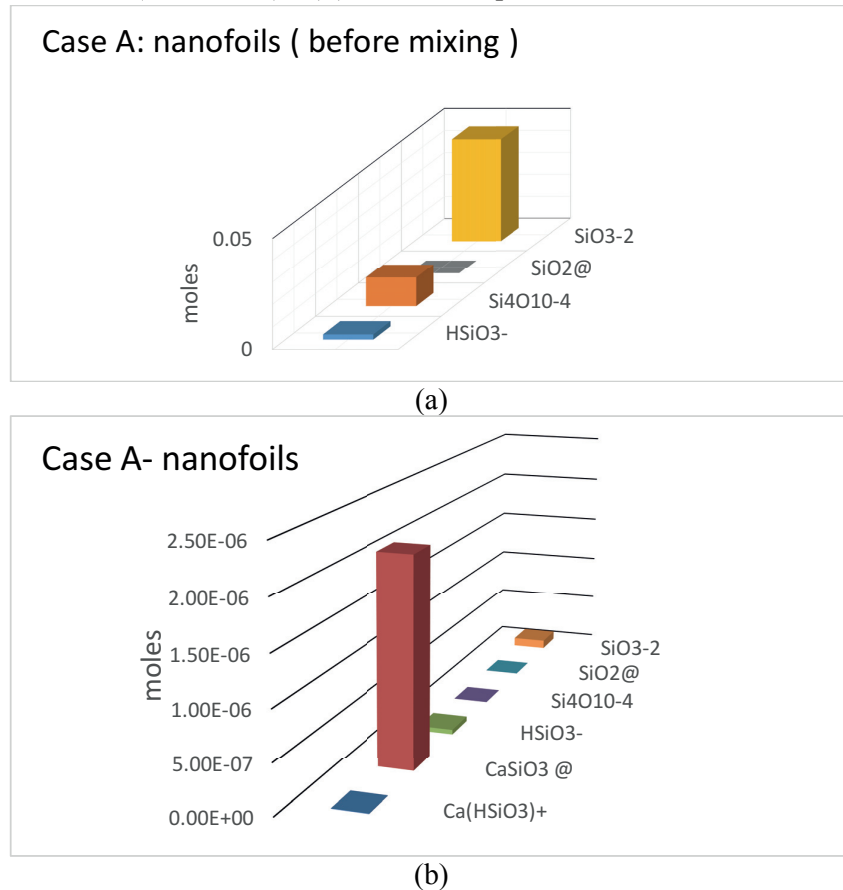


Figure 36: Silicate species predicted from GEMS modeling in Case A (a) Before mixing of calcium (b) after mixing of calcium (the @represents a water molecule in the full chemical formula)

The precipitation of C-S-H under these conditions leads to the formation of a nanofoil or sheet-like morphology (Figure 37(a)) previous work has shown these foils to have a Ca:Si ratio of 2 under these reaction conditions<sup>107</sup>. Figure 37(b), shows the monomeric silicate species ( $\text{Q}_0$ ,  $\text{H}_2\text{SiO}_4^{2-}$ ) at high pH conditions which converts to dimeric units in the precipitated C-S-H once mixed with the calcium nitrate solution. This suggests that under these chemical conditions

calcium induces the condensation of the monomeric silicate growth species into dimers, with growth favoured in two directions and limited in one direction.

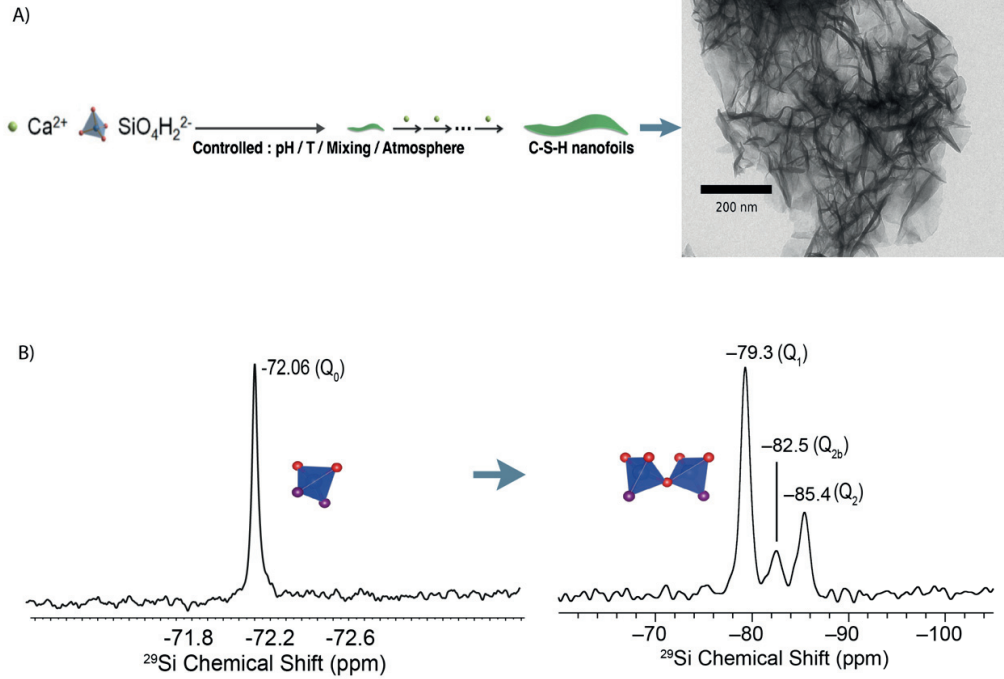
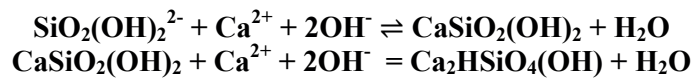


Figure 37: a) Nanofolios morphology of C-S-H b) Liquid state NMR of reacting silicate solution and final Solid state NMR of the C-S-H

So in our silicate solution before mixing with calcium nitrate the dominating silicate species is the  $\text{H}_2\text{SiO}_4^{2-}$  (or  $\text{SiO}_2(\text{OH})_2^{2-}$ ) - a monomeric species - stabilized by a strong electrostatic repulsion between the anionic silicate species<sup>12</sup>. With constant high pH and high concentrations, we constrain the species found in solution, but their availability is initially unlimited and this leads to a single dominating chemical reaction. The probable reaction leading to the formation of homogeneous C-S-H phase of Ca:Si ratio 2 is:



The possible formation mechanism or pathway is discussed after the presentation of the three cases studies.

**Case B:** The conditions in this case are i)  $\text{Ca}^{2+}$  - 0.2M and Si – 0.175 mM, i.e. about 500 times less Si, therefore a significantly limited availability of Si in the system. ii) pH is maintained throughout above 13. iii) The speciation diagram predicted by the GEMS 3 shows little change in the major species in the silicate solution before mixing and precipitation, again the neutral complex  $\text{CaSiO}_3 \cdot \text{H}_2\text{O}$  dominating as shown in Figure 38.

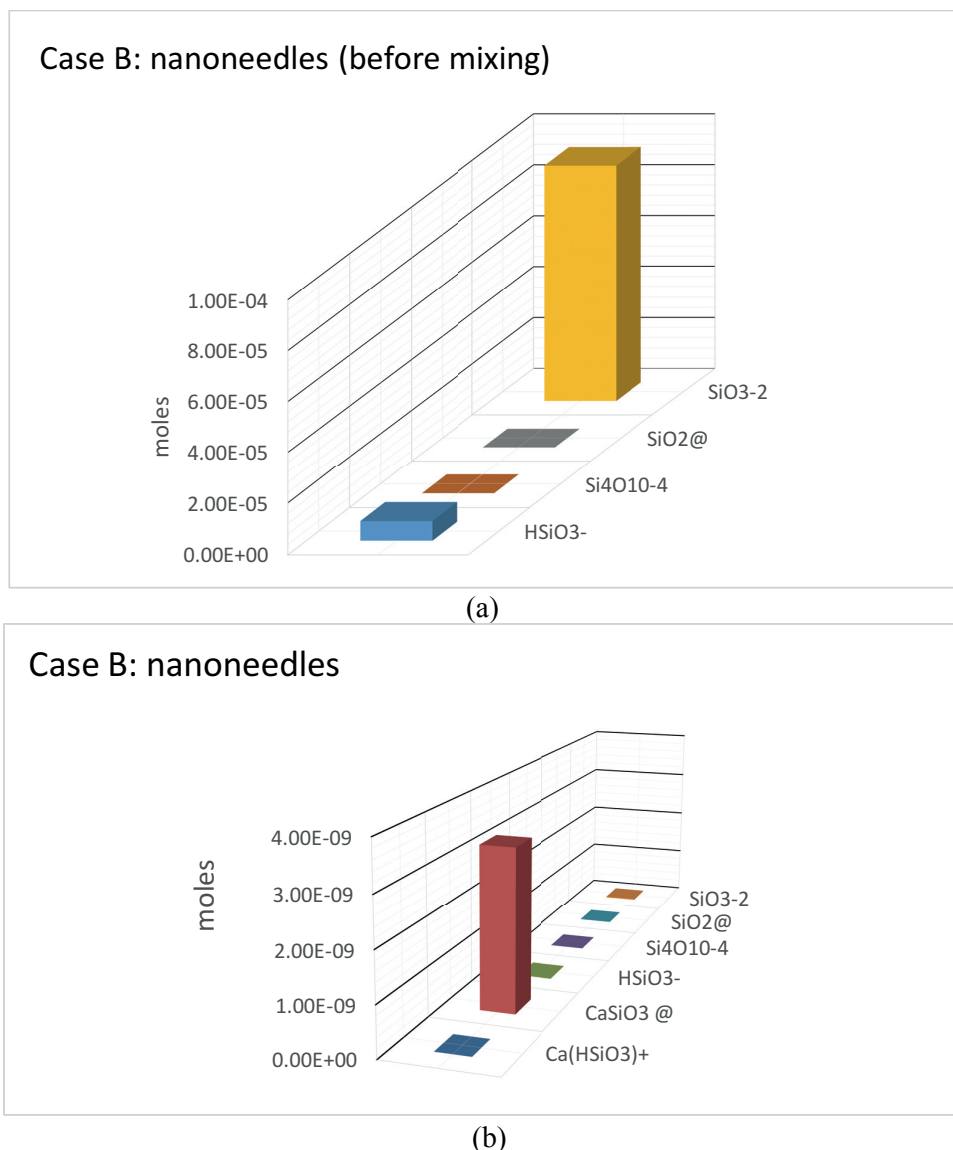


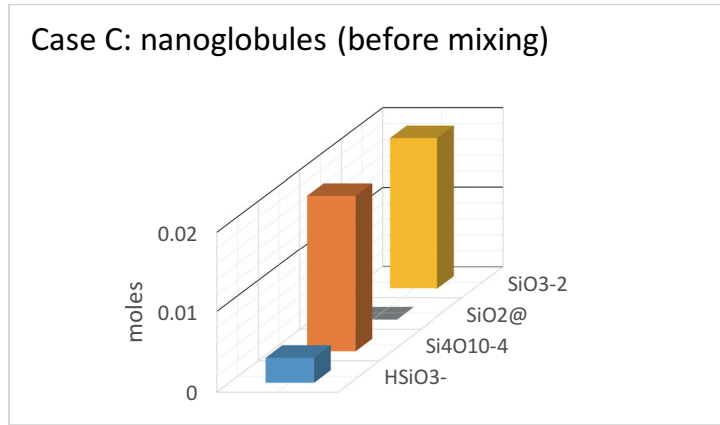
Figure 38: Silicate species predicted from GEMS modeling in Case B (a) Before mixing of calcium (b) After mixing of calcium (the @ represents a water molecule in the full chemical formula):

We have manipulated the system by reducing the concentration of the silicate solution by a factor of 500 from 0.1 M to 175  $\mu$ M and hence reduced the overall availability of silicate growth species at these chemical conditions. The rest of conditions (pH, mixing, T etc.) are the same as used in case A. The reduced concentration in the silicate species means, there will be excess of calcium available that will tend to form  $\text{Ca}(\text{OH})_2$  as the second most thermodynamically favoured solid. So, there are two chemical scenarios here, one in presence of silicate and one in absence of silicate. Hence it means we induce heterogeneity in the final precipitate by forming at least two solids as shown in figure 06 box B where CH particles and some tapered foils or nanoneedles of C-S-H, as identified by XRD and SEM can be observed. In the first chemical scenario with presence of silicate, in the presence of calcium, the silicate condenses to form the dimeric structures but the growth into nanofoils seems to be very limited presumably because of the low concentration of silicates. We see instead *tapered foils or*

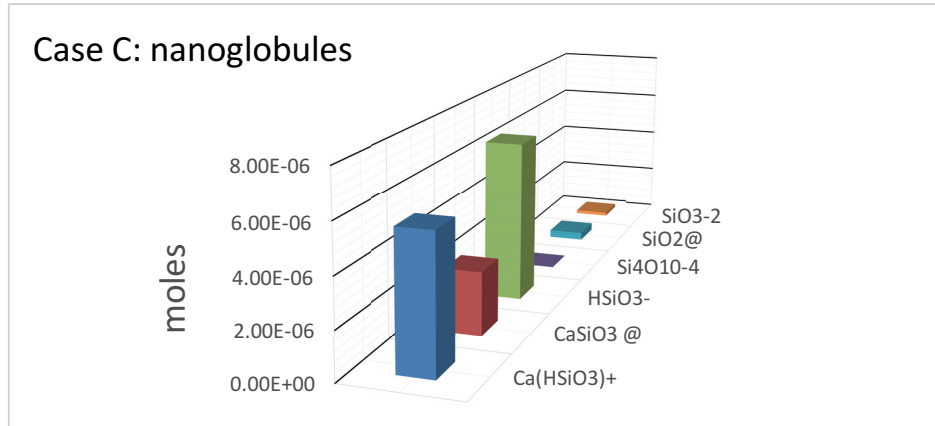
*nanoneedles* which grow more quickly in a direction perpendicular to the condensing silicate sheets. One possible reason is the high concentration of calcium ions can complete the calcium oxide layers in our defective tobermorite-like C-S-H [15] quicker than the silicate can condense into sheets. In the second scenario, with absence of silicates (once they have been consumed in the C-S-H formation), a saturated  $\text{Ca}(\text{OH})_2$  will simply precipitate  $\text{Ca}(\text{OH})_2$  particles.

**Case C:**

The conditions in this case are i)  $\text{Ca}^{2+}$  - 0.2M and Si – 0.1M, high concentrations. ii) pH is maintained below 11. iii) the speciation diagram predicted by the GEMS is shown in Figure 39 and shows a significant change in the dominating silicate species in our solutions before mixing to precipitate C-S-H. At  $\text{pH} \leq 11$ , the silicate species exists in an oligomeric form with units of  $\text{HSiO}_3^-$  or  $\text{Ca}(\text{HSiO}_3)^+$  <sup>67,70,199</sup>



(a)

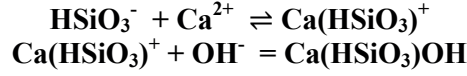


(B)

Figure 39: : Silicate species predicted from GEMS modeling in Case C (a) Before mixing of calcium (b) After mixing of calcium (the @represents a water molecule in the full chemical formula):

While keeping the other conditions as for Case A (high concentration  $\text{Ca}^{2+}$ , temperature, high mixing) and by changing the  $\text{pH} (\leq 11)$  we change only the reacting silicate species found in solution. *Oligomerization* leading to bigger silicate species occurs for pH values of 11 and 12 whereas it is prevented or at least slowed down for pH 13 <sup>67</sup>. In Figure 41(Box C), we see that the C-S-H is now precipitated in the form of nanoglobules, these are still very uniform in Ca/Si content ( $\text{Ca.Si} = 1 \pm 0.06$ , <sup>107</sup>) but have different NMR signals to that of nanofolds obtained in case A as shown in Figure 41(Box A). The NMR results <sup>107</sup> show that the C-S-H nanoglobules

belong to a different structural family, whereas at synthetic C-S-Hs with Ca:Si  $\geq 1.25$  to 2 all followed same structural family <sup>107</sup>. The probable reaction leading to the formation of homogeneous C-S-H phase of Ca:Si ratio 1 is:

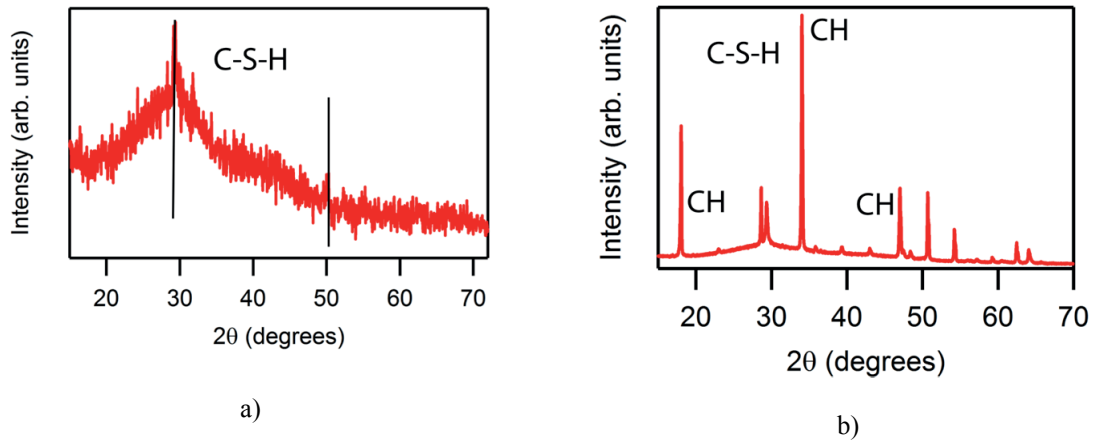


This globular morphology, is not noticed with other cation such as magnesium <sup>113</sup>, where it participate in the solid formation solely as charge balancing for the silicate chains <sup>113</sup>. The chemical uniformity is maintained as the concentration and availability of the both the reaction species is high and hence no secondary phases such as  $\text{Ca}(\text{OH})_2$  are formed. In Table 14, Q speciation quantification obtained by Gaussian fitting of the NMR data obtained from the Case A and Case C <sup>107</sup> are presented. For these two cases, A and C, we obtained homogeneous C-S-H phases with Ca:Si ratios of 2 and 1, respectively. The mean chain length is longer and fraction of Q1 (dimers) lower for case C suggesting that the existing oligomers condense in a more random fashion in the presence of Calcium at these lower pH conditions.

| Cases | Ca:Si | Q <sup>1</sup> | Q <sup>2p</sup> | Q <sup>2b</sup> | Q <sup>2p</sup> /Q <sup>2b</sup> | MCL  |
|-------|-------|----------------|-----------------|-----------------|----------------------------------|------|
| A     | 2.0   | 0.83           | 0.11            | 0.06            | <b>2.0</b>                       | 2.43 |
| C     | 1.0   | 0.31           | 0.52            | 0.17            | <b>3.1</b>                       | 4.08 |

Table 14: Q speciation and MCL for homogeneous phases of C-S-H in case A and C.

XRD analysis for the three different morphologies identified (Figure 40) reveals absolutely no peaks at all observed for nanoglobules (Figure 40 (C)) indicating a very high degree of disorder. For the nanofoils, poor order with only the characteristic Ca-O bonds lengths for the Ca-O layers which are presumably well ordered enough but the silicate dimers are still not well ordered enough to give discrete signals. For the tapered foils or nanoneedles we see the crystalline calcium hydroxide and quite well defined peaks for the C-S-H as previously seen for dried synthetic C-S-H <sup>10,105</sup>.



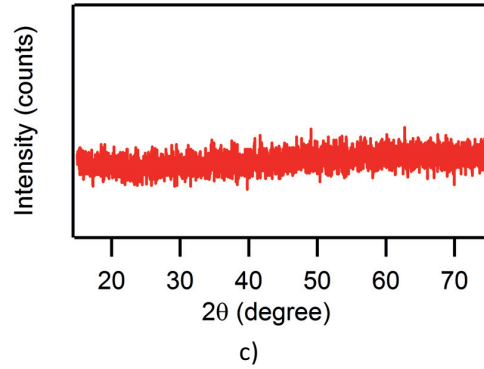


Figure 40: XRD analysis a) Nanofoils b) Tapered Nanofoils c) Nanoglobules

In Figure 41, we summarise all three cases indicating the possible different growth mechanisms or pathways of C-S-H for our 3 model cases A, B and C. In case A we have Nanofoils: Formed by condensation of monomeric silicate species at high pH condition in solution by Calcium to dimeric structures in the solid, favouring a two-dimensional growth (X-Y axis here). It shows low crystallinity and from our earlier work<sup>107</sup> the Ca/Si ratio can vary between 1.25 to 2. The formation mechanism for case A is thought to pass from the silicate and calcium species via the neutral Ca Si complex,  $\text{CaSiO}_2(\text{OH})_2$  to form dimers. These dimers are then either connected via a single silicate unit to form a pentamer or a bridging  $\text{Ca}^{2+}$  ion to form coupled dimers (Figure 41 (Box A)). The importance of the bridging calcium ions has been highlighted in our recent NMR and atomistic simulation study<sup>107</sup> We discovered that bridging interlayer calcium ions are the defining structural characteristic of calcium silicate hydrate at high Ca:Si, inducing strong hydrogen bonding that is responsible for stabilizing the structure.

For case B we see the formation of C-S-H Nanoneedles: the blue circles show C-S-H nanoneedles, the red circles show the formation of Calcium hydroxide (Figure 6 box B). The C-S-H seems to be formed by growth favoured in one direction (Z-axis here). This is proposed to be due to the limited silicate availability (500 time less than case A) with an excess of Ca species making it easier and quicker to create the calcium layer than the silicate layers. These gives high Ca/Si ratio & highest crystallinity compared to the other morphologies as indicated by the XRD results above (Figure 40). Perhaps the scenarios of silicate and calcium and only calcium can be thought of as kinetic effects. As we add calcium dropwise to the low concentration silicate solution we form C-S-H with readily available  $\text{Ca}^{2+}$ . Then when the silicate has been consumed we just form  $\text{Ca}(\text{OH})_2$  because it is supersaturated. A kinetic study under these condition would be necessary to back up this proposed reaction pathway but is beyond the scope of the current study.

For case C we form nanoglobules (Figure 41 (BoxC)): A completely disordered amorphous structure is formed at these relatively lower pH conditions where the initial silicate species occur as oligomers with negative charges<sup>70</sup>. They seem to have no preferred growth direction giving a 3-dimensional calcium-silicate associated growth via the oligomeric units, the Ca:Si ratio seems to be limited to maximum Ca:Si between 1 and 1.25. Exactly where the transition from nanoglobules to nanofoils occurs needs further experiments between these ratios to delimit transition point more accurately.



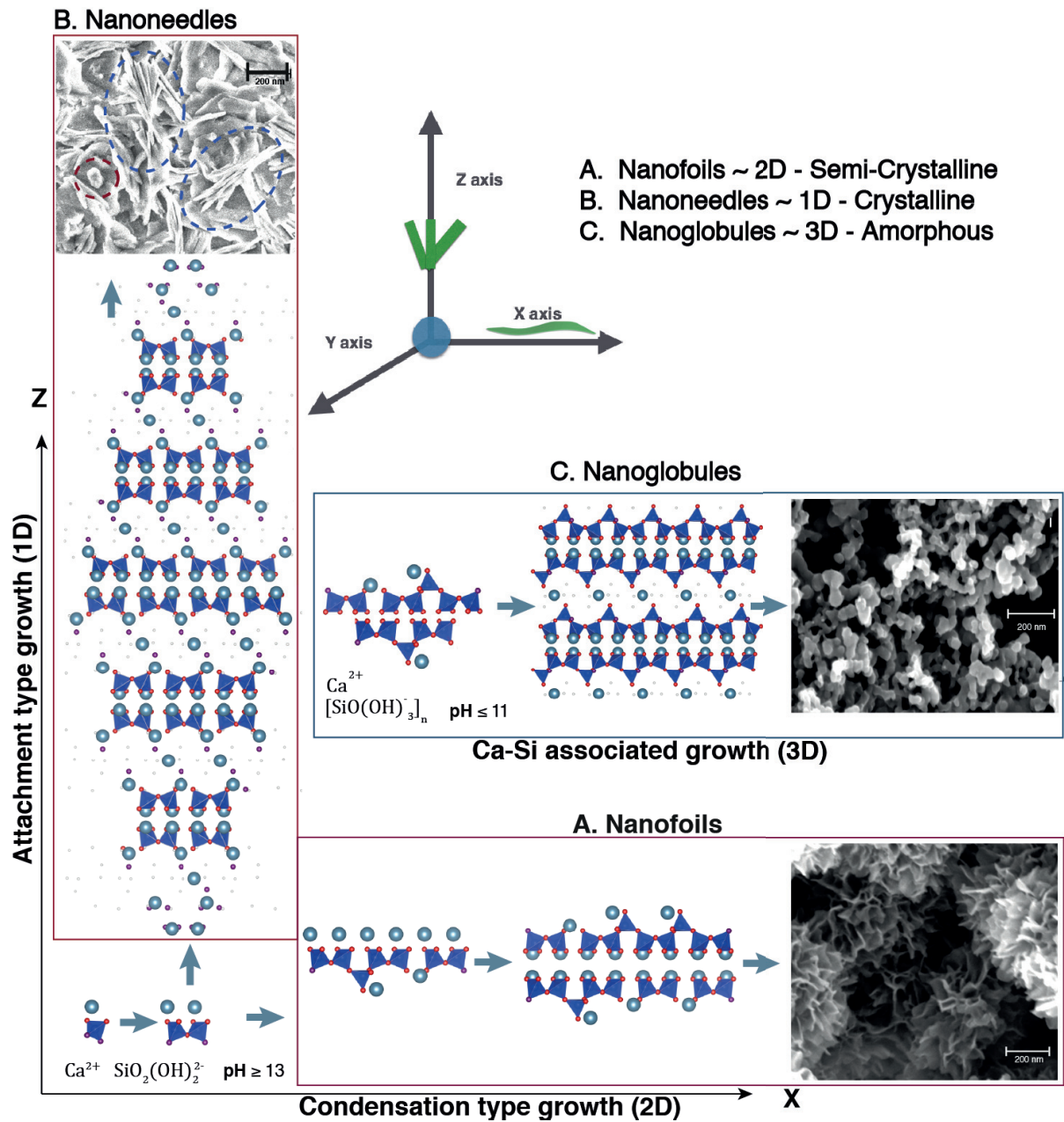


Figure 41: The Different growth mechanisms of C-S-H; A) **Nanofoils**: 2 B) **Nanoneedles**: Blue circle shows C-S-H nanoneedles, red circle shows the formation of Calcium hydroxide. C) **Nanoglobules**

### Alite hydration and its explanation w.r.t. synthetic C-S-H formation.

**Case D:** Alite is an impure tri-calcium silicate compound upon dissolution gives calcium and silicate ions in solution that precipitate to give C-S-H and portlandite phases in OPC systems. Figure 42, shows the calorimetry curve for the hydration of alite at a water to solid ratio (W/S) of 0.7. The blue curve shows the heat released (left y-axis) and orange curve show the pH (right

y-axis) as a function of time (x axis). The morphology of C-S-H formation are shown in different time zones as reported in the literature for  $\text{Ca}^{2+}$  and silicate concentrations for this W/S ratio<sup>11</sup>.

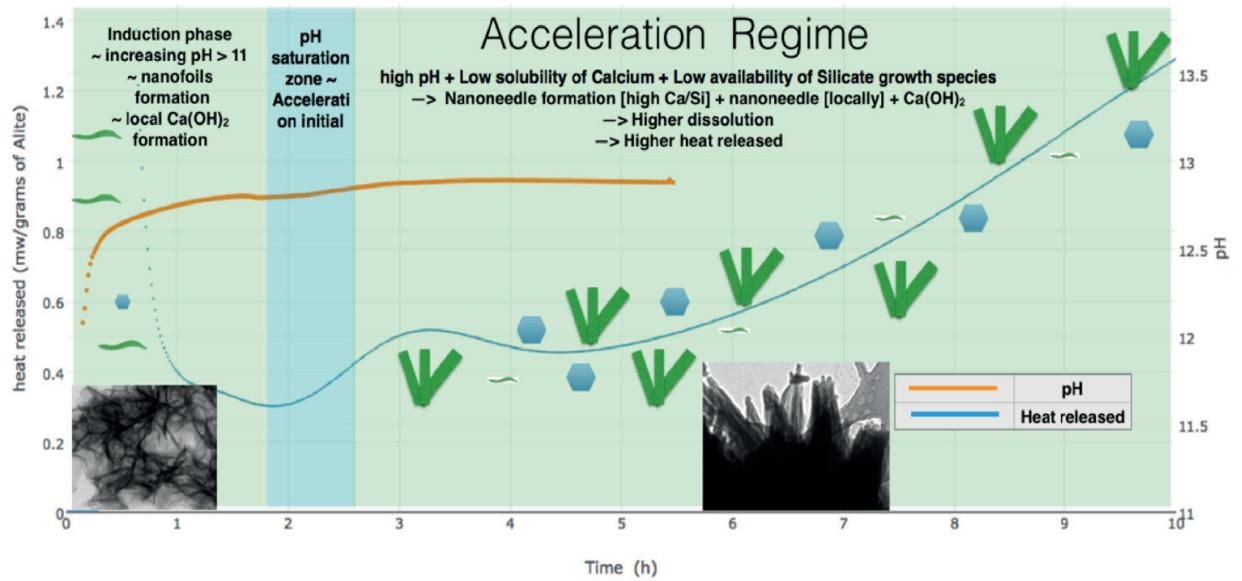


Figure 42: Alite hydration: alite hydration at W/S 0.7, where  $Y_{\text{left}}$ -axis shows the heat released per grams of Alite and X-Axis shows the time in hours,  $Y_{\text{right}}$ -axis show the pH changes during the hydration. Around 2hr, the acceleration regime begins with the formation of Nanoneedles. The peak is reached around 10h.

Due to the complete absence of any sort of mixing in the system the product formation will be function of the local conditions. At constant temperature and at low supersaturation, Mobility is a constraining factor as dissolution occurs in non-mixing conditions. Availability of the reacting species will be constrained by the dissolution rate of alite and diffusion rate in the solution. With knowledge we have gained from the synthetic C-S-H system above, we know the dominating reacting silicate species at different pH conditions. with the pH indicated in figure 7 we know that system reaches  $\text{pH} \geq 12.5$  after about 15 minutes. Two types of surfaces can affect the reaction progress and are accounted for here, one being the unreacted alite surfaces and one from the precipitated solid phase, both can provide heterogeneous surfaces and effect nucleation and growth. We will now propose a reaction pathway for the hydration of alite under these conditions.

Assuming congruent dissolution of alite, at the beginning of the hydration ( $t < 1\text{h}$ ) the  $\text{Ca}^{2+}$  ions combine with silicate species to form C-S-H (nanofoils, high Ca:Si ratio around 2) and locally formed Calcium hydroxide crystals as seen by TEM images for cements under high alkali conditions<sup>50,200</sup>, Soon,  $\text{Ca}^{2+}$  ion will be in excess ( $t > 1\text{h}$ ) compared to the silicate species and C-S-H will tend to form more tapered foil like morphologies, according to our synthetic C-S-H analysis above. As the pH continues to increase  $\text{pH} > 12.5$  and starts to saturate, we see the start of the acceleration period. At this point, amount of calcium in solution exceeds its maximum solubility limits and would like to leave the system by precipitating either C-S-H (nanoneedles/tapered foils) or Calcium hydroxide. Faster removal of Calcium leads to higher dissolution rates, as the system tries to regain equilibrium with the depleting calcium in solution (le-chatelier principle) and higher heat release is observed in calorimetry. As the solid continues to precipitate, the mobility of the system gets restricted more and more. Local

equilibria start to build up. At the peak of heat curve ( $\sim 10$  hours), system can no more easily transfer calcium from alite due to restricted mobility and availability of the growth species (diminishing surface of alite) taking system towards a deceleration regime and the start of inwards growth to form inner C-S-H. The explanation can equally be verified by the available Ca and silicate ion concentration data in literature <sup>11,153</sup>. Moreover, the formation of Q<sup>1</sup> silicate species from 2hrs until end of acceleration regime reported is due to formation of C-S-H (nanoneedle or nanofoils – mostly dimers) <sup>194</sup>.

**Case E:** If the above hypothesis in Case D holds true then we can imagine an experiment whereby we provide the hydration system with i) a ready-made  $\text{pH} \geq 12.5$ , and ii) an high mobility of ions, we should observe un-restricted formation of C-S-H/ $\text{Ca}(\text{OH})_2$  and the system would be always in a deceleration mode. When considering congruent dissolution, mobility may be low but availability of the growth species should be abundant (mostly silicates, since calcium is abundant anyway in the alite phase). So, we designed an experiment with a W/S ratio set to be 250, to give high mobility. This allows the alite phase to hydrate with minimum interaction of the precipitating phases. Hydration at the set higher pH conditions ensures the presence of growth *species* right from the beginning of the hydration leading to formation of C-S-H (nanofoils/nanoneedles) or  $\text{Ca}(\text{OH})_2$ . Hence the experiments were conducted with saturated lime solution at pH 12.5, ensuring no further time is needed for pH saturation. Finally, no external surfaces were introduced and at high W/S ratio the effect of reactor walls and dissolving alite etc. can be neglected. Figure 44, shows the calorimetric curves with the formation of C-S-H with no acceleration period. From the analysis of figure 6 we would predict the formation of nanofoils in the first few minutes of hydration ( $\text{pH} > 12.5$  and equal silicate and calcium availability, case A) and at 30 minutes of hydration we expect the formation of nanoneedles or tapered foils as the calcium becomes in excess (case B). The TEM images after (a) before hydration (b) 2 minutes and (c) 30 mins of hydration is presented in Figure 43 for Case E.

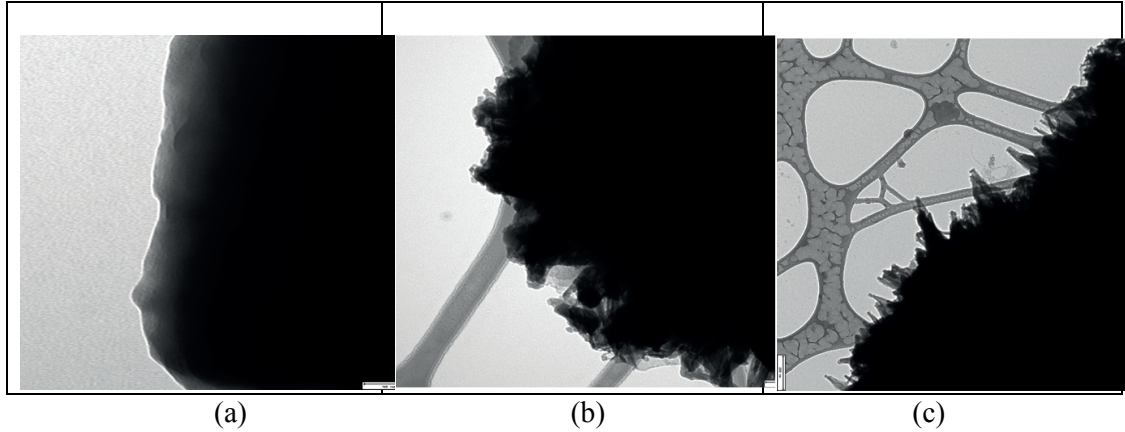


Figure 43: TEM imaging for case E (a) before hydration (b) 2 minutes (c) 30 minutes of hydration

This prediction is supported by the results reported for the dissolution experiments presented in literature <sup>29</sup> where after 2 minutes nanofoils are clearly observed, which after 30 minutes become nanoneedles and sheaf of wheat C-S-H morphologies, Whereas the authors <sup>29</sup> also report under similar hydrating conditions with water rather than saturated lime no such phenomenon is observed mainly due to lower pH ( $\leq 11$ ) even after 30 minutes of hydration.

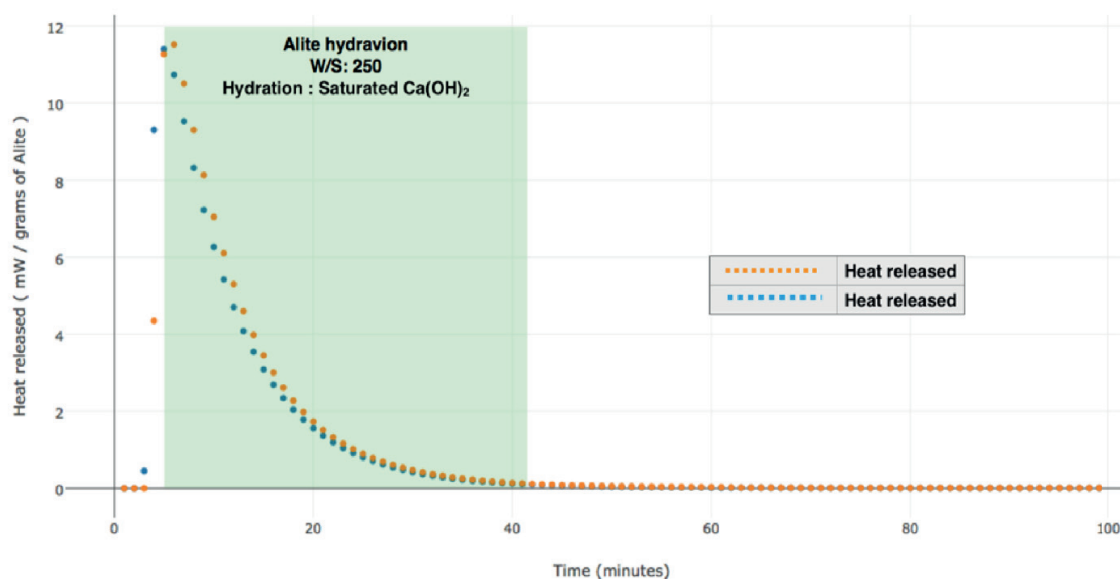


Figure 44;) Calorimetric curves for alite hydration at W/S 250, where Y-axis is heat released and X-axis is time in minutes. The experiment is quite reproducible as shown by the two repetitions (blue and orange dots) presented. The increase in the heat is the manipulation and placement of the samples holder into the calorimeter, the real heat release measurement starts at the green block after 5 minutes.

## Conclusion

A new insight into the hydration of alite phase is presented considering the solid formed out of the pore solution (i.e.) C-S-H and  $\text{Ca(OH)}_2$ . We demonstrate the important role of calcium in formation of different morphologies of C-S-H. Different silicate species dominates at different pH conditions in the presence of calcium that participates in principal precipitation reaction. Alite hydration is accelerated once the pH approaches the solubility of dissolved calcium and unstable pore solution tend to precipitate calcium bearing solid out of solution in form either C-S-H in abundance of reacting species or in form of  $\text{Ca(OH)}_2$  in absence of reacting silicate species. Further we extended our understanding to avoid the acceleration period and correlating the morphological observation to the one reported in the literature.

## Acknowledgement

Authors would like to thank Swiss national foundation for financing this project (Grants No. 153044). We would also like to thank Dr. V.K. Parashar, Dr. Jean Daraspe and Prof. Bruno Humbel for their fruitful discussion.

## Competing financial interests

The authors declare no competing financial interests.

## 7 Doping effect of other divalent ions

### 7.1 Introduction

In this chapter we extend our understanding of C-S-H formation and examine the effect of the other commonly known ions present in real cementitious system. My contribution as experimentalist was to collect and interpret the experimental characterized datas. Most of the interpretations are based on the morphology of precipitating calcium silicate hydrates that still needs further characterization by STEM- EDX and XRD are needed to confirm the discussion and speculations put forwards in this chapter.

### 7.2 Manuscript

#### Initial observations: Effect of the presence of divalent ions ( $\text{Ba}^{2+}$ , $\text{Mg}^{2+}$ , $\text{Zn}^{2+}$ ) on the morphology of precipitating calcium silicate

Abhishek Kumar<sup>11</sup>, Jirawan Siramanont<sup>1,3</sup>, Karen Scrivener<sup>2</sup>, Paul Bowen<sup>1</sup>

<sup>1</sup>Powder Technology Laboratory, Institut des Matériaux, Ecole Polytechnique Fédérale de Lausanne (EPFL), CH-1015 Lausanne, Switzerland

<sup>2</sup>Construction Material Laboratory, Institut des Matériaux, Ecole Polytechnique Fédérale de Lausanne (EPFL), CH-1015 Lausanne, Switzerland

<sup>3</sup>Siam Research and Innovation Co. Ltd., SCG Cement–Building Materials, Saraburi, 18260, Thailand

#### Abstract

Apart from calcium, many other divalent ions such as  $\text{Ba}^{2+}$ ,  $\text{Mg}^{2+}$  and  $\text{Zn}^{2+}$  co-exist in cementitious systems that can potentially effect the morphology development of the principal product of cement hydration – Calcium Silicate Hydrate (C-S-H). Hence, it is interesting to analyse the individual effect of these ion on the morphology of the precipitating C-S-H system. Further the morphological interaction of these divalent ions with only a silicate system in absence of calcium was investigated. The results reveal the uniqueness of the  $\text{Ca}^{2+}$  ion, in condensing monomeric silicate species at high pH to form *nanofolds/tapered-nanofolds* morphologies and disintegrate the oligomers or polymeric silicate species at lower pH to form *nanoglobules*. This feature is not shown by any other divalent ion tested. In fact, by appearance the morphology trend is reversed. None of the elements studied here could condensate silicates at  $\text{pH} \geq 11$ , and form a *nanoglobule*-like morphology even with high dopant concentrations, whereas at low  $\text{pH} \leq 11$ , they form a *nanofold*-like morphology. Notably, the *nanoglobules* and *nanofolds* obtained by these other divalent ions are structurally different from the ones obtained from the  $\text{Ca}^{2+}$  ion and hence termed as *dopantglobules* and *dopantfolds*. When the calcium and divalent ions are together in equal concentrations at high pH, conditions still favour formation of C-S-H nanofolds (condensated with calcium) and the other divalent ions tends to form their

---

<sup>1</sup> Corresponding Author  
Email: abhishek.kumar@epfl.ch



hydroxide with a *dopantglobule* morphology in most cases. Zinc hydroxide is an exception and forms a sharp pyramidal morphology often previously found at high pH conditions.

**Keywords:** C-S-H, morphology, nanoglobules, nanofoils, precipitation.

## Introduction

Portland cement is a complex mixture of numerous compounds. The anhydrous phases react with water to form various hydration products. It is difficult to investigate both the solid and aqueous phases during hydration because of this complexity. To understand the overall influence of each element, in particular minor elements, is almost impossible to analyze in such a system. Further carbonation of the hydration products on exposure to atmospheric air also complicates the picture. The knowledge of how different elements influence the hydration kinetics and microstructural formation is becoming of greater importance as most Portland cements are now blended with calcite or with other supplementary cementitious materials (SCM) increasing the variety and concentration of different elements. Possible modifications brought about in the C-S-H structure by foreign elements may result in consequent changes in the early age strength, either in negative or positive fashion.<sup>4,6,82</sup>

The main reactions of hydration occur within the first 24 hours although the hydration will continue until exhaustion of reactants<sup>4,6,109,110</sup>. The first period (stage I) is generally referred to as the initial dissolution period in which the rate of dissolution rapidly slows. The reaction period in stage II is called the induction period. The reaction rate of this stage is low even without the presence of retarding admixtures. At the end of the induction period, C-S-H and Portlandite start to grow rapidly to a maximum in heat evolution (approx. 3-12 h, stage III) and then the reaction decelerates (stage IV) to a slow long term (years) reaction to consume remaining anhydrous material (Stage V).<sup>29,83</sup> Tri-calcium silicate ( $C_3S$ ) is the major unhydrated phase in cement. Therefore, much research has been focused on the mechanisms governing the hydration of this “pure” cement phase<sup>29,166,193</sup> to allow a simpler interpretation without the competing reactions of the other cement phases. Bazzoni et al<sup>201</sup> investigated the effect of Mg and Zn ions on the hydration of  $C_3S$ . Calorimetry showed the reactivity of  $C_3S$  is increased by the presence of zinc giving a significantly higher degree of hydration (approximately double) during the same time frame as pure  $C_3S$ . Whereas magnesium shows a similar acceleration curve to  $C_3S$  but it continues for a longer period (30-60 minutes longer) than pure  $C_3S$  hydration. From electron microscopy the Zn doped  $C_3S$  also showed much longer calcium silicate hydrate (C-S-H) particles during the acceleration period, again about double that of the pure  $C_3S$ . The role of these ions on the dissolution and/or growth during the hydration is as of yet unexplained.

One of the difficulties in discerning how foreign ions may modify C-S-H formation is the inherent difficulty of characterizing C-S-H because of its poor crystallinity and variable stoichiometry.  $^{29}Si$  NMR has been one of the most relevant methods to study the Si arrangement in C-S-H<sup>6,45,53,54,127</sup>. Recently Pustovgar et al<sup>48</sup> investigated  $C_3S$  hydration by using in-situ NMR measurement and isothermal calorimetry. By using  $^{29}Si$ -enriched  $C_3S$  and they

monitored the evolution of C-S-H and revealed the relation between the surface phenomenon such and the occurrence of different stages of alite hydration and the importance of surface hydroxylation. It provides a new understanding in the complex kinetic behaviour related to calcium silicate systems.

To identify effects of individual parameters on nucleation and growth of C-S-H precipitation is an attractive alternative. Our recent systematic synthesis studies of pure phase C-S-H, in controlled conditions allowed the better understanding of the atomic structure of C-S-H<sup>107</sup>. Using DNP-NMR, solid state NMR, atomistic simulation and thorough characterization, we showed that the inclusion of calcium in the interlayer at bridging sites is necessary to produce the pure phase C-S-H. This bridging interlayer Ca induces strong hydrogen bonding responsible for the formation of stable high Ca:Si ratio C-S-H without invoking a secondary calcium rich phases<sup>107</sup>.

There are different C-S-H morphologies, *nanofolds*, often seen in high-alkali cement<sup>196,200</sup>, *tapered nanofolds* or *needles* (outer C-S-H)<sup>87,200,201</sup> and *nanoglobules* (inner C-S-H)<sup>87</sup>. We suspect these morphologies depend on the local chemical environment in which they grow. Hence with a synthetic system that we can control (representing different local chemical conditions) we can explore how different conditions and “dopants” effect the formation of C-S-H.

In our earlier precipitation studies were able to control the Ca:Si ratio, we noticed a morphological transformation point, from nanoglobules to nanofolds as a function of pH<sup>107</sup>..

We have synthesized C-S-H under 3 different conditions, resulting in three different morphologies i) low pH (<11) to form a nanoglobular C-S-H, ii) at high pH ( $\geq 13$ ) to form a nanofolds C-S-H and iii) at low silicate concentration to simulate Si concentrations normally found in hydrating Portland (or C<sub>3</sub>S) cement pore solutions resulting in nanoneedles or tapered nanofolds [Chapter 06]. Moreover, we also showed in the previous work [Chapter 06] that the variation of silicate species in solution and their interaction with calcium ions as a function of pH was shown to be a major contributing factor to this morphological changes. Hence in this study, we have analyzed the morphological changes in presence of different divalent ions in a controlled synthetic precipitation system with the aim of understanding their interaction with the precipitating C-S-H and their individual interaction with the silicate system.

## Materials and Methods

### *Synthesis of C-S-H with divalent ions elements*

To understand the effect of other divalent ions elements a series of experiments at high pH (>13) were conceived

Table 15. The divalent ions are added as 0.2 M solutions in all cases, same concentration as Calcium (even in the absence of Calcium).. The silicate concentration was fixed at 175  $\mu$ M for all experiments. It is also worth noting the difference in the interacting orbitals present in the elements tested. Ca, Mg, Ba belong to Alkali earth metals (IIA) and Zinc belongs to transition metals, with 2d and 4f orbitals respectively.



| Experiment name | Divalent ions (M) | Reactant A<br>0.2M   | Reactant B (.5H <sub>2</sub> O)<br>175 $\mu$ M | pH                          |
|-----------------|-------------------|--|--|-----------------------------|
| <b>M1</b>       | Mg                | Mg(NO <sub>3</sub> ) <sub>2</sub> .6H <sub>2</sub> O   | Na <sub>2</sub> SiO <sub>3</sub>               | 13.3 $\pm$ 0.1 ( $\geq$ 13) |
| <b>M2</b>       | Mg + Ca           | Mg(NO <sub>3</sub> ) <sub>2</sub> .6H <sub>2</sub> O<br>Ca(NO <sub>3</sub> ) <sub>2</sub> .4H <sub>2</sub> O | Na <sub>2</sub> SiO <sub>3</sub>               | 13.3 $\pm$ 0.1 ( $\geq$ 13) |
| <b>Z1</b>       | Zn                | Zn(NO <sub>3</sub> ) <sub>2</sub> .6H <sub>2</sub> O   | Na <sub>2</sub> SiO <sub>3</sub>               | 13.3 $\pm$ 0.1 ( $\geq$ 13) |
| <b>Z2</b>       | Zn+ Ca            | Zn(NO <sub>3</sub> ) <sub>2</sub> .6H <sub>2</sub> O<br>Ca(NO <sub>3</sub> ) <sub>2</sub> .4H <sub>2</sub> O | Na <sub>2</sub> SiO <sub>3</sub>               | 13.3 $\pm$ 0.1 ( $\geq$ 13) |
| <b>B1</b>       | Ba                | Ba(NO <sub>3</sub> ) <sub>2</sub> .6H <sub>2</sub> O   | Na <sub>2</sub> SiO <sub>3</sub>               | 13.3 $\pm$ 0.1 ( $\geq$ 13) |
| <b>B2</b>       | Ba+ Ca            | Ba(NO <sub>3</sub> ) <sub>2</sub> .6H <sub>2</sub> O<br>Ca(NO <sub>3</sub> ) <sub>2</sub> .4H <sub>2</sub> O | Na <sub>2</sub> SiO <sub>3</sub>               | 13.3 $\pm$ 0.1 ( $\geq$ 13) |

Table 15: Overall experimental conditions

### Characterization

High resolution scanning electronic microscopy (HRSEM) analysis was performed on a Zeiss Merlin, equipped with the GEMINI II column which combines ultra-fast analytics with high resolution imaging using advanced detection modes. Micrographs were obtained by coating the samples with 6 nm of osmium (gas phase coating). The metallization reduces charging and provides enhanced image contrast. Samples were analyzed with an acceleration voltage of 1 kV with a probing current of 300 nA. On-axis in-lens secondary electron detection mode was employed for imaging. In Transmission electron microscopy (TEM), the samples were imaged at room temperature using a Tecnai F20 (FEI, The Netherlands) operating at an acceleration voltage of 100kV LaB<sub>6</sub> gun with a line resolution of 0.34 nm, with images being recorded on a high sensitivity 4k x 4k pixel CCD camera. For HRSEM and TEM analysis, 50 mg of sample was dispersed in 40 mL of isopropanol. A drop of the dispersed precipitate was allowed to dry on a copper grid (200 mesh grids). The copper grids were glow discharged prior to sample disposition.

### Results and Discussions

As presented in detail in [Chapter 06], we expect to form three different morphologies which are presented in the Figure 45 (a-c). In the case where there is the formation of a secondary phase (i.e.) portlandite, interestingly a change in the C-S-H morphology towards tapered nanofoils or nanoneedles is observed, somewhat reminiscent of those seen in Portland cement and C<sub>3</sub>S systems in the presence of alkali<sup>196</sup>.

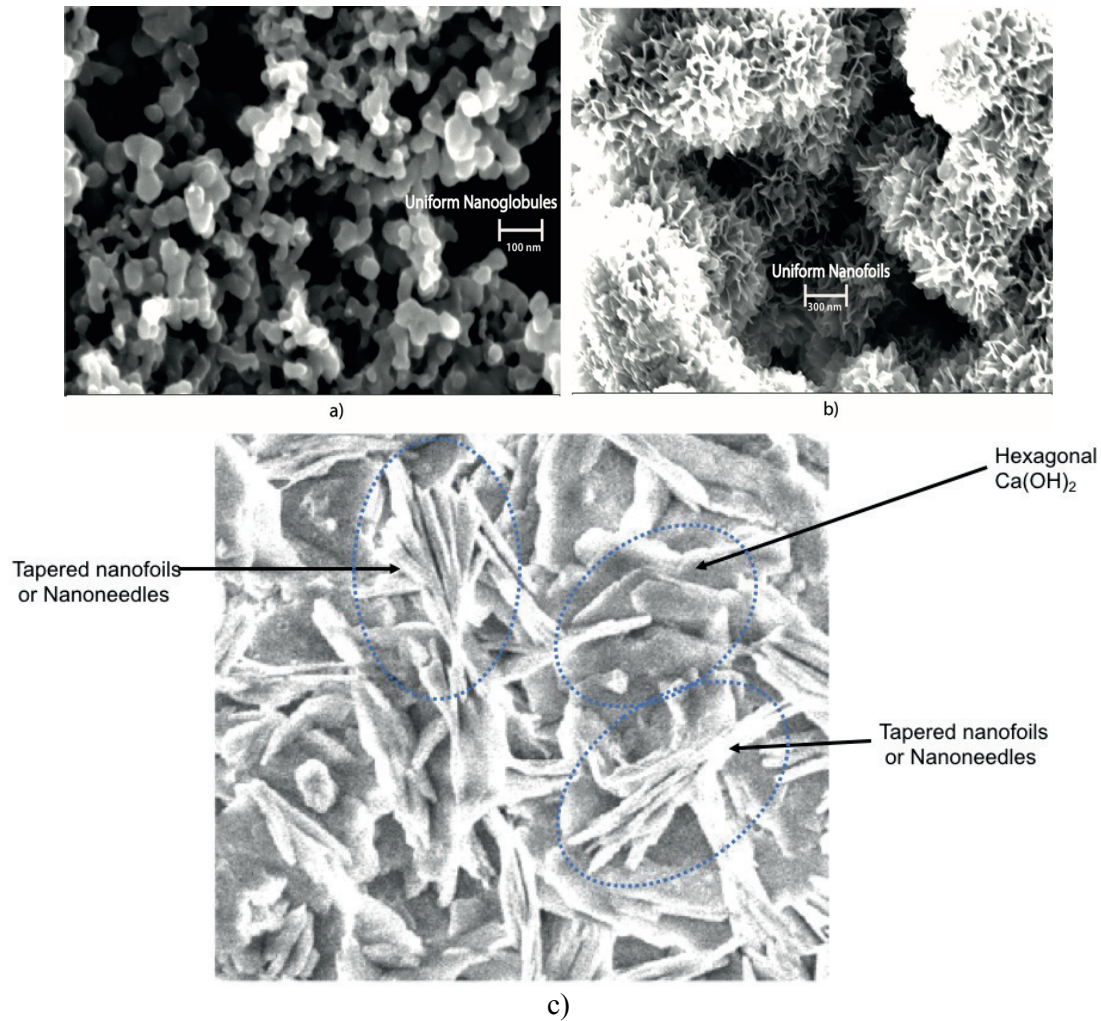


Figure 45: Difrenet C-S-H morphologies as a function of precipitation conditions a) Uniform nanoglobules b) Uniform nanofoils c) Tapered nanofoils and Calcium hydroxide.

For divalent ions  $\text{Ba}^{2+}$ ,  $\text{Mg}^{2+}$  and  $\text{Zn}^{2+}$ , the effect was investigated with and without the presence of the calcium ion. For the experiments B1, M1, Z1 without the presence of calcium, the divalent ions tend to form homogeneous dopantglobules of sizes varying from 30-100 nm, Figure 46(a), Figure 47(a) and Figure 48(a-c). In the experiments B2, M2, Z2 with presence of calcium we observe the formation of mixed morphologies with the appearance of nanofoils and dopantglobules. It is worth noticing that with the limited amount of silicate in the reacting system, we have shown in previous studies [chapter 6] that the system tends to form a nano(tapered)foil-like C-S-H morphology. For future publication, EDX and XRD analysis are needed to confirm the speculation and further insight into the formation of these mixed morphologies. The remaining divalent ions that have not been incorporated into the C-S-H formed between the calcium and the silicate tend to form their corresponding supersaturated hydroxide phases, as seen for experiments M2 and B2 in Figure 46(b) and Figure 47(b). In experiment Z2, Zinc hydroxide forms conical pyramidal morphology at these high pH conditions unlike any other ions studied here (Figure 49(a-c)).

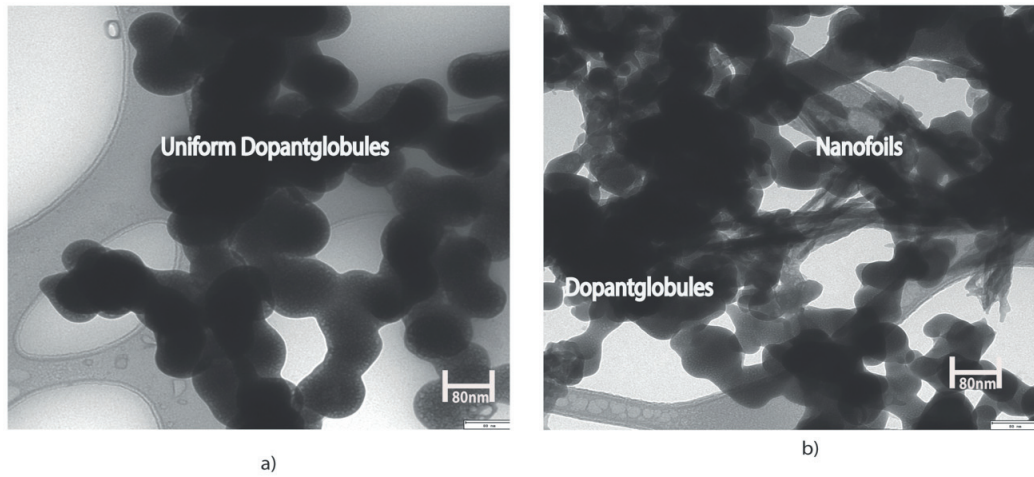


Figure 46 a) Barium Silicates dopantglobolues (B1) without  $\text{Ca}^{2+}$  b) Mixed morphology of C-S-H nanofoils and Ba dopantglobules (B2)

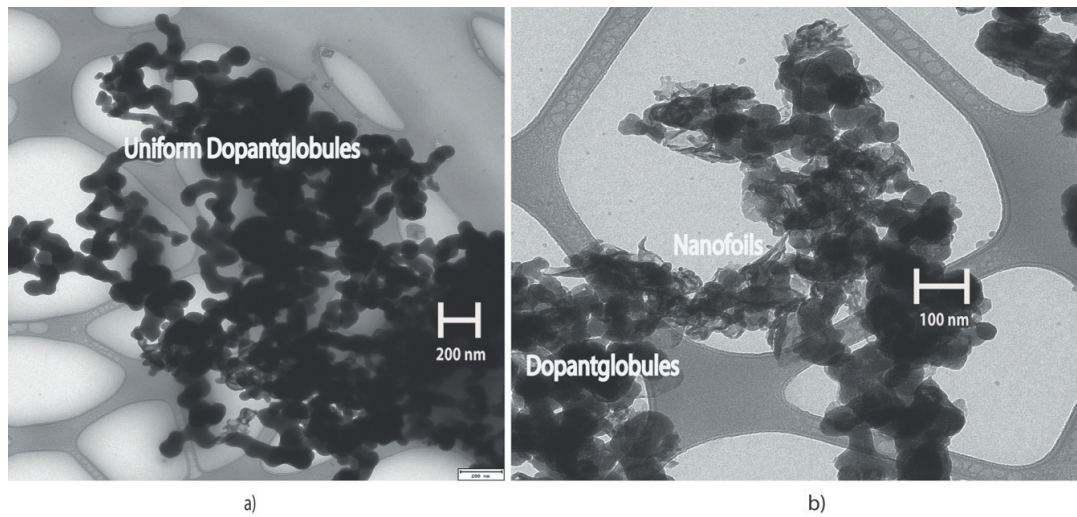


Figure 47 a) Magnesium Silicate dopantglobolues (M1) without  $\text{Ca}^{2+}$  b) Mixed morphology of C-S-H nanofoils and Mg dopantglobules (M2)



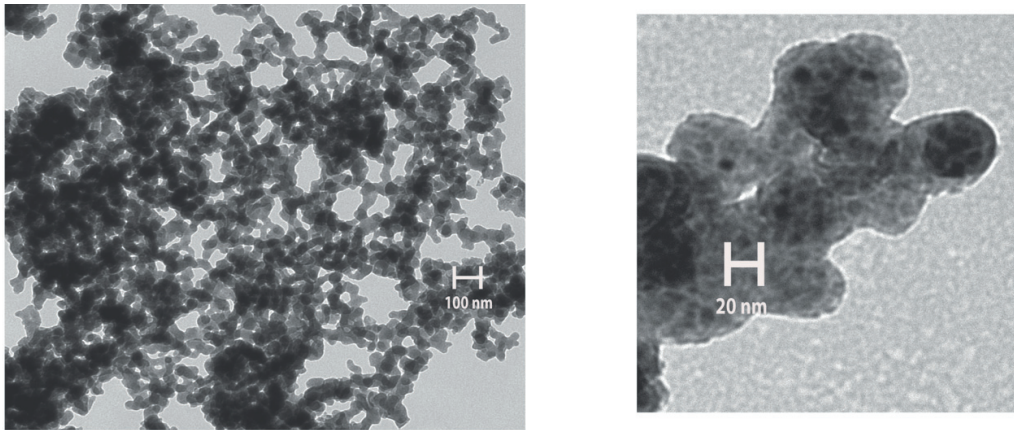


Figure 48: Zinc Silicate dopant globules (Z1) without  $\text{Ca}^{2+}$

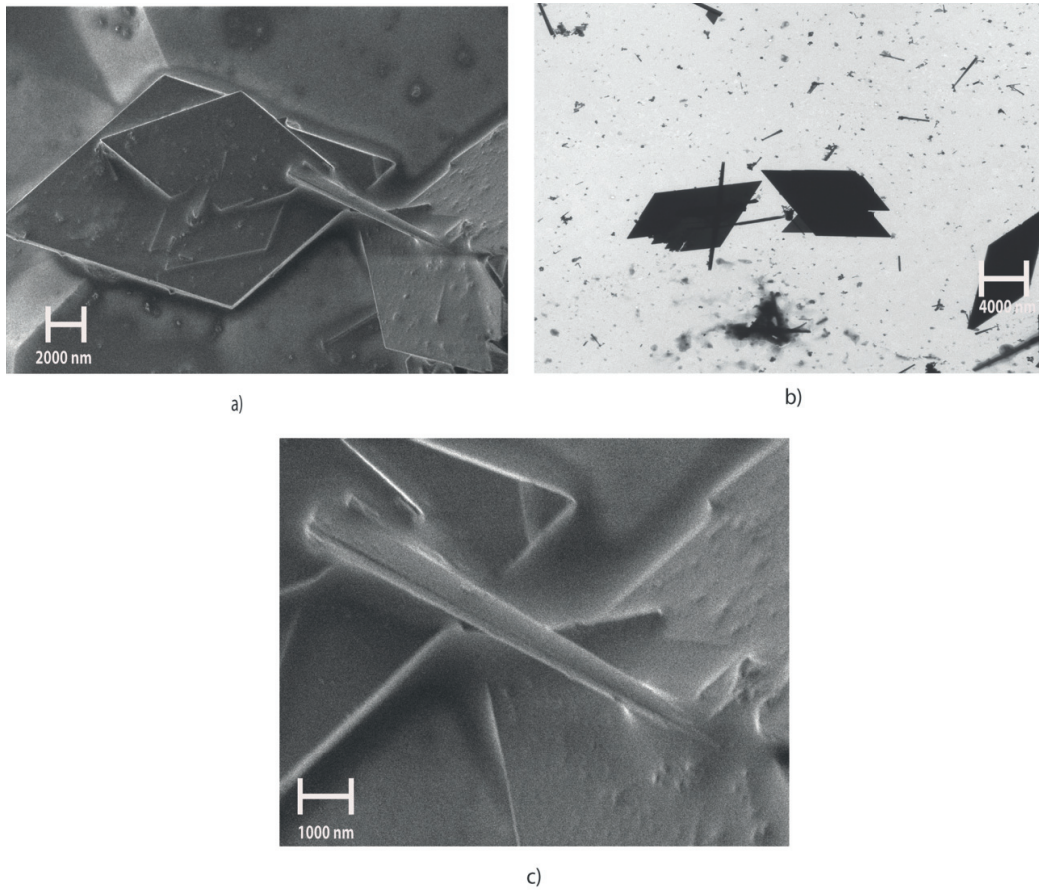


Figure 49: Mix morphology of C-S-H nanoneedles and dopant conical pyramids (Z2)

For the synthetic system we are using, we have from previous studies<sup>107</sup> inferred that the pH is a defining parameter for precipitation and ultimately controlling the Ca:Si ratio and morphology. This is a consequence of the predominant silicate species available in solution for reaction (i.e.) and its availability over the course of precipitation. In addition to pH, the silicate species which appear in an aqueous system is a sensitive function of cation type and

concentration. With the assumption of no physical constraint from mixing of the reactant, in the current studies, at pH  $13.3 \pm 0.1$ , a chemical equilibrium favoring the silicate species  $\text{SiO}_2(\text{OH})_2^{2-}$  is achieved<sup>67,74,112</sup>. This species is electrostatically more stable and tends to exist as its monomeric form<sup>12</sup>. This has been verified for our synthetic conditions by using liquid  $^{29}\text{Si}$  NMR and the results are shown in chapter 06, where over 90% of the silicate species exists as monomers.

In the presence of calcium, these silicates species are capable of condensing to form solids dominated by dimeric structures<sup>48,89,193,194,202</sup> and in these high alkali conditions form a nanofoil-like morphology [chapter 6]. With the other divalent ions without the presence of  $\text{Ca}^{2+}$ , we only see the formation of silicates with globular morphologies. This may be related to the stability of the silicate tetrahedra that bonds with the divalent ions via the oxygen atom. Ions other than  $\text{Ca}^{2+}$  may interfere with the stability of the silicate tetrahedra because of a stronger interaction with the connecting oxygen owing to their ionic size and charge. Presumably, if the bond strength of the cation – O exceeds certain value that may leads to destabilization of silicate. Noticeably, the ionic sizes of the divalent ions examined here are  $\pm 10\%$  of the size of the calcium. To further validate such hypothesis one could envisage using ab-initio simulations, for example using the AIRSS approach<sup>203</sup>, but is beyond the scope of this article.

In summary we see that depending on the pH the simple calcium silicate system can precipitate a solid and uniform C-S-H phase either in the form of nanoglobules or nanosheets, without any secondary phases. When the calcium is in excess and the silicate supply is limited (i.e. low concentration) then we get a second phase, calcium hydroxide (hexagonal platelets) and tapered nanofoils almost needle-like C-S-H. When other divalent ions are used at high pH, we see the formation of their silicates in the form of nanoglobules, which we assume do not contain the dimeric species seen in the C-S-H nanofoils. Although to verify this assumption we need to perform the XRD to look into the crystal structure and in case found to be amorphous, Solid state DNP NMR could characterize the states of these globules. When calcium is present in equal concentrations to the other divalent ions, it seems to dominate the silicate interactions forming nanofoils or nanoneedles and the other divalent ions form their hydroxides. This suggests that calcium has a special interaction with the silicate species present at these thermodynamic conditions. GEMS predicts relatively higher supersaturation index for C-S-H formation.

The studies presented by Lothenbach.et.al<sup>113</sup>, the formation of distinctly different morphologies by calcium and magnesium operating at pH 10.5. Magnesium forming more like nanofoil-like morphology (structurally different to that formed by calcium at high pH), where magnesium is doing mere charge balancing role than any role in condensation of Silicates. Calcium in same system formed nanoglobule-like morphology similar to that reported in our studies [chapter 6]. As presented previously, calcium alters the silicates speciation in the solution to promote certain type of precipitation reaction as demonstrated before and after mixing with silicate solution presented in chapter 06. Such features make calcium a special and essential in formation for C-S-H, not possible by other divalent ions. Consider the Figure 50, showing the speciation distribution before mixing of any cation. Whereas Figure 51, shows the

promotion of single speciation in majority towards single reaction. In Figure 52, the silicate speciation is not influenced when mixed with magnesium.

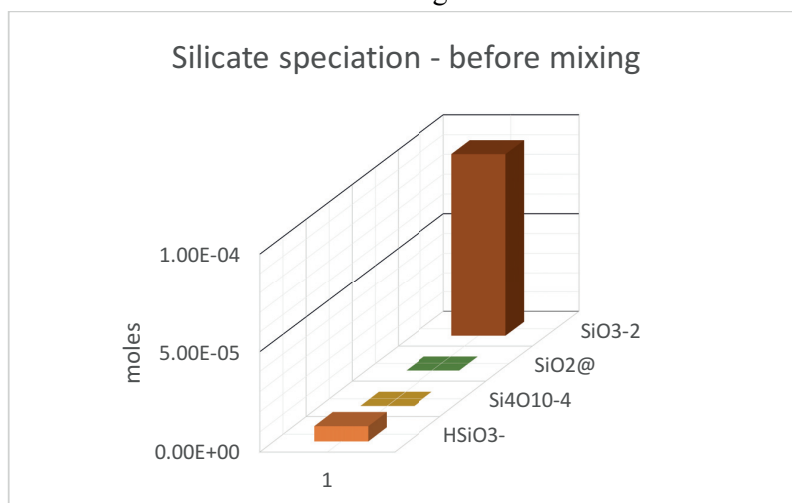


Figure 50: Silicate speciation at 0.175mM before mixing

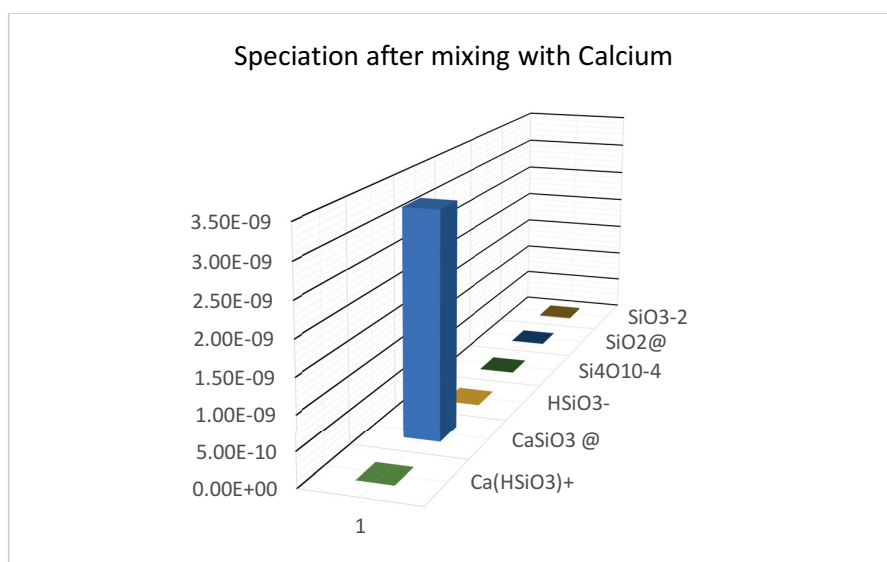


Figure 51: Speciation distribution when mixed with calcium

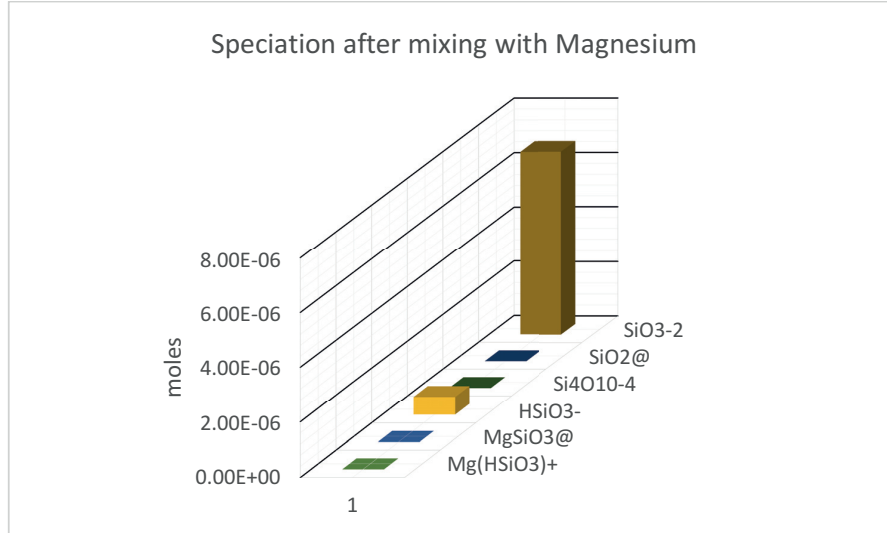


Figure 52: Speciation distribution when mixed with Magnesium

Consider the Figure 53 (a), It shows the starting conditions of the precipitation,  $\text{pH} > 13$  with the silicate monomeric species, the calcium ions and dopant ions in solution. With calcium (blue sphere) the silicate goes on to form uniform nanofoils like morphology under these conditions. Now in Figure 53(c) where calcium and dopants are present in equal amounts, the thermodynamically favoured solid (highest supersaturation) continue to form first (in this case C-S-H). The remaining divalent ions in the solution form their hydroxide appearing as spherical morphology except Zinc. Zinc hydroxide forms flat pyramidal structure morphology (close to the equilibrium shape for the crystal lattice under consideration). Another interesting finding is when dopants are reacted without any Calcium, shown in Figure 53(d) they do not condense the monomeric silicate species to form foils, they form a spherical morphology but this time it's not their hydroxides but their silicates. Calcium seems to fit perfectly in that criteria compared to any other elements tested. Although it needs to be verified by either first principle or NMR experiment with the different elemental silicates to calculate the bonding parameters.

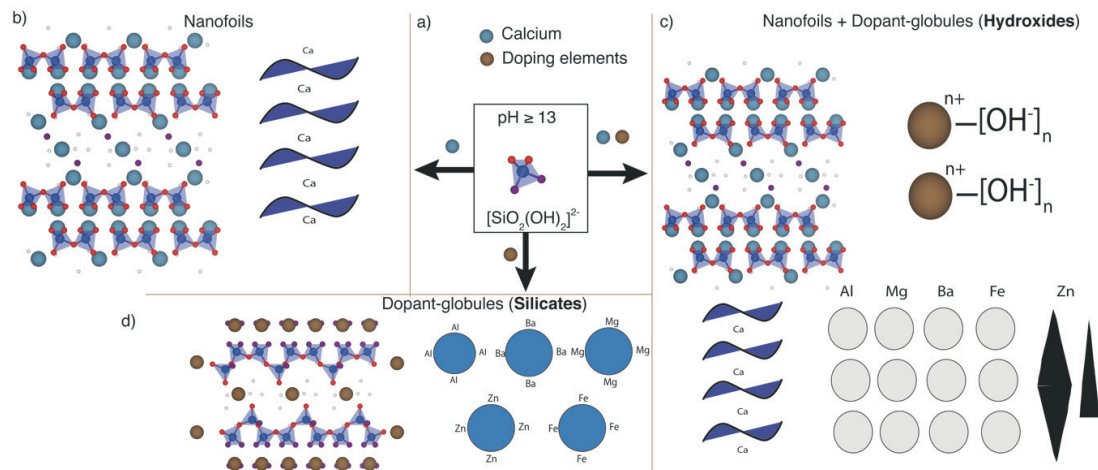


Figure 53::Morphology mechanism (The representation is not scale to actual sizes); a) Silicate ions at high pH b) Calcium condensed nanofoils formation c) Calcium condensed tapered foils and formation of ion-hydroxide. d) Dopantglobules formation.



## **Conclusion**

At high pH conditions, Calcium is special and essential to the formation of C-S-H at highly alkaline conditions. No other elements examined showed similar properties. This property may be attributed to ionic size and charge of the calcium and other ions, that ultimately affect the stability of the silicate species in the solid formation. Although this still needs to be verified perhaps by molecular dynamics<sup>204</sup>. All other divalent ions are unable to condense monomeric silicate species at these chemical conditions and end up forming dopantglobular silicates or hydroxides depending on the availability of the silicates. We also show that formation of C-S-H (nanofibers) at high pH condition is favoured above any other supersaturated solid in the system unless constrained. We form nanofibers in abundance of reacting species and nanoneedle in species constrained environment. At lower pH conditions calcium again tends to be special compared to other elements, by disrupting the silicate polymeric units to form nanoglobules. Whereas all other ions, tends to play charge balance role and end up forming dopantfibers.

## **Acknowledgement**

We would like to thank Prof. Lyndon Emsley, Dr. Brennan Walder, Dr. Dimitri Kulik and Dr. Barbara Lothenbach for their fruitful discussion. We would also like to thank Swiss National Foundation for financing this thesis work (SNF\_153044).

## 8 Kinetic analysis of Calcium silicate hydrate formation

### 8.1 Introduction

In this chapter, we emphasise the collection of kinetic data to understand the growth mechanism of synthetic C-S-H in our experimental system. There is hardly any kinetic models available for C-S-H growth and none for Ca:Si ratio  $\geq 1.6$ . Modeling of the system is necessary for a better understanding of how modifications in chemistry may modify the strength development as a function of time. Here we are concentrating on the atomist scale growth mechanisms which lead to C-S-H formation the glue of cement and concrete. As stated by Jim Trainham (DuPont)- “If you can’t model your process, you don’t understand it. If you don’t understand it, you can’t improve it”. We believe that our current understanding is sufficient to model the C-S-H system. In this chapter we collected kinetic data ( $\text{Ca}^{2+}$  activity, conductivity, yield, pH) using the “reverse dropwise” method described in chapter 3 with data recorded directly online. The experiments are repeated thrice at three different optimized flowrates best suited for kinetic data collection in the synthetic system. This section consists of the main draft and the Supplementary information of the draft is presented in annexure. As the second author in the manuscript, my role being an experimentalist was to provide kinetic data from the synthesis of pure C-S-H for population balance modeling. The modeling part was handled at the PSI by Mr. Andalibi under guidance of Dr. Andreas Testino. Further I helped in interpretation of data and developing the parameter choice for the multiscale modeling.

### 8.2 Manuscript

#### A Simplified model for Calcium Silicate Hydrate growth from solution

Mohammad Reza Andalibi,<sup>4</sup> Abhishek Kumar,<sup>1</sup> Bhuvanesh Srinivasan,<sup>1,3</sup> Andreas Testino,<sup>4</sup> Karen Scrivener,<sup>2</sup> Paul Bowen<sup>1</sup>

Powder Technology Laboratory, Institut des Matériaux, Ecole Polytechnique Fédérale de Lausanne (EPFL), CH-1015 Lausanne, Switzerland

Construction Material Laboratory, Institut des Matériaux, Ecole Polytechnique Fédérale de Lausanne (EPFL), CH-1015 Lausanne, Switzerland

Department of Earth & Environmental Sciences, Ludwig-Maximilian University, D-80333, Munich, Germany  
Bioenergy and Catalysis Laboratory (LBK, Chemical Processes and Materials) PSI, Villigen, Switzerland

#### Abstract

Calcium Silicate hydrates (C-S-H) is precipitated by double decomposition of Calcium and silicate bearing salts in alkaline aqueous solution, using an in-house developed synthetic system. C-S-H precipitates are X-ray amorphous, their growth mechanism and structure is still not fully resolved. The synthetic system allows kinetics data collection such as  $\text{Ca}^{2+}$  activity, conductivity and pH under controlled conditions. We use these kinetic data for a modeling framework based on population balance equations (PBEs) coupled with elemental mass balances. We assume the particle to be spherical, for a simpler first approach. The PBE set is

composed of terms describing nucleation and molecular growth of particles, which are inferred from atomistic considerations governing the former processes. It demonstrates the role of secondary nucleation in the formation of secondary particles from the primary particle. The mean crystallite and secondary particle sizes predicted by the model were very close to those already measured experimentally or predicted by different simulation studies as we could include the polydispersity of the C-S-H particle into the model. It provides a good handle on kinetics of C-S-H formation and with further sophisticated input can improve the model towards the modelling of precipitated synthetic C-S-H.

**Keywords:** Calcium Silicate hydrates, Population balance modeling, Supersaturation, Nucleation, growth rate

## Introduction

Calcium Silicate hydrates (C-S-H) is the principal phase formed during the cement hydration constituting to about 60% of the total hydrated product and responsible for early age strength of the material. It is complex, existing in different morphologies and Calcium to Silicate ratios. Cementitious material production contributes to about 10% of the world Carbon emission, making it a large contributor to greenhouse gasses. Therefore, the requirements for sustainable construction materials is in demand. Industry tries to face this challenge with replace some part of cement with sophisticated products that can modify properties of cementitious material by effecting the growth of C-S-H. In order to continue the use of Cementitious material with a minimized environmental impact, a better understanding of C-S-H growth mechanism will help in preparing better recipe for construction materials. C-S-H is difficult to study in real cementitious systems due to presence of many phases and multi-variation in the C-S-H phase itself. We adopted a synthetic route to produce pure C-S-H, by precipitation or reactive crystallization. It is rapid crystallization method conducted in a high supersaturation regime with high nucleation rates. Several factors such as agglomeration, mixing can greatly affect the precipitation process and determine the crystal size distribution (CSD) and hence influence the properties of the final product to a significant extent. At an atomistic level more or less, the cement community come to a common agreement with C-S-H being similar to defective tobermorite like structure, whereas at the meso level it is still an ongoing debate between two group – Feldman/Sereda<sup>57</sup> or Jennings type<sup>205</sup>. The modelling could also help shed light on the meso scale details of the C-S-H.

With a well-designed synthetic system, we had the liberty of collecting useful kinetics data *in-situ* for modelling the system. In the current system, we work in a fed batch synthetic route to produce pure phase C-S-H. Time evolution of  $\text{Ca}^{2+}$  activity over time has been tracked for different flow rates of silicate/NaOH solution. Considering the particulate nature of C-S-H<sup>205,206</sup>, the experimentally measured values have been deconvoluted into individual physicochemical phenomena (including nucleation and growth processes) by fitting a coupled set of population balance equations (PBEs), describing particle formation process, and elemental mass balances into the observed  $\text{Ca}^{2+}$  molar amounts. Similar coupled experimental-

modelling work were successfully applied to other particulate materials precipitating from aqueous solutions (e.g., BaTiO<sub>3</sub><sup>133,207</sup> and CaCO<sub>3</sub> polymorphs<sup>208</sup>). Using this approach, we were able to describe the physical mechanisms leading to the observed C-S-H mesoscale structure, a problem that, to the best of our knowledge, is being tackled for the first time.

## Population balance modelling

The population balance is a well-established approach as the mathematical framework for dealing with particulate systems. These kinds of processes involve formation of entities, growth, breakage or aggregation of particles, as well as dispersion of one phase in another one, and are, therefore, present in a large range of applications, like polymerization, crystallization, bubble towers, aerosol reactors, biological processes, fermentation or cell culture. Consider a system containing particulate material. In such a system, a particle can be represented by two sets of coordinates denoted as external and internal coordinates. External coordinates represent the spatial position of the particle in the physical space,  $\mathbf{x} \equiv (x_1, x_2, x_3)$ . On the other hand, internal coordinates describe some intrinsic properties of the population, e.g., particle size, particle velocity, temperature, composition, etc. To quantitatively describe the variations in the population of particles across the external and internal spaces one may resort to the so-called number-density function (NDF). Consider a population of dispersed entities in an infinitesimal control volume  $d\mathbf{x} \equiv dx_1 dx_2 dx_3$  centered at the physical point  $\mathbf{x}$  in the external space. Let  $\mathbf{L} \equiv (L_1, L_2, \dots, L_M)$  be the internal coordinate vector containing the respective  $M$  internal coordinates. The NDF  $n(t, \mathbf{x}, \mathbf{L})$  is defined as the number of particles in the infinitesimal physical volume  $d\mathbf{x}$  and infinitesimal phase space volume  $d\mathbf{L}$ . The NDF is therefore a function of time ( $t$ ), space ( $\mathbf{x}$ ), and the internal coordinate vector ( $\mathbf{L}$ ) and may be further normalized by the total physical volume of the system being considered. It is worth noting the NDF is an average quantity representative of particle populations in infinitesimal control volumes with differential dimensions in both internal and external spaces<sup>209</sup>. Hereafter, we concentrate on population distributions which are homogeneous across the external space, and only track particle diameter as an internal coordinate. Hence, NDF would merely be a function of time and particle size,  $n(t, L)$ .

The second important definition is that of  $k^{\text{th}}$  order moment of the density function:

$$m_k \equiv \int_{\Omega_L} L^k n(t, L) dL \quad (1)$$

where  $\Omega_L$  is the particle size domain (theoretically  $0-\infty$ ). As it can be readily understood from Eq. (1), for univariate size-based NDF the zeroth and first moments represent the total particle number and total particle length per unit volume of system, respectively. Moreover, the second and third moments are proportional to total particle surface and total particle volume per unit volume system, respectively. In the two latter cases, the proportionality constants are surface and volume shape factors ( $k_A$  and  $k_V$ , respectively). Total mass concentration is further related to total volume concentration via particle density ( $\rho_{\text{solid}}$ ). Number-averaged values can be easily obtained through dividing the respective moment by the zeroth moment theory<sup>210</sup>. Furthermore, an average particle size can be defined by  $m_{k+1}/m_k$  for any value of  $k$  (e.g., for Sauter mean diameter  $k = 2$ ). Other useful definitions can be found in general texts<sup>209,210</sup>

For a homogeneous system (uniform NDF across the physical space) the general population balance equation (PBE) describing the variation of NDF over time and phase space can be written as<sup>210</sup>

$$\frac{\partial n}{\partial t} + \frac{\partial}{\partial L}(nG_L) + n \frac{d(\ln V)}{dt} = - \sum_{j=1}^F \frac{Q_j n_j}{V} + h \quad (2)$$

where  $G_L$  is the rate of change of particle size ( $\frac{dL}{dt}$ ; linear growth rate),  $V$  is the system volume,  $F$  is the number of input and output flows (taken as positive for flow out of suspension and negative for flow into suspension), and  $h$  represents discontinuous jumps signifying discrete events (e.g., nucleation, aggregation, or breakage)<sup>209</sup>. Now let us multiply both sides of Eq. (2) by  $L^k$  and integrate from zero to infinity. After simplification

$$\frac{dm_k}{dt} + m_k \frac{d(\ln V)}{dt} = k \int_0^\infty n(t, L) G_L L^{k-1} dL - \sum_{j=1}^F \frac{Q_j m_{k,j}}{V} + \bar{h}_k \quad (3)$$

where  $m_{k,j}$  is the  $k^{\text{th}}$  moment in the  $j^{\text{th}}$  flow and  $\bar{h}_k$  is

$$\bar{h}_k = \int_0^\infty h L^k dL \quad (4)$$

In order to solve Eq. (3) for a particulate system, the set of equations for the first  $k$  moments of interest should be closed. The details are presented in appendix (SI C).

## Material and methods

### Experimental details

As shown in Figure 54, experimental data is collected from an in-house developed synthetic reactor system working in a fed batch manner. The system operates under nitrogen to avoid carbonation. With the aim to produce Ca:Si ratio of 2 in the final precipitate, 22 mL of a 10 M aqueous Sodium hydroxide (NaOH) solution was mixed with 200 mL of a 0.1 M Sodium silicate ( $\text{Na}_2\text{SiO}_3 \cdot 5\text{H}_2\text{O}$ ) solution and was added in a dropwise manner to a 200 mL solution of 0.2 M Calcium Nitrate ( $\text{Ca}(\text{NO}_3)_2 \cdot 4\text{H}_2\text{O}$ ). The flow rate of the silicate stream was varied in different sets of experiment ( $Q_1 = 2.00, 0.50, 0.11$ , and  $0.05$  ml/min), effecting the number of drops added. Sodium hydroxide solution ensures the right pH conditions in the reacting volume for uniform precipitation of C-S-H (chapter 4 & chapter 5). The data collected are  $\text{Ca}^{2+}$  ion activity, conductivity, pH and in some separate experiment, additionally, yield as function of time. To calculate the yield, a fixed volume of the reaction volume is withdrawn from the reactor and reaction is stopped by introducing this volume into liquid ethane.

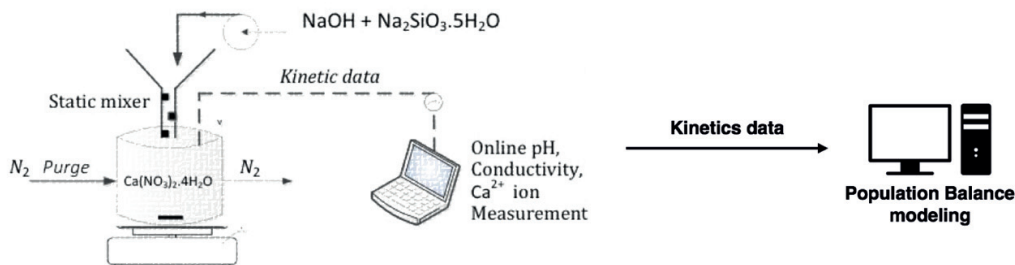


Figure 54: Experimental conditions and data recording

## Computational details

### *Estimation of kinetic parameters for model C-S-H precipitation system*

The time-dependent experimental data ( $\text{Ca}^{2+}(\text{aq})$  concentration as a function of time) already collected on the precipitation of C-S-H will be used in order to examine the kinetics of this model system. The overall framework is algorithmically shown in Annexure. As can be seen the first step would be to introduce the experimental data into the model along with initial conditions for all the ordinary differential equations (ODEs). Furthermore, appropriate initial guesses should be provided for unknown model parameters. Having the initial amounts of various components (e.g., Ca and Si), an initial speciation calculation shall be used to determine the concentrations of various aqueous species in the solution assuming equilibrium is attained quickly in the liquid phase while the subsequent precipitation process would be the rate limiting step (local-equilibrium assumption)<sup>208,211–214</sup>.

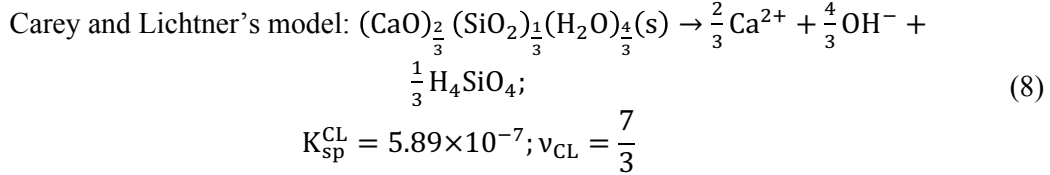
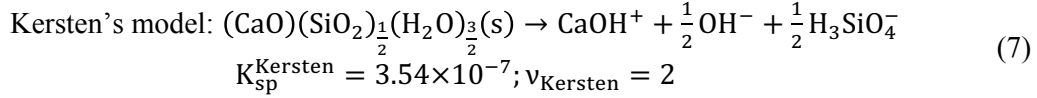
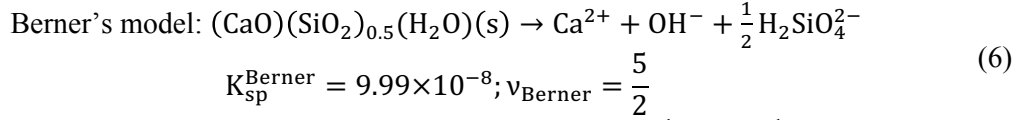
### *Aqueous speciation and thermodynamic driving force for solid formation*

There are several solid solution model available for C-S-H formation with  $\text{Ca}:\text{Si} \leq 1.5$ , whereas solid phase those proposed by Berner<sup>215,216</sup>, Kersten<sup>217</sup>, and Carey and Lichtner<sup>218</sup> allow for the formation of a homogeneous phase with  $\text{Ca}:\text{Si} = 2$  (the composition of interest to us). Other model attempts to model solid aqueous solution by introducing portlandite in the system beyond 1.5, that is in contrast to our observation of mere C-S-H ( $\text{Ca}:\text{Si} = 2$ ) precipitation without any portlandite forming from solution (chapters 4,5,6). Our C-S-H phase corresponds to a 1:1 solid solution of  $\text{Ca}(\text{OH})_2$  and  $\text{CaH}_2\text{SiO}_4$  end-members in Berner's model,<sup>216</sup> 1:1 solid solution of  $\text{Ca}(\text{OH})_2$  and  $\text{CaHSiO}_{3.5} \cdot 1.5\text{H}_2\text{O}$  end-members in Kersten's model, and 1:2 solid solution of  $\text{SiO}_2 \cdot 2\text{H}_2\text{O}$  and  $\text{Ca}(\text{OH})_2$  end-members in Carey and Lichtner's model.

As Prieto discussed<sup>219</sup>, for practical purposes the so-called stoichiometric *solubility* product shall be used to describe the dissolution behaviour of solid solutions. In reality the former represents a metastable equilibrium condition which assumes the solid solution to be a stoichiometric phase (i.e., a pure single-component solid with fixed stoichiometry) dissolving in a congruent manner. This concept arises from experimental observations that solid solutions tend to dissolve in a congruent manner until an initial saturation is built up. Nevertheless, an aqueous solution may remain in metastable state of saturation with respect to stoichiometric solid because reaching the true equilibrium necessitates dissolution-precipitation of solid solution, which can be an extremely sluggish process. Indeed, according to Berner such a simplifying assumption is reasonable for C-S-H precipitation at room temperature within the time scales of experimental setups<sup>216</sup>. Having the former in mind and in line with many studies in the literature that use the concept of stoichiometric solubility product in explaining the precipitation of solid solutions<sup>220–223</sup>, we will apply the same framework to define the thermodynamic driving force for C-S-H precipitation. By definition, the stoichiometric solubility product (superscript 'st') for a binary solid solution with end-member solubility constants  $K_1$  and  $K_2$  reads

$$K_{\text{sp}}^{\text{st}} = (K_1 X_1 \lambda_1)^{X_1} (K_2 X_2 \lambda_2)^{X_2} \quad (5)$$

where  $X_1$  and  $X_2 = 1 - X_1$  are mole fractions of end-members composing one mole of solid solution, and  $\lambda_1$  and  $\lambda_2$  are their activity coefficients, respectively. Writing the dissolution reaction for our particular C-S-H phase according to the three selected models described earlier



where  $v$  is the total number of ions produced upon the dissolution one of mole C-S-H in each model. Knowing the solubility product, the (molal) activities of aqueous species ( $\text{Ca}^{2+}$ ,  $\text{OH}^-$ , and  $\text{H}_2\text{SiO}_4^{2-}$  for the model of Berner;  $\text{CaOH}^+$ ,  $\text{OH}^-$ , and  $\text{H}_3\text{SiO}_4^-$  for the model of Kersten; and  $\text{Ca}^{2+}$ ,  $\text{OH}^-$ , and  $\text{H}_4\text{SiO}_4$  for the model of Carey and Lichtner) are needed for the calculation of IAP<sup>6,224</sup>

$$\text{IAP}^{\text{Berner}} = a_{\text{Ca}^{2+}} \times a_{\text{OH}^-} \times a_{\text{H}_2\text{SiO}_4^{2-}}^{\frac{1}{2}} \quad (9)$$

$$\text{IAP}^{\text{Kersten}} = a_{\text{CaOH}^+} \times a_{\text{OH}^-}^{\frac{1}{2}} \times a_{\text{H}_3\text{SiO}_4^-}^{\frac{1}{2}} \quad (10)$$

$$\text{IAP}^{\text{CL}} = a_{\text{Ca}^{2+}}^{\frac{2}{3}} \times a_{\text{OH}^-}^{\frac{4}{3}} \times a_{\text{H}_4\text{SiO}_4}^{\frac{1}{3}} \quad (11)$$

with  $a_x$  denoting molal activities of different aqueous species. Subsequently, the supersaturation ratio is defined as<sup>74</sup>

$$S^{\text{modelX}} = \left( \frac{\text{IAP}^{\text{modelX}}}{K_{\text{sp}}^{\text{modelX}}} \right)^{1/v_{\text{modelX}}} \quad (12)$$

with modelX denoting respective C-S-H models. To calculate molal activities used in IAP expressions, consistent with the general practice used in modelling precipitation processes we assume that after each perturbation (i.e., overall change of elemental balance) the aqueous species attain equilibrium state quickly compared to the time-scale of solid formation process. In this manner, the system is assumed to always experience a locally-equilibrated state where aqueous species attain their equilibrium distribution quickly before they contribute to the formation of solid phase, the latter being the rate limiting step<sup>225,226</sup>. This view necessitates the calculation of speciation in the aqueous phase over the period of kinetic process.

One further step in the selection of a suitable C-S-H model was to compare the mole amount of  $\text{Ca}^{2+}$  in solution after the system has reached equilibrium. For higher flow rates (2 and 0.5  $\text{mL} \cdot \text{min}^{-1}$ ) equilibrium was reached after reasonable periods of time (after  $\sim 200$  and  $600$  minutes, respectively). Comparison between the experimentally measured equilibrium  $\text{Ca}^{2+}$  mole amount and that predicted using different C-S-H models revealed that Kersten's model reproduces the experimental data better than the other two models. However, minor adjustment in the value of  $\text{pK}_{\text{sp}}$  ( $\sim 0.7$  pK units) rendered the C-S-H model completely consistent with the experimental data. The preceding adjustment is justified in the light of the relatively large



scatter in experimental C-S-H solubility data used to fit solid solution models<sup>81</sup>. Therefore, a value of  $K_{sp}^{Kersten,adjusted} = 5.97 \times 10^{-8}$  will be used in all the simulations.

As Kulik et al. discuss<sup>80</sup>, a thermodynamic equilibrium solver to be integrated into a kinetic modelling code must be very efficient and accurate. In order to abstain from computationally expensive communication with external equilibrium calculation codes (*c.f.*, Braatz et al. for an example of interfacing OLI with population balance modelling) we chose to develop our own aqueous equilibrium solver (Appendix SI C). Such a general approach would be particularly useful when dealing with systems for which input parameters are not available in pre-existing programs.<sup>227,228</sup>

In the current study, the speciation is calculated by solving the system of equations composed of nonlinear laws of mass action (LMAs) and linear component and charge balance constraints<sup>228</sup>. Consider an aqueous solution comprised of NS species (including water solvent, ions, and aqueous ion pairs) and NC independent components (either elements like Ca and Si, or group of elements like OH and NH<sub>4</sub>). Knowing the overall amount of all components and considering charge neutrality for electrolyte solutions, (NS-NC-1) independent LMAs should be written to have a complete set of equations solvable for NS unknown amounts. The set of equations to be solved would then be

$$\text{Charge balance: } \Psi_1 = 0 = \sum_{i=1}^{NS} z_i n_i \quad (13)$$

$$\text{Component balance: } \Psi_j = 0 = -B_e + \sum_{i=1}^{NS} b_{e,i} n_i ; j = 2, \dots, NC + 1; e = j - 1 \quad (14)$$

$$\text{LMAs: } \Psi_j = 0 = -\log_{10} K_k + \sum_{i=1}^{NS} v_{k,i} \log_{10}(m_i \gamma_i) ; j = NC + 2, \dots, NS; k = j - NC - 1 \quad (15)$$

where  $n_i$ ,  $z_i$ ,  $b_{e,i}$ ,  $v_{k,i}$ ,  $m_i$ , and  $\gamma_i$  are mole amount, signed valence, stoichiometry of component  $e$ , signed stoichiometric coefficient in law of mass action  $k$ , molality (mol.kg<sup>-1</sup>), and molal activity coefficient for the  $i^{\text{th}}$  species, respectively.  $B_e$  is the overall molar amount of component  $e$ , and  $K_k$  is equilibrium constant for the  $k^{\text{th}}$  LMA. The system of equations made up by Eqs. (13), (14), and (15) is often solved using an iterative Newton-Raphson-type approach<sup>228,229</sup>. The details of the model, parameter calculation is presented in details in Annexure (SI C).

Figure 55 shows the simulation results for C-S-H precipitation experiments described in Section – experimental details over a period of 20 hours, using OLI Studio software (with solid and vapor phases turned off) and our aqueous speciation code (called aqEQBRM). Both pH and molal ionic strength values are predicted with excellent accuracy when compared to OLI output as reference (Figure 55; small differences due to using different activity coefficient models as discussed in Thomsen et al<sup>230</sup>). The differences in predicted pH values are generally less than 0.1 pH units which is in the acceptable range of discrepancy between experimentally measured and calculated values<sup>231,232</sup>. Figure 55(d-e) depicts supersaturation ratios for both portlandite and C-S-H (different solid solutions models) using OLI (markers) and aqEQBRM (lines). Once again, there is an excellent match between aqEQBRM and OLI, with the small discrepancies attributable to different activity coefficient models (TJ for aqEQBRM and MSE for OLI).<sup>63</sup> Analogous to our experimental observation (no portlandite precipitating out of solution), for all C-S-H models the supersaturation ratio with respect to portlandite is smaller than that of C-S-H. The difference in C-S-H supersaturation ratio calculated based on different solid solution models could be ascribed to discrepancy in C-S-H models being calibrated using various experimental data sets. Such discrepancy is anticipated to be around 0.2-0.6 pK units

in solubility product<sup>81</sup>. Simple hand calculation shows that the former is equivalent to supersaturation discrepancies by a factor of  $\sim 1.2$ - $1.7$  for  $K_{sp} \approx 10^{-7}$ . Comparing the value shown in Figure 55(d-f) reveals that the former is in fact consistent with C-S-H supersaturation ratios having an upper bound correspondent to Kersten's model and a lower bound correspondent to Carey and Litchner's model (assuming the intermediate Berner's model represents the mean values).

A very similar approach was adopted to calculate solid-liquid equilibria (SLE) once the supersaturation of C-S-H exceeds unity. The C-S-H precipitation reaction is added to the set of LMAs while mass balances are amended to account for the elements leaving the aqueous solution and forming the solid material. A new initial guess using the output of aqEQBRM code will be generated by successively reducing relevant elements out of the solution re-calculating the supersaturation using aqEQBRM until it is close to unity. Afterwards, the initial guess is passed to a Newton-Raphson based scheme solving for the new set of linear and nonlinear equations. Throughout this work we will refer to this SLE code as EQBRM.

Table 16: Considered species and their TJ activity coefficient parameters

| Species name                                  | Truesdell-Jones Parameters |       |
|---|----------------------------|-------|
|   | $a_i$                      | $b_i$ |
| H <sub>2</sub> O                              | 0.000                      | 0.000 |
| H <sup>+</sup>                                | 4.780                      | 0.240 |
| OH <sup>-</sup>                               | 10.650                     | 0.210 |
| Ca <sup>2+</sup>                              | 4.860                      | 0.150 |
| H <sub>3</sub> SiO <sub>4</sub> <sup>-</sup>  | 4.500                      | 0.060 |
| Na <sup>+</sup>                               | 4.320                      | 0.060 |
| NO <sub>3</sub> <sup>-</sup>                  | 3.580                      | 0.000 |
| NaNO <sub>3</sub>                             | 0.000                      | 0.080 |
| CaNO <sub>3</sub> <sup>+</sup>                | 3.930                      | 0.060 |
| H <sub>4</sub> SiO <sub>4</sub>               | 0.000                      | 0.050 |
| H <sub>2</sub> SiO <sub>4</sub> <sup>2-</sup> | 3.740                      | 0.000 |
| CaOH <sup>+</sup>                             | 3.950                      | 0.060 |
| CaHSiO <sub>3</sub> <sup>+</sup>              | 3.220                      | 0.010 |
| CaH <sub>2</sub> SiO <sub>4</sub>             | 0.000                      | 0.050 |
| NaHSiO <sub>3</sub>                           | 0.000                      | 0.050 |

Table 17: Mass action equations for model C-S-H precipitation system

| Index | Law of mass action  | $\log_{10}(K_i)$ |
|-------|---|------------------|
| 1     | $H^+ + OH^- \rightleftharpoons H_2O$                        | 14.000           |
| 2     | $H_3SiO_4^- + H^+ \rightleftharpoons H_4SiO_4$              | 9.850            |
| 3     | $H_2SiO_4^{2-} + H^+ \rightleftharpoons H_3SiO_4^-$         | 13.100           |
| 4     | $Na^+ + H_3SiO_4^- \rightleftharpoons NaHSiO_3 + H_2O$      | 2.083            |
| 5     | $NaNO_3 \rightleftharpoons Na^+ + NO_3^-$                   | 0.910            |
| 6     | $CaOH^+ \rightleftharpoons Ca^{2+} + OH^-$                  | -1.230           |
| 7     | $CaNO_3^+ \rightleftharpoons Ca^{2+} + NO_3^-$              | -0.420           |
| 8     | $Ca^{2+} + H_3SiO_4^- \rightleftharpoons CaHSiO_3^+ + H_2O$ | 1.258            |
| 9     | $Ca^{2+} + H_2SiO_4^{2-} \rightleftharpoons CaH_2SiO_4$     | 4.749            |

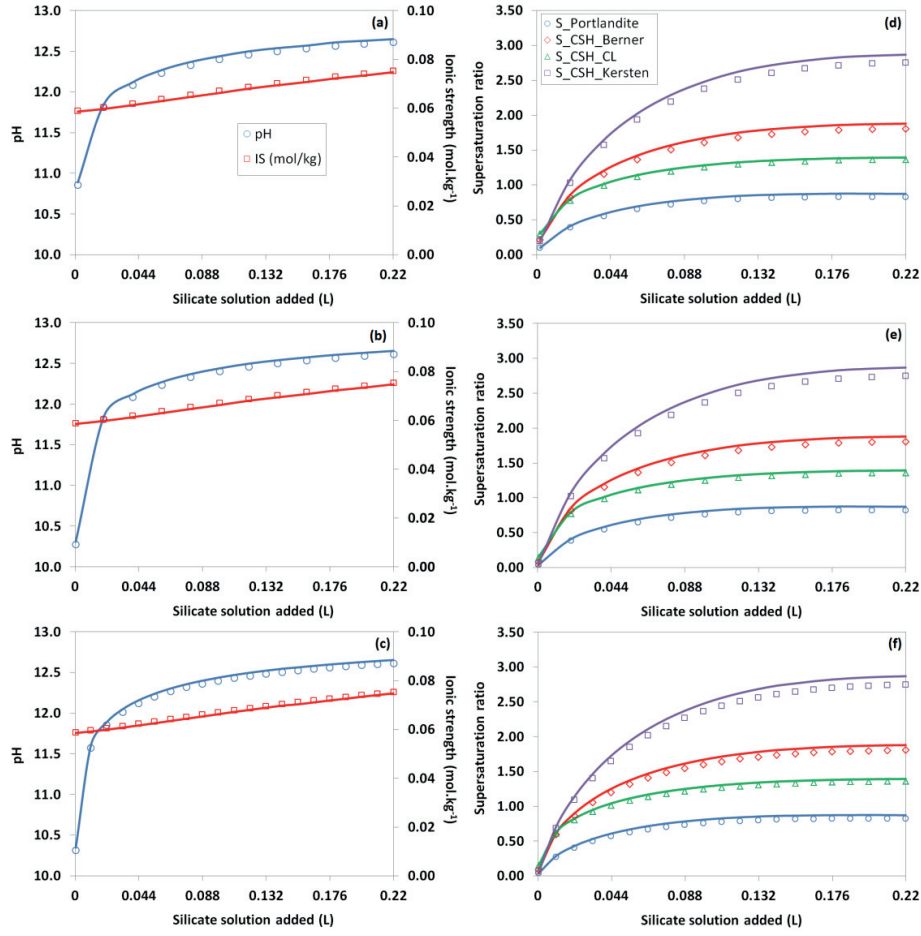


Figure 55: pH and molal ionic strengths (a-c) and the corresponding portlandite and C-S-H supersaturation ratios (d-f) as a function of  $\text{Na}_2\text{SiO}_3 + \text{NaOH}$  solution added at 2.00 (a, d), 0.5 (b, e), and 0.11 (c, f)  $\text{mL} \cdot \text{min}^{-1}$  flow rates calculated by OLI software (open markers) and our speciation code aqEQBRM (lines) (legends common for both graphs).

## Precipitation kinetics and implementation in PBEs

The precipitation of particulate solids is multi-step process governed by a variety of elementary processes. Among the former, nucleation and growth are oftentimes the dominant phenomena and precede the so-called *secondary* changes of the precipitated phase, the latter including recrystallization, ageing, and aggregation<sup>74,233</sup>. In the current work, we are interested in the early stages of C-S-H precipitation and therefore, we only consider nucleation and growth as detailed in the following sections.

### Nucleation

In the absence of preformed solid particles, nucleation would be the first step in the precipitation of a solid phase from a liquid solution. Broadly speaking, nucleation is classified as either primary or secondary nucleation. In contrast to primary nucleation, secondary nucleation takes place merely in the presence of already formed precipitant particles. Further, primary nucleation could be either homogeneous or heterogeneous which, respectively, proceed in the absence or presence of foreign surfaces. The theoretical frameworks for the two primary nucleation mechanisms are similar, differing only in the magnitude of interfacial tension used in their mathematical description (discussed further below)<sup>234</sup>. Among secondary nucleation mechanisms discussed in the literature, true secondary nucleation is a prevalent

process, in the formation of nanosized particles, once we have precipitated particles in solution. Indeed, the former allows for the formation of nuclei at lower supersaturation ratios due to favourable interaction between existing embryos and already precipitated particles<sup>207,234,235</sup>. According to Nielsen<sup>75</sup> and also following Testino et al.<sup>207</sup> the rate of primary and secondary nucleation (nuclei.m<sup>-3</sup> solution.s<sup>-1</sup>) shall respectively be expressed as

$$J_I = \frac{D}{\Omega^{\frac{5}{3}}} \cdot \exp \left[ \frac{-B\gamma^3 \Omega^2}{k_B^3 T^3 (\nu \ln S)^2} \right] \quad (16)$$

$$J_{II} = \frac{D}{\Omega^{\frac{4}{3}}} \cdot \exp \left[ \frac{-B\gamma_{\text{eff}}^3 \Omega^2}{k_B^3 T^3 (\nu \ln S)^2} \right] \times x_A A_T \quad (17)$$

where  $B = \frac{4k_A^3}{27k_V^2}$  is a geometric shape factor, with  $k_A$  and  $k_V$  being the surface and volume shape factors, respectively (e.g., for spheres with diameter as the size variable,  $k_A = \pi$ ;  $k_V = \frac{\pi}{6}$ ;  $B = \frac{16\pi}{3}$ ),  $\gamma$  is the interfacial tension between the precipitated C-S-H phase and aqueous solution (J.m<sup>-2</sup>),  $\Omega$  is the molecular volume of the precipitating solid ( $8.0370 \times 10^{-29}$  m<sup>3</sup> for  $(\text{CaO})(\text{SiO}_2)_{\frac{1}{2}}(\text{H}_2\text{O})_{\frac{3}{2}}$ , calculated according to the formalism proposed by Thomas et al.<sup>71</sup>),  $k_B$  is the Boltzmann constant ( $1.38 \times 10^{-23}$  J.K<sup>-1</sup>),  $T$  is the absolute temperature (K), and  $S$  is the supersaturation ratio defined in Section 4.2 with  $\nu$  being the overall stoichiometry of precipitating solid.  $x_A$  is the fraction of overall particle surface  $A_T$  (m<sup>2</sup>.m<sup>-3</sup> suspension calculated using the second moment,  $A_T = k_A m_2$ ) available for secondary nucleation and

$$\gamma_{\text{eff}} = \frac{\gamma k_V}{k_A} \left( \frac{k_A}{k_V} - \frac{\sigma}{\gamma} \right) \quad (18)$$

with  $\gamma_{\text{eff}}$  being the effective interfacial tension in the presence of already formed surface (e.g., precipitated C-S-H surface) and  $\sigma$  accounts for the energy of adhesion of the embryos on the substrate (J.m<sup>-2</sup>). The values of  $\sigma$  lies between  $0-2\sigma$  corresponding to the absence of substrate and perfect epitaxial growth, respectively.<sup>20</sup> The corresponding critical nucleus size would then be

$$L_I = \frac{2k_A \Omega \gamma}{3k_V \nu k_B T \ln(S)} \quad (19)$$

$$L_{II} = \frac{2k_A \Omega \gamma_{\text{eff}}}{3k_V \nu k_B T \ln(S)} \quad (20)$$

with  $L_I$  and  $L_{II}$  denoting the critical size of primary and secondary nuclei, respectively. It has been shown that C-S-H nucleation at lower supersaturation ratios (e.g.,  $< 10$ ) does not proceed in a homogeneous manner anymore. Instead, either heterogeneous or secondary nucleation (in the absence or presence of foreign nuclei, respectively) is responsible for the formation of C-S-H nuclei<sup>36</sup>. Therefore, accounting for homogeneously produced nuclei has to be augmented by an expression accounting for the rate of secondary produced nuclei. Secondary nucleation has been chosen rather than heterogeneously produced ones because their formation is generally more favourable<sup>72</sup> and also the formed C-S-H solid is highly polycrystalline and aggregated<sup>53</sup>. Additionally, dust-free distilled water was used for all the

syntheses in our experimental system where no surfaces other than the reactor and stirrer are present.

#### Growth

There are a number of steps involved in the growth of solid particles the first being the diffusion of building units from the solution bulk to the surface of particles. A solid particle grows fastest when its faces are completely covered with kink sites. Under the above conditions, the particle growth is only limited by the diffusion of building blocks toward the particle surface. Therefore, diffusion-controlled growth theoretically dictates the highest growth rate a particle can achieve at a particular supersaturation<sup>73,234</sup>. The mathematical expression for the maximum linear growth rate would then be

$$G = \frac{k_A D}{3k_V \rho_{\text{solid}} L} (K_{\text{sp}})^{\frac{1}{v}} (S - 1) \quad (21)$$

where  $L$  is the particle size,  $\rho_{\text{solid}}$  is the *molar* density of the precipitated solid ( $2.0661 \times 10^4 \text{ mol.m}^{-3}$  for  $(\text{CaO})(\text{SiO}_2)_{\frac{1}{2}}(\text{H}_2\text{O})_{\frac{3}{2}}$ ;  $K_{\text{sp}}$  is the molar solubility product ( $\approx$  molal solubility product, considering dilute system in which we are interested; *see also* Ref. <sup>217</sup>, and  $S$  is the supersaturation ratio. Additionally,  $D$  is an *apparent* diffusion coefficient approximated by the smallest diffusivity of ions into which the solid dissociates<sup>74</sup>. It is simply Fick's first law, for dilute solutions (i.e., very low solute volume fraction), correlating diffusive flux with concentration gradient, the latter approximated by relative supersaturation ratio ( $S - 1$ ). As can be seen in Figure 56, under very fast surface integration reaction the equilibrium concentration ( $C^*$ ) is roughly equal to interfacial concentration ( $C_I$ ). Therefore, the diffusion driving force ( $C - C_I$ ) can be approximated by ( $C - C^*$ ). Further mathematical manipulation of diffusion flux on the particle surface gives<sup>73</sup>. It is worth mentioning that for particles smaller than 5-10  $\mu\text{m}$ , the thickness of stagnant film is much greater than the particle size and convective mass transfer can be safely ignored<sup>74</sup>.

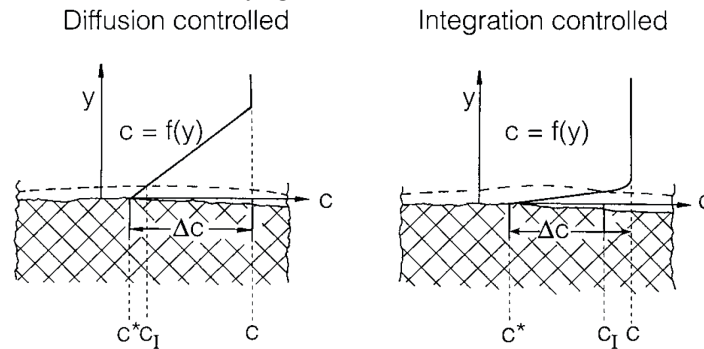


Figure 56: Concentration profiles for diffusion- and integration-controlled growth<sup>74</sup>

On the other extreme, crystal growth might be controlled by the integration of building units (monomers) onto surface of particles. Integration-limited growth may obey a plethora of mechanisms (e.g., screw dislocation, birth and spread, and polynuclear growth) depending on the operational conditions and also on the system under investigation. Even in a single system, under different conditions (e.g., supersaturation rise or depletion) there might be a transition from one mechanism to another with unknown borderline. To overcome this complication, a

viable approach would be to define an integration-controlled growth rate analogous to that employed in diffusion-reaction theory<sup>73,74,236</sup>

$$G = \frac{k_A k_r}{3k_v \rho_{\text{solid}}} (K_{\text{sp}})^{\frac{g}{v}} (S - 1)^g \quad (22)$$

where the exponent  $g \geq 1$  is the order of integration-controlled crystal growth rate and  $k_r$  is the rate constant for the integration process. The value of exponent  $g$  qualitatively points toward the dominant integration mechanism at work. A value  $g = 1$  indicates the dominance of either rough surface growth (or spiral growth at very high supersaturations) while  $g = 2$  represents spiral growth at low supersaturations (parabolic law)<sup>233</sup>. Values  $g > 2$ , denoting stronger supersaturation dependence of growth rate, can arise under the dominance of surface nucleation mechanisms (birth and spread or polynuclear growth mechanisms) taking place at higher supersaturations<sup>74</sup>. Finally,  $1 < g < 2$  would imply a combination of different regimes being at work. This last situation could happen when the range of supersaturation over which growth is happening is relatively wide so that not a single but a spectrum of mechanisms governs the growth process. Figure 57, summarizes the above discussion schematically.

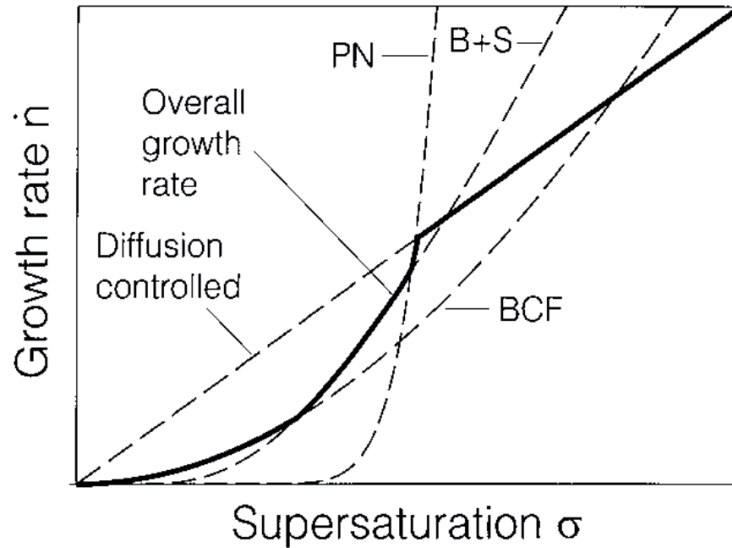


Figure 57: Competing growth mechanisms as a function of supersaturation<sup>234</sup>

Optimization of kinetics parameters is presented in Annexure and in Table 18, are the optimized kinetics bounds.

Table 18: Bound for unknown kinetics parameters

| Kinetic parameter | $\gamma$ (J.m <sup>-2</sup> )<br>Interfacial tension | $\frac{\sigma}{\gamma}$<br>Adhesion/Tension | $x_A$ | $D$ (m <sup>2</sup> .s <sup>-1</sup> )<br>Diffusion | $K_G$<br>Geometric factor | $g$<br>(Growth rate exponent) |
|-------------------|--|---|-------|---|---------------------------|-------------------------------|
| Lower bound       | 0.01   | 0   | 0     | 10 <sup>-11</sup>                                   | 10 <sup>-13</sup>         | 1                             |
| Upper bound       | 0.15   | 2   | 1     | 10 <sup>-9</sup>                                    | 10 <sup>-7</sup>          | 3                             |
| Scale factor      | 10   | 1   | 1     | 10 <sup>-9</sup>                                    | 10 <sup>-9</sup>          | 1                             |



## Results and discussion

The TEM analysis of C-S-H precipitates reveals the morphology to be nanofolds as shown in Figure 58, with thickness ranging from 5-10 nm with length up to 100 nm.

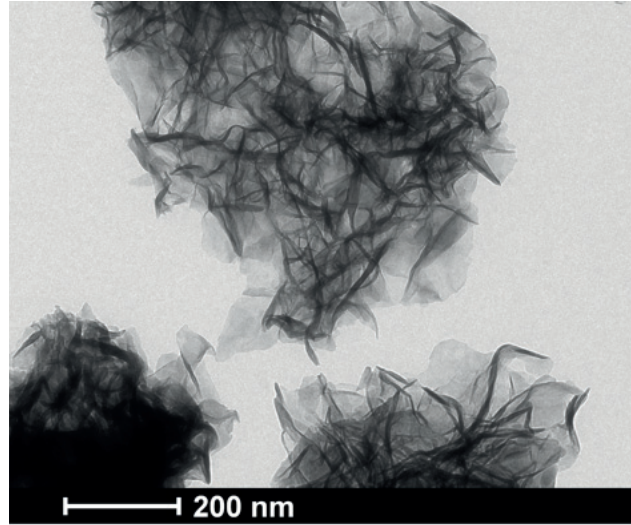


Figure 58: Nanofolds morphology for Ca:Si -2

Initial attempts to fit the experimental data collected at  $2 \text{ mL} \cdot \text{min}^{-1}$  inlet flow rate with a PBE model embracing primary nucleation, secondary nucleation, and diffusion-controlled growth, as done by Testino et al. for  $\text{BaTiO}_3$ ,<sup>207</sup> required the introduction of very small (in the order of  $10^{-8}$ ) diffusional effectiveness factors. The former is the ratio of actual growth rate to the one that would occur if diffusion controlled the overall growth process<sup>233</sup>. Very small values obtained for C-S-H precipitation indicate the dominance of integration control, consistent with a previous report by Ntafalias and Koutsoukos<sup>112</sup>. It is worth noting that often very small particles ( $< 100 \text{ }\mu\text{m}$ ) grow under an integration-controlled regime<sup>8,234</sup>. Indeed, both PBE simulations discussed in the following paragraphs and experimental evidences show that the precipitated C-S-H particles (i.e., primary particles discussed further below) are generally smaller than  $10 \text{ nm}$ <sup>53</sup>. Besides, direct AFM observations confirm the initial formation of remarkably smooth surfaces of C-S-H followed by the precipitation of layers with enhanced roughness<sup>237</sup>. As a result, the surface roughness has to be built up gradually ruling out the dominance of diffusion-controlled growth mechanism. Therefore, all the modeling was done using an integration-controlled growth rate expression summarizes the optimal kinetic parameters obtained from fitting the experimental data with a PBE model comprised of primary nucleation, secondary nucleation, and integration-controlled growth (Figure 59).

The values found for the interfacial tension of C-S-H in contact with its mother solution are consistent with those estimated from the linear correlation with solubility proposed by Sohnel, giving a value of  $\sim 0.1 \text{ J} \cdot \text{m}^{-2}$  which is slightly larger than the fitted values here<sup>238</sup>. This is no surprise as the former correlation was developed using a large number of literature data available for different crystalline solids. The value obtained from Sohnel's linear correlation was also used in the HydratiCA model by Bullard and coworkers<sup>239</sup>. Lower interfacial tension values were estimated based on C-S-H precipitation experiments in the studies by Garrault-Gauffinet and Nonat for Ca:Si = 1 ( $0.012 \text{ J} \cdot \text{m}^{-2}$ ),<sup>36</sup> and by Ntafalias and Koutsoukos assuming



Greenberg's C-S-H model ( $0.03 \text{ J.m}^{-2}$ )<sup>112</sup>. The currently fitted value sounds to be the most reliable one for the system of interest (Ca:Si = 2) as the other values have been obtained bearing many assumptions and estimations, probably for variable Ca:Si ratio's. It has already been shown that secondary nucleation mechanism, can directly account for polycrystalline nature and *mesoscale ordering* of some precipitated solid materials, an observation that an aggregative mechanism is not capable to describe<sup>207,240–243</sup>. In fact, each C-S-H nanocrystal generated by a primary nucleation event undergoes a succession of secondary nucleation events, producing more three-dimensional (single) nanocrystals in the close vicinity of primary nuclei, which is followed by growth of these crystallites, leading to distinct polycrystalline particles (Figure 60). In the context of combined primary and true secondary nucleation, individual particles grown upon primary and secondary nucleation events are called *primary particles* (crystallites for crystalline solids). On the other hand, the polycrystalline particles, each of which being composed of a *single* primary nucleation-generated particle and possibly one or more primary particles generated by secondary nucleation, are called secondary particles (Figure 60). Such a combined nucleation framework would nicely account for the nematic order, that is order in orientation with no or poor position order, frequently reported for solution grown C-S-H<sup>53,237</sup>. The degree of ordering is directly dictated by the energy of adhesion of the embryos on the substrate<sup>207</sup>. In this regard, null adhesion energy translates into a zero affinity between the embryos and the substrate (particles already formed) and thus, secondary nucleation is not a nucleus formation mechanism. On the contrary, for positive adhesion energies there would be an energy gain in nucleating particles on the substrate rather than in the bulk of solution. For values smaller than the maximum ( $\sigma = 2\gamma$ ) the interaction between embryos and the substrate is limited and there is generally mismatch between the lattice structure of secondary nuclei and the substrate (primary nucleus that may have grown). The former situation gives rise to polycrystalline secondary particles. Finally, having the maximum value of adhesion energy, one would observe an epitaxial growth, meaning the secondary nuclei are perfectly oriented with respect to the lattice structure of the substrate. This last scenario corresponds to a growth mechanism provoked by surface nucleation, leading to a single-crystalline structure (e.g., B+S or polynuclear growth)<sup>207,244,245</sup>. True secondary nuclei have the same structure and composition as the substrate and hence, the adhesion energy should be at its maximum. Nevertheless, the presence of solvent molecules and adsorbed ions on the surface of the substrate often reduces the actual adhesion energy leading to the formation of polycrystalline particles<sup>245</sup>.

In the case of C-S-H precipitation studied here, at higher inlet flow rates the interfacial tension is slightly smaller than at larger flow rates. This difference being in the order of  $10^{-3} \text{ J.m}^{-2}$  is due to excess lattice ions and/or specifically adsorbed substituting ions, attracting the oppositely charged ions from the bulk of the liquid and reducing the interfacial tension<sup>214,234,246</sup>. The same reasoning holds for slightly larger apparent diffusion coefficients at higher flow rates. The faster diffusing ions accumulate on the particle surface attracting counterions via electrostatic interactions which in turn facilitate the diffusion process<sup>234</sup>.

As can be seen in Table 19, both the relative adhesion energy and its absolute value decrease by flow rate. Earlier it was discussed that solvent molecules and ions present on the surface of already formed particles reduce the adhesion energy between embryos and the substrate surface. Additionally, it is well known that the surfaces of precipitated C-S-H particles are

covered by interstitial electrolyte solution (mainly calcium-bearing and hydroxide ions plus solvent molecules) rendering them highly charged<sup>247</sup>. Therefore, at higher flow rates where the solution ionic strength is generally larger, the extent of adsorption would be more reducing the adhesion energy. Looking at Table 19, it is clear that the surface adsorbed ions have the most profound impact on the effective adhesion energy of embryos on the substrate, followed by their milder influence on apparent diffusivity of ions toward the surface. The smallest effect is imposed on the interfacial tension between the solid and solution. Corroborating the above discussion, Monte Carlo simulations have already shown the non-DLVO behavior of C-S-H particle interaction and its strong sensitivity to surface charge density as well as exchangeable ion nature (size and valence)<sup>248</sup>.

The general precipitation pathway can be described as follow: upon the addition of sodium silicate + sodium hydroxide solution as the inlet flow the solution primarily undersaturated with respect to C-S-H moves toward supersaturated state gradually. Once a critical supersaturation is reached, primary nucleation takes place forming critically-sized nuclei of C-S-H solid phase. The former depletes solution out of C-S-H precursors, reducing supersaturation ratio. On the other hand, the continuous addition of sodium silicate + sodium hydroxide enhances the supersaturation ratio. Having solid particles present in the system, secondary nucleation starts once its critical supersaturation has been reached. This happens with a 5 min lag at the highest flow rate and with 60 min lag at the lowest flow rate (Figure 62(b, d, f)). Simultaneous to nucleation events, particle growth also proceeds as soon as particles appear in the system. All these phenomena deplete supersaturation until primary nucleation, and later secondary nucleation cease. At still lower supersaturation, particle growth will also cease. The above kinetic pathway lies between the theoretical prediction made assuming no precipitation (aqEQBRM, blue curves) and that assuming system reaches thermodynamic equilibrium instantaneously (EQBRM, red curves; Figure 59, Figure 61).

When compared to experiments with lower flow rates, at higher inlet flow the system experiences greater supersaturation ratios over a larger fraction of period necessary to reach the end of precipitation (i.e., when  $G < 10^{-14} \text{ m.s}^{-1}$ ; Figure 63). This is observable from Figure 59 and Figure 61, Figure 62(a, c, e), and more clearly in Figure 63(a). In Figure 59 and Figure 61 the state of stronger supersaturation at higher flow rates is obvious from a larger departure from the red curves representing system behavior dictated by thermodynamic equilibrium. In Figure 62 (a-c) and also Figure 63(a) one can discern the state of stronger supersaturation at the highest flow rate quantitatively (using supersaturation ratio). Under this condition, there is enough amount of precursor in solution provided by the fast addition of reactant that supersaturation depletion is less when compared to slower precursor addition exhibiting almost complete drop in supersaturation upon nucleation events. The higher supersaturation in the former case also extend the period (relative to the overall precipitation duration) over which primary and secondary nucleation events are happening (Figure 63(c, d)). Another observation is upon reducing the inlet flow rate, the number of primary nuclei decreases by three orders of magnitude while the number of secondary nuclei remains the same order of magnitude (Figure 62 (d-f) and Figure 63(c, d)). This way, at lower flow rates secondary nucleation takes over, enhancing the number of crystallites (primary particles) per secondary particle, in a meaningful manner (Annexure) In this respect, for instance at the end of the precipitation process conducted at a flow rate of  $0.11 \text{ mL.min}^{-1}$ , polycrystalline (secondary) particles of C-S-H with

an average size of  $\sim 60$  nm (assuming spherical), composed of  $> 1500$  crystallites of  $\sim 5 \pm 0.4$  nm form. The primary and secondary particle size can be predicted from the PBE kinetic analysis and is presented in Annexure. Although, we have restricted ourselves to spherical spheres, which is not really representative of our precipitated nanofoils, but gives an indication of the power of this approach once we can include a more sophisticated form factor.

Consequently, it is obvious that as secondary nucleation dominates primary nucleation, the ordered network of crystallites composing the secondary particles extends further. Therefore, it appears that true secondary nucleation mechanism discussed here provides the answer to the open question posed by Pellenq and colleagues about the origin of mesoscale order in precipitated C-S-H<sup>237,249</sup>. Additionally it resolves the dilemma posed by Skinner and coworkers about why C-S-H nanograins, if they exist, do not grow larger<sup>250</sup>. To be more precise, energetically favorable secondary nucleation events consume significant amounts of building blocks (constituting ions), that otherwise could have got involved in molecular growth, so as to produce nanograins oriented in the vicinity of primary-nucleated particles. Moreover, due to lower surface energy, they (tapered foils, nanofoils) never ripens.

As discussed earlier in this section, under the operating conditions applied here, we get a very good fit to experimental data when the C-S-H growth is assumed to follow an integration-controlled regime. At higher flow rates, considering the fact that supersaturation is generally higher than that at lower inlet flows, the exponent of driving force in growth rate expression is slightly larger. It is also notable that all the exponents lie between 1 and 2 implying a combination of integration-controlled growth mechanisms operating during the precipitation process, possibly ranging from surface nucleation regimes to rough growth. The latter prevails once the number of favourable sites on the surface are so high that the rate of growth only depends on the difference between the flux of impinging building units and those leaving the surface, which turn out to be first-order in driving force  $(S - 1)^{236}$ .

Table 19: Optimized kinetic parameters

| Inlet flow rate<br>(mL.min <sup>-1</sup> ) | $\gamma$ (J.m <sup>-2</sup> )<br>Interfacial<br>tension | $\sigma$ (J.m <sup>-2</sup> )<br>Adhesion | $x_A$ | D<br>(m <sup>2</sup> .s <sup>-1</sup> )<br>Diffusion | $K_G$<br>Shape<br>Factor | g<br>Growth<br>coefficient | R <sup>2</sup> | Absolute<br>residual |
|--|---|---|-------|--|--------------------------|----------------------------|----------------|----------------------|
| 2.0  | 0.0665  | 0.0328                                    | 0.45  | $7.0 \times 10^{-10}$                                | $2.8 \times 10^{-9}$     | 1.65                       | 0.99<br>95     | $3.8 \times 10^{-5}$ |
| 0.5  | 0.0681  | 0.0456                                    | 0.47  | $5.9 \times 10^{-10}$                                | $4.3 \times 10^{-9}$     | 1.54                       | 0.99<br>95     | $3.7 \times 10^{-5}$ |
| 0.11                                       | 0.0686  | 0.0491                                    | 0.47  | $5.4 \times 10^{-10}$                                | $4.8 \times 10^{-9}$     | 1.50                       | 0.99<br>96     | $3.7 \times 10^{-5}$ |

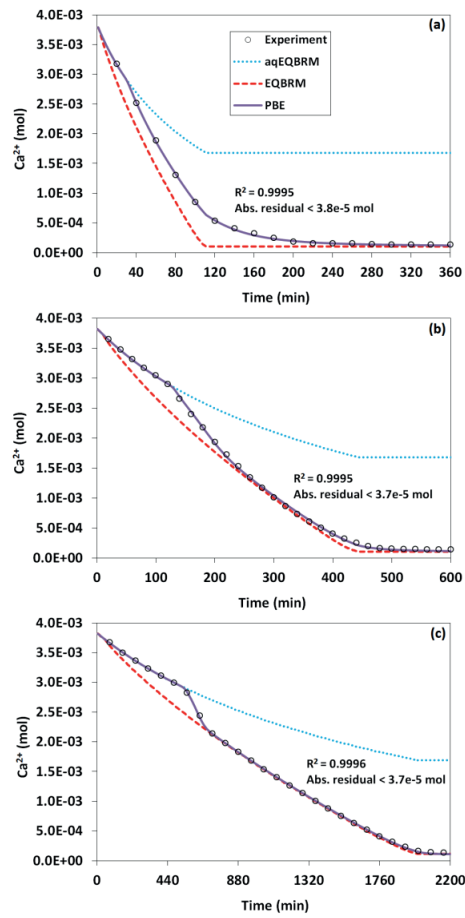


Figure 59: Experimental  $\text{Ca}^{2+}$  mole amounts (open circles) and predicted values (lines) based on aqEQBRM, EQBRM, and PBE modeling for 2 (a), 0.50 (b), and 0.11  $\text{mL}\cdot\text{min}^{-1}$  (c) inlet flow rates; legends are common for all graphs.

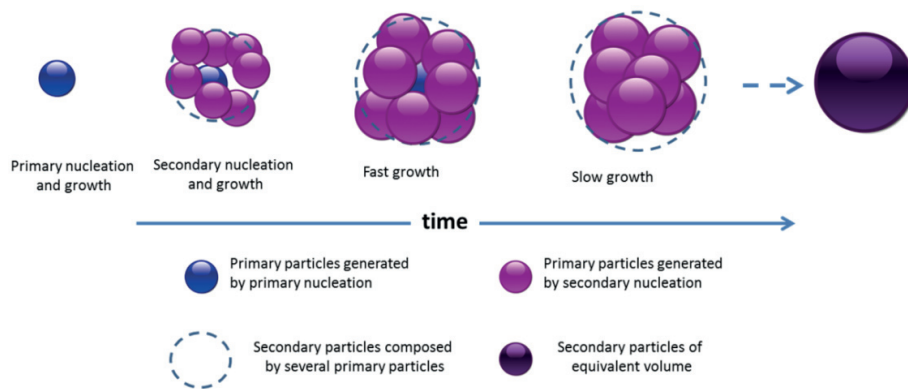


Figure 60: Simple schematic representation of possible pathways and type of associated particles

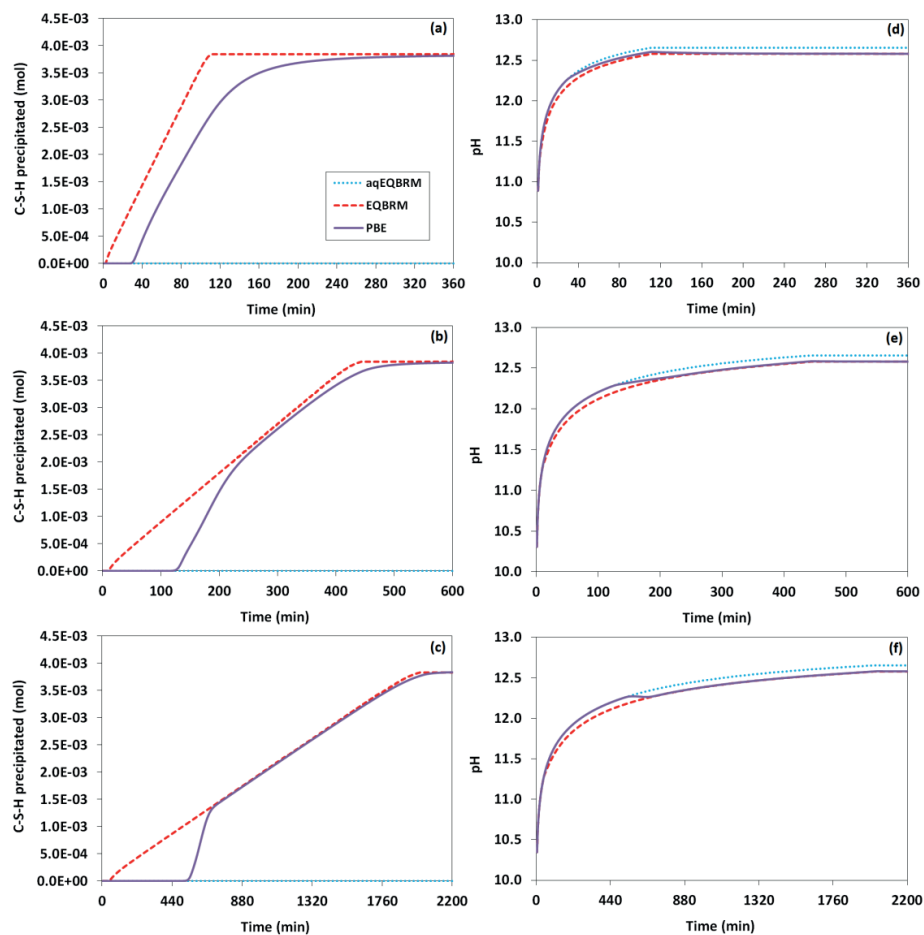


Figure 61: Amount of C-S-H precipitated from solution and the corresponding pH values for 2 (a, d), 0.50 (b, e), and 0.11 mL.min<sup>-1</sup> (c, f) inlet flow rates.

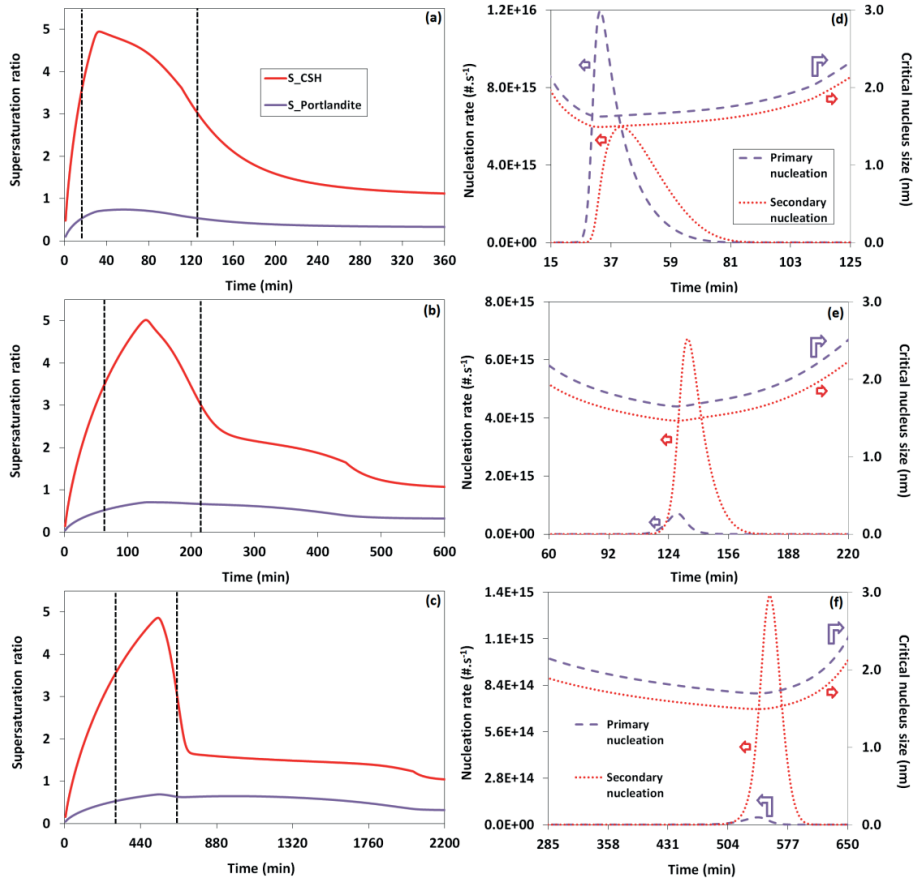


Figure 62: Temporal evolution of supersaturation with respect to C-S-H and portlandite, and the corresponding C-S-H nucleation events for 2 (a, d), 0.50 (b, e), and 0.11 mL.min<sup>-1</sup> (c, f) inlet flow rates; vertical dashed lines in supersaturation graphs indicate the period over which nucleation takes place as plotted in (d-f)

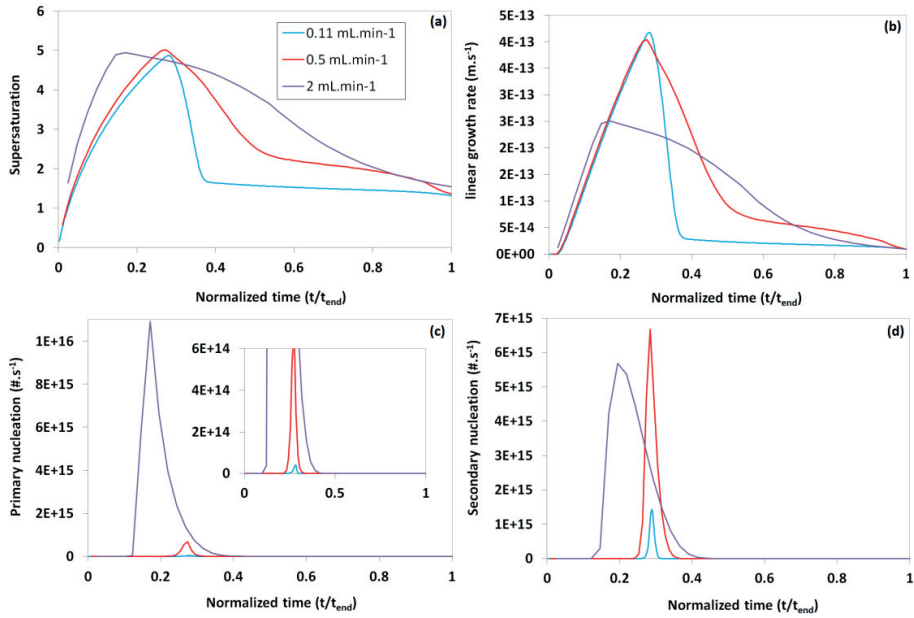


Figure 63: Overlaid plots of supersaturation with respect to C-S-H (a), linear growth rate (b), primary nucleation (c), and secondary nucleation (d) for different inlet flow rates as a function of time normalized with  $t_{\text{end}}$  (time at there is no more nucleation and  $G < 10^{-14} \text{ m} \cdot \text{s}^{-1}$ )



## Conclusion

In this article we introduce a simplified kinetic modelling of C-S-H based on population balance equations (PBEs) coupled with elemental mass balances. Kinetic data were collected over three different flow rates with three different datasets. This approach has never been attempted before. In the current work a spherical shape was assumed because of its simplicity for this first approach. Despite this assumption, compared to any prior modelling of C-S-H, the results are by far the best kinetic description of C-S-H precipitation path that agree with general experimental observations. By fitting the concentration profile, the supersaturation could be calculated and consequently the primary, secondary nucleation and growth rates. The PBE set is generally coupled to elemental mass balances via the supersaturation ratio, being the driving force envisaged for the elementary processes governing the overall particle formation. The solution to mass balance ODE set results in time evolution of elemental abundances in solution, which in turn can be inserted into a thermodynamic speciation code to calculate the absolute amount of different chemical species. The former information is necessary to calculate the supersaturation and close the modelling loop. The equations describing nucleation and molecular growth have particular parameters each representing a physical aspect of the underlying phenomenon. For this current work, atomistic scale simulations will be needed to better define the primary particle atomistic structure and surface terminations, to help better define the particle shape and terminating surface interfacial energies. Improvements in terms of considering non-spherical shapes shall introduce additional complication in PBE modelling, particularly if the particle cannot be described merely by one characteristic size, in which case additional internal coordinates might be necessary each describing a different dimension. For future line of research would involve more realistic shapes for C-S-H primary particles, possibly ellipsoids, disks, bricks, or platelets. This should then lead to better description of C-S-H at the meso scale as well as capturing the growth kinetics.

## Acknowledgement

We would like to thank Dr. Andreas Testino for useful discussion and guidance. Authors would like to thank Swiss national foundation for financing this project (Grants No. SNF\_153044)

## 9 Summary of thesis and Quo Vadis

“Calcium silicate hydrates” – the main phase of hydrated cementitious materials, acts as a glue to hold all aggregates together is synthesised and studied in this thesis. It exists in various compositions and morphologies at different local conditions in hydrated cementitious materials, all of which could be replicated in our in-house developed synthetic system. We showed the possibility to make homogeneous, uniform C-S-H phases with high Ca:Si ratio, without the presence of Calcium hydroxide (commonly occurring 2<sup>nd</sup> phase) under a controlled environment. This was never achieved in over 4 decades of prior synthetic work. Morphologies appearing in real Portland cement systems are observed by High-resolution SEM and TEM imaging in the synthetic system. A video of the 3D tomography of the nanofoils is presented in the next chapter as an appendix. Working with good mixing conditions, at high supersaturation and high pH ensure the abundance of single dominating Silicate species that condensate with Calcium in these conditions for the entire period of the precipitation reaction. Further with Raman micro-spots and STEM EDX analysis, we showed the uniformity of Ca:Si ratio in these precipitates at 1  $\mu$ m and 3nm respectively. It shows the formation of C-S-H proceeds via a single dominating reaction in the system. GEMS, thermodynamic modelling software, loaded with cemdata<sup>80</sup> showed good correspondence with our experimental conditions for Ca:Si  $\leq$  1.6 and for Ca:Si  $\geq$  1.6, once the formation of portlandite was prohibited. With regards to the synthetic system, further experiments can be made at lower supersaturation and introduction of insoluble solid surfaces to induce heterogeneous nucleation to approach conditions more representative of the hydration of Portland cement. Moreover, the inclusion of organic molecules and their effects can be also investigated in the same synthetic system.

In the spectroscopic Studies: the produced C-S-H powder with Ca:Si ratio from 1 to 2, were studied by DNP-NMR, 1D <sup>29</sup>Si, 2D <sup>29</sup>Si-<sup>29</sup>Si correlation and <sup>29</sup>Si-<sup>1</sup>H, along with DFT calculation and atomistic simulations, we elucidated a family of possible structures of pure phase C-S-H. We confirmed the reason of such a high Ca:Si ratio is due to the presence of Calcium in the interlayer in particular replacing the silica in the bridging site, which is a necessary condition to induce the strong hydrogen bonding to keep the structure intact. Possible disruption in these H-bonding can be the limiting factor for growth and stability of C-S-H. Combined with FTIR studies and Raman micro-spectroscopy, we showed that the C-S-H falls into one structural family going from Ca:Si ratio 1.25 to 2. Also, the same Gaussian model could fit the NMR data quite well, suggesting one base set of structures. In FTIR and Raman studies, we showed, specially for higher Ca:Si ratio  $\geq$  1.6, the systematic consistent shift of Si-O(Q<sup>2</sup>) asymmetric (U3) towards lower frequencies (decreasing polymerization) and prominent appearance of Q<sup>1</sup> tetrahedra with increasing Ca:Si ratio (i.e.) incorporation of Ca in the structure. We show the band peak at 1044 cm<sup>-1</sup>, that is designated to Si-O (Q<sup>2b</sup>) bridging tetrahedra, decreases in intensity with increasing Ca:Si ratio consistent with de-bridging of silicate tetrahedra. Although the position of these peaks was already speculated upon in prior literature, they had never been clearly identified. In all these spectroscopic studies, the synthesised C-S-H demonstrate close resemblance towards a defective tobermorite structure. Overall in a well understood and controlled synthetic system employed to study complex real

cementitious system allowed us to understand the formation and stability of the C-S-H family, hence improving our understanding for early hydration period or strength development. One can now think of formulating the SCM that can ensure the formation such H-bonding, the strength development of a material with low carbon footprint. Further investigation is needed to provide more constraints for structural refinement and for general understanding. <sup>43</sup> Ca NMR<sup>94</sup> could really help in a strong refinement in the structural model of C-S-H and narrow down to the family of plausible structures. It will also help in measuring the interlayer distance and should put an end to many unresolved debates.

In the kinetic studies: a challenging task, we used ion selection calcium electrode, pH electrode and conductivity electrode to monitor in-situ the reaction progress, built-into the synthetic system, with data periodically recorded on the computer. By controlling the rate of addition of silicate (flow rate by pumps) to the Calcium solution, we calculated the consumption of Calcium (by Calcium electrode) in precipitation reaction as a function of time, assuming the single dominating reaction with the formation of highly uniform C-S-H. Optimal operating conditions were calculated theoretically from GEMS. In a different set of experiments, a fixed volume is drawn periodically from reacting solutions, washed and vacuum filtered to calculate the yield and were also compared to GEMS. These kinetic data were used in a population balance modelling and an empirical correlation was developed for our synthetic C-S-H system. The empirical equation captures well the kinetic data and predicts both primary and secondary nucleation followed by growth. As a first simplistic approach we assumed a spherical type particle for secondary nucleation and growth. Further kinetic experiments at lower supersaturation can be performed and the developed empirical equation can be verified. At very low supersaturation, advance methods such as in-situ bio-electron microscopy can be adopted to see the evolution of morphology as shown by Sakalli & Trettin.<sup>63</sup> In-situ FTIR<sup>251</sup> and Raman<sup>252</sup> could be helpful to provide essential much needed kinetic data for developing a more reliable and general growth equation.

With all the experimental experience and literature survey the keys to the formation of pure phase C-S-H at high Ca:Si ratio has been possible and its growth mechanism proposed., This was achieved by working at high supersaturations ensuring an abundance of the same solution species at given pH condition with excellent mixing. This provides a high mobility and with no external solid or surface effect, the system continues to form the most stable solid phase possible in that condition (i.e.) C-S-H, where Ca(OH)<sub>2</sub> formation kinetically limited (very low supersaturation). Calcium showed unique characteristics to condensate the monomeric silicate species at high pH  $\geq 13$ , to form a nanofibers like morphology and is the most favoured solid to form at these chemical conditions. Whereas at pH  $\leq 11$ , it forms nanoglobules, ironically, silicates exist as polymeric units which are disintegrated by calcium. The phenomena are not observed by any other elements tested assumed to be due to the difference in ionic size and charge, albeit within 10% when compared to calcium. All other elements tested form nanoglobules of monomeric silicates at the high pH  $\geq 13$  condition, whereas their respective hydroxides if competing against the calcium in the same environment. Since most elements tested formed nano globular morphology in their hydroxide form, Zinc stands out at forming pyramidal hydroxides at high pH conditions. At lower pH condition  $\leq 11$ , these tested elements

tend to form nanofoils like morphology, structurally very different from the C-S-H nanofoils though, being incapable to destabilise the existing polymeric silicates in the solution but merely contributing to structures as a charge balancing entities. The effect of these doping elements in presence of calcium and without calcium showed the importance of calcium for the formation of C-S-H necessary for strength development in cementitious systems.

Overall, starting from the synthesis of standard material to characterization and modelling its growth, we covered the entire spectrum of understanding C-S-H formation. With the acquired knowledge during the thesis on precipitation methods, knowledge about synthetic and real cement system some interesting products of commercial interest have been developed, for example, to accelerate or retard early age strength during hydration. Three patents were consequently filed. It demonstrates that with a fundamental understanding of the C-S-H system developments applicable to real world applications can be made by a knowledge-based approach and not the empirical trial and error that has been predominant in cement technology development over the past 100 years. Combined with some other expertise and material concepts the launch of a spin-off is planned in the very near future.

## Reference:

1. Suhendro, B. Toward Green Concrete for Better Sustainable Environment. *Procedia Eng.* **95**, 305–320 (2014).
2. Benhelal, E., Zahedi, G., Shamsaei, E. & Bahadori, A. Global strategies and potentials to curb CO<sub>2</sub> emissions in cement industry. *J. Clean. Prod.* **51**, 142–161 (2013).
3. Ylmén, E. R. Early Hydration of Portland Cement - An Infrared Spectroscopy Perspective Complemented by Calorimetry and Scanning Electron Microscopy. (Department of Chemical and Biological Engineering, Chalmers university of technology, Gothenburg, Sweden, 2013).
4. Scrivener, K. L. & Nonat, A. Hydration of cementitious materials, present and future. *Cem. Concr. Res.* **41**, 651–665 (2011).
5. Schneider, M., Romer, M., Tschudin, M. & Bolio, H. Sustainable cement production—present and future. *Cem. Concr. Res.* **41**, 642–650 (2011).
6. Lothenbach, B. & Nonat, A. Calcium silicate hydrates: Solid and liquid phase composition. *Cem. Concr. Res.* doi:10.1016/j.cemconres.2015.03.019
7. Allen, A. J., Thomas, J. J. & Jennings, H. M. Composition and density of nanoscale calcium-silicate-hydrate in cement. *Nat Mater* **6**, 311–316 (2007).
8. Richardson, I. G. The calcium silicate hydrates. *Cem. Concr. Res.* **38**, 137–158 (2008).
9. Allen, A. J. & Thomas, J. J. Analysis of C–S–H gel and cement paste by small-angle neutron scattering. *Cem. Concr. Res.* **37**, 319–324 (2007).
10. Renaudin, G., Russias, J., Leroux, F., Cau-dit-Coumes, C. & Frizon, F. Structural characterization of C–S–H and C–A–S–H samples—Part II: Local environment investigated by spectroscopic analyses. *J. Solid State Chem.* **182**, 3320–3329 (2009).
11. Brown, P. W., Franz, E., Frohnsdorff, G. & Taylor, H. F. W. Analyses of the aqueous phase during early C3S hydration. *Cem. Concr. Res.* **14**, 257–262 (1984).
12. Picker, A. Influence of Polymers on Nucleation and Assembly of Calcium Silicate Hydrates. *Einfluss von Polymeren auf die Nukleation und Aggregation von Calciumsilikathydraten* (2013).
13. Chen, C., Habert, G., Bouzidi, Y. & Jullien, A. Environmental impact of cement production: detail of the different processes and cement plant variability evaluation. *J. Clean. Prod.* **18**, 478–485 (2010).
14. Huntzinger, D. N. & Eatmon, T. D. A life-cycle assessment of Portland cement manufacturing: comparing the traditional process with alternative technologies. *J. Clean. Prod.* **17**, 668–675 (2009).
15. Josa, A., Aguado, A., Cardim, A. & Byars, E. Comparative analysis of the life cycle impact assessment of available cement inventories in the EU. *Cem. Concr. Res.* **37**, 781–788 (2007).
16. woods, H., Steinour, H. H. & Starke, H. R. Effect of Composition of Portland Cement on Heat Evolved during hardening. *Ind. Eng. Chem.* **24**, 1207–1214 (1932).
17. Mehta, P. & Monteiro, P. J. M. *Concrete: Microstructure, Properties, and Materials*. (McGraw-Hill Education, 2006).
18. Sowoidnich, T. A Study of Retarding Effects on Cement and Tricalcium Silicate Hydration induced by Superplasticizers. (2015).
19. Bullard, J. W. *et al.* Mechanisms of cement hydration. *Conf. Spec. Cem. Hydration Kinet. Model. Quebec City 2009 CONMOD10 Lausanne 2010* **41**, 1208–1223 (2011).
20. Morin, V., Garrault, S., Begarin, F. & Dubois-Brugger, I. The influence of an ion-exchange resin on the kinetics of hydration of tricalcium silicate. *Cem. Concr. Res.* **40**, 1459–1464 (2010).
21. Bellmann, F., Damidot, D., Möser, B. & Skibsted, J. Improved evidence for the existence of an intermediate phase during hydration of tricalcium silicate. *Cem. Concr. Res.* **40**, 875–884 (2010).
22. Gartner, E. M. & Jennings, H. M. Thermodynamics of Calcium Silicate Hydrates and Their Solutions. *J. Am. Ceram. Soc.* **70**, 743–749 (1987).
23. Jennings, H. M. & Pratt, P. L. An experimental argument for the existence of a protective membrane surrounding portland cement during the induction period. *Cem. Concr. Res.* **9**, 501–506 (1979).
24. Kantro, D. L., Brunauer, S. & Weise, C. H. Development of surface in the hydration of Calcium Silicates II. Extension of investigation to earlier and later stages of hydration. *J. Phys. Chem.* **66**, 1804–1809 (1962).
25. Cordes, S. & Odler, I. Initial hydration of tricalcium silicate as studied by secondary neutrals mass spectrometry: I. Sample preparation and calibration. *Cem. Concr. Res.* **32**, 1071–1075 (2002).
26. Stein, H. N. & Stevels, J. M. Influence of silica on the hydration of 3 CaO,SiO<sub>2</sub>. *J. Appl. Chem.* **14**, 338–346 (1964).
27. Barret, P. & Bertrandie, D. Saturated Solutions of Anhydrous Phases in the System Lime-Silica-Water: Example of  $\beta$ -C<sub>2</sub>S. *J. Am. Ceram. Soc.* **73**, 3486–3492 (1990).

28. Barret, P. & Ménétrier, D. Filter dissolution of C3S as a function of the lime concentration in a limited amount of lime water. *Cem. Concr. Res.* **10**, 521–534 (1980).
29. Juilland, P., Gallucci, E., Flatt, R. & Scrivener, K. Dissolution theory applied to the induction period in alite hydration. *Cem. Concr. Res.* **40**, 831–844 (2010).
30. Barnes, P. & Bensted, J. *Structure and Performance of Cements, Second Edition*. (CRC Press, 2002).
31. Fierens, P. & Verhaegen, J. P. Hydration of tricalcium silicate in paste — Kinetics of calcium ions dissolution in the aqueous phase. *Cem. Concr. Res.* **6**, 337–342 (1976).
32. Fierens, P. & Verhaegen, J. P. Induction period of hydration of tricalcium silicate. *Cem. Concr. Res.* **6**, 287–292 (1976).
33. Begarin, F., Garrault, S., Nonat, A. & Nicoleau, L. Hydration of alite containing aluminium. *Adv. Appl. Ceram.* **110**, 127–130 (2011).
34. Jennings, H. M. Aqueous Solubility Relationships for Two Types of Calcium Silicate Hydrate. *J. Am. Ceram. Soc.* **69**, 614–618 (1986).
35. Garrault, S. & Nonat, A. Hydrated Layer Formation on Tricalcium and Dicalcium Silicate Surfaces: Experimental Study and Numerical Simulations. *Langmuir* **17**, 8131–8138 (2001).
36. Garrault-Gauffinet, S. & Nonat, A. Experimental investigation of calcium silicate hydrate (C-S-H) nucleation. *J. Cryst. Growth* **200**, 565–574 (1999).
37. Garrault, S., Finot, E., Lesniewska, E. & Nonat, A. Study of C-S-H growth on C3S surface during its early hydration. *Mater. Struct.* **38**, 435–442 (2005).
38. Tadros, M. E., Skalny, J. & Kalyoncu, R. S. Early Hydration of Tricalcium Silicate. *J. Am. Ceram. Soc.* **59**, 344–347 (1976).
39. Young, J. F., Tong, H. S. & Berger, R. L. Compositions of Solutions in Contact with Hydrating Tricalcium Silicate Pastes. *J. Am. Ceram. Soc.* **60**, 193–198 (1977).
40. Gastaldi, D., Canonico, F. & Boccaleri, E. Ettringite and calcium sulfoaluminate cement: investigation of water content by near-infrared spectroscopy. *J. Mater. Sci.* **44**, 5788–5794 (2009).
41. Mindess, S., Young, J. F. & Darwin, D. *Concrete*. (Pearson, 2002).
42. Richardson, I. G. & Groves, G. W. Microstructure and microanalysis of hardened cement pastes involving ground granulated blast-furnace slag. *J. Mater. Sci.* **27**, 6204–6212 (1992).
43. Grudemo, A. Variation with solid-phase concentration of composition, structure and strength of cement pastes at high age. *Cem. Concr. Res.* **14**, 123–132 (1984).
44. Mohan, K. & Taylor, H. F. W. A trimethylsilylation study of tricalcium silicate pastes. *Cem. Concr. Res.* **12**, 25–31 (1982).
45. Brunet, F., Bertani, P., Charpentier, T., Nonat, A. & Virlet, J. Application of <sup>29</sup>Si Homonuclear and <sup>1</sup>H–<sup>29</sup>Si Heteronuclear NMR Correlation to Structural Studies of Calcium Silicate Hydrates. *J. Phys. Chem. B* **108**, 15494–15502 (2004).
46. Skibsted, J. & Hall, C. Characterization of cement minerals, cements and their reaction products at the atomic and nano scale. *Cem. Concr. Res.* **38**, 205–225 (2008).
47. Klur, I. *et al.* NMR Cross-Polarization when TIS>T1ρ; Examples from Silica Gel and Calcium Silicate Hydrates. *J. Phys. Chem. B* **104**, 10162–10167 (2000).
48. Pustovgar, E. *et al.* Understanding silicate hydration from quantitative analyses of hydrating tricalcium silicates. *Nat. Commun.* **7**, 10952 (2016).
49. Angstadt, R. L. & Hurley, F. R. Hydration of the Alite Phase in Portland Cement. *Nature* **197**, 688–688 (1963).
50. Richardson, I. G. Tobermorite/jennite- and tobermorite/calcium hydroxide-based models for the structure of C-S-H: applicability to hardened pastes of tricalcium silicate, β-dicalcium silicate, Portland cement, and blends of Portland cement with blast-furnace slag, metakaolin, or silica fume. *Cem. Concr. Res.* **34**, 1733–1777 (2004).
51. Bonaccorsi, E., Merlino, S. & Kampf, A. R. The Crystal Structure of Tobermorite 14 Å (Plombierite), a C–S–H Phase. *J. Am. Ceram. Soc.* **88**, 505–512 (2005).
52. Garbev, K. *et al.* Structural Features of C?S?H(I) and Its Carbonation in Air?A Raman Spectroscopic Study. Part I: Fresh Phases. *J. Am. Ceram. Soc.* **90**, 900–907 (2007).
53. Nonat, A. The structure and stoichiometry of C-S-H. *Cem. Concr. Res.* **34**, 1521–1528 (2004).
54. Cong, X. & Kirkpatrick, R. J. <sup>29</sup>Si MAS NMR study of the structure of calcium silicate hydrate. *Adv. Cem. Based Mater.* **3**, 144–156 (1996).
55. Grutzeck, M. W. A new model for the formation of calcium silicate hydrate (C-S-H). *Mater. Res. Innov.* **3**, 160–170 (1999).
56. Taylor, H. F. w. Proposed Structure for Calcium Silicate Hydrate Gel. *J. Am. Ceram. Soc.* **69**, 464–467 (1986).
57. Feldman, R. F. & Sereda, P. J. A new mode for hydrated Portland cement and its practical implications. *Eng. J. Can.* (1970).



58. Gartner, E. M., Kurtis, K. E. & Monteiro, P. J. M. Proposed mechanism of C-S-H growth tested by soft X-ray microscopy. *Cem. Concr. Res.* **30**, 817–822 (2000).
59. Gartner, E. M. A proposed mechanism for the growth of C S H during the hydration of tricalcium silicate. *Cem. Concr. Res.* **27**, 665–672 (1997).
60. Diamond, S. The microstructure of cement paste and concrete—a visual primer. *Cem. Concr. Compos.* **26**, 919–933 (2004).
61. Gallucci, E., Mathur, P. & Scrivener, K. Microstructural development of early age hydration shells around cement grains. *Cem. Concr. Res.* **40**, 4–13 (2010).
62. Scrivener, K. L. Backscattered electron imaging of cementitious microstructures: understanding and quantification. *Cem. Concr. Compos.* **26**, 935–945 (2004).
63. Sakalli, Y. & Trettin, R. Investigation of C3S hydration by environmental scanning electron microscope. *J. Microsc.* **259**, 53–58 (2015).
64. Pauling, L. THE PRINCIPLES DETERMINING THE STRUCTURE OF COMPLEX IONIC CRYSTALS. *J. Am. Chem. Soc.* **51**, 1010–1026 (1929).
65. Pauling, L. The nature of silicon-oxygen bonds. *Am Miner.* **65**, 321–323 (1980).
66. Burdett, J. K. Perspectives in structural chemistry. *Chem. Rev.* **88**, 3–30 (1988).
67. Brinker, C. J. & Scherer, G. W. *Sol-gel Science: The Physics and Chemistry of Sol-gel Processing*. (Gulf Professional Publishing, 1990).
68. Chrysafi, R., Perraki, T. & Kakali, G. Sol–gel preparation of 2CaO·SiO<sub>2</sub>. *J. Eur. Ceram. Soc.* **27**, 1707–1710 (2007).
69. Meiszterics, A. & Sinkó, K. Sol–gel derived calcium silicate ceramics. *Colloids Surf. Physicochem. Eng. Asp.* **319**, 143–148 (2008).
70. Iller, R. *The Chemistry of Silica: Solubility, Polymerization, Colloid and Surface Properties and Biochemistry of Silica*. (1979).
71. Cölfen, H. & Antonietti, M. Physico-Chemical Principles of Crystallization. in *Mesocrystals and Nonclassical Crystallization* 7–50 (John Wiley & Sons, Ltd, 2008).
72. J. A. DIRKSEN and T. A. RING+. Fundamental of crystallization: Kinetic effects on particle size distributions and morphology. (1991).
73. Mullin, J. W. *Crystallization*. (Butterworth-Heinemann, 2001).
74. Söhnel, O. & Garside, J. *Precipitation: Basic Principles and Industrial Applications*. (Butterworth-Heinemann, 1992).
75. Nielsen, A. E. *Kinetics of Precipitation*. (Pergamon Press; [distributed in the Western Hemisphere by Macmillan, New York], 1964).
76. Walton, A. G. *The Formation and Properties of Precipitates*. (Interscience Publishers, 1976).
77. Haruta, M. & Delmon, B. Preparation of homodisperse solids. *J. Chim. Phys.* **83**, 859–868 (1986).
78. Helmut Cölfen, Markus Antonietti. Mesocrystals and Nonclassical Crystallization.
79. Hulburt, H. M. & Katz, S. Some problems in particle technology. *Chem. Eng. Sci.* **19**, 555–574 (1964).
80. Kulik, D. A. *et al.* GEM-Selektor geochemical modeling package: revised algorithm and GEMS3K numerical kernel for coupled simulation codes. *Comput. Geosci.* **17**, 1–24 (2012).
81. Kulik, D. A. Improving the structural consistency of C-S-H solid solution thermodynamic models. *Cem. Concr. Res.* **41**, 477–495 (2011).
82. Scrivener, K., Snellings, R. & Lothenbach, B. *A Practical Guide to Microstructural Analysis of Cementitious Materials*. (CRC Press, 2016).
83. Chen, J. J., Thomas, J. J., Taylor, H. F. W. & Jennings, H. M. Solubility and structure of calcium silicate hydrate. *Cem. Concr. Res.* **34**, 1499–1519 (2004).
84. Renaudin, G., Russias, J., Leroux, F., Frizon, F. & Cau-dit-Coumes, C. Structural characterization of C–S–H and C–A–S–H samples—Part I: Long-range order investigated by Rietveld analyses. *J. Solid State Chem.* **182**, 3312–3319 (2009).
85. L'Hôpital, E., Lothenbach, B., Kulik, D. A. & Scrivener, K. Influence of calcium to silica ratio on aluminium uptake in calcium silicate hydrate. *Cem. Concr. Res.* **85**, 111–121 (2016).
86. Richardson, I. G. & Groves, G. W. Microstructure and microanalysis of hardened ordinary Portland cement pastes. *J. Mater. Sci.* **28**, 265–277 (1993).
87. Rossen, J. E. Composition and morphology of C-A-S-H in pastes of alite and cement blended with supplementary cementitious materials. (2014). doi:10.5075/epfl-thesis-6294, urn:nbn:ch:bel-epfl-thesis6294-0
88. Cong, X. & Kirkpatrick, R. J. 17O MAS NMR Investigation of the Structure of Calcium Silicate Hydrate Gel. *J. Am. Ceram. Soc.* **79**, 1585–1592 (1996).
89. Beaudoin, J. J., Raki, L. & Alizadeh, R. A 29Si MAS NMR study of modified C–S–H nanostructures. *Cem. Concr. Compos.* **31**, 585–590 (2009).

90. Bortolotti, V., Brizi, L., Brown, R. J. S., Fantazzini, P. & Mariani, M. Nano and Sub-nano Multiscale Porosity Formation and Other Features Revealed by  $^1\text{H}$  NMR Relaxometry during Cement Hydration. *Langmuir* **30**, 10871–10877 (2014).
91. Brunet, F., Bertani, P., Charpentier, T., Nonat, A. & Virlet, J. Application of  $^{29}\text{Si}$  Homonuclear and  $^1\text{H}$ – $^{29}\text{Si}$  Heteronuclear NMR Correlation to Structural Studies of Calcium Silicate Hydrates. *J Phys Chem B* **108**, 15494–15502 (2004).
92. Brough, A. R., Dobson, C. M., Richardson, I. G. & Groves, G. W. In situ solid-state NMR studies of  $\text{Ca}_3$ . *J. Mater. Sci.* **29**, 3926–3940
93. Muller, A. C. A., Scrivener, K. L., Gajewicz, A. M. & McDonald, P. J. Densification of C–S–H Measured by  $^1\text{H}$  NMR Relaxometry. *J. Phys. Chem. C* **117**, 403–412 (2013).
94. Sangodkar, R. P. *et al.* Influences of Dilute Organic Adsorbates on the Hydration of Low-Surface-Area Silicates. *J. Am. Chem. Soc.* **137**, 8096–8112 (2015).
95. Alizadeh, R., Raki, L., Makar, J. M., Beaudoin, J. J. & Moudrakovski, I. Hydration of tricalcium silicate in the presence of synthetic calcium-silicate-hydrate. *J. Mater. Chem.* **19**, 7937–7946 (2009).
96. García-Lodeiro, I., Fernández-Jiménez, A., Blanco, M. T. & Palomo, A. FTIR study of the sol–gel synthesis of cementitious gels: C–S–H and N–A–S–H. *J. Sol-Gel Sci. Technol.* **45**, 63–72 (2007).
97. García Lodeiro, I., Macphee, D. E., Palomo, A. & Fernández-Jiménez, A. Effect of alkalis on fresh C–S–H gels. FTIR analysis. *Cem. Concr. Res.* **39**, 147–153 (2009).
98. Yu, P., Kirkpatrick, R. J., Poe, B., McMillan, P. F. & Cong, X. Structure of Calcium Silicate Hydrate (C–S–H): Near-, Mid-, and Far-Infrared Spectroscopy. *J. Am. Ceram. Soc.* **82**, 742–748 (1999).
99. Kirkpatrick, R. J., Yarger, J. L., McMillan, P. F., Ping, Y. & Cong, X. Raman spectroscopy of C–S–H, tobermorite, and jennite. *Adv. Cem. Based Mater.* **5**, 93–99 (1997).
100. Richardson, I. G., Skibsted, J., Black, L. & Kirkpatrick, R. J. Characterisation of cement hydrate phases by TEM, NMR and Raman spectroscopy. *Adv. Cem. Res.* **22**, 233–248 (2010).
101. Wu, J., Zhu, Y.-J. & Chen, F. Ultrathin Calcium Silicate Hydrate Nanosheets with Large Specific Surface Areas: Synthesis, Crystallization, Layered Self-Assembly and Applications as Excellent Adsorbents for Drug, Protein, and Metal Ions. *Small* **9**, 2911–2925 (2013).
102. Richardson, I. G. The nature of C–S–H in hardened cements. *Cem. Concr. Res.* **29**, 1131–1147 (1999).
103. Richardson, I. G. Model structures for C–(A)–S–H(I). *Acta Crystallogr. Sect. B Struct. Sci. Cryst. Eng. Mater.* **70**, 903–923 (2014).
104. Ping Yu. Structure of Calcium Silicate Hydrate (C–S–H): Near-, Mid-, and Far-Infrared Spectroscopy. *J Am Ceram Soc* **82** 3 742–48 1999
105. García Lodeiro, I., Fernández-Jimenez, A., Palomo, A. & Macphee, D. E. Effect on fresh C–S–H gels of the simultaneous addition of alkali and aluminium. *Cem. Concr. Res.* **40**, 27–32 (2010).
106. García-Lodeiro, I., Fernández-Jiménez, A., Blanco, M. T. & Palomo, A. FTIR study of the sol–gel synthesis of cementitious gels: C–S–H and N–A–S–H. *J. Sol-Gel Sci. Technol.* **45**, 63–72 (2007).
107. Kumar, A. *et al.* The Atomic-Level Structure of Cementitious Calcium Silicate Hydrate. *J. Phys. Chem. C* (2017). doi:10.1021/acs.jpcc.7b02439
108. Nonat, A. & Lecoq, X. The Structure, Stoichiometry and Properties of C–S–H Prepared by C3S Hydration Under Controlled Condition. in *Nuclear Magnetic Resonance Spectroscopy of Cement-Based Materials* (eds. Colombet, P., Zanni, H., Grimmer, A.-R. & Sozzani, P.) 197–207 (Springer Berlin Heidelberg, 1998). doi:10.1007/978-3-642-80432-8\_14
109. Taylor, H. F. W. *et al.* The hydration of tricalcium silicate. *Matér. Constr.* **17**, 457–468 (1984).
110. Fujii, K. & Kondo, W. Communications of the American Ceramic Society Estimation of Thermochemical Data for Calcium Silicate Hydrate (C–S–H). *J. Am. Ceram. Soc.* **66**, C-220 (1983).
111. Stade, W. Zum Aufbau schlecht geordneter Calciumhydrogensilicate. I. Bildung und Eigenschaften einer schlecht geordneten Calciumhydrogendisilicaphase - Stade - 2004 - Zeitschrift für anorganische und allgemeine Chemie - Wiley Online Library. Available at: <http://onlinelibrary.wiley.com/doi/10.1002/zaac.19804660107/pdf>. (Accessed: 10th August 2015)
112. Ntalias, E. & Koutsoukos, P. G. Spontaneous precipitation of calcium silicate hydrate in aqueous solutions. *Cryst. Res. Technol.* **45**, 39–47 (2010).
113. Lothenbach, B., Nied, D., L'Hôpital, E., Achiedo, G. & Dauzères, A. Magnesium and calcium silicate hydrates. *Cem. Concr. Res.* **77**, 60–68 (2015).
114. Jennings, H. M. Aqueous Solubility Relationships for Two Types of Calcium Silicate Hydrate. *J. Am. Ceram. Soc.* **69**, 614–618 (1986).
115. Gartner, E. M. & Jennings, H. M. Thermodynamics of Calcium Silicate Hydrates and Their Solutions. *J. Am. Ceram. Soc.* **70**, 743–749 (1987).
116. Kulik, D. A. *et al.* GEM-Selektor geochemical modeling package: revised algorithm and GEMS3K numerical kernel for coupled simulation codes. *Comput. Geosci.* **17**, 1–24 (2013).

117. Wagner, T., Kulik, D. A., Hingerl, F. F. & Dmytrieva, S. V. GEM-SELEKTOR GEOCHEMICAL MODELING PACKAGE: TSolMod LIBRARY AND DATA INTERFACE FOR MULTICOMPONENT PHASE MODELS. *Can. Mineral.* **50**, 1173–1195 (2012).
118. Matschei, T., Lothenbach, B. & Glasser, F. P. Thermodynamic properties of Portland cement hydrates in the system  $\text{CaO}-\text{Al}_2\text{O}_3-\text{SiO}_2-\text{CaSO}_4-\text{CaCO}_3-\text{H}_2\text{O}$ . *Cem. Concr. Res.* **37**, 1379–1410 (2007).
119. Dilnesa, B. Z., Lothenbach, B., Renaudin, G., Wichser, A. & Kulik, D. Synthesis and characterization of hydrogarnet  $\text{Ca}_3(\text{Al}_x\text{Fe}_{1-x})_2(\text{SiO}_4)_y(\text{OH})_4(3-y)$ . *Cem. Concr. Res.* **59**, 96–111 (2014).
120. Yousuf, M. *et al.* Chemical and physical effects of sodium lignosulfonate superplasticizer on the hydration of portland cement and solidification/stabilization consequences. *Cem. Concr. Res.* **25**, 671–682 (1995).
121. García Lodeiro, I., Macphee, D. E., Palomo, A. & Fernández-Jiménez, A. Effect of alkalis on fresh C–S–H gels. FTIR analysis. *Cem. Concr. Res.* **39**, 147–153 (2009).
122. Ethanol. *Senseair* Available at: <http://www.senseair.com/senseair/gases-applications/ethanol/>. (Accessed: 29th July 2015)
123. IR-frequencies. Available at: <http://www2.ups.edu/faculty/hanson/Spectroscopy/IR/IRfrequencies.html>. (Accessed: 29th July 2015)
124. IR Absorption Table. Available at: <http://www.chem.ucla.edu/~webspectra/irtable.html>. (Accessed: 29th July 2015)
125. Govindarajan, D. & Gopalakrishnan, R. Spectroscopic Studies on Indian Portland Cement Hydrated with Distilled Water and Sea Water. *Front. Sci.* **1**, 21–27 (2012).
126. Ylmén, R., Jäglid, U., Steenari, B.-M. & Panas, I. Early hydration and setting of Portland cement monitored by IR, SEM and Vicat techniques. *Cem. Concr. Res.* **39**, 433–439 (2009).
127. Galmarini, S. & Bowen, P. Atomistic simulation of the adsorption of calcium and hydroxyl ions onto portlandite surfaces — towards crystal growth mechanisms. *Cem. Concr. Res.* **81**, 16–23 (2016).
128. Macphee, D. E., Luke, K., Glasser, F. P. & Lachowski, E. E. Solubility and Aging of Calcium Silicate Hydrates in Alkaline Solutions at 25°C. *J. Am. Ceram. Soc.* **72**, 646–654 (1989).
129. Wu, Y. Theoretical study of the local structure and Raman spectra of  $\text{CaO}-\text{SiO}_2$  binary melts. Available at: <http://scitation.aip.org/content/aip/journal/jcp/121/16/10.1063/1.1800971>. (Accessed: 10th August 2015)
130. McMillian, P. Raman spectroscopic studies of silicate and related glass structure—a review. Available at: [http://www.researchgate.net/profile/Paul\\_Mcmillan4/publication/260423813\\_Raman\\_spectroscopic\\_studies\\_of\\_silicate\\_and\\_related\\_glass\\_structure-a\\_review/links/0a85e531304ad6a699000000.pdf](http://www.researchgate.net/profile/Paul_Mcmillan4/publication/260423813_Raman_spectroscopic_studies_of_silicate_and_related_glass_structure-a_review/links/0a85e531304ad6a699000000.pdf). (Accessed: 10th August 2015)
131. Garbev, K., Beuchle, G., Bornefeld, M., Black, L. & Stemmermann, P. Cell Dimensions and Composition of Nanocrystalline Calcium Silicate Hydrate Solid Solutions. Part 1: Synchrotron-Based X-Ray Diffraction. *J. Am. Ceram. Soc.* **91**, 3005–3014 (2008).
132. Garbev, K., Bornefeld, M., Beuchle, G. & Stemmermann, P. Cell Dimensions and Composition of Nanocrystalline Calcium Silicate Hydrate Solid Solutions. Part 2: X-Ray and Thermogravimetry Study. *J. Am. Ceram. Soc.* **91**, 3015–3023 (2008).
133. Testino, A. *et al.* Kinetics and Mechanism of Aqueous Chemical Synthesis of  $\text{BaTiO}_3$  Particles. *Chem. Mater.* **16**, 1536–1543 (2004).
134. Haas, J. & Nonat, A. From C–S–H to C–A–S–H: Experimental study and thermodynamic modelling. *Cem. Concr. Res.* **68**, 124–138 (2015).
135. Leal, A. M. M., Kulik, D. A. & Saar, M. O. Enabling Gibbs energy minimization algorithms to use equilibrium constants of reactions in multiphase equilibrium calculations. *Chem. Geol.* **437**, 170–181 (2016).
136. Leal, A. M. M., Kulik, D. A., Smith, W. R. & Saar, M. O. An overview of computational methods for chemical equilibrium and kinetic calculations for geochemical and reactive transport modeling. *Pure Appl. Chem.* **89**, 597–643 (2017).
137. Lothenbach, B. & Nonat, A. Calcium silicate hydrates: Solid and liquid phase composition. *Cem. Concr. Res.* **78**, Part A, 57–70 (2015).
138. Richardson, I. G. Model structures for C-(A)-S-H(I). *Acta Crystallogr. Sect. B Struct. Sci. Cryst. Eng. Mater.* **70**, 903–923 (2014).
139. Prati, C. & Gandolfi, M. G. Calcium silicate bioactive cements: Biological perspectives and clinical applications. *Dent. Mater.* **31**, 351–370 (2015).
140. Ho, C.-C., Wei, C.-K., Lin, S.-Y. & Ding, S.-J. Calcium silicate cements prepared by hydrothermal synthesis for bone repair. *Ceram. Int.* **42**, 9183–9189 (2016).
141. Okano, K. *et al.* Amorphous calcium silicate hydrates and their possible mechanism for recovering phosphate from wastewater. *Sep. Purif. Technol.* **144**, 63–69 (2015).
142. Zhao, J. *et al.* Chitosan-coated mesoporous microspheres of calcium silicate hydrate: Environmentally friendly synthesis and application as a highly efficient adsorbent for heavy metal ions. *J. Colloid Interface Sci.* **418**, 208–215 (2014).

143. Dezerald, L. *et al.* Cement As a Waste Form for Nuclear Fission Products: The Case of  $^{90}\text{Sr}$  and Its Daughters. *Environ. Sci. Technol.* **49**, 13676–13683 (2015).
144. Taylor, H. F. W. *Cement Chemistry*. (Thomas Telford, 1997).
145. Scrivener, K. L. & Nonat, A. Hydration of cementitious materials, present and future. *Cem. Concr. Res.* **41**, 651–665 (2011).
146. Richardson, I. G. & Groves, G. W. Microstructure and microanalysis of hardened ordinary Portland cement pastes. *J. Mater. Sci.* **28**, 265–277 (1993).
147. Chen, J. J., Sorelli, L., Vandamme, M., Ulm, F.-J. & Chanvillard, G. A Coupled Nanoindentation/SEM-EDS Study on Low Water/Cement Ratio Portland Cement Paste: Evidence for C–S–H/ $\text{Ca}(\text{OH})_2$  Nanocomposites. *J. Am. Ceram. Soc.* **93**, 1484–1493 (2010).
148. Grangeon, S., Claret, F., Linard, Y. & Chiaberge, C. X-ray diffraction: a powerful tool to probe and understand the structure of nanocrystalline calcium silicate hydrates. *Acta Crystallogr. Sect. B Struct. Sci. Cryst. Eng. Mater.* **69**, 465–473 (2013).
149. Walker, C. S., Sutou, S., Oda, C., Mihara, M. & Honda, A. Calcium silicate hydrate (C–S–H) gel solubility data and a discrete solid phase model at 25 °C based on two binary non-ideal solid solutions. *Cem. Concr. Res.* **79**, 1–30 (2016).
150. Grangeon, S. *et al.* Quantitative X-ray pair distribution function analysis of nanocrystalline calcium silicate hydrates: a contribution to the understanding of cement chemistry. *J. Appl. Crystallogr.* **50**, 14–21 (2017).
151. Hirljac, J., Wu, Z.-Q. & Young, J. F. Silicate polymerization during the hydration of alite. *Cem. Concr. Res.* **13**, 877–886 (1983).
152. Nicoleau, L. & Bertolim, M. A. Analytical Model for the Alite (C3S) Dissolution Topography. *J. Am. Ceram. Soc.* **99**, 773–786 (2016).
153. Brown, P. W., Pommersheim, J. & Frohnsdorff, G. A kinetic model for the hydration of tricalcium silicate. *Cem. Concr. Res.* **15**, 35–41 (1985).
154. Hall, D. A. *et al.* Polarization-enhanced NMR spectroscopy of biomolecules in frozen solution. *Science* **276**, 930–932 (1997).
155. Maly, T. *et al.* Dynamic nuclear polarization at high magnetic fields. *J. Chem. Phys.* **128**, 52211 (2008).
156. Ni, Q. Z. *et al.* High frequency dynamic nuclear polarization. *Acc. Chem. Res.* **46**, 1933–1941 (2013).
157. Lothenbach, B. & Winnefeld, F. Thermodynamic modelling of the hydration of Portland cement. *Cem. Concr. Res.* **36**, 209–226 (2006).
158. Rosay, M. *et al.* Solid-state dynamic nuclear polarization at 263 GHz: spectrometer design and experimental results. *Phys Chem Chem Phys* **12**, 5850–5860 (2010).
159. Galmarini, S., Kunhi Mohamed, A. & Bowen, P. Atomistic Simulations of Silicate Species Interaction with Portlandite Surfaces. *J. Phys. Chem. C* **120**, 22407–22413 (2016).
160. Todorov, I. T., Smith, W., Trachenko, K. & Dove, M. T. DL\_POLY\_3: new dimensions in molecular dynamics simulations via massive parallelism. *J. Mater. Chem.* **16**, 1911–1918 (2006).
161. Perdew, J. P., Burke, K. & Ernzerhof, M. Generalized Gradient Approximation Made Simple. *Phys. Rev. Lett.* **77**, 3865–3868 (1996).
162. Giannozzi, P. *et al.* QUANTUM ESPRESSO: a modular and open-source software project for quantum simulations of materials. *J. Phys. Condens. Matter* **21**, 395502 (2009).
163. Yates, J. R., Pickard, C. J. & Mauri, F. Calculation of NMR chemical shifts for extended systems using ultrasoft pseudopotentials. *Phys. Rev. B* **76**, 24401 (2007).
164. Pack, J. D. & Monkhorst, H. J. Special points for Brillouin-zone integrations. *Phys. Rev. B* **16**, 1748–1749 (1977).
165. Rejmak, P., Dolado, J. S., Stott, M. J. & Ayuela, A.  $^{29}\text{Si}$  NMR in Cement: A Theoretical Study on Calcium Silicate Hydrates. *J. Phys. Chem. C* **116**, 9755–9761 (2012).
166. Nicoleau, L., Nonat, A. & Perrey, D. The di- and tricalcium silicate dissolutions. *Cem. Concr. Res.* **47**, 14–30 (2013).
167. Brough, A. R., Dobson, C. M., Richardson, I. G. & Groves, G. W. Application of Selective  $^{29}\text{Si}$  Isotopic Enrichment to Studies of the Structure of Calcium Silicate Hydrate (C–S–H) Gels. *J. Am. Ceram. Soc.* **77**, 593–596 (1994).
168. Skibsted, J. & Hall, C. Characterization of cement minerals, cements and their reaction products at the atomic and nano scale. *Cem. Concr. Res.* **38**, 205–225 (2008).
169. Rawal, A. *et al.* Molecular Silicate and Aluminate Species in Anhydrous and Hydrated Cements. *J. Am. Chem. Soc.* **132**, 7321–7337 (2010).
170. Alizadeh, R., Raki, L., Makar, J. M., Beaudoin, J. J. & Moudrakovski, I. Hydration of tricalcium silicate in the presence of synthetic calcium–silicate–hydrate. *J. Mater. Chem.* **19**, 7937 (2009).
171. Foley, E. M., Kim, J. J. & Reda Taha, M. M. Synthesis and nano-mechanical characterization of calcium-silicate-hydrate (C–S–H) made with 1.5 CaO/SiO<sub>2</sub> mixture. *Cem. Concr. Res.* **42**, 1225–1232 (2012).



172. Pustovgar, E. *et al.* Understanding silicate hydration from quantitative analyses of hydrating tricalcium silicates. *Nat. Commun.* **7**, 10952 (2016).
173. Sauvée, C. *et al.* Highly Efficient, Water-Soluble Polarizing Agents for Dynamic Nuclear Polarization at High Frequency. *Angew. Chem. Int. Ed.* **52**, 10858–10861 (2013).
174. Lesage, A. *et al.* Surface Enhanced NMR Spectroscopy by Dynamic Nuclear Polarization. *J. Am. Chem. Soc.* **132**, 15459–15461 (2010).
175. Rossini, A. J. *et al.* Dynamic Nuclear Polarization Surface Enhanced NMR Spectroscopy. *Acc. Chem. Res.* **46**, 1942–1951 (2013).
176. Becerra, L. R., Gerfen, G. J., Temkin, R. J., Singel, D. J. & Griffin, R. G. Dynamic nuclear polarization with a cyclotron resonance maser at 5 T. *Phys. Rev. Lett.* **71**, 3561–3564 (1993).
177. Thomas, J. J., Jennings, H. M. & Allen, A. J. Determination of the Neutron Scattering Contrast of Hydrated Portland Cement Paste using H<sub>2</sub>O/D<sub>2</sub>O Exchange. *Adv. Cem. Based Mater.* **7**, 119–122 (1998).
178. Gajan, D. *et al.* Solid-Phase Polarization Matrixes for Dynamic Nuclear Polarization from Homogeneously Distributed Radicals in Mesostuctured Hybrid Silica Materials. *J. Am. Chem. Soc.* **135**, 15459–15466 (2013).
179. Alemany, L. B., Grant, D. M., Pugmire, R. J., Alger, T. D. & Zilm, K. W. Cross polarization and magic angle sample spinning NMR spectra of model organic compounds. 2. Molecules of low or remote protonation. *J Am Chem Soc* **105**, 2142–2147 (1983).
180. Lesage, A., Bardet, M. & Emsley, L. Through-Bond Carbon–Carbon Connectivities in Disordered Solids by NMR. *J. Am. Chem. Soc.* **121**, 10987–10993 (1999).
181. Lee, D. *et al.* Untangling the Condensation Network of Organosiloxanes on Nanoparticles using 2D <sup>29</sup>Si–<sup>29</sup>Si Solid-State NMR Enhanced by Dynamic Nuclear Polarization. *J Am Chem Soc* **136**, 13781–13788 (2014).
182. Xue, X. & Kanzaki, M. Proton Distributions and Hydrogen Bonding in Crystalline and Glassy Hydrous Silicates and Related Inorganic Materials: Insights from High-Resolution Solid-State Nuclear Magnetic Resonance Spectroscopy. *J. Am. Ceram. Soc.* **92**, 2803–2830 (2009).
183. Merlino, S., Bonaccorsi, E. & Armbruster, T. The real structures of clinotobermorite and tobermorite 9 Å: OD character, polytypes, and structural relationships. *Eur. J. Mineral.* 411–429 (2000). doi:10.1127/0935-1221/2000/0012-0411
184. Merlino, S., Bonaccorsi, E. & Armbruster, T. The real structure of tobermorite 11 Å. *Eur. J. Mineral.* **13**, 577–590 (2001).
185. Bonaccorsi, E., Merlino, S. & Kampf, A. R. The crystal structure of tobermorite 14 Å (plombierite), a C–S–H phase. *J. Am. Ceram. Soc.* **88**, 505–512 (2005).
186. Renaudin, G., Russias, J., Leroux, F., Frizon, F. & Cau-dit-Coumes, C. Structural characterization of C–S–H and C–A–S–H samples-Part I: Long-range order investigated by Rietveld analyses. *J. Solid State Chem.* **182**, 3312–3319 (2009).
187. Grangeon, S., Claret, F., Linard, Y. & Chiaberge, C. X-ray diffraction: A powerful tool to probe and understand the structure of nanocrystalline calcium silicate hydrates. *Acta Crystallogr. Sect. B Struct. Sci. Cryst. Eng. Mater.* **69**, 465–473 (2013).
188. Roos, C. *et al.* Distribution of Water in Synthetic Calcium Silicate Hydrates. *Langmuir* **32**, 6794–6805 (2016).
189. Nonat, A. & Lecoq, X. The Structure, Stoichiometry and Properties of C–S–H Prepared by C<sub>3</sub>S Hydration Under Controlled Condition. in *Nuclear Magnetic Resonance Spectroscopy of Cement-Based Materials* (eds. Colombet, D. P., Zanni, P. H., Grimmer, D. A.-R. & Sozzani, P. P.) 197–207 (Springer Berlin Heidelberg, 1998). doi:10.1007/978-3-642-80432-8\_14
190. Richardson, I. G. Tobermorite/jennite- and tobermorite/calcium hydroxide-based models for the structure of C–S–H: applicability to hardened pastes of tricalcium silicate, β-dicalcium silicate, Portland cement, and blends of Portland cement with blast-furnace slag, metakaolin, or silica fume. *Cem. Concr. Res.* **34**, 1733–1777 (2004).
191. Hirljac, J., Wu, Z.-Q. & Young, J. F. Silicate polymerization during the hydration of alite. *Cem. Concr. Res.* **13**, 877–886 (1983).
192. Marchon, D., Juilland, P., Gallucci, E., Frunz, L. & Flatt, R. J. Molecular and submolecular scale effects of comb-copolymers on tri-calcium silicate reactivity: Toward molecular design. *J. Am. Ceram. Soc.* **100**, 817–841 (2017).
193. Nicoleau, L. Accelerated growth of calcium silicate hydrates: Experiments and simulations. *Cem. Concr. Res.* **41**, 1339–1348 (2011).
194. Nicoleau, L. & Nonat, A. A new view on the kinetics of tricalcium silicate hydration. *Cem. Concr. Res.* **86**, 1–11 (2016).
195. Juilland, P. & Gallucci, E. Morpho-topological investigation of the mechanisms and kinetic regimes of alite dissolution. *Cem. Concr. Res.* **76**, 180–191 (2015).

196. Mota Gassó, B. Impact of alkali salts on the kinetics and microstructural development of cementitious systems. (2015). doi:10.5075/epfl-thesis-6763, urn:nbn:ch:bel-epfl-thesis6763-4
197. Catauro, M. *et al.* Synthesis of SiO<sub>2</sub> and CaO rich calcium silicate systems via sol-gel process: Bioactivity, biocompatibility, and drug delivery tests. *J. Biomed. Mater. Res. A* **102**, 3087–3092 (2014).
198. Alexander, G. B., Heston, W. M. & Iler, R. K. The Solubility of Amorphous Silica in Water. *J. Phys. Chem.* **58**, 453–455 (1954).
199. Dove, P. M. & Rimstidt, J. D. Silica-water interactions. *Rev. Mineral. Geochem.* **29**, 259–308 (1994).
200. Tajuelo Rodriguez, E. Relation between composition, structure and morphology in C-S-H. (University of Leeds, 2015).
201. Bazzoni, A. *et al.* The Effect of Magnesium and Zinc Ions on the Hydration Kinetics of C3S. *J. Am. Ceram. Soc.* **97**, 3684–3693 (2014).
202. Nicoleau, L., Gädt, T., Chitu, L., Maier, G. & Paris, O. Oriented aggregation of calcium silicate hydrate platelets by the use of comb-like copolymers. *Soft Matter* **9**, 4864–4874 (2013).
203. Pickard, C. J. & Needs, R. J. Ab initio random structure searching. *J. Phys. Condens. Matter* **23**, 53201 (2011).
204. Raiteri, P., Demichelis, R. & Gale, J. D. Thermodynamically Consistent Force Field for Molecular Dynamics Simulations of Alkaline-Earth Carbonates and Their Aqueous Speciation. *J. Phys. Chem. C* **119**, 24447–24458 (2015).
205. Jennings, H. M. Refinements to colloid model of C-S-H in cement: CM-II. *Cem. Concr. Res.* **38**, 275–289 (2008).
206. Constantinides, G. & Ulm, F.-J. The nanogranular nature of C–S–H. *J. Mech. Phys. Solids* **55**, 64–90 (2007).
207. Testino, A., Buscaglia, V., Buscaglia, M. T., Viviani, M. & Nanni, P. Kinetic Modeling of Aqueous and Hydrothermal Synthesis of Barium Titanate (BaTiO<sub>3</sub>). *Chem. Mater.* **17**, 5346–5356 (2005).
208. Schroeder, B. B., Harris, D. D., Smith, S. T. & Lignell, D. O. Theoretical Framework for Multiple-Polymorph Particle Precipitation in Highly Supersaturated Systems. *Cryst. Growth Des.* **14**, 1756–1770 (2014).
209. Marchisio, D. L. & Fox, R. O. Computational models for polydisperse particulate and multiphase systems. *CERN Document Server* (2013). Available at: <http://cds.cern.ch/record/1617052>. (Accessed: 25th June 2017)
210. Ranodolph, A. *Theory of Particulate Processes: Analysis and Techniques of Continuous Crystallization*. (Elsevier, 2012).
211. Hanhoun, M. *et al.* Simultaneous determination of nucleation and crystal growth kinetics of struvite using a thermodynamic modeling approach. *Chem. Eng. J.* **215**, 903–912 (2013).
212. Galbraith, S. C. & Schneider, P. A. Modelling and simulation of inorganic precipitation with nucleation, crystal growth and aggregation: A new approach to an old method. *Chem. Eng. J.* **240**, 124–132 (2014).
213. Zhu, Z. *et al.* Crystallization of Calcium Sulphate During Phosphoric Acid Production: Modeling Particle Shape and Size Distribution. *Procedia Eng.* **138**, 390–402 (2016).
214. Donnet, M., Bowen, P. & Lemaitre, J. A thermodynamic solution model for calcium carbonate: Towards an understanding of multi-equilibria precipitation pathways. *J. Colloid Interface Sci.* **340**, 218–224 (2009).
215. BERNER, U. R. Modelling the Incongruent Dissolution of Hydrated Cement Minerals. *Radiochim. Acta* **44–45**, 387–394 (1988).
216. Berner, U. R. Evolution of pore water chemistry during degradation of cement in a radioactive waste repository environment. *Waste Manag.* **12**, 201–219 (1992).
217. Kersten, M. Aqueous Solubility Diagrams for Cementitious Waste Stabilization Systems. 1. The C-S-H Solid-Solution System. *Environ. Sci. Technol.* **30**, 2286–2293 (1996).
218. Mobasher, B., Skalny, J. & Society, A. C. *Transport Properties and Concrete Quality: Materials Science of Concrete*. (John Wiley & Sons, 2007).
219. Prieto, M. Thermodynamics of Solid Solution-Aqueous Solution Systems. *Rev. Mineral. Geochem.* **70**, 47–85 (2009).
220. Thorstenson, D. C. & Plummer, L. N. Equilibrium criteria for two-component solids reacting with fixed composition in an aqueous phase; example, the magnesian calcites. *Am. J. Sci.* **277**, 1203–1223 (1977).
221. Prieto, M., Putnis, A., Fernández-Díaz, L. & López-Andrés, S. Metastability in diffusing-reacting systems. *J. Cryst. Growth* **142**, 225–235 (1994).
222. Pina Martínez, C. M., Putnis, A., Pina Martínez, C. M. & Putnis, A. The kinetics of nucleation of solid solutions from aqueous solutions: A new model for calculating non-equilibrium distribution coefficients. *Geochim. Cosmochim. Acta* **66**, 185–192 (2002).
223. Pina, C. M., Putnis, A. & Astilleros, J. M. The growth mechanisms of solid solutions crystallising from aqueous solutions. *Chem. Geol.* **204**, 145–161 (2004).
224. Lothenbach, B. Thermodynamic equilibrium calculations in cementitious systems. *Mater. Struct.* **43**, 1413–1433 (2010).
225. Vanbriesen, J. M., Small, M., Weber, C. & Wilson, J. *Modelling Chemical Speciation: Thermodynamics, Kinetics and Uncertainty*.



226. Rubin, J. Transport of reacting solutes in porous media: Relation between mathematical nature of problem formulation and chemical nature of reactions. *Water Resour. Res.* **19**, 1231–1252 (1983).
227. Anderson, G. *Thermodynamics of Natural Systems: Theory and Applications in Geochemistry and Environmental Science*. (Cambridge University Press, 2017).
228. Anderson, G. M. & Crerar, D. A. *Thermodynamics in Geochemistry: The Equilibrium Model*. (Oxford University Press, 1993).
229. Acton, F. S. *Numerical Methods that Work*. (MAA, 1990).
230. Lin, Y. *et al.* Comparison of activity coefficient models for electrolyte systems. *AIChE J.* **56**, 1334–1351 (2010).
231. Leito, I., Strauss, L., Koort, E. & Pihl, V. Estimation of uncertainty in routine pH measurement. *Accreditation Qual. Assur.* **7**, 242–249 (2002).
232. Meinrath, G. & Spitzer, P. Uncertainties in Determination of pH. *Microchim. Acta* **135**, 155–168 (2000).
233. Yoreo, J. J. D. & Vekilov, P. G. Principles of Crystal Nucleation and Growth. *Rev. Mineral. Geochem.* **54**, 57–93 (2003).
234. Mersmann, A. *Crystallization Technology Handbook*. (CRC Press, 2001).
235. Mersmann, A. & Bartosch, K. How to predict the metastable zone width. *J. Cryst. Growth* **183**, 240–250 (1998).
236. Lewis, A., Seckler, M., Kramer, H. & Rosmalen, G. van. *Industrial Crystallization: Fundamentals and Applications*. (Cambridge University Press, 2015).
237. Pellenq, R. J.-M., Lequeux, N. & van Damme, H. Engineering the bonding scheme in C–S–H: The iono-covalent framework. *Cem. Concr. Res.* **38**, 159–174 (2008).
238. Söhnel, O. Electrolyte crystal-aqueous solution interfacial tensions from crystallization data. *J. Cryst. Growth* **57**, 101–108 (1982).
239. Bullard, J. W., Scherer, G. W. & Thomas, J. J. Time dependent driving forces and the kinetics of tricalcium silicate hydration. *Cem. Concr. Res.* **74**, 26–34 (2015).
240. Myint, A. A. *et al.* One pot synthesis of environmentally friendly lignin nanoparticles with compressed liquid carbon dioxide as an antisolvent. *Green Chem.* **18**, 2129–2146 (2016).
241. Liu, J., Chen, X., Wang, W., Song, B. & Huang, Q. Secondary Facet-Selective Nucleation and Growth: Highly Oriented Straight SnO<sub>2</sub> Nanowire Arrays on Primary Microrods. *Cryst. Growth Des.* **9**, 1757–1761 (2009).
242. Fang, J. *et al.* Gold Mesostructures with Tailored Surface Topography and Their Self-Assembly Arrays for Surface-Enhanced Raman Spectroscopy. *Nano Lett.* **10**, 5006–5013 (2010).
243. Sounart, T. L. *et al.* Secondary Nucleation and Growth of ZnO. *J. Am. Chem. Soc.* **129**, 15786–15793 (2007).
244. Vale, H. M. & McKenna, T. F. Solution of the Population Balance Equation for Two-Component Aggregation by an Extended Fixed Pivot Technique. *Ind. Eng. Chem. Res.* **44**, 7885–7891 (2005).
245. Di, M. On the use of bi-variate population balance equations for modelling barium titanate nanoparticle precipitation. *Chem. Eng. Sci.* **64**, 697–708 (2009).
246. Shvab, I., Brochard, L., Manzano, H. & Masoero, E. Precipitation Mechanisms of Mesoporous Nanoparticle Aggregates: Off-Lattice, Coarse-Grained, Kinetic Simulations. *Cryst. Growth Des.* **17**, 1316–1327 (2017).
247. Lesko, S., Lesniewska, E., Nonat, A., Mutin, J.-C. & Goudonnet, J.-P. Investigation by atomic force microscopy of forces at the origin of cement cohesion. *Ultramicroscopy* **86**, 11–21 (2001).
248. Pellenq, R. J.-M., Caillol, J. M. & Delville, A. Electrostatic Attraction between Two Charged Surfaces: A (N,V,T) Monte Carlo Simulation. *J. Phys. Chem. B* **101**, 8584–8594 (1997).
249. Abdolhosseini Qomi, M. J. *et al.* Combinatorial molecular optimization of cement hydrates. *Nat. Commun.* **5**, 4960 (2014).
250. Skinner, L. B., Chae, S. R., Benmore, C. J., Wenk, H. R. & Monteiro, P. J. M. Nanostructure of Calcium Silicate Hydrates in Cements. *Phys. Rev. Lett.* **104**, 195502 (2010).
251. Chen, Y. *et al.* Applications of Micro-Fourier Transform Infrared Spectroscopy (FTIR) in the Geological Sciences—A Review. *Int. J. Mol. Sci.* **16**, 30223–30250 (2015).
252. Montes-Hernandez, G. & Renard, F. Time-Resolved in Situ Raman Spectroscopy of the Nucleation and Growth of Siderite, Magnesite, and Calcite and Their Precursors. *Cryst. Growth Des.* **16**, 7218–7230 (2016).

## 10 Appendix

SI A: Supplementary information for the article – The Atomic level information for cementitious Calcium silicate hydrates.

SI B: Supplementary information on thermodynamics modeling

SI C: Supplementary information for the article – Kinetics analysis for Calcium silicate hydrate formation.

.



## **SI A: Supplementary information for the article – The Atomic level information for cementitious Calcium silicate hydrates.**

### **I. Supporting Analysis**

*XRD*: X-ray diffraction data was collected with a Bruker D8 Discover X-Ray diffractometer using double bounced monochromatic CuK alpha radiation ( $\lambda=1.54 \text{ \AA}$ ) with a fixed divergence slit size  $0.5^\circ$  and rotating sample stage. Freshly prepared C-S-H collected after washing with a water-ethanol solution followed by vacuum filtration was placed onto the sample stage and XRD patterns were recorded.

*STEM EDX*: Uniformity of the C-S-H was proved by chemical mapping or EDX measurements in STEM mode, using an FEI Tecnai Osiris analytical TEM instrument optimized for speed and sensitivity. The four windowless Super-X SDD EDX detectors integrated into the pole piece allow detection of 200,000 X-ray counts/s over a  $0.9 \text{ srad}$  solid angle. A high brightness XFEG gun allows EDX maps to be acquired in seconds to minutes. With a 11 Mpx Gatan Orius CCD camera, the microscope is also suitable for conventional BF/DF and high resolution TEM imaging. A BF, two ADF, and an HAADF STEM detector provide a wide range of diffraction and Z-contrast conditions. It operates with 200 kV high brightness XFEG with a point resolution of 0.24 nm and a probe current of 2 nA for EDX studies. The sample was prepared by dispersing 50 mg of C-S-H in 40 mL of isopropanol. A drop of the suspended liquid was allowed to dry on a 300 mesh copper grid.

*XRF*: In order to cross check the ICP results the samples were analyzed using X-Ray fluorescence spectroscopy (Optim'X 9900 Ceram XRF model). 20 g of hydrated sample was dried at  $105^\circ\text{C}$  for 24 hours and ignited at  $950^\circ\text{C}$  for 1 hour. 7.7 g of lithium tetraborate ( $\text{Li}_2\text{B}_4\text{O}_7$ ) was added to the 0.7 g of calcinated sample to make a fused bead.

*TGA*: Samples were heated at  $10^\circ\text{C}/\text{min}$  from  $30^\circ\text{C}$  to  $1000^\circ\text{C}$  to record the weight losses in setup from Mettler Toledo AG (TGA/SDTA851e). The total water bound in C-S-H was quantified from the total water loss between  $30$  and  $250^\circ\text{C}$ . The amount of portlandite is quantified from the water loss around of the peak in the range from  $400 - 480^\circ\text{C}$  and calcium carbonate was around  $630 - 710^\circ\text{C}$ . No prior sample preparation involved.

*ICP*: ICP was performed on an ICPE-9000 series (Shimadzu) instrument, a multi-type ICP emission spectrometer with a near ppb detection limit. The sample compositions were analyzed using Optical Emission Spectroscopy mode (ICP-OES). 7 mL of 65%  $\text{HNO}_3$  was added to a 0.25 g sample of C-S-H, then another 5 mL of fuming 100% ultra-pure  $\text{HNO}_3$  was added to ensure complete dissolution. Each analysis consists of verification at further levels of 1-, 10-, and 100-fold dilution in pure water, with the 10-fold dilution affording concentrations best situated in the calibrated range of the instrument. Each analysis was repeated three times to check consistency.

## II. Synthetic apparatus

The reaction system was fabricated in-house for the synthesis of C-S-H. The construction material is poly(methyl methacrylate), which is chemically stable under acidic or basic conditions. Figure S1 shows a schematic of the reactor. It has four main parts – base, cylindrical wall, lid and micromixer unit. Calcium ion selective, conductivity, and pH measurement electrodes are inserted into the lid for real-time monitoring of the reaction conditions. There are also channels that allow for a purging flow of nitrogen gas across the main reaction chamber and an opening used for withdrawing small amounts of sample for kinetic analysis. A micromixer system is mounted on top of the vessel, consisting of three channels emerging from a central vertical column. The length of the column is fitted with a spiral static mixer to combine the reactant solutions prior to admission into the reaction chamber. A magnetic stirrer is located at the base of the reactor chamber.

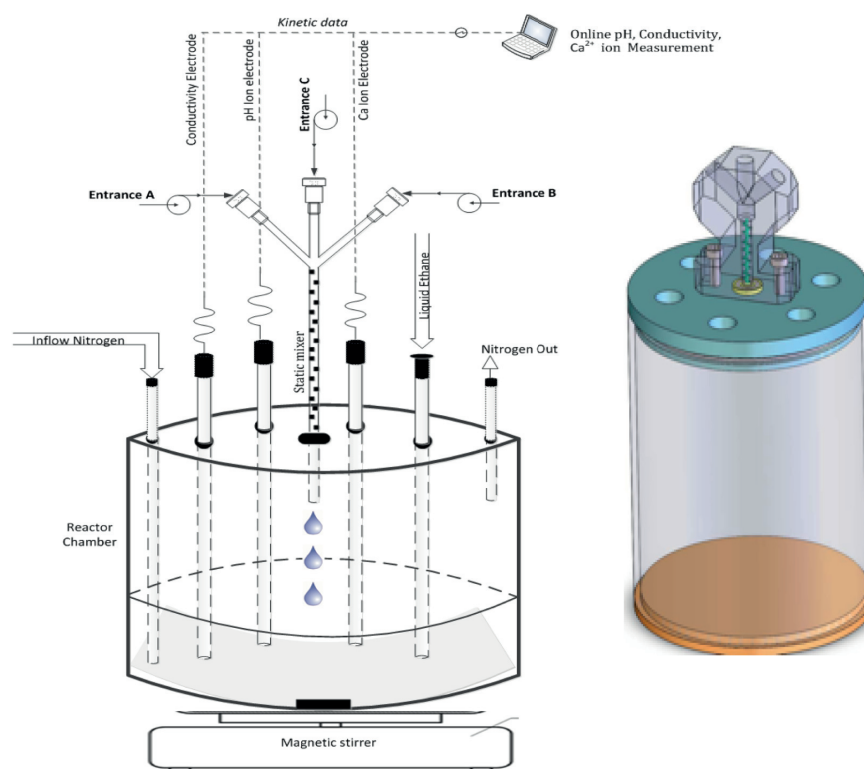


**Figure S1 | Schematic of the reaction vessel.** A low pulsation piston pump was used to feed the reactants into the channels A, B, and C at rates between 0.01 mL/min to 5 mL/min. The off-axis reactant channels join the mixing column at an angle of 60°. The stirring rate was 700-800 rpm. Calcium ion selective, conductivity, and pH measurement electrodes are inserted into the lid for real-time monitoring of the reaction conditions. There are also channels that allow for a purging flow of nitrogen gas across the main reaction chamber and an opening used for withdrawing small amounts of sample for kinetic analysis.

Nitrogen gas flowing at a rate of 20 mL/min was used to purge the chamber over the course of the reaction. Data was Recorded on a PC using LabX software (Mettler-Toledo).

### III. Preparation and recovery

Solutions of calcium nitrate and sodium silicate were prepared in decarbonized water by boiling demineralized ultra-pure water (milliQ) for one hour and cooling in an ice bath. Solutions were immediately prepared after cooling. The quantity of solute used was measured with high accuracy. Measuring electrodes were calibrated twice before each synthesis. To avoid premature nucleation, all chemical glassware was washed and dried under laminar flow hood (Skanair®, Scan AG). After crystallization, the precipitated solids were recovered by washing and vacuum filtration. For each 200 mL aliquot, an equal amount of ultra-pure water mixed with ethanol (50:50 v:v), followed by pure ethanol, was used for the wash. Vacuum filtration was done on 20 nm filter paper (Whatman™, GE health care, ø 50 mm) to recover the washed C-S-H. The precipitated gel was carefully taken off the filter paper and stored in an airtight container. For characterization by TGA and XRD, drying of the filtered solid was necessary. This was performed under nitrogen flow at 70°C for 3 hours or 6 hours. All other characterizations were carried out in the native gel form.

### IV. Synthesis and characterization

For the current synthetic system, pH is a determining parameter for precipitation and ultimately controls the Ca:Si ratio and morphology. This is a consequence of how pH determines the predominant type of silicate species available in solution for reaction. Orthosilicic acid ( $\text{Si}(\text{OH})_4$ ) resists hydrolyzation even near neutral pH conditions owing to its small ionic radius (0.42 Å) and is therefore the predominant solution species below pH 7. In addition to pH, the silicate species which appear in an aqueous system is a sensitive function of cation type and concentration, such that the presence of small quantities of impurities can yield different synthetic results. In general, hydrolysis proceeds according to the following reaction to produce anionic species:

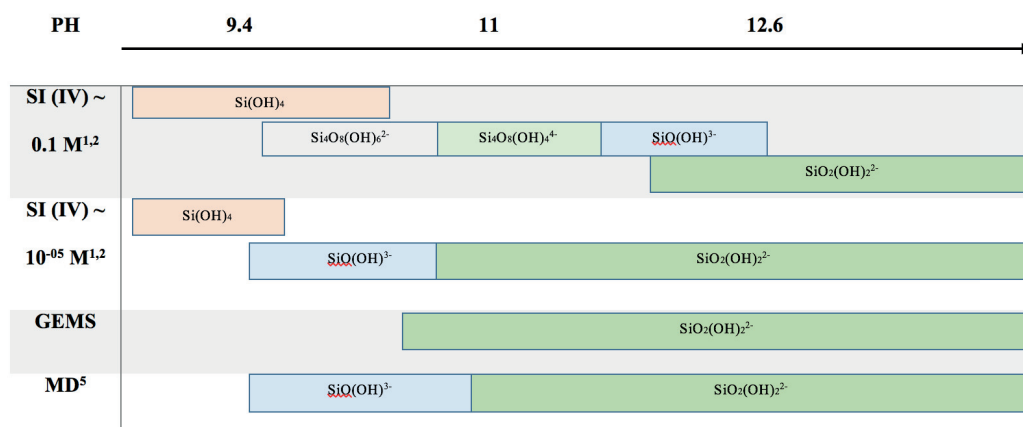


Figure S2 | Predominant silicate species in aqueous solution as a function of pH according to different conditions and methods.<sup>1,2</sup>



Sodium silicate solutions at high pH are likely to contain silicates such as  $\text{SiO}_2(\text{OH})_2^{2-}$ . Gibbs energy minimization software<sup>3</sup> (GEMS) predicts the same species in solution under these conditions. In conjunction with molecular dynamics (MD)<sup>4</sup>, we summarize the presumable possible silicate species in solution as a function of pH in Figure S2. As long as an appropriate target pH range ( $\text{pH} > 11$ ) is maintained, a chemical equilibrium favoring the silicate species  $\text{SiO}_2(\text{OH})_2^{2-}$  can be achieved under a wide variety of chemical conditions even at high silicate concentrations. In other words, regardless of whether or not an initially high concentration (high supersaturation) or low concentration (low supersaturation) of aqueous silicates is used, the pH can be used to favor high concentrations of the important silicate species  $\text{SiO}_2(\text{OH})_2^{2-}$ , leading to the production of pure uniform product C-S-H, so long as the mixing is adequate.

We begin by setting a 2:1 ratio of calcium to silicon in the starting solution using equal volumes of 0.2 M and 0.1 M calcium nitrate to sodium silicate. GEMS<sup>3,5</sup> was used to calculate the pH required to achieve different Ca:Si ratios, and this pH was achieved during synthesis by adding an appropriate amount of concentrated NaOH, which is given in Table S1. Precipitation was allowed to occur for 24 hours before the product was collected and analyzed. The pH calculated according to GEMS agrees with the experimentally measured pH. We see the amount of  $\text{OH}^-$  added in the system leads to a consistently increasing Ca:Si ratio in the solid precipitating phase.

TEM analysis shows that the morphology of the precipitated particles changes at pH 11 and a Ca:Si ratio of 1.25. The morphology resembles foils (*nanofaols*) for  $\text{pH} \geq 11$ ,  $\text{Ca:Si} \geq 1.25$ ; and globules (*nanoglobules*) for  $\text{pH} < 11$ ,  $\text{Ca:Si} < 1.25$ . Repeat analysis confirms that these results can be easily replicated by our synthetic apparatus.

| Target Ca:Si<br>(GEMS) | NaOH<br>(GEMS) | pH<br>(GEMS) | pH<br>(Experiment) |
|------------------------|----------------|--------------|--------------------|
| 1.0                    | 0.05 mL        | 10.87        | 11.1               |
| 1.25                   | 5.16 mL        | 11.47        | 12.5               |
| 1.5                    | 10.58 mL       | 12.05        | 12.6               |
| 1.75                   | 16.62 mL       | 12.55        | 12.7               |
| 2                      | 20.00 mL       | 12.81        | 12.8               |

**Table S1 | Amount of NaOH added to the reaction in order to achieve the pH necessary to produce the targeted Ca:Si ratio according to GEMS. The actual pH during the reaction is given in the final column.**

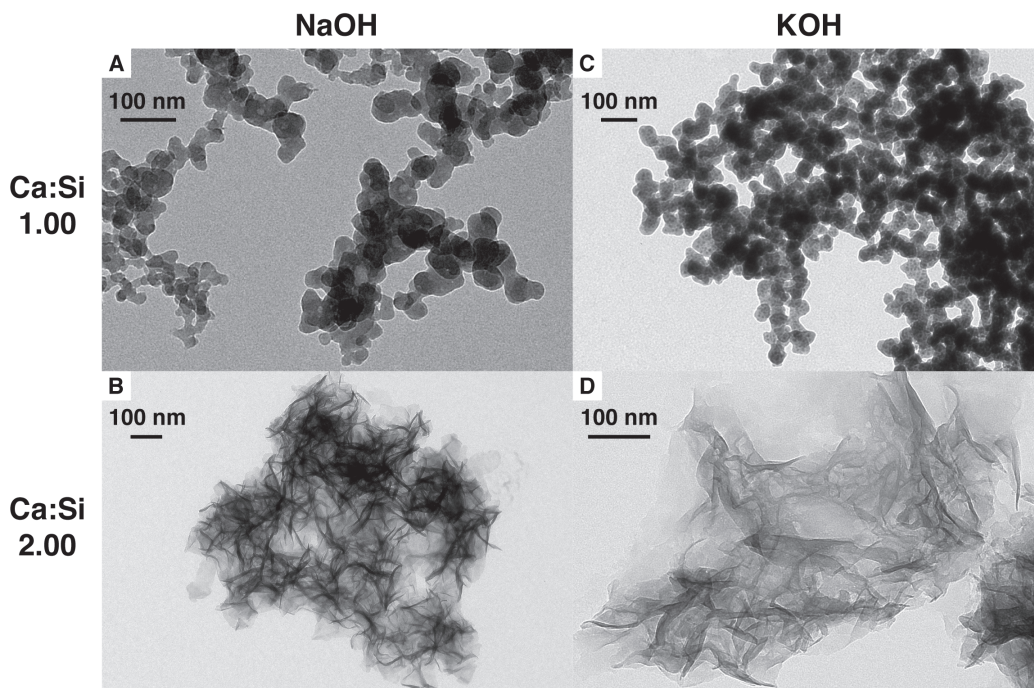


**Figure S3 | TEM imagery showing the morphology of the C-S-H produced for the Ca:Si ratio extremes when different alkali cations are present in the reaction. (A) Globule morphology produced for the Ca:Si = 1.00 composition using NaOH as pH regulator. (B) Foil morphology produced in the NaOH regulated reaction for the Ca:Si = 2.00 composition. (C,D) Same as A and B, respectively, but for the KOH regulated reactions.**

The composition of C-S-H produced by the rapid precipitation method is summarized in Table S2. Elemental analysis for calcium, silicon, and sodium by ICP-OES indicates that the rapid precipitation method described here succeeds in synthesizing C-S-H with the targeted Ca:Si ratios. Despite the low measured sodium concentration, we cannot completely exclude the possibility that inclusion of some sodium may affect the structure. Nevertheless, when KOH is used as the pH regulator, we observe the formation of C-S-H globules for the Ca:Si = 1.00 composition and C-S-H foils for the Ca:Si = 2.00 composition. These products have the same morphological properties as the product obtained when NaOH is used as the pH regulator, as shown in Figure S3. On the other hand, the presence of cations such as  $\text{Mg}^{2+}$  or  $\text{Ba}^{2+}$  leads to the formation of a heterogeneous mixture of products. This strongly suggests that alkali cations are not critical structure determining factors, and that they serve primarily as charge balancing spectators.

Furthermore, our key structural insight is the necessity of the bridging calcium,  $\text{Ca}_\text{B}$ , which we propose is attendant to almost every defect site at high Ca:Si ratios. Considering sodium substitution of  $\text{Ca}_\text{B}$ , we calculate the Na: defect ratio,  $2(n_\text{Na}/n_\text{Si})/P(\text{Q}^{(1)})$ , where  $n_\text{Na}/n_\text{Si}$  is the Na:Si mole ratio by ICP-OES and  $P(\text{Q}^{(1)})$  is the population of  $\text{Q}^{(1)}$  sites determined by NMR. We find this ratio is between 10 mol% and 30 mol% for each of the compositions with Ca:Si mole ratios at or above 1.25. This means that even in the worst-case scenario, in which

every sodium atom substitutes a bridging calcium in a one-to-one fashion (for which we see no driving force), there is not enough sodium to accommodate every defect. In consideration of these matters, we remain confident that the key structural properties of our C-S-H systems can be analyzed in neglect of the small residual alkali content.

| Nominal<br>Ca:Si | Ca:Si<br>(XRF) | Ca:Si<br>(ICP-OES) | Na:Ca<br>(ICP-OES) | Na:defect<br>(ICP-OES/NMR) |
|------------------|----------------|--------------------|--------------------|----------------------------|
| 1.00             | 1.04           | 1.01 ± 0.03        | 0.13 ± 0.01        | 0.88 ± 0.13                |
| 1.25             | 1.21           | 1.24 ± 0.01        | 0.05 ± 0.02        | 0.20 ± 0.07                |
| 1.50             | 1.51           | 1.51 ± 0.03        | 0.02 ± 0.01        | 0.09 ± 0.06                |
| 1.75             | 1.77           | 1.78 ± 0.04        | 0.07 ± 0.02        | 0.30 ± 0.08                |
| 2.00             | 1.94           | 2.00 ± 0.07        | 0.05 ± 0.01        | 0.25 ± 0.04                |

Table S2 | Mole ratios of important C-S-H components determined by various characterization methods.

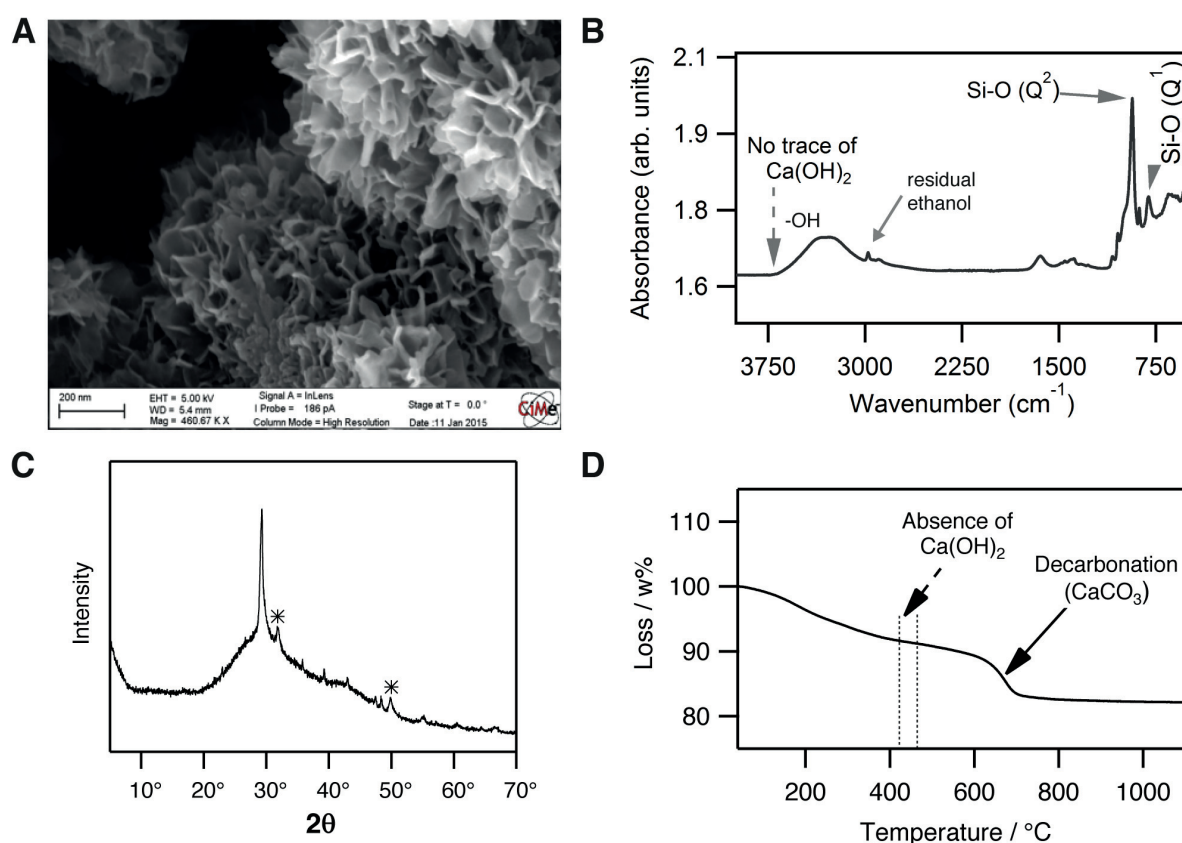


Figure S4 | Characterization of freshly prepared C-S-H for Ca:Si ratio of 2. (A) SEM image showing foil morphology. (B) FTIR analysis. (C) XRD analysis. Resolved peaks corresponding to C-S-H are indicated with stars. Minor peaks correspond to calcium carbonate, which also contributes to the major peak at 29° where it overlaps a C-S-H peak. (d) TGA analysis. A calcium hydroxide phase is never observed, but XRD and TGA reveal that C-S-H is susceptible to the formation of calcium carbonate after prolonged air exposure.

These results confirm that our synthetic procedure yields particles of C-S-H with the targeted Ca:Si ratios. Importantly, the formation of  $\text{Ca}(\text{OH})_2$  is never observed, as illustrated by the FTIR, TGA and XRD analyses of the Ca:Si = 2.00 sample shown in Figure S4. It is worth noting, however, that long exposure of fresh C-S-H samples in open air (for example in TGA or XRD analysis) does eventually lead to the formation of  $\text{CaCO}_3$ .

## V. Sample uniformity

### Determination by non-invasive Raman microscopy

We demonstrated compositional uniformity on pellet of C-S-H with a smoothed surface. The spot analysis ( $1\ \mu\text{m}^2$ ) analyzed more than 30 points on the particle surface. At depths of  $4\ \mu\text{m}$  and  $8\ \mu\text{m}$  the characteristic peaks positions in the C-S-H do not change, indicating the chemical environment uniformity of the sample at the micron level. A visual overview of the sampling and the results are given in Figure S5.

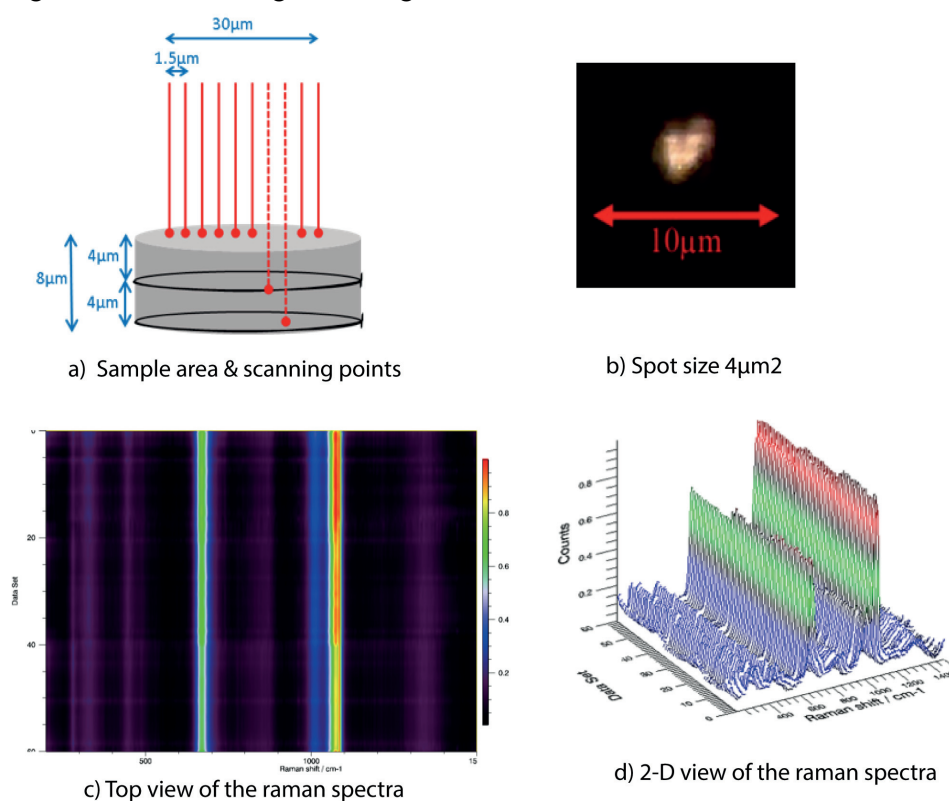


**Figure S5 | Raman microscopic analysis: a) Sample pellet preparation, b) Spot size used for analysis, c) intensity plot comparing Raman spectra of all 30 spots, d) stacked plot comparing Raman spectra of all 30 spots.**

## Determination by STEM-EDX

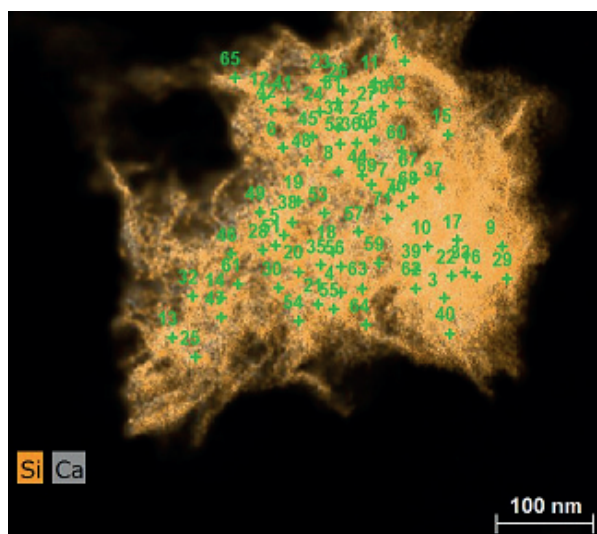


Figure S6 | C-S-H chemical map revealing the spots used for the EDX analysis.

In order to prove the uniformity and consistency of the C-S-H samples to an even greater degree of spatial resolution, EDX in STEM mode was performed on the predefined grids. Once STEM micrographs are obtained, post-processing is performed using Bruker Esprit 1.8 software to obtain the corresponding chemical maps for the samples. The exported STEM image is processed for several parameters like detector effect corrections, Bremsstrahlung background, and Cliff-Lorimer quantification. The major constituents of our C-S-H system are defined for elemental identification. The maps are binned after defining the evaluation methods. As shown in Figure S6, about 50 – 60 points are analyzed individually from the chemical maps. Each spot corresponds to one pixel whose size is 2.34 nm x 2.34 nm. The signal obtained from each spot is processed to arrive at the final Ca:Si ratio at these points. A large background contribution to the signal is removed throughout the signal range spectra deconvolution is to be performed to address overlapped lines in the spectrum. The final quantification results of Ca:Si for each of these spots are recorded. For each sample, the standard deviation of the Ca:Si ratios measurements is less than 1%. EDX analysis provides us with useful information on the consistency of the Ca:Si ratio within the structure but due to the difficulty of accurately calibrating the instrument the actual Ca:Si determined ratio systematically less than that obtained from the XRF and ICP methods.



## VI. DNP enhanced NMR experiments

### A: Sample preparation

Table S3 describes the formulation of the samples, which were prepared as described in the Methods section of the main text.

| Sample       | $m_{\text{gel}}$ / mg | $m_{\text{agent}}$ / mg | $m_{\text{in}}$ / mg | $t_{\text{prep}}$ / min |
|--------------|-----------------------|-------------------------|----------------------|-------------------------|
| Ca:Si = 1.00 | 124.1                 | 25                      | -                    | 60                      |
| Ca:Si = 1.25 | 133.3                 | 33.3                    | 26.6                 | 75                      |
| Ca:Si = 1.50 | 119.3                 | 31.8                    | 23.8                 | 15                      |
| Ca:Si = 1.75 | 114.1                 | 27.0                    | 23.4                 | 15                      |
| Ca:Si = 2.00 | 121.0                 | 30.6                    | 25.4                 | 15                      |

**Table S3 | Formulation of samples used for DNP experiments.**  $m_{\text{gel}}$  gives the mass of gel mixed with  $m_{\text{agent}}$  amount of DNP polarization agent.  $m_{\text{in}}$  is the amount of DNP ready C-S-H slurry that was put into in the rotor.  $t_{\text{prep}}$  is the estimated out of time between release of the C-S-H from storage in a saturated atmosphere to insertion of the sample into the DNP probe at 100 K.

The C-S-H gels do not have an indefinite shelf life and are observed to harden over several weeks to months even in airtight containers. Driving off supernatant water from the gels accelerates this process. By drying the gels on a watch glass for about half an hour, very high DNP enhancements approaching 100 could be obtained, but the line shape would exhibit comparatively large  $Q^{(2)}$  signals. Occasionally, signals from  $Q^{(3)}$  and  $Q^{(4)}$  species were observed, confirming that silicate polymerization accompanied the drying process.

### B: NMR parameters

Table S4 gives the list of experimental parameters common to all NMR experiments, unless otherwise noted.

|                            |                       |
|----------------------------|-----------------------|
| MAS rate                   | 12.5 kHz              |
| $^1\text{H}$ contact rf    | 60 kHz                |
| $^1\text{H}$ pulse/dec rf  | 100 kHz               |
| $^1\text{H}$ ramp profile  | 0.9 $\rightarrow$ 1.0 |
| X contact RF               | 46 kHz                |
| X pulse rf                 | 66 kHz                |
| Recycle delay <sup>a</sup> | 3.0 s                 |

<sup>a</sup>Recycle delay of 1.5 s used for 2D experiments on the Ca:Si = 1.00 sample.

**Table S4 | Parameters common to all NMR experiments.**

All processing for the spectra presented here was performed using *RMN*.<sup>6</sup> Line shape analysis was performed using *gnuplot*. 1D CP MAS shifted echo experiments were performed using the sequence shown in Figure S7. In the presence of significant inhomogeneous broadening, advantages of the shifted echo experiment over conventional CP-detect are an improvement in sensitivity and improved accuracy of phase correction procedures.



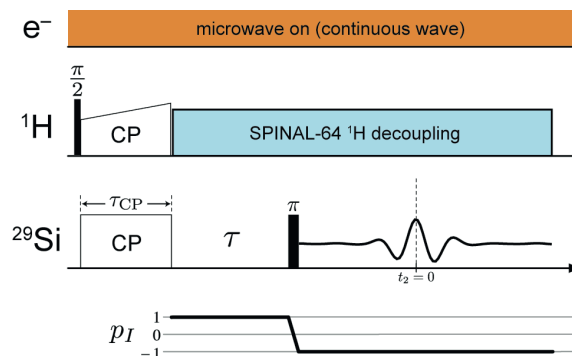


**Figure S7 | DNP enhanced CP MAS shifted echo pulse sequence used in this work.**

For each sample,  $\tau = 9.6$  ms,  $\tau_{CP} = 7$  ms, and 32 transients were collected for a total experiment time of 1.6 min each. Gaussian apodization with a  $\sigma$  of 4.243 ms was applied to the  $t_2$  signal envelope.

This experiment formed the basis of the variable contact time experiments, which nonuniformly sampled 49 different values of  $\tau_{CP}$ : 200  $\mu$ s to 2 ms (200  $\mu$ s increment), 2.5 ms to 12 ms (500  $\mu$ s increment), 14 ms to 30 ms (2 ms increment), and 35 ms to 80 ms (5 ms increment). 2D CP MAS refocused whole echo INADEQUATE experiments<sup>7</sup> were performed using the sequence shown in Figure S8. In addition to the use of hyper complex acquisition<sup>8</sup> to collect echo and anti-echo pathways, acquisition was initiated after the final  $\pi$  pulse in order to collect the entire signal envelope. This improves the sensitivity of the experiment and minimizes phasing artifacts during processing.

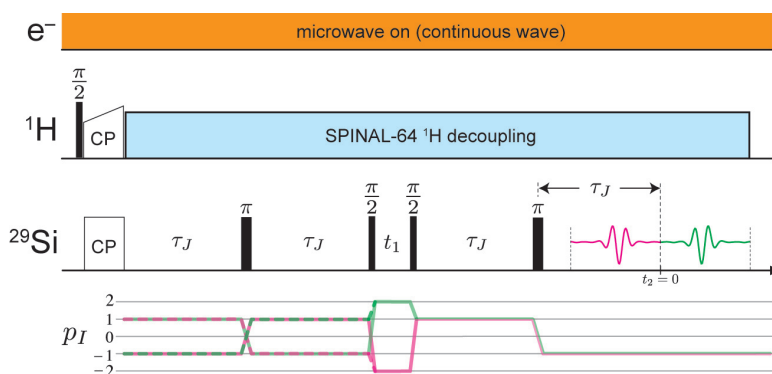


**Figure S8 | DNP enhanced CP MAS refocused whole echo INADEQUATE pulse sequence used in this work. The two  $p_I$  symmetry pathways (dashed and solid green) and anti-pathways (dashed and solid magenta) were collected and processed using hypercomplex acquisition. Whole signal envelopes were acquired during  $t_2$  for path and anti-pathways.**

For each sample,  $\tau_J = 36$  ms,  $\tau_{CP} = 7$  ms. The  $t_1$  increment used was 240  $\mu$ s. 16 complex  $t_1$  points were collected. Other acquisition parameters are given in Table S5 below.

| Sample                    | Transients | Experiment Time |
|---------------------------|------------|-----------------|
| Ca:Si = 1.00 <sup>a</sup> | 640        | 9.6 h           |
| Ca:Si = 1.25              | 320        | 9.0 h           |
| Ca:Si = 1.50              | 320        | 9.0 h           |
| Ca:Si = 1.75              | 512        | 14.5 h          |
| Ca:Si = 2.00              | 512        | 14.5 h          |

<sup>a</sup>A gyrotron outage, lasting about an hour, occurred near the end of the experiment. The spectrum is qualitatively unaffected.

**Table S5 | Acquisition parameters for 2D refocused INADEQUATE experiments**

A shearing transformation was used to create a representation of the 2D INADEQUATE data that correlates two independent single-quantum dimensions.<sup>9</sup> Gaussian apodization with  $\sigma$  of 6 ms and 3 ms were applied to the  $t_2$  and  $t_1$  signal envelopes, respectively. The HETCOR echo sequence was performed using the sequence shown in Figure S9, utilizing the eDUMBO-22 homonuclear decoupling scheme<sup>10,11</sup> to suppress the line broadening from  $^1\text{H}$  –  $^1\text{H}$  dipolar interactions. This also scales the chemical shift and introduces an additional offset into the spectrum which were determined by comparison to a reference HETCOR spectrum of L-alanine. These values were used to present a corrected  $^1\text{H}$  chemical shift dimension for the spectra shown in Figure S14 and Figure S15, as well as the main text Figure 3.

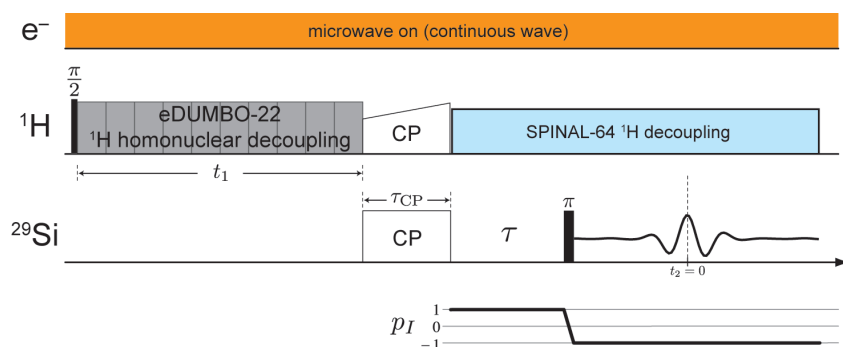


**Figure S9 | DNP enhanced HETCOR echo sequences used in this work. Hypercomplex acquisition was used to collect path and anti-pathways for  $t_1$  evolution. Homonuclear decoupling was applied during  $t_1$ . Whole signal envelopes were acquired during  $t_2$  for path and anti-pathways.**

For each sample,  $\tau = 9.6$  ms. The eDUMBO pulse length was 32  $\mu\text{s}$ . Other acquisition parameters are given in Table S6 below.

| Sample       | $\tau_{CP}$ | Complex $t_1$ points | $\Delta t_1$     | Transients | Experiment Time |
|--------------|-------------|----------------------|------------------|------------|-----------------|
| Ca:Si = 1.00 | 0.7 ms      | 48                   | 32 $\mu\text{s}$ | 24         | 61 min          |
|              | 7 ms        | 48                   | 32 $\mu\text{s}$ | 8          | 20 min          |
| Ca:Si = 1.25 | 0.7 ms      | 48                   | 32 $\mu\text{s}$ | 12         | 59 min          |
|              | 7 ms        | 48                   | 32 $\mu\text{s}$ | 4          | 20 min          |
| Ca:Si = 1.50 | 0.7 ms      | 44                   | 32 $\mu\text{s}$ | 12         | 55 min          |
|              | 7 ms        | 48                   | 32 $\mu\text{s}$ | 4          | 20 min          |
| Ca:Si = 1.75 | 0.7 ms      | 20                   | 64 $\mu\text{s}$ | 32         | 66 min          |
|              | 7 ms        | 20                   | 64 $\mu\text{s}$ | 16         | 33 min          |
| Ca:Si = 2.00 | 0.7 ms      | 20                   | 64 $\mu\text{s}$ | 32         | 66 min          |
|              | 7 ms        | 20                   | 64 $\mu\text{s}$ | 16         | 33 min          |

**Table S6 | Acquisition parameters for HETCOR experiments.**

Gaussian apodization with decay constant of 4.243 ms and 1.2 ms were applied to the  $t_2$  and  $t_1$  signal envelopes, respectively. The apodization was applied to the  $t_1$  dimension prior to multiplying the sampling interval by the chemical shift correction factor  $\lambda_{cs} = 0.57$ .

## VII. Sensitivity of DNP

For each sample,  $^1\text{H}$  spectra were acquired both in the presence and absence of microwaves to measure the DNP enhancement of the protons. The enhancement level could not be determined accurately on the basis of the  $^1\text{H}$  spectra alone due to a nonuniform enhancement of the broad line shape. The estimated proton enhancements  $\epsilon_{\text{DNP}}(^1\text{H})$  are shown in Table S7 below. Whereas a nonexponential recovery was observed for a  $^1\text{H}$  saturation recovery experiment with approximate  $T_{\text{DNP}}(^1\text{H}) = 1.3$  s, a  $^{29}\text{Si}$  CP saturation recovery experiment revealed a nearly exponential buildup with  $T_{\text{DNP}}(\{^1\text{H}\}^{29}\text{Si}) = 2.4$  s. This suggests polarization relay into C-S-H particles with a steady state polarization reached after about ten seconds.

| Sample       | $\epsilon_{\text{DNP}}(^1\text{H})$ |
|--------------|-------------------------------------|
| Ca:Si = 1.00 | 40                                  |
| Ca:Si = 1.25 | 70                                  |
| Ca:Si = 1.50 | 40                                  |
| Ca:Si = 1.75 | 45                                  |
| Ca:Si = 2.00 | 35                                  |

**Table S7 | Proton signal enhancements.**

The sensitivity enhancement for DNP is called  $\Sigma^\dagger$  and can be written as the product of several factors,<sup>12</sup>

$$\Sigma^\dagger = \epsilon_{\text{DNP}} \theta d_{\text{formulation}} \left( \frac{S_{100\text{K}}}{S_{298\text{K}}} \right) \sqrt{\frac{T_1}{T_{\text{DNP}}}}. \quad (\text{S1})$$

$\theta$  is the fraction of observable nuclei in the sample, which is less than unity due to depolarization and quenching by the radical.  $d_{\text{formulation}}$  is a dilution factor related to the fact that additional of the polarization agent may reduce the amount of sample that can be placed into the rotor. The ratio  $S_{100\text{K}}/S_{298\text{K}}$  is generally accounts for the improvement in sensitivity gained by going to 100 K due to the  $\sim 2.8$  improvement in the Boltzmann polarization as well as, e.g., an improvement in the probe quality factors.  $T_{\text{DNP}}$  is the approximate polarization build up time of the protons under DNP, and is to be compared room temperature proton  $T_1$  values for C-S-H measured to be around 0.2 s<sup>13</sup>

Equation (S1) applies strictly only to signal from the polarizing agent and surface signals. Because the proton polarization is relayed into the C-S-H nanoparticles by proton spin diffusion, it is only of approximate validity. Nonetheless, taking  $\theta \approx 1$  (signal is dominated

by bulk C-S-H),  $d_{\text{formulation}} \approx 0.8$  (on the basis of Table S3),  $S_{100\text{K}}/S_{298\text{K}} \approx 5$ , and  $(T_1/T_{\text{DNP}})^{1/2} \approx 0.25$ , and the proton enhancements measured in Table S7, the sensitivity enhancement by DNP is generally the same as  $\varepsilon_{\text{DNP}}(^1\text{H})$ , indicating reduction of corresponding cross-polarization experiment times by  $(\varepsilon_{\text{DNP}}(^1\text{H}))^2$ , or about three orders of magnitude.

## VIII. Quantification of Q species populations

Relative signal intensities in DNP enhanced CP MAS experiments are not usually in proportion to the relative populations of the nuclei generating the signal as they often are in experiments using direct excitation without hyperpolarization. Nonetheless, we can still use these signals for site quantification provided we assume that:

1. The length scale of hyperpolarization nonuniformity is larger than the unit cell of the particle, and
2. Cross-polarization kinetics can be measured and used to adjust the signal intensities appropriately.

The size of the C-S-H particles are sufficiently small (characteristic length  $\sim 100$  nm) and have a proton density sufficient for nearly uniform polarization of the particles over the recycle period. To the second point, we performed cross-polarization measurements for different values of the cross-polarization contact time  $\tau_{\text{CP}}$ , as shown in the first column of Figure III. This data was fit to a simple *IS* model of CP kinetics for each site<sup>14</sup>. For our kinetic model, the signal intensities due to cross-polarization are given as a function of the cross-polarization contact time  $\tau_{\text{CP}}$  by

$$I(\tau_{\text{CP}}) = I_0 \frac{e^{-\frac{\tau_{\text{CP}}}{T_{1\rho}}} - e^{-\frac{\tau_{\text{CP}}}{T_{\text{IS}}}}}{1 - \frac{T_{\text{IS}}}{T_{1\rho}}} \quad (\text{S2})$$

where  $T_{1\rho}$  is the spin-lattice relaxation constant during rf irradiation and  $T_{\text{IS}}$  is the cross-relaxation time.  $I_0$  is the base intensity, proportional to the equilibrium magnetization and hence number of nuclei generating the NMR signal for the given site. The 1D CP echo line shape was used in an initial unconstrained fit to three independent Gaussian functions, each representing the  $Q^{(1)}$ ,  $Q^{(2b)}$ , and  $Q^{(2p)}$  contributions. From this a set of mean Gaussian shift ( $\delta$ ) and widths ( $\sigma$ ) for the frequency spectrum was determined and used to constrain the fit to the variable contact time data for the cross-polarization kinetic parameters. Stack plots representing the best fit and residual plots to this data are shown as the second and third columns of Figure S10. The cross-polarization kinetic parameters we determine from this analysis is given in Table S8.

| Sample       | $Q^{(1)}$               |                             | $Q^{(2b)}$              |                             | $Q^{(2p)}$              |                             |
|--------------|-------------------------|-----------------------------|-------------------------|-----------------------------|-------------------------|-----------------------------|
|              | $T_{1\rho} / \text{ms}$ | $T_{\text{IS}} / \text{ms}$ | $T_{1\rho} / \text{ms}$ | $T_{\text{IS}} / \text{ms}$ | $T_{1\rho} / \text{ms}$ | $T_{\text{IS}} / \text{ms}$ |
| Ca:Si = 1.00 | $32.5 \pm 0.6$          | $1.81 \pm 0.04$             | $25.6 \pm 0.8$          | $1.09 \pm 0.04$             | $44.4 \pm 0.6$          | $4.07 \pm 0.06$             |
| Ca:Si = 1.25 | $27.1 \pm 0.3$          | $2.31 \pm 0.02$             | $26.1 \pm 0.9$          | $1.41 \pm 0.05$             | $38.2 \pm 0.9$          | $5.14 \pm 0.13$             |
| Ca:Si = 1.50 | $33.8 \pm 0.3$          | $2.19 \pm 0.02$             | $34.6 \pm 2.1$          | $1.24 \pm 0.09$             | $45.6 \pm 1.7$          | $4.78 \pm 0.18$             |
| Ca:Si = 1.75 | $25.9 \pm 0.2$          | $2.22 \pm 0.02$             | $28.6 \pm 1.9$          | $1.49 \pm 0.12$             | $38.1 \pm 1.9$          | $4.62 \pm 0.24$             |
| Ca:Si = 2.00 | $28.0 \pm 0.2$          | $2.40 \pm 0.02$             | $30.9 \pm 2.7$          | $1.29 \pm 0.14$             | $40.3 \pm 2.5$          | $4.91 \pm 0.32$             |

**Table S8 | Cross-polarization kinetic parameters determined by the variable contact time experiments.**

To complete the quantification, the 1D CP echo data was refit using Equation (S2) for the base intensities as well as new Gaussian shift parameters. The previously determined  $T_{1\rho}$ ,  $T_{IS}$ , and Gaussian width parameters, averaged across the compositions with Ca:Si  $\geq 1.25$  for each site, were used for determination of the base intensities. The exception was the Ca:Si = 1.00 composition, where its own  $T_{1\rho}$  and  $T_{IS}$  parameters were used. In accordance with the *dreierketten* model, the additional constraint  $I_0(Q^{(2p)}) = 2 I_0(Q^{(2b)})$  was enforced. The 1D CP echo spectra, best fit to this constrained 1D model, and best fit residuals are shown in Figure S11. Associated Gaussian shift and width parameters are given in Table S9.

| Sample       | $Q^{(1)}$         |                 | $Q^{(2b)}$        |                 | $Q^{(2p)}$        |                 |
|--------------|-------------------|-----------------|-------------------|-----------------|-------------------|-----------------|
|              | $\delta$ / ppm    | $\sigma$ / ppm  | $\delta$ / ppm    | $\sigma$ / ppm  | $\delta$ / ppm    | $\sigma$ / ppm  |
| Ca:Si = 1.00 | -79.71 $\pm$ 0.08 | 1.34 $\pm$ 0.05 | -82.72 $\pm$ 0.08 | 1.08 $\pm$ 0.11 | -85.77 $\pm$ 0.04 | 1.29 $\pm$ 0.03 |
| Ca:Si = 1.25 | -79.17 $\pm$ 0.02 | 1.25 $\pm$ 0.03 | -81.85 $\pm$ 0.08 | 1.42 $\pm$ 0.31 | -85.33 $\pm$ 0.03 | 1.25 $\pm$ 0.04 |
| Ca:Si = 1.50 | -79.10 $\pm$ 0.01 | 1.31 $\pm$ 0.02 | -81.64 $\pm$ 0.07 | 1.03 $\pm$ 0.21 | -85.17 $\pm$ 0.03 | 1.27 $\pm$ 0.06 |
| Ca:Si = 1.75 | -78.90 $\pm$ 0.01 | 1.27 $\pm$ 0.01 | -81.54 $\pm$ 0.07 | 1.20 $\pm$ 0.19 | -84.90 $\pm$ 0.03 | 1.24 $\pm$ 0.05 |
| Ca:Si = 2.00 | -78.87 $\pm$ 0.01 | 1.27 $\pm$ 0.01 | -81.53 $\pm$ 0.08 | 1.11 $\pm$ 0.15 | -84.81 $\pm$ 0.03 | 1.30 $\pm$ 0.05 |

**Table S9 | Shift ( $\delta$ ) and width ( $\sigma$ ) parameters determined by the three Gaussian fit to the 1D CP MAS shifted echo data. The  $\delta$  parameters were found in a fit subject to the constraint  $I_0(Q^{(2p)}) = 2 I_0(Q^{(2b)})$ ;  $\sigma$  parameters were carried over from a prior unconstrained fit.**

By normalizing the sum of the base intensities to unity, we determine the Q species populations, reported in Table S10. As the residuals in Figure S11 indicate, the analysis is not valid for the Ca:Si = 1.00 composition.

| Sample       | $P(Q^{(1)})$      | $P(Q^{(2b)})$     | $P(Q^{(2p)})$     |
|--------------|-------------------|-------------------|-------------------|
| Ca:Si = 1.00 | 0.290 $\pm$ 0.027 | 0.237 $\pm$ 0.009 | 0.473 $\pm$ 0.018 |
| Ca:Si = 1.25 | 0.597 $\pm$ 0.107 | 0.134 $\pm$ 0.036 | 0.269 $\pm$ 0.071 |
| Ca:Si = 1.50 | 0.700 $\pm$ 0.051 | 0.100 $\pm$ 0.017 | 0.200 $\pm$ 0.034 |
| Ca:Si = 1.75 | 0.783 $\pm$ 0.053 | 0.072 $\pm$ 0.018 | 0.145 $\pm$ 0.035 |
| Ca:Si = 2.00 | 0.830 $\pm$ 0.036 | 0.057 $\pm$ 0.012 | 0.113 $\pm$ 0.024 |

**Table S10 | Q species populations, subject to the constraint  $P(Q^{(2p)}) = 2 P(Q^{(2b)})$ .**

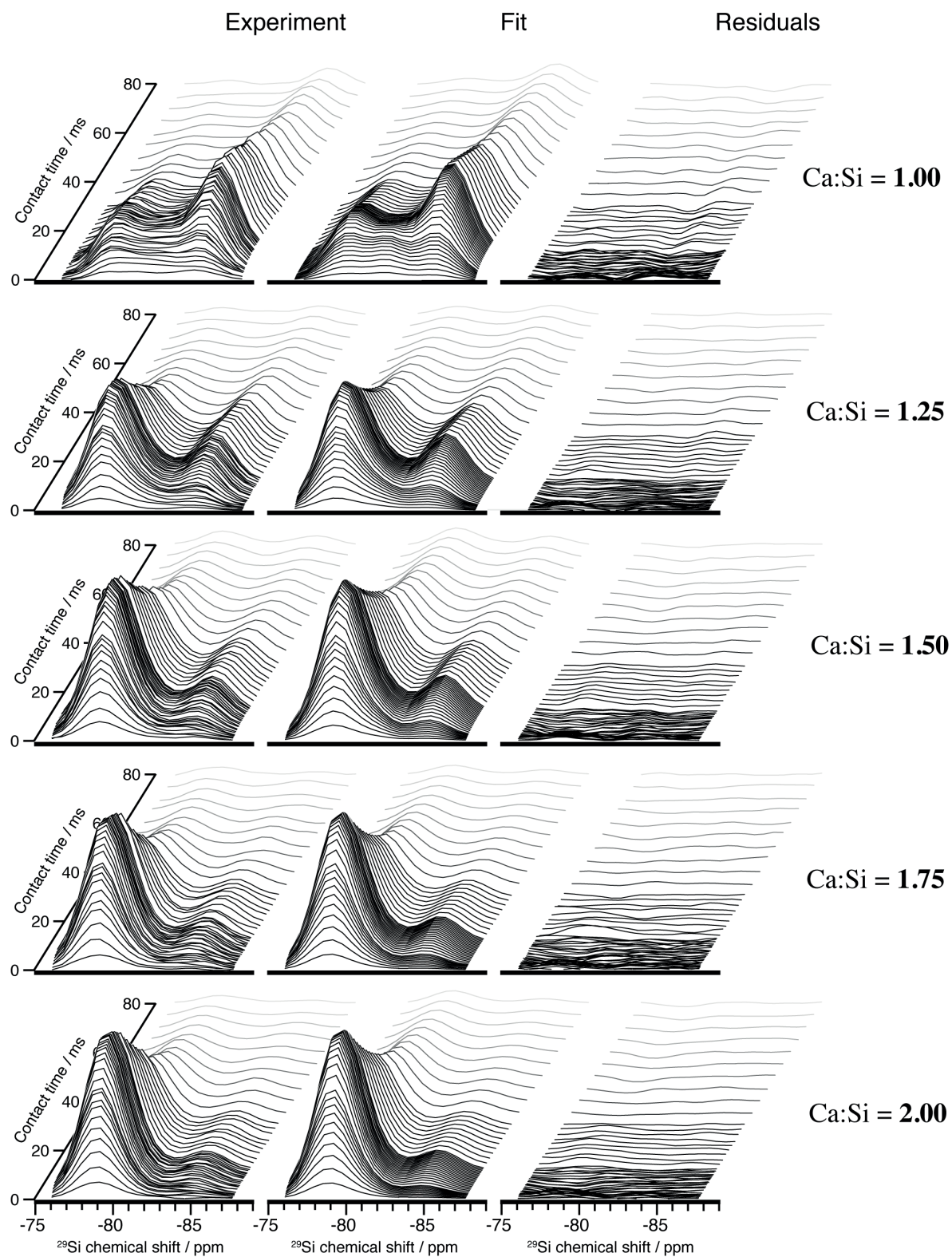


**Figure S10 | Stacked plots for the variable contact time spectra, best fit using the kinetic model, and the best fit residuals.**



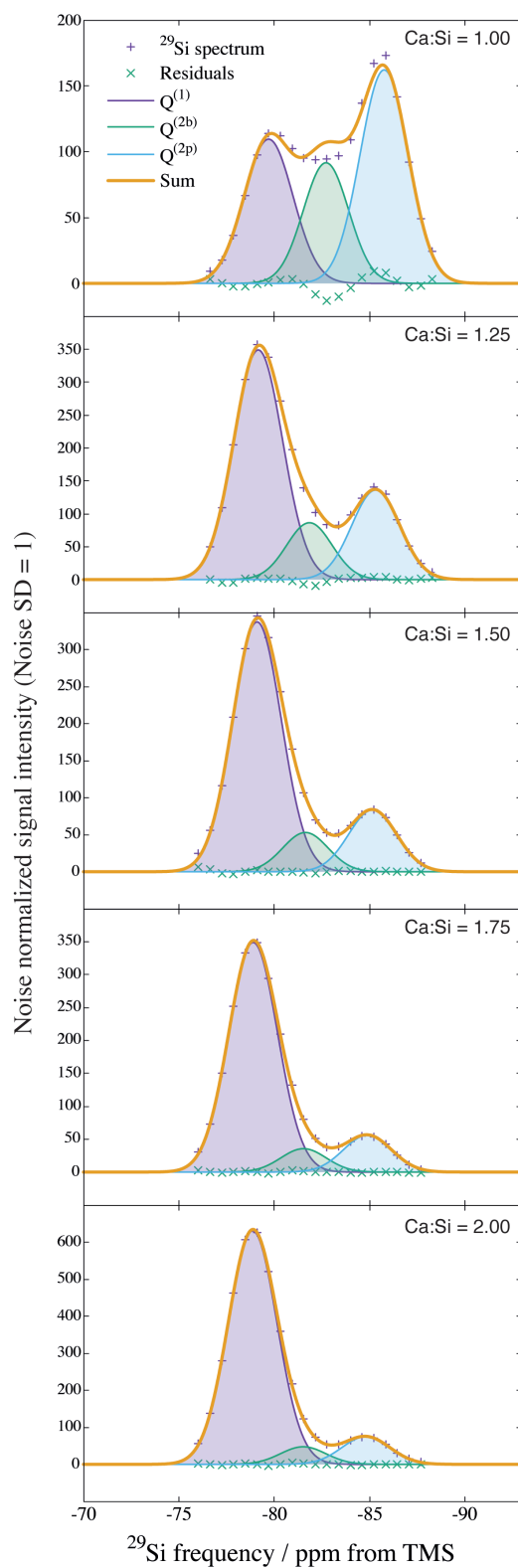


**Figure S11 | Deconvolution of the line shapes obtained in the DNP enhanced 1D CP MAS shifted echo experiments using the three Gaussian model described in the main text. The intensities are subject to the constraint  $I_0(Q^{(2p)}) = 2 I_0(Q^{(2b)})$ .**

## IX. Quantification of chain distributions

Each peak in the A-B chemical shift correlation line shapes presented by the INADEQUATE spectra in the first column of Figure S12 were modeled by a 2D Gaussian function with zero correlation between independent A and B chemical shift dimensions. The shifts of the Gaussian functions along each dimension was constrained to the values shown in Table S9. The Gaussian width parameters were fixed to the same values for each fit, which were obtained by fitting the 1D projection onto the A chemical shift axis to three independent 1D Gaussian functions for the  $\text{Ca:Si} \geq 1.25$  compositions and taking the mean for each corresponding Q site. The 2D line shape model permits up to nine independent 2D Gaussian functions to be used; however, the functions corresponding to the  $\text{Q}^{(1)}\text{-Q}^{(2b)}$ ,  $\text{Q}^{(2b)}\text{-Q}^{(1)}$ , and  $\text{Q}^{(2b)}\text{-Q}^{(2b)}$  correlation peaks were omitted on the basis of the *dreierketten* model and validated by the absence of significant signal in the corresponding regions of the INADEQUATE spectra. The 2D experimental line was then fit for the intensities of the six constituent 2D Gaussian functions. The second and third columns of Figure S12 shows the best fit results and residuals. Table S11 gives the unnormalized peak intensities.

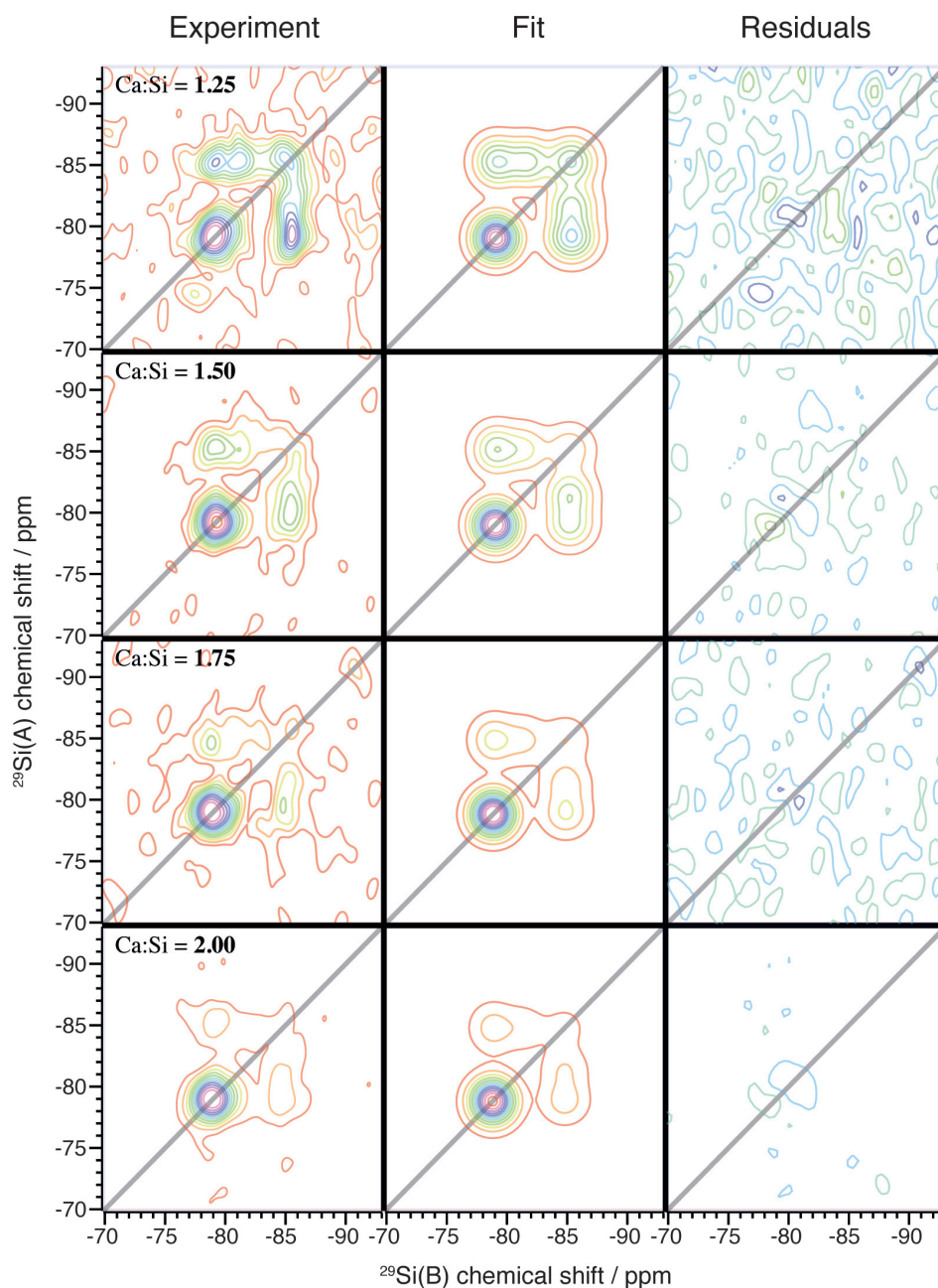


**Figure S12 | Experimental A-B correlated 2D refocused INADEQUATE spectra, best fit to the 2D Gaussian model, and best fit residuals for the C-S-H compositions with  $\text{Ca:Si} \leq 1.25$ . Contours are drawn in 10% intervals beginning at 5% of the maximum signal intensity; the residual plots are relative to the experimental maximum and both positive (blue) and negative (green) contours are shown.**

| Sample       | $I(Q^{(1)} Q^{(2p)})$ | $I(Q^{(2b)} Q^{(2p)})$ | $I(Q^{(2p)} Q^{(2p)})$ | $I(Q^{(2p)} Q^{(2b)})$ | $I(Q^{(1)} Q^{(1)})$ | $I(Q^{(2p)} Q^{(1)})$ |
|--------------|-----------------------|------------------------|------------------------|------------------------|----------------------|-----------------------|
| Ca:Si = 1.25 | 78.95                 | 59.84                  | 86.91                  | 58.78                  | 153.31               | 94.12                 |
| Ca:Si = 1.50 | 135.28                | 72.49                  | 83.05                  | 113.60                 | 347.60               | 122.16                |
| Ca:Si = 1.75 | 64.82                 | 34.32                  | 36.35                  | 40.77                  | 247.07               | 59.04                 |
| Ca:Si = 2.00 | 94.99                 | 44.51                  | 44.13                  | 60.77                  | 498.70               | 95.04                 |

**Table S11 | Unnormalized best fit intensities of the A-B correlation peaks of the 2D refocused INADEQUATE spectra to the 2D Gaussian line shape model.**

The intensity of an A-B correlation peak, denoted  $I(B|A)$ , is given by

$$I(B|A) = f(B|A)P(B|A)P_w(A) \quad (S3)$$

We solve for the conditional probability  $P(B|A)$ : the probability that a  $^{29}\text{Si}$  nucleus of species B was detected given that it evolved with partner  $^{29}\text{Si}$  nucleus of species A. They are normalized,

$$\sum_B P(B|A) = 1,$$

and Baye's theorem relates  $P(B|A)$  to  $P(A|B)$ :

$$P(B|A) = \frac{P(A|B)P_w(B)}{P_w(A)}.$$

$P_w(A)$  is the population of species A weighted for pair participation. At the sparse 4.7% natural abundance of  $^{29}\text{Si}$ , the  $Q^{(2)}$  sites are nearly twice as likely to have a  $^{29}\text{Si}$  partner; therefore,  $P_w(Q^{(2b)})$  and  $P_w(Q^{(2p)})$  are obtained from the populations measured in the 1D experiments by doubling the population measured from the 1D experiments and renormalizing. Note that the sparse labeling simplifies the weighting analysis since the entire NMR signal is assumed to be derived only from isolated pairs and not triplets, etc. Finally,  $f(B|A)$  is an amplitude transfer factor that accounts for Q site differences in e.g. CP efficiency,  $T_2'$  relaxation, and  $J$ -coupling distributions, and were assumed not to change as a function of Ca:Si ratio.

The experimental intensities were normalized for each composition by dividing out  $I(Q^{(1)}|Q^{(1)})$ . Through the laws given above and the constraints imposed by the *dreierketten* model, any other conditional probability can be determined once  $P(Q^{(1)}|Q^{(1)})$  is known. Upon substitution of Equation (S3) for each composition and using  $P_w(A)$  values determined from the 1D quantitative analysis, the five transfer factor ratios (Table S12) and  $P(Q^{(1)}|Q^{(1)})$  for each composition were determined through a simultaneous fit of the twenty intensity ratios (five for each composition).

| $f(Q^{(1)} Q^{(2p)})$ | $f(Q^{(2b)} Q^{(2p)})$ | $f(Q^{(2p)} Q^{(2p)})$ | $f(Q^{(2p)} Q^{(2b)})$ | $f(Q^{(1)} Q^{(1)})$ | $f(Q^{(2p)} Q^{(1)})$ |
|-----------------------|------------------------|------------------------|------------------------|----------------------|-----------------------|
| 1.64                  | 0.64                   | 2.09                   | 0.72                   | 1 (defined)          | 1.74                  |

**Table S12 | Transfer factors determined for each type of correlation peak.**

The conditional probabilities are related to the distribution of chain species by

$$P(Q^{(1)}|Q^{(1)}) = x_0$$

$$P(Q^{(1)}|Q^{(2p)}) = \frac{\sum_{n=1} x_n}{\sum_{n=1} x_n(2n)}$$

$$P(Q^{(2b)}|Q^{(2p)}) = \frac{1}{2}$$

$$P(Q^{(2p)}|Q^{(2p)}) = \frac{\sum_{n=1} x_n (n-1)}{\sum_{n=1} x_n(2n)}$$

where the mole fractions of chains with repeat index  $n$  is denoted  $x_n$ . Application of the laws of conditional probability lead to the constraints reported in the main text. The parameters determined by our analysis are given in Table 1 of the main text.

Recalling that previous studies have generally focused on  $\text{Ca:Si} < 1.50$ , which are not relevant to industrial formulations, we highlight that the  $\text{Ca:Si} = 1.00$  composition is remarkable in that silicate dimers appear to be completely absent ( $x_0 = 0$ ), as noted by the lack of a prominent  $Q^{(1)}\text{-}Q^{(1)}$  correlation peak observed for all of the other C-S-H compositions. This is shown in Figure S13.

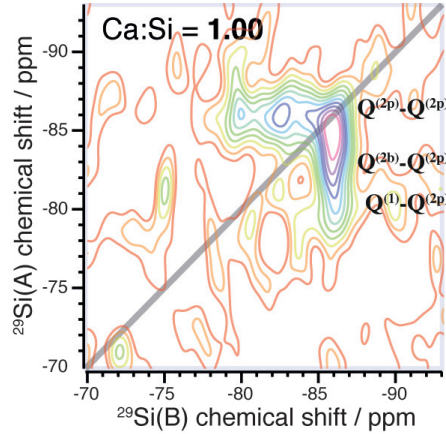


**Figure S13 | Experimental A-B correlated 2D refocused INADEQUATE spectrum for  $\text{Ca:Si} = 1.00$ . A gyrotion outage, lasting about an hour, occurred near the end of the experiment. The spectrum is qualitatively unaffected.**

## X. Heteronuclear $\{^1\text{H}\}^{29}\text{Si}$ correlation

For each composition, a 2D HETCOR experiment using the pulse sequence described in Figure S9 was performed for both a short (0.7 ms) and long (7 ms) values of  $\tau_{\text{CP}}$ . The use of a short contact time biases the contribution to the NMR signal from those protons that are close to the correlating  $^{29}\text{Si}$  nuclei, though without significant proton density fewer than three bonds away from the Si nuclei, the notion of a well-defined cutoff distance for the signals which appear in the correlation spectrum loses significance.<sup>14</sup>

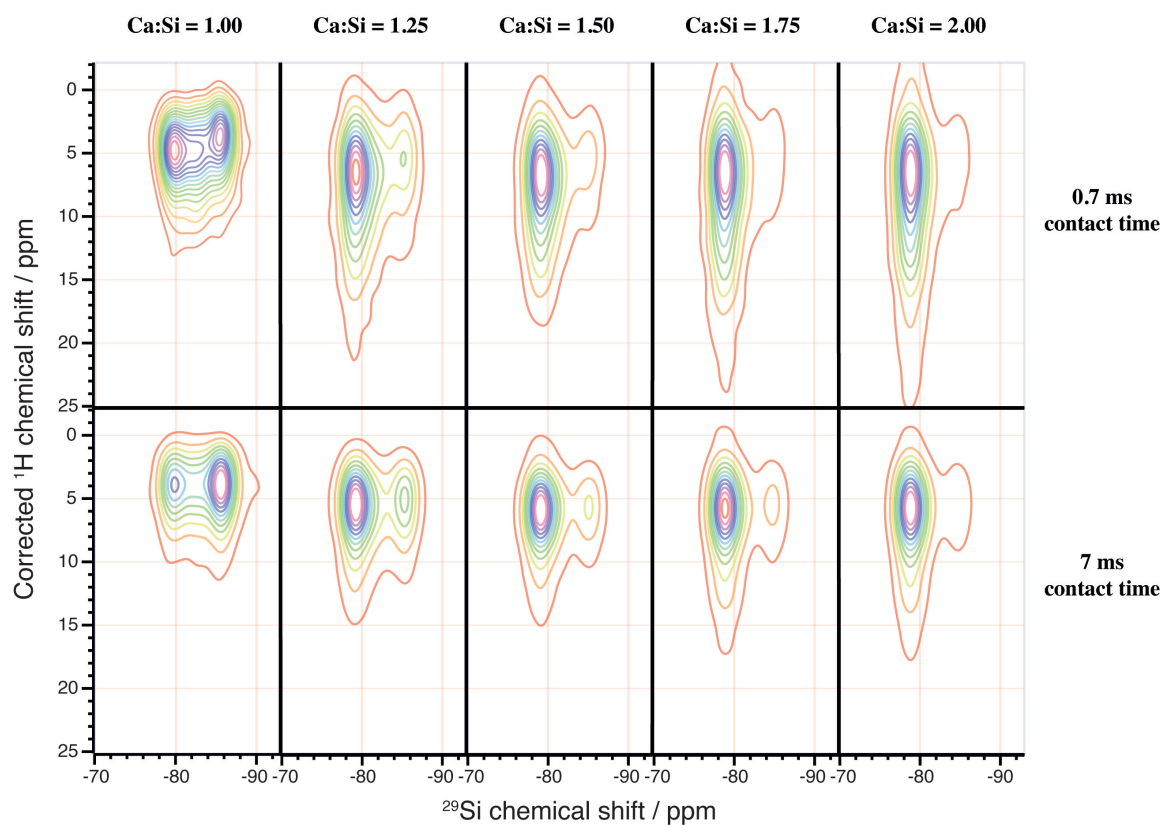


**Figure S14 | Complete series of DNP enhanced HETCOR spectra at both short and long contact times for all compositions studied.**



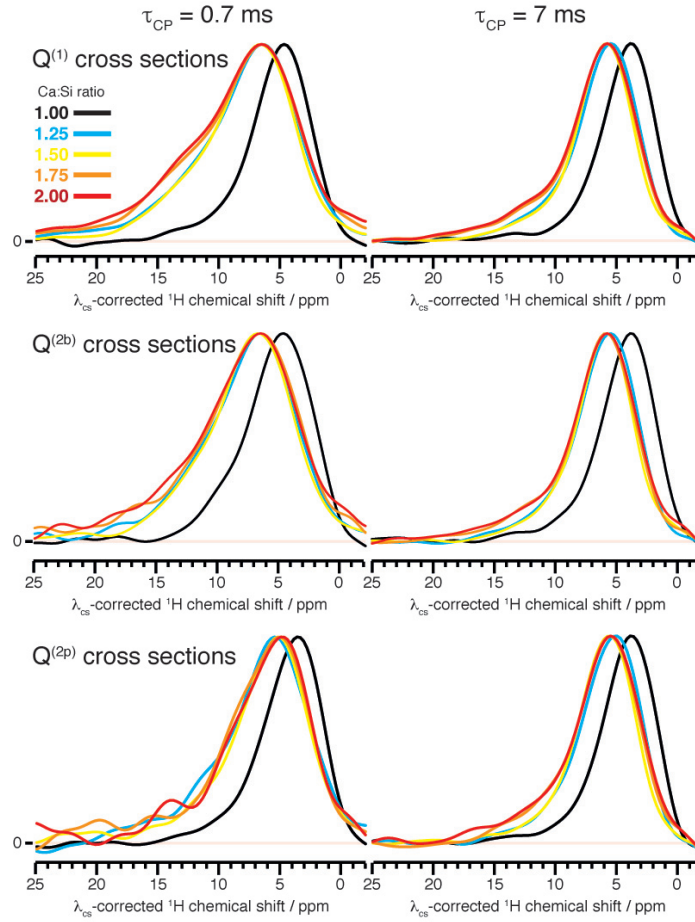


**Figure S15 |  $^{29}\text{Si}$  site correlated  $^1\text{H}$  spectra taken as cross sections from the full 2D HETCOR spectra at the appropriate  $^{29}\text{Si}$  chemical shifts.**

## XI. Structural model

It is known that C-S-H resembles a defective tobermorite.<sup>15,16</sup> To create a structure based on defective tobermorite that possesses high Ca:Si ratios, we build substructures of C-S-H according to the following procedure:

- Deprotonate silanol in the bridging tetrahedrons and replace it with a  $\text{CaOH}^+$  ion in the interlayer.
- Remove a bridging silicate tetrahedron, performing charge compensation by adding two protons or a proton and a  $\text{CaOH}^+$  ion or addition of a  $\text{Ca}^{2+}$  to coordinate the bridging site ( $\text{Ca}_\text{B}$  site in Figure S16).
- Add  $\text{Ca}(\text{OH})_2$  units in the interlayer space ( $\text{Ca}_\text{I}$  and  $\text{Ca}_\text{A}$ ) to obtain higher Ca:Si ratios.

We study the effect of these different defect units (Figure S16A) on the  $^1\text{H}$  chemical shifts. Reduced unit cells are constructed by connecting the defect units through an aqueous interlayer or an aqueous interlayer with a  $\text{Ca}_\text{I}$  and additional  $\text{OH}^-$  for charge balance (Figure

S16B). In order to study medium range effects, we also consider different ways to combine the reduced unit cells, resulting in chain, dimer, and pentamer motifs (Figure S16C).

All the structures are first partially relaxed with energy minimization using METADISE<sup>17</sup> with a force field potential previously used for cementitious materials.<sup>18</sup> If the atomic bond distances, calcium coordination and local charge neutrality are satisfactory then they are relaxed using density function theory (DFT). For the former two criteria, we require specifically that Ca-O bonds are between 2.2 Å and 2.9 Å and that calcium coordination numbers are near six. The condition of local charge neutrality is implemented as systems with large distances between charged species consistently exhibit higher energies than systems for which this is not the case. Additional water molecules can be added to the interlayer to help satisfy these criteria. Depending on the initial atomic coordinates, especially those that specify the positioning of the interlayer water, the reduced unit cells may relax into different structures with the same defect classification.

These structures are again checked for the calcium coordination, lack of disruption of the main layer calcium-silicate backbone chain, and local charge neutrality. Once all the criteria are met, <sup>1</sup>H and <sup>29</sup>Si chemical shift calculations are performed on the candidates. The chemical shielding  $\sigma_{calc}$  was calculated using the generalized gradient approximation (GGA) functional PBE<sup>19</sup> within the Quantum Espresso code<sup>20</sup> and the GIPAW method.<sup>21</sup> For each calculation a plane-wave maximum cutoff energy of 80 Ry, and a Monkhorst-Pack grid of  $k$ -points<sup>22</sup> corresponding to 0.033 Å<sup>-1</sup> in reciprocal space was employed. These values were tested for convergence of calculated energy and chemical shielding.

The convergence criteria for force, energy and pressure for structural relaxation were set to 10<sup>-3</sup> E<sub>h</sub>/a<sub>0</sub>, 10<sup>-4</sup> E<sub>h</sub>, and 500 bar respectively. The final pressure of each relaxed structure was less than 150 bar. For structures which contain Ca<sub>1</sub>, the final pressure was usually below 50 bar. To ensure this 500 bar threshold was sufficient, we performed an additional DFT relaxation of the structure based upon the ACcav2 motif, setting a cell pressure threshold of 0.01 bar. Because of this stricter convergence criteria, O – O distances throughout the structure change by 0.05 - 0.1 Å, resulting in a <sup>1</sup>H chemical shift RMSD of 0.59 ppm and a <sup>29</sup>Si chemical shift RMSD of 0.34 ppm relative to the structure calculated with the higher convergence threshold for pressure. The higher <sup>1</sup>H chemical shift RMSD corresponds to the fact that proton chemical shifts are more sensitive to changes in the hydrogen bonding network than <sup>29</sup>Si. In NMR crystallography, two systems are considered identical if the <sup>1</sup>H chemical shift RMSD is below 0.5 ppm.<sup>23</sup> We justify a slightly higher limit for the C-S-H considering that most of the protons of weakly bonded interlayer species have lower barriers to conformational rearrangement relative to crystals of small organic molecules. Indeed, there is a correlation between the largest <sup>1</sup>H chemical shift changes occur for species near 0 ppm, as shown in Figure S17. If the proton chemical shifts corresponding to these non-hydrogen bonded H<sub>2</sub>O are excluded from the comparison, we calculate a <sup>1</sup>H chemical shift RMSD of 0.38 ppm, which is well below the cutoff of 0.5 ppm. Therefore, a stricter convergence criterion for the DFT relaxation does not affect our interpretation of the <sup>1</sup>H chemical shifts nor the conclusions drawn from them.

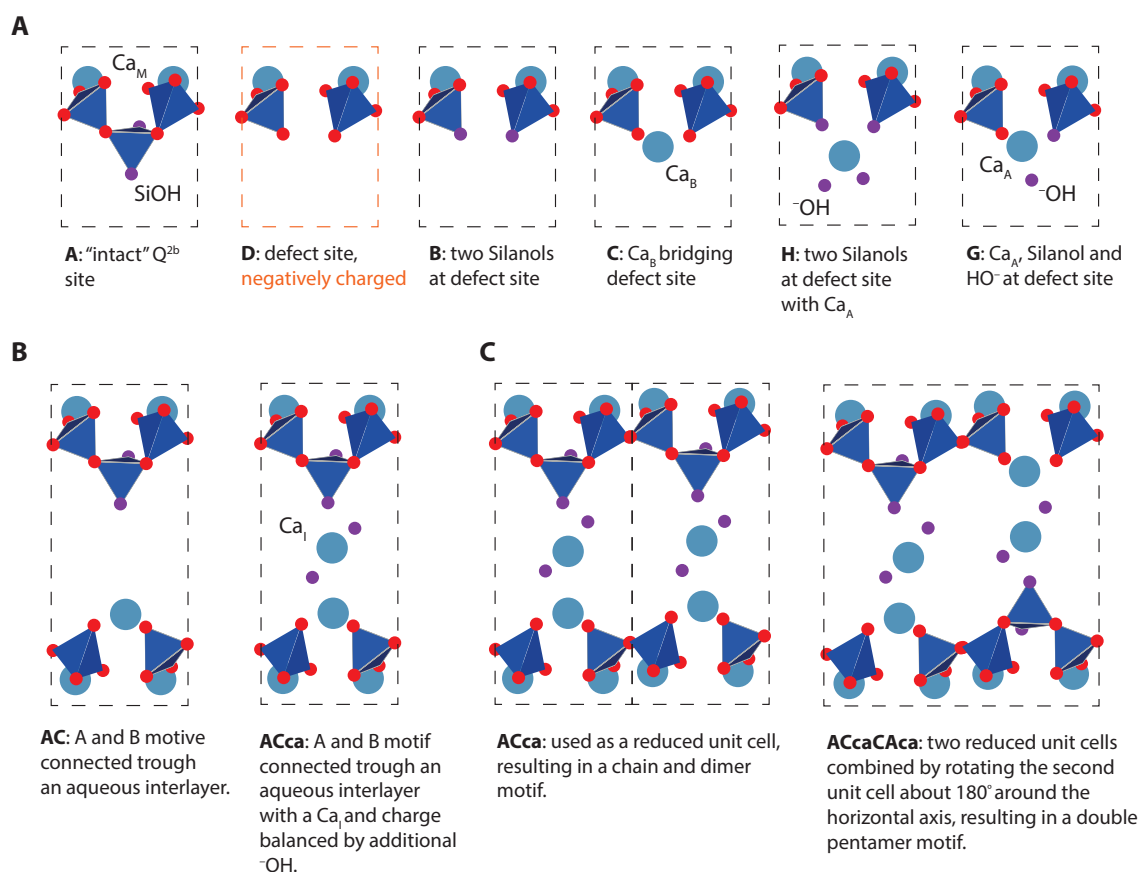


**Figure S16 | Defect classification. (A) Simple defect units. (B) Simple defect units are combined with added interlayer water to form reduced unit cells.  $^1H$  chemical shifts are calculated for structurally viable reduced unit cells. (C) Two possible ways of combining two reduced unit cells, showing how infinite chain, dimer, and pentamer motifs can be generated. The water in the aqueous interlayer and the hydrogen atoms are not shown.**

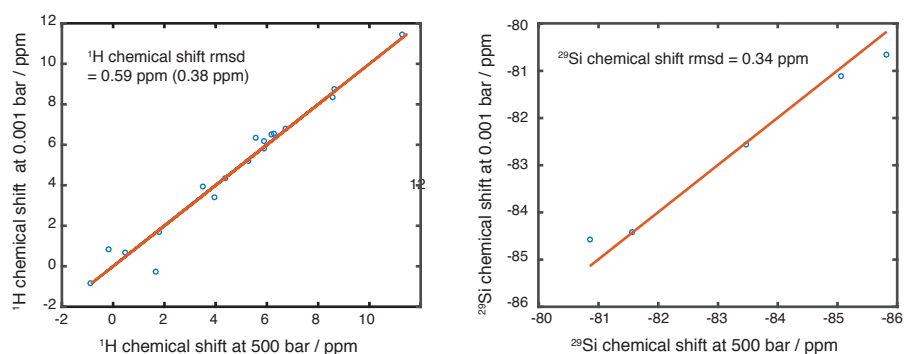


**Figure S17 | Calculated chemical shift correlations between DFT structures of C-S-H based upon the ACcaV2 motif at 500 bar and 0.001 bar.**

Using the constraints from 1D  $^{29}\text{Si}$  NMR and INADEQUATE experiments, we have calculated the number of dimers and the mean repeat index of the distribution. These two values are then used to fit a chain distribution, which was determined using the following Monte Carlo procedure:

1. We define a cutoff of  $n = 10$  for the repeat index ( $x_n = 0$  for  $n \geq 11$ ).
2. For  $n \geq 2$ , the mole fractions are generated by a random number that is uniformly distributed between 0 to its theoretical maximum value given by the contribution to the  $\text{Q}^{(2\text{p})}$ - $\text{Q}^{(2\text{p})}$  correlation for that Ca:Si ratio:

$$x_{n \geq 2} = r \text{ where } 0 \leq r \leq \frac{1-x_0}{n-1}$$

3. Pentamers constitute the remaining fraction.
4. A chain distribution is accepted only if the difference between mean repeat index ( $\sum_n x_n n$ ) obtained from the distribution and that calculated from the NMR constraints is less than 0.0005.
5. This procedure is iterated and the average fractions are stored.
6. The iteration is continued until the average values of the distribution converge to a unique distribution.

The random chain distributions calculated for each Ca:Si ratio are shown in Figure S19. For constructing our representative C-S-H structures, the longest chain used is a tetradecamer ( $n = 4$ ), as indicated in Figure S19C.

The reduced unit cells deemed likely structural elements (see Section XIII) are permuted and stacked in the directions of the crystal axes in order to build a three-dimensional crystal structure satisfying all of our experimental NMR constraints. The proposed structures are shown in Figure S18 and their silicate species distributions are compared with the experimental values in Figure S19 (A and B).

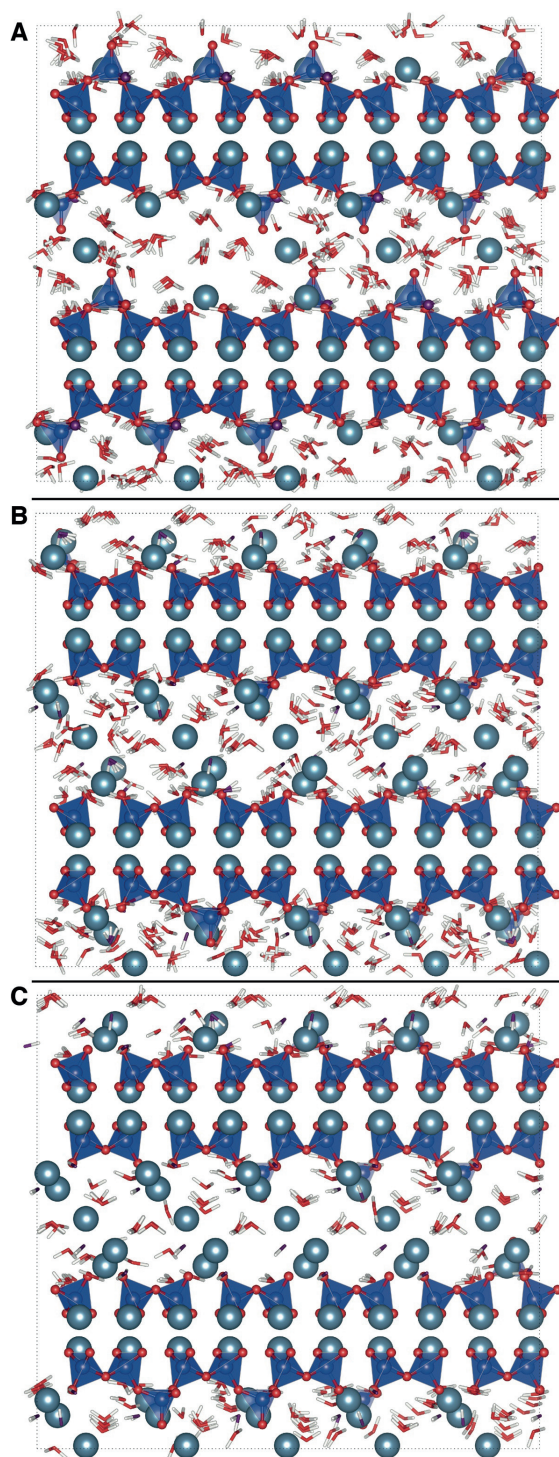


**Figure S18 | Proposed structures satisfying the NMR constraints for Ca:Si = 1.25 (A), Ca:Si = 1.75 (B) and Ca:Si = 2.00 (C) viewed along the [100] direction. The relative positions of hydroxyls and water molecules have been relaxed with energy minimization at 0 K. Corresponding relaxed structures using MD are shown in Figure S20.**

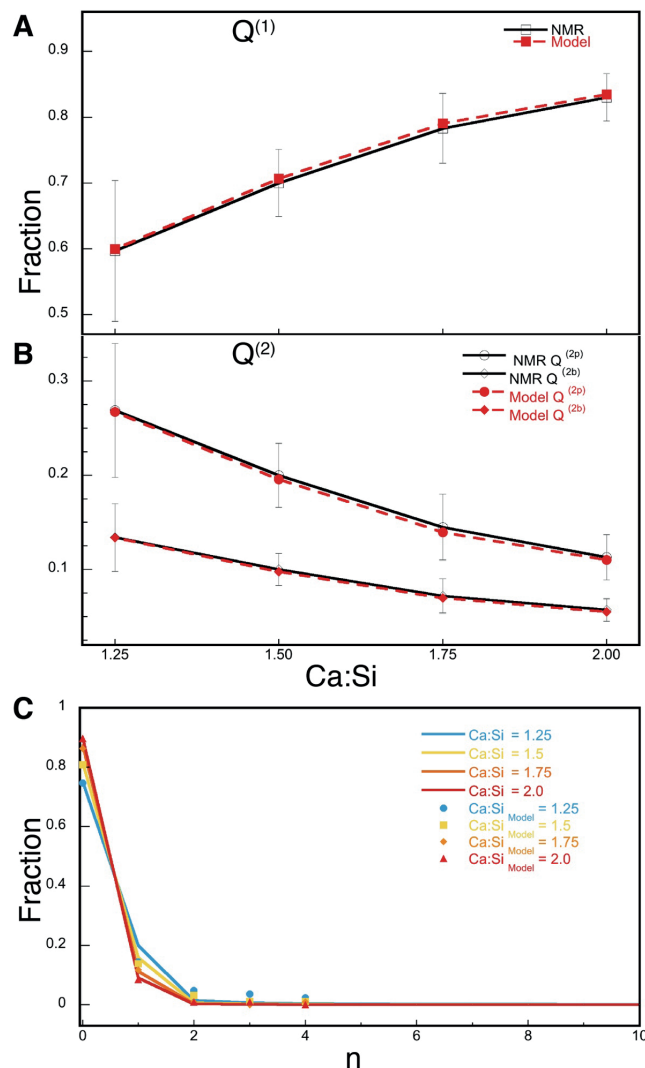


**Figure S19 | Distribution of silicate species determined by NMR compared to those predicted by the random distribution model. (A) Comparison between  $Q^{(1)}$  populations and (B)  $Q^{(2)}$  populations. The experimental values are shown in unfilled markers connected by solid lines whereas the corresponding values in our proposed structures are shown in filled markers connected by dashed lines. (C) Distribution of silicate chains according to the random distribution model. The mole fractions (up to  $n = 4$ ) used in our representative C-S-H structures are shown as markers.**

## XII. Structural Relaxation

Initial structural relaxation was performed with classical molecular dynamics using force field potentials. The force field parameters used are known to describe well cementitious material systems.<sup>18</sup> Simulations were done using a constant pressure ensemble at 300 K and a time step of 0.7 fs using Velocity Verlet integration algorithms implemented in DLPOLY.<sup>24</sup> Ewald summation was used to take into account the long range forces above a cutoff distance of 8.5 Å. Snapshots after 2 ns of molecular dynamics simulation of each structure are shown in Figure S20 and are found to be structurally stable. Stoichiometry of the structures, bond distances and average calcium coordination numbers of bulk structures minimized after 2 ns



are presented in Table S13. The bond distances from MD simulations are realistic. Histograms showing the distribution of coordination numbers for main phase calcium, interlayer calcium, and grand total of all calcium in these bulk C-S-H representations are shown in Figure S21. A systematic shift of the coordination number toward lower values is inevitable due to anharmonic vibrational motion of the atoms with respect to their proper equilibrium positions, an effect which is a function of the choice of force field used for the simulations. To estimate the magnitude of this shift for these systems, we carried out MD simulations on the known structure of 14 Å tobermorite for which 20% of the calcium are six coordinate and 80% are seven coordinate. The 2 ns MD snapshot of 14 Å tobermorite indicates roughly 30% fivefold coordination and 70% sixfold coordination. Therefore, we expect the results in Figure S21 to systematically underestimate a proper coordination number by nearly one.

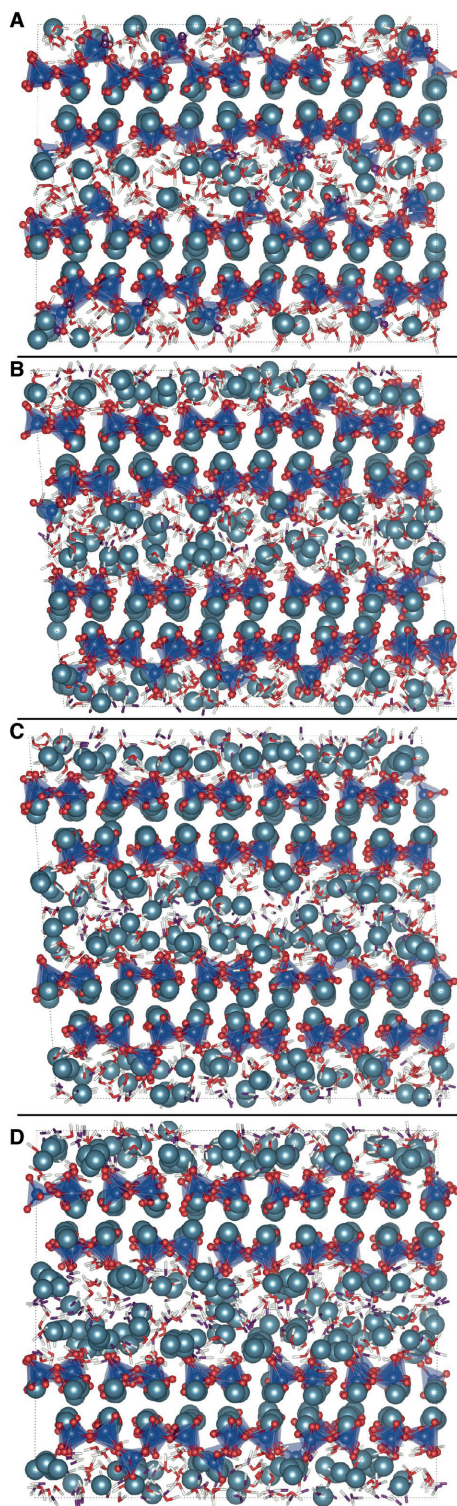


**Figure S20 | Snapshots of bulk structures relaxed for 2 ns using classical MD simulations. The structures shown are (A) Ca:Si = 1.25, (B) Ca:Si = 1.5 , (C) Ca:Si = 1.75 and (D) Ca:Si = 2.0 respectively viewed along the [100] axes. All simulations produced structurally stable defective tobermorite features.**

| Ca:Si | Chemical formula                                  | $Ca - OH / Ca$<br>[%] | $Ca - O$<br>[Å] | $Si - O$<br>[Å] | CN<br>(Ca-O) |
|-------|---|-----------------------|-----------------|-----------------|--------------|
| 1.25  | $Ca_{1.25} Si O_{3.2} (OH)_{0.1} (H_2O)_{1.82}$   | 0                     | $2.3 \pm 0.12$  | $1.55 \pm 0.08$ | 5.9          |
| 1.50  | $Ca_{1.5} Si O_{3.35} (OH)_{0.30} (H_2O)_{1.91}$  | 10                    | $2.3 \pm 0.12$  | $1.55 \pm 0.08$ | 5.9          |
| 1.75  | $Ca_{1.75} Si O_{3.39} (OH)_{0.71} (H_2O)_{1.72}$ | 20.1                  | $2.3 \pm 0.12$  | $1.55 \pm 0.08$ | 5.8          |
| 2.00  | $Ca_2 Si O_{3.41} (OH)_{1.18} (H_2O)_{1.31}$      | 29.4                  | $2.3 \pm 0.12$  | $1.55 \pm 0.08$ | 5.8          |

**Table S13 | Structural characteristics of the representative C-S-H structures. These values are given for MD structures relaxed for 2 ns. These values show that the chemical and physical environment in the structures are realistic. Ca-OH/Ca indicates the percentage of Ca atoms charge compensated by hydroxyl ions. The errors on the force field were estimated to be around 5% on distances<sup>25</sup>**

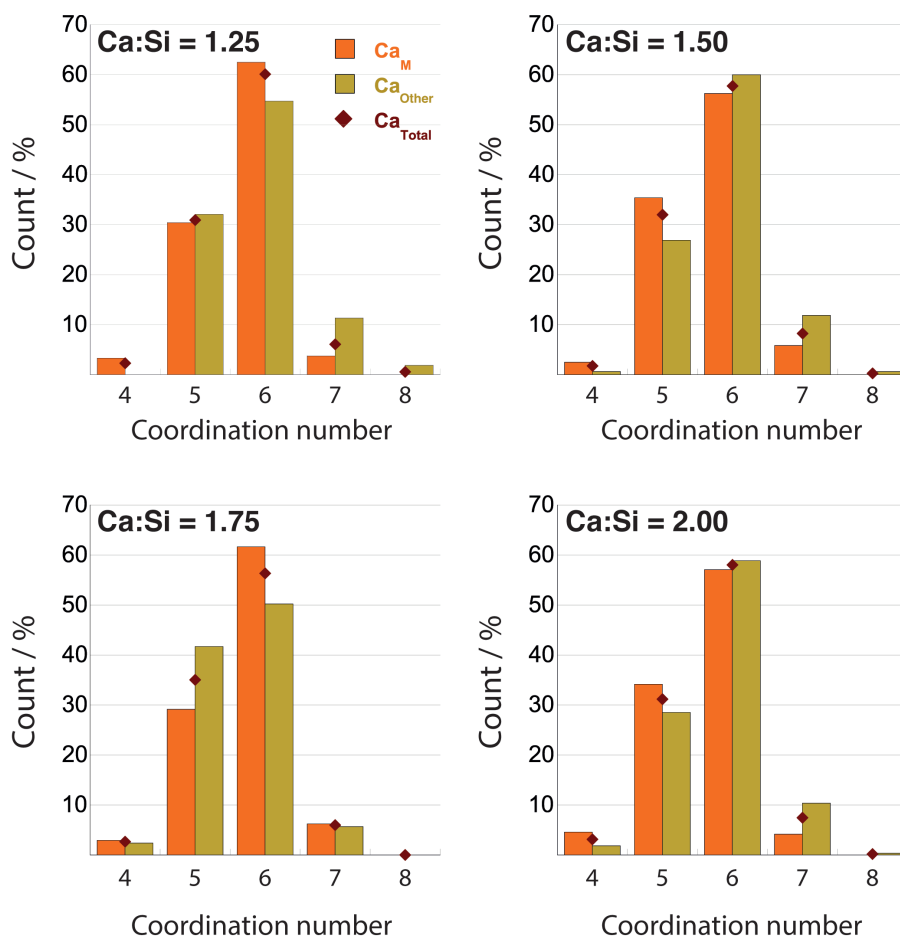


**Figure S21 | Histograms showing populations of coordination numbers for each of the representative C-S-H structures. These values are given for MD structures relaxed for 2 ns. Orange and green bars indicate coordination of main phase and all other calcium, defined as  $Ca_M$  and  $Ca_{Other}$ . The black markers indicate the coordination over all calcium in the structure ( $Ca_{Total}$ ). Owing to positional bias in the MD simulated structures, the populations are systematically shifted toward lower coordination number by nearly one.**

We also find that in the Ca:Si = 1.75 structure 20% of Ca atoms are charge compensated by hydroxyl ions. Thomas et al.<sup>26</sup> calculated this value to be 23% in C-S-H with Ca:Si = 1.7 in hydrated cement samples and argued that such a bonding is possible only if a structural motif resembling jennite is present. Our results show that the jennite structural motif is not required to give this hydroxyl charge compensation – a highly defective tobermorite is sufficient. We have not considered any structures with a defective jennite motif, in which a missing dimer is replaced by two OH<sup>-</sup> groups. Pentamers, octamers, undecamers and tetradecamers are the only non-dimers in our proposed structures limited by the box size considered. Generally, the interlayer separation distance shrinks up to 2 Å (down from 14 Å) upon structural relaxation for Ca:Si ≤ 1.5, affirming our choice of 14 Å tobermorite as a reasonable base structure. Clinotobermorite or other orthotobermorites can also be treated as the base structure satisfying the <sup>29</sup>Si and <sup>1</sup>H NMR constraints but without additional information describing the calcium environment in C-S-H it is difficult to evaluate which form of tobermorite would serve as the best base structure.

### XIII. Proton chemical shift calculations

The <sup>1</sup>H chemical shift calculations are performed on the set of reduced unit cells displayed in Figure S22. These reduced unit cells are selected to ensure a wide variety of different local defect environments, classified according to Figure S16A, are captured. We also probe the influence of Ca<sub>I</sub> in the aqueous interlayer and perform a test of the influence of medium range interactions by studying the containing pentamers rather than infinitely long silicate chains and dimers, which are the only types of chains possible without juxtaposition of different reduced unit cells. Calculated proton chemical shift spectra for each of these structural candidates are shown in Figure S23. Structures that are not distinguishable on the basis of defect classification may have different arrangements of water molecules in the interlayer, representing viable structures with different local energy minima and indicated as different “versions” in Figure S23.

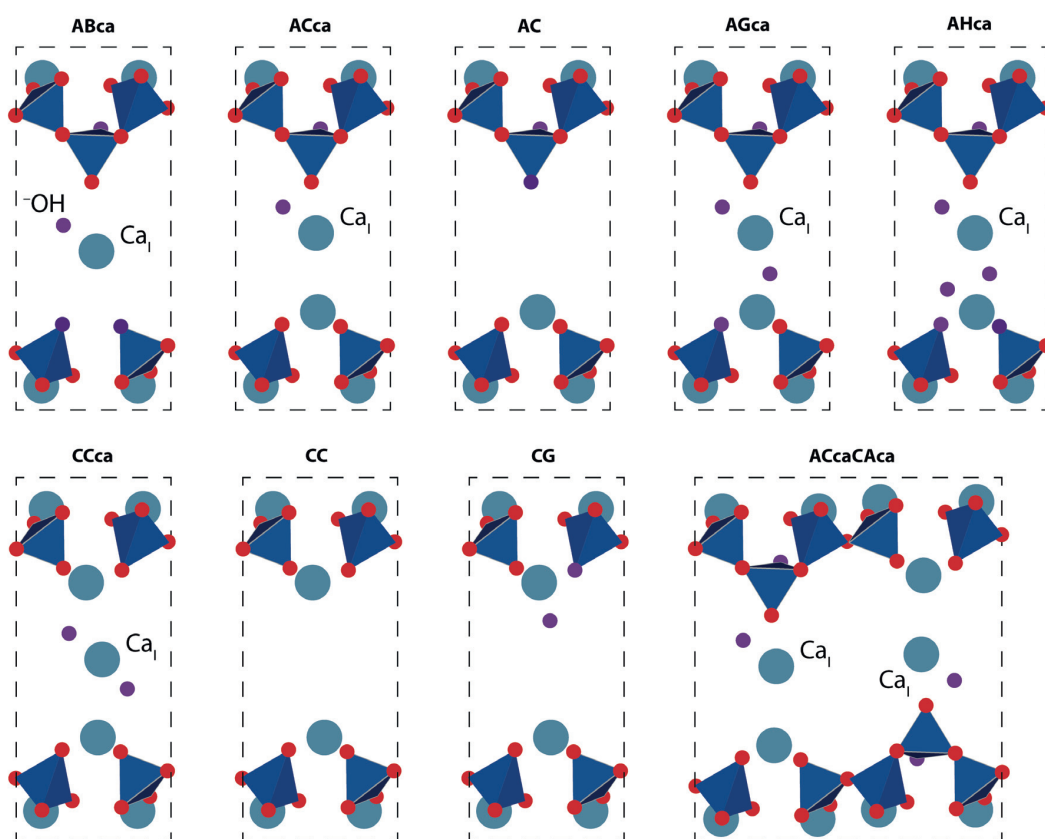


Figure S22 | Reduced unit cells used in  $^1\text{H}$  and  $^{29}\text{Si}$  chemical shift calculations. Interlayer water molecules are not shown.

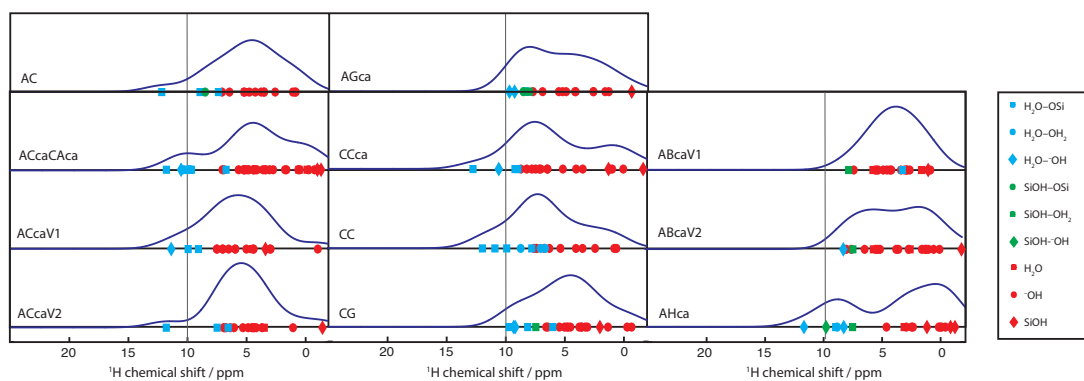


Figure S23 | Calculated spectra of  $^1\text{H}$  GIPAW isotropic magnetic shifts for the investigated reduced unit cells of C-S-H. The line-shapes  $S(\delta)$  are extrapolated from the calculated chemical shifts  $\delta_{calc}$  as  $S(\delta) = \frac{1}{\sqrt{2\pi R^2}} \exp \left[ -\frac{1}{2} \left( \frac{\delta - \delta_{calc}}{R} \right)^2 \right]$  with  $R = 1.5$  ppm. In general, structures with  $\text{Ca}_B$  at the bridging site (types AC, CC, CG) better reproduce the characteristic tail in the  $^1\text{H}$  line shape above 10 ppm. Structures that

are identical according to our defect classification scheme but possess different arrangements of water molecules in the interlayer are distinguished by V1 or V2.

#### XIV. $^{29}\text{Si}$ chemical shift calculations

In addition to the  $^1\text{H}$  chemical shift calculations, we also calculate  $^{29}\text{Si}$  chemical shift parameters (Figure S24) for all structures used in Figure S23. The calculated  $^{29}\text{Si}$  chemical shifts are compared to previous calculations<sup>27</sup> and to our experimental results. To the level of intrinsic accuracy of  $^{29}\text{Si}$  chemical shift calculations, there is good agreement between the three datasets, allowing us to conclude that the C-S-H models proposed here are a good approximation of the studied systems.

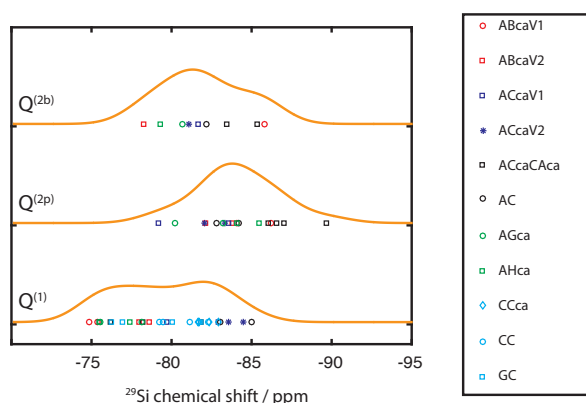


Figure S24 | Overlap of calculated  $^{29}\text{Si}$  GIPAW isotropic magnetic shift spectra for each different Si site in the calculated structures shown in Figure S23. The line-shapes  $S(\delta)$  are extrapolated from the calculated chemical shifts  $\delta_{calc}$  as  $S(\delta) = \frac{1}{\sqrt{2\pi}R} \exp\left[-\frac{1}{2}\left(\frac{\delta - \delta_{calc}}{R}\right)^2\right]$  with  $R = 1.5$  ppm.

#### XV. References

- (1) Brinker, C. J.; Scherer, G. W. *Sol-Gel Science: The Physics and Chemistry of Sol-Gel Processing*; Gulf Professional Publishing, 1990.
- (2) Iller, R. K. *The Chemistry of Silica: Solubility, Polymerization, Colloid and Surface Properties and Biochemistry of Silica*; Wiley, 1979.
- (3) Kulik, D. A.; Wagner, T.; Dmytrieva, S. V.; Kosakowski, G.; Hingerl, F. F.; Chudnenko, K. V.; Berner, U. R. GEM-Selektor Geochemical Modeling Package: Revised Algorithm and GEMS3K Numerical Kernel for Coupled Simulation Codes. *Comput. Geosci.* **2012**, *17* (1), 1–24.
- (4) Galmarini, S. Atomistic Simulation of Cementitious Systems, Ecole Polytechnique Fédérale de Lausanne: Lausanne, 2013.
- (5) Kulik, D. A. Improving the Structural Consistency of C-S-H Solid Solution Thermodynamic Models. *Cem. Concr. Res.* **2011**, *41* (5), 477–495.
- (6) *RMN*, version 1.8.4; software for multi-dimensional signal processing; PhySy Ltd: Grandview Heights, OH, 2016.
- (7) Lesage, A.; Bardet, M.; Emsley, L. Through-Bond Carbon–Carbon Connectivities in Disordered Solids by NMR. *J. Am. Chem. Soc.* **1999**, *121* (47), 10987–10993.



- (8) States, D. J.; Haberkorn, R. A.; Ruben, D. J. A Two-Dimensional Nuclear Overhauser Experiment with Pure Absorption Phase in Four Quadrants. *J Magn. Reson.* **1982**, *48*, 286–292.
- (9) Ernst, R. R.; Bodenhausen, G.; Wokaun, A. *Principles of Nuclear Magnetic Resonance in One and Two Dimensions*; International Series of Monographs on Chemistry; Clarendon Press, 1987.
- (10) van Rossum, B.-J.; Förster, H.; de Groot, H. J. M. High-Field and High-Speed CP-MAS  $^{13}\text{C}$  NMR Heteronuclear Dipolar-Correlation Spectroscopy of Solids with Frequency-Switched Lee–Goldburg Homonuclear Decoupling. *J. Magn. Reson.* **1997**, *124* (2), 516–519.
- (11) Elena, B.; de Paëpe, G.; Emsley, L. Direct Spectral Optimisation of Proton–Proton Homonuclear Dipolar Decoupling in Solid-State NMR. *Chem. Phys. Lett.* **2004**, *398* (4–6), 532–538.
- (12) Rossini, A. J.; Zagdoun, A.; Lelli, M.; Gajan, D.; Rascón, F.; Rosay, M.; Maas, W. E.; Copéret, C.; Lesage, A.; Emsley, L. One Hundred Fold Overall Sensitivity Enhancements for Silicon-29 NMR Spectroscopy of Surfaces by Dynamic Nuclear Polarization with CPMG Acquisition. *Chem Sci* **2012**, *3* (1), 108–115.
- (13) Brunet, F.; Bertani, P.; Charpentier, T.; Nonat, A.; Virlet, J. Application of  $^{29}\text{Si}$  Homonuclear and  $^1\text{H}$ – $^{29}\text{Si}$  Heteronuclear NMR Correlation to Structural Studies of Calcium Silicate Hydrates. *J. Phys. Chem. B* **2004**, *108* (40), 15494–15502.
- (14) Alemany, L. B.; Grant, D. M.; Pugmire, R. J.; Alger, T. D.; Zilm, K. W. Cross Polarization and Magic Angle Sample Spinning NMR Spectra of Model Organic Compounds. 2. Molecules of Low or Remote Protonation. *J. Am. Chem. Soc.* **1983**, *105* (8), 2142–2147.
- (15) Richardson, I. G. The Nature of C-S-H in Hardened Cements. *Cem. Concr. Res.* **1999**, *29* (8), 1131–1147.
- (16) Cong, X.; Kirkpatrick, R. J.  $^{29}\text{Si}$  MAS NMR Study of the Structure of Calcium Silicate Hydrate. *Adv. Cem. Based Mater.* **1996**, *3* (3–4), 144–156.
- (17) Watson, G. W.; Kelsey, E. T.; Leeuw, N. H. de; Harris, D. J.; Parker, S. C. Atomistic Simulation of Dislocations, Surfaces and Interfaces in MgO. *J. Chem. Soc., Faraday Trans.* **1996**, *92* (3), 433–438.
- (18) Galmarini, S.; Kunhi Mohamed, A.; Bowen, P. Atomistic Simulations of Silicate Species Interaction with Portlandite Surfaces. *J. Phys. Chem. C* **2016**, *120* (39), 22407–22413.
- (19) Perdew, J. P.; Burke, K.; Ernzerhof, M. Generalized Gradient Approximation Made Simple. *Phys. Rev. Lett.* **1996**, *77* (18), 3865–3868.
- (20) Giannozzi, P.; Baroni, S.; Bonini, N.; Calandra, M.; Car, R.; Cavazzoni, C.; Ceresoli, D.; Chiarotti, G. L.; Cococcioni, M.; Dabo, I.; et al. QUANTUM ESPRESSO: A Modular and Open-Source Software Project for Quantum Simulations of Materials. *J. Phys. Condens. Matter* **2009**, *21*, 395502.
- (21) Yates, J. R.; Pickard, C. J.; Mauri, F. Calculation of NMR Chemical Shifts for Extended Systems Using Ultrasoft Pseudopotentials. *Phys. Rev. B* **2007**, *76* (2), 24401.
- (22) Pack, J. D.; Monkhorst, H. J. Special Points for Brillouin-Zone Integrations. *Phys. Rev. B* **1977**, *16* (4), 1748–1749.
- (23) Salager, E.; Day, G. M.; Stein, R. S.; Pickard, C. J.; Elena, B.; Emsley, L. Powder Crystallography by Combined Crystal Structure Prediction and High-Resolution  $^1\text{H}$  Solid-State NMR Spectroscopy. *J. Am. Chem. Soc.* **2010**, *132* (8), 2564–2566.
- (24) Todorov, I. T.; Smith, W.; Trachenko, K.; Dove, M. T. DL\_POLY\_3: New Dimensions in Molecular Dynamics Simulations via Massive Parallelism. *J. Mater. Chem.* **2006**, *16* (20), 1911–1918.

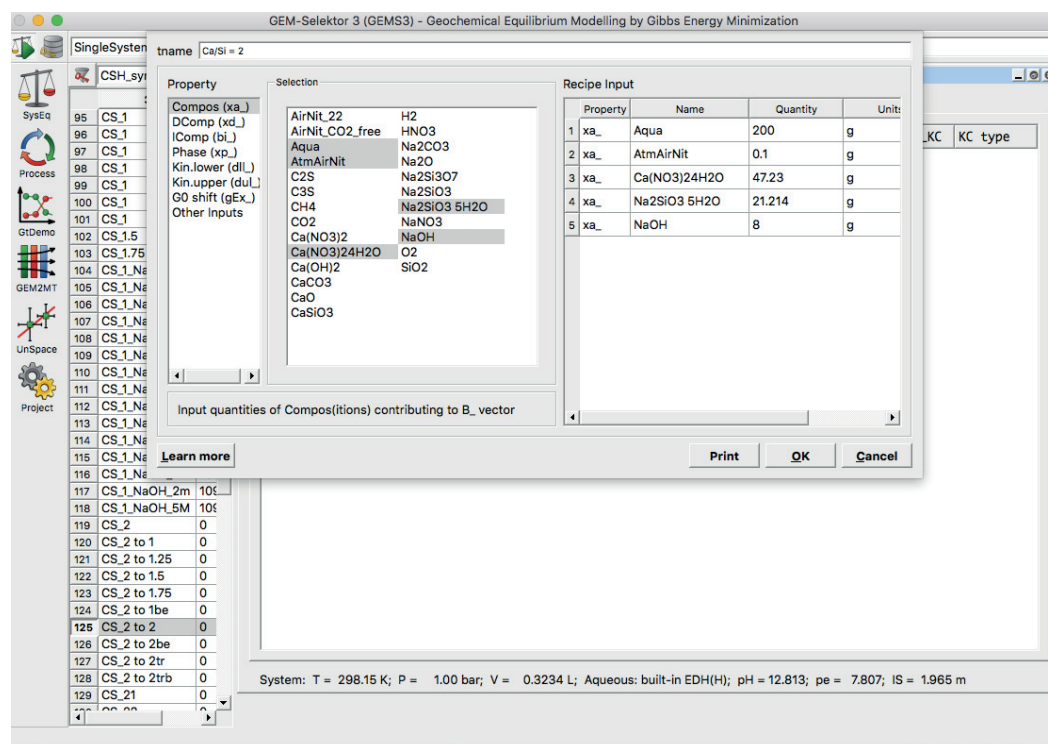
- (25) Galmarini, S.; Bowen, P. Atomistic Simulation of the Adsorption of Calcium and Hydroxyl Ions onto Portlandite Surfaces — towards Crystal Growth Mechanisms. *Cem. Concr. Res.* **2016**, *81*, 16–23.
- (26) Thomas, J. J.; Chen, J. J.; Jennings, H. M.; Neumann, D. A. Ca–OH Bonding in the C–S–H Gel Phase of Tricalcium Silicate and White Portland Cement Pastes Measured by Inelastic Neutron Scattering. *Chem. Mater.* **2003**, *15* (20), 3813–3817.
- (27) Rejmak, P.; Dolado, J. S.; Stott, M. J.; Ayuela, A.  $^{29}\text{Si}$  NMR in Cement: A Theoretical Study on Calcium Silicate Hydrates. *J. Phys. Chem. C* **2012**, *116* (17), 9755–9761.



## SI B: Supplementary information for thermodynamics modeling and fluid mechanics calculations.

### I. GEMS

GEMS<sup>1-4</sup> is thermodynamics speciation calculating software employed throughout this thesis work. For the synthesis of C-S-H at Ca:Si =2, starting with a solution of Calcium nitrate at 0.2M and Sodium silicate at 0.1M with NaOH added as pH regulator is presented below.

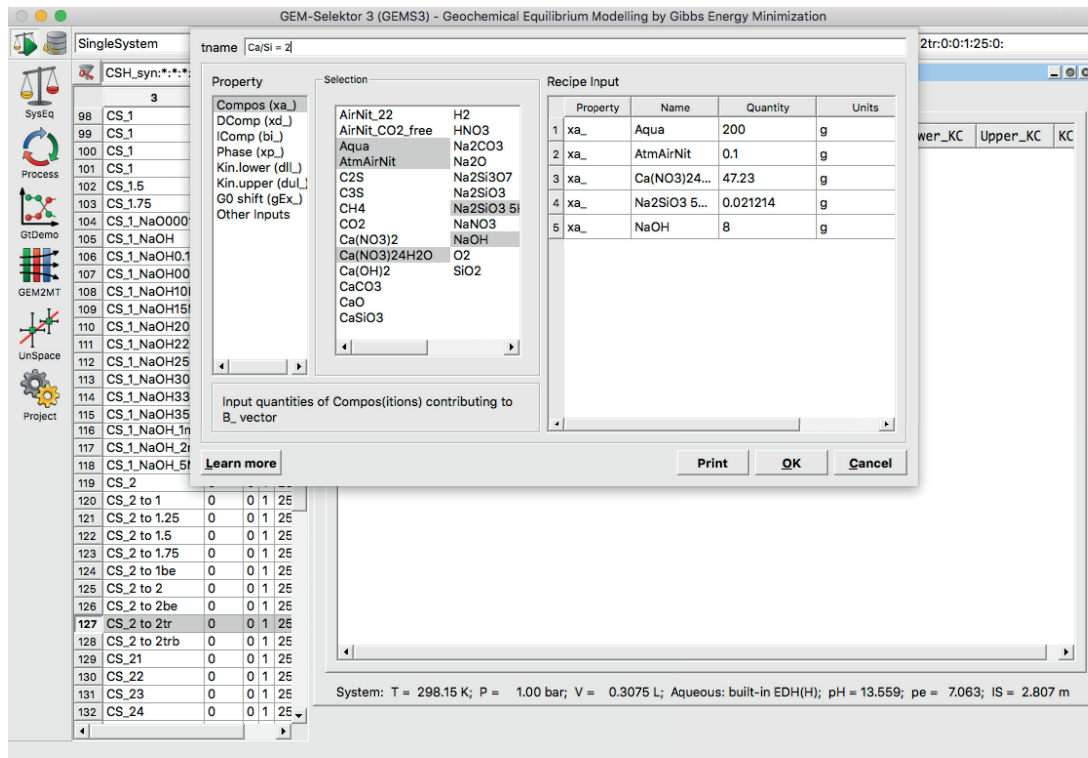


This recipe leads to the formation of Ca:Si ratio of 2 in the solid C-S-H but GEMS only predicts this ratio's once the formation of Calcium hydroxide (CH) is switched off. In normal circumstances the maximum Ca:Si ratio shown by C-S-H is 1.6 without the formation of CH. Similarly for other ratio the amount of NaOH can be decreased simultaneously, The amount of NaOH needed for formation of different Ca:Si ratio is presented below.

| Target Ca:Si<br>(GEMS) | NaOH (GEMS)<br>10M |
|------------------------|--------------------|
| 1.0                    | 0.05 mL            |
| 1.25                   | 5.16 mL            |
| 1.5                    | 10.58 mL           |
| 1.75                   | 16.62 mL           |
| 2                      | 20.00 mL           |

Table 1: Amount of 10M NaOH needed for different Ca:Si ratios

For *nanoneedle* formation, same recipe as for nanofoils is followed with reduction in the silicate concentration by 3 order of magnitude (similar to hydrating cementitious system)<sup>5</sup>



## II. Fluid mechanics Calculations

It is important aspect to verify if we are constrained with the any physical parameter. We put down the standard values, later used for calculation in mixing time.

- **Flow rate:** 0.1 ml/min to 5 ml/min
- **Volume of each drop:** 0.132 ml
- **Time between each drop:** 4.5 s
- **Rotational Stirring ( $\omega$ ):** 700 rpm
- **Diameter of reactor (d):** 20 cm = 0.2m
- **Diffusional constant in Aqueous system:**  $D_m = 1.00E-08$  Pa.s
- **Dynamic Viscosity ( $\mu$ ):**  $0.9E-03$  Pa.s, N s/m<sup>2</sup>
- **Density of fluid ( $\rho$ ):** 1 kg/m<sup>3</sup>
- **Velocity (u) =  $\omega d$ :** 140 m/s
- **Kinematic viscosity ( $\nu = \mu/\rho$ ):**  $9E-06$  m<sup>2</sup>/s

|                             | Definition  | Equations                  | Calculation |
|-----------------------------|---|----------------------------|-------------|
| <b>Reynolds number (Re)</b> | $\frac{\text{inertial forces}}{\text{Viscous forces}}$        | $\frac{\rho * V * L}{\mu}$ | 3.15E+04    |
| <b>Schmidt number (Sc)</b>  | $\frac{\text{momentum diffusivity}}{\text{mass diffusivity}}$ | $\frac{\mu}{\rho * D_m}$   | 8.90E+04    |
| <b>Peclet number</b>        | $\frac{\text{Convection}}{\text{Diffusion}}$                  | Re*Sc                      | 2.80E+09    |

|                                  |   |   |                                  |
|----------------------------------|---|---|----------------------------------|
| Power number ( $N_p$ )           | $\frac{\text{resistance force}}{\text{inertia forces}}$ | $\frac{P}{N^3 * D^5 * \rho} = Ne * N^3 * D^5 * \rho$                        | 1                                |
| Specific Power $\epsilon$ (W/kg) | Power input per kg                                      | $\frac{Np * N^3 * D^5}{V}$  | 548800 (flowrate 0.1ml/min)      |
| Flow number ( $N_q$ )            | Re  | $\frac{\rho * V * L}{\mu}$  | 3.15E+04 (flowrate 0.1ml/min)    |
| Mean Shear rate                  | Watt/Kg   | $\dot{\gamma} = \left( \left( \frac{\epsilon}{2 * V} \right) \right)^{0.5}$ | 234.2648074 (flowrate 0.1ml/min) |

- **Micromixing mode:** The mixing is contributed by diffusion (Small dimension) and shear (created by static mixer).

We can apply, Slab diffusion model: Mixing time (Diffusion + shear)<sup>6-9</sup>

$$tm = \left( \frac{1}{2 * \dot{\gamma}} \right) * \operatorname{arcsinh} \left( \frac{0.76 * \dot{\gamma} * \delta^2}{D_m} \right) \dots \dots \dots [1]$$

Where, mean shear deformation rate in tube:

$$\dot{\gamma} = \left( \left( \frac{\epsilon}{2 * V} \right) \right)^{0.5} \dots \dots \dots [2]$$

Pressure drop (Hagen-Poiseuille):  $\frac{\Delta P}{L} = \frac{32 * \mu * u}{d^2} \dots \dots \dots [3]$

Power dissipation:  $\epsilon = \frac{Q * \Delta P}{\rho * V} \dots \dots \dots [4]$

From equation 2-4, the equation can be simplified as following

$$tm = \left( \frac{d}{8 * u} \right) * \ln(1.52 * Pe) \text{ or } tm = \left( \frac{d}{8 * u} \right) * \ln \left( \frac{u * 1.52 * d}{Dm} \right)$$

Mixing time in the flowrate range of our experiment, with fixed diameter of micromixer and diffusion constant



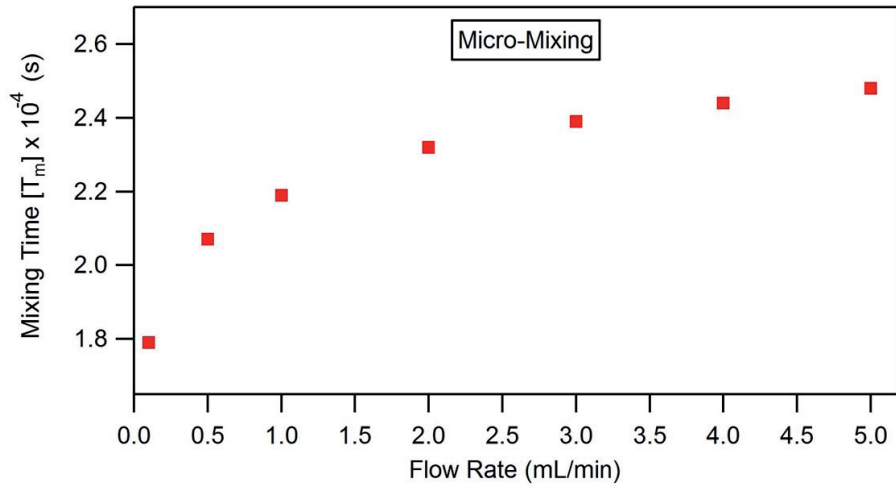


Figure 1: Mixing time vs. flow rate in *micromixer* mode

- **Dropwise / Reverse-dropwise** mode: Mixing time calculated for a single drop to be mixed with the solution and compared with the time before the next drop arrive. In this system, the Peclet number is very high indicating mixing is governed by convection not diffusion. Hence is directly proportional to the power input by rotating magnetic stirrer in overcoming opposing forces in solution. It can be empirically expressed as<sup>9</sup>

$$tm = 0.0075 * \epsilon^{-0.5}$$

Where  $\epsilon$ , is power input to the solution given by

$$\epsilon = \frac{Np * N^3 * D^5}{V}$$

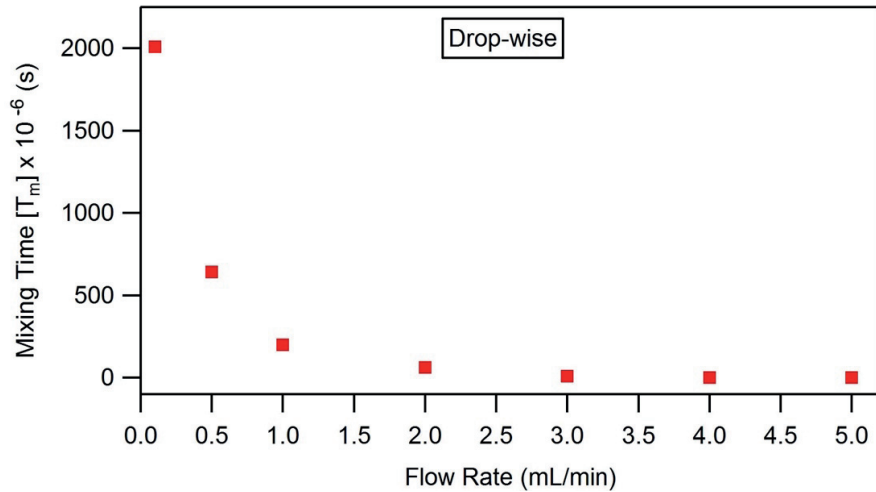


Figure 2: Mixing time vs. flow rate in *dropwise* mode

### III References

1. Kulik, D. A. *et al.* GEM-Selektor geochemical modeling package: revised algorithm and GEMS3K numerical kernel for coupled simulation codes. *Comput. Geosci.* **17**, 1–24 (2012).
2. Kulik, D. A. Improving the structural consistency of C-S-H solid solution thermodynamic models. *Cem. Concr. Res.* **41**, 477–495 (2011).
3. Kulik, D. A. *et al.* GEM-Selektor geochemical modeling package: revised algorithm and GEMS3K numerical kernel for coupled simulation codes. *Comput. Geosci.* **17**, 1–24 (2013).
4. Leal, A. M. M., Kulik, D. A., Smith, W. R. & Saar, M. O. An overview of computational methods for chemical equilibrium and kinetic calculations for geochemical and reactive transport modeling. *Pure Appl. Chem.* **89**, 597–643 (2017).
5. Brown, P. W., Pommersheim, J. & Frohnsdorff, G. A kinetic model for the hydration of tricalcium silicate. *Cem. Concr. Res.* **15**, 35–41 (1985).
6. Bałdyga, J., Makowski, Ł. & Orciuch, W. Interaction between Mixing, Chemical Reactions, and Precipitation. *Ind. Eng. Chem. Res.* **44**, 5342–5352 (2005).
7. Henzler, H.-J. Continuous Mixing of Fluids. in *Ullmann's Encyclopedia of Industrial Chemistry* (Wiley-VCH Verlag GmbH & Co. KGaA, 2000).
8. Kraume, M., Merz, C. & Henzler, H.-J. Continuous Mixing of Fluids. in *Ullmann's Encyclopedia of Industrial Chemistry* (Wiley-VCH Verlag GmbH & Co. KGaA, 2000).
9. Kashid, M. N., Renken, A. & Kiwi-Minsker, L. *Microstructured Devices for Chemical Processing*. (John Wiley & Sons, 2014).



## SI C: Supplementary information for the article – The Kinetics analysis of C-S-H formation.

### I. Solving PBE

In order to solve for a particulate system, the set of equations for the first  $k$  moments of interest should be closed, i.e., involve only functions of the moments themselves, which is in most cases not the case.<sup>24, 25</sup> Since moments depend on time, the moment closure problem has to be solved every time step during the numerical integration of the differential equations. Therefore, the numerical algorithm has to be efficient and fast. For this purpose quadrature-based moment methods (QBMM) that reconstruct the NDF from a finite set of moments will be employed.<sup>22</sup>

In univariate quadrature method of moments (QMOM) the closure problem (i.e., calculating integrals dependent on  $n(t, L)$ ) is overcome by resorting to an interpolation formula:

$$\int_{\Omega_L} n(t, L)g(L)dL \approx \sum_{\alpha=1}^N w_{\alpha}g(L_{\alpha}) \quad (1)$$

where  $g(L)$  is any function of interest while  $w_{\alpha}$  and  $L_{\alpha}$  are, respectively, the weights and nodes of the interpolation formula, and  $N$  is the number of nodes used to approximate the NDF (quadrature order). Unit consistency dictates that  $w_{\alpha}$  have units equivalent to  $n(t, L)dL$  (# particles.m<sup>-3</sup> suspension). QMOM takes advantage of Gaussian quadrature of order  $N$  which offers a degree of accuracy of  $2N-1$ . Therefore, it will be able to capture the first  $2N-1$  moments of the weight function. Conversely,  $N$  nodes (abscissas) and  $N$  weights shall be obtained by solving the following nonlinear system, assuming the knowledge of the first  $2N-1$  moments of the NDF.

$$\begin{aligned} m_0 &= \sum_{\alpha=1}^N w_{\alpha}, \\ m_1 &= \sum_{\alpha=1}^N w_{\alpha} L_{\alpha}, \\ &\dots \\ m_{2N-1} &= \sum_{\alpha=1}^N w_{\alpha} L_{\alpha}^{2N-1} \end{aligned} \quad (2)$$

Since the above system requires a very good initial guess in order to ensure convergence, one may take advantage of the orthogonal polynomials theorem. According to this theory, a Gaussian quadrature is an interpolation formula whose  $N$  nodes are the roots of polynomial  $P_N(L)$  orthogonal to the weight function  $n(L)$ .<sup>26</sup> Among the algorithms available in order to calculate the weights and abscissas from the knowledge of a moment set, the product-difference (PD) algorithm of Gordon<sup>27</sup> and the Wheeler algorithm<sup>28, 29</sup> are useful for an arbitrary NDF. However, the latter is more stable, and is able to handle distributions with zero mean ( $m_1 = 0$ ).<sup>22</sup> schematically shows the application of the Wheeler algorithm in order to approximate a size distribution using 3, 4, and 5 quadrature nodes.

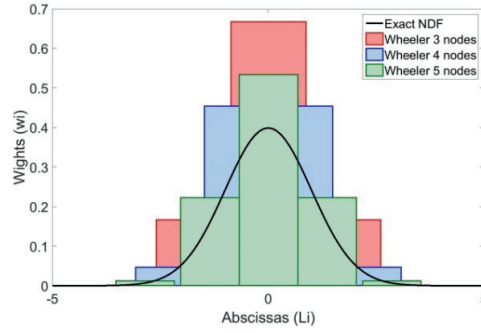


Fig. 1. Quadrature approximation of a normal distribution using Wheeler algorithm.

## II. Estimation of kinetic parameters for model C-S-H precipitation system

Knowing the aqueous speciation one may calculate the driving force for the formation of new solid phase, the supersaturation ratio, by comparing the ion activity product (IAP) of relevant species with their corresponding equilibrium value ( $K_{sp}$ ).<sup>33</sup> Having the supersaturation ratio, kinetic equations describing different particle formation processes (e.g., nucleation, growth, and aggregation) can be used to calculate various terms in the PBE set which is marched over time along with mass balances and changes in the system volume. After each time step in the integration of the ODE set, speciation should be done using the updated amounts of components. Further, recently calculated moments are introduced into the Wheeler algorithm to calculate corresponding quadrature nodes and weights necessary for some integral terms in the PBE set. The former along with the updated supersaturation ratio are used to advance the ODE set one more time step. This (internal) loop is iterated over until we reach the end of modeling period (literally the period for which experimental data is available). At this step, an external loop (optimization scheme) constructs an objective function using the summed absolute differences between the experimental data ( $Ca^{2+}(aq)$  concentration as a function of time) and equivalent calculated values. The unknown model parameters are adjusted in response to objective function values larger than a pre-defined tolerance and passed to the internal loop for coupled thermodynamic-kinetic modeling. Iteration over the external loop will finally give the optimal model parameters describing the experimental data most accurately. In the following section we will discuss the foregoing steps in more details. Throughout this work, we use MATLAB 2015b as the programming language.

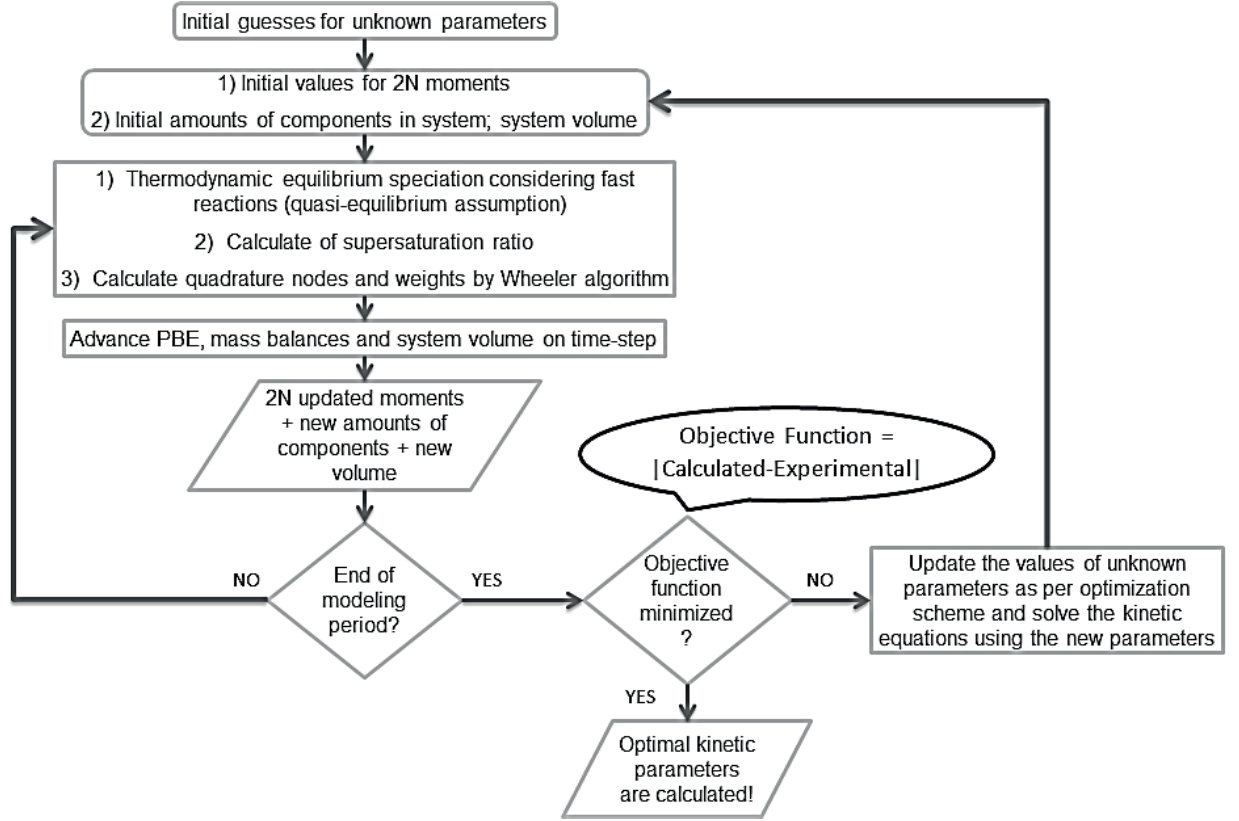


Fig. 2. Algorithm for computational estimation of kinetic parameters in precipitation processes.

### III. Aqueous speciation and thermodynamic driving force for solid formation

In the current study, the speciation is calculated by solving the system of equations composed of nonlinear laws of mass action (LMAs) and linear component and charge balance constraints.<sup>51</sup> Consider an aqueous solution comprised of NS species (including water solvent, ions, and aqueous ion pairs) and NC independent components (either elements like Ca and Si, or group of elements like OH and NH<sub>4</sub>). Knowing the overall amount of all components and considering charge neutrality for electrolyte solutions, (NS-NC-1) independent LMAs should be written to have a complete set of equations solvable for NS unknown amounts. The set of equations to be solved would then be

$$\text{Charge balance: } \Psi_1 = 0 = \sum_{i=1}^{NS} z_i n_i \quad (3)$$

$$\text{Component balance: } \Psi_j = 0 = -B_e + \sum_{i=1}^{NS} b_{e,i} n_i ; j = 2, \dots, NC + 1; e = j - 1 \quad (4)$$

$$\text{LMAs: } \Psi_j = 0 = -\log_{10} K_k + \sum_{i=1}^{NS} v_{k,i} \log_{10}(m_i \gamma_i) ; j = NC + 2, \dots, NS; k = j - NC - 1 \quad (5)$$

where  $n_i$ ,  $z_i$ ,  $b_{e,i}$ ,  $v_{k,i}$ ,  $m_i$ , and  $\gamma_i$  are mole amount, signed valence, stoichiometry of component  $e$ , signed stoichiometric coefficient in law of mass action  $k$ , molality (mol.kg<sup>-1</sup>), and molal activity coefficient for the  $i^{\text{th}}$  species, respectively.  $B_e$  is the overall molar amount of component  $e$ , and  $K_k$  is equilibrium constant for the  $k^{\text{th}}$  LMA. The system of equations made

up by Eqs. (3)(4) and (5) is often solved using an iterative Newton-Raphson-type approach.<sup>51, 53</sup> Any appropriate framework could be used to estimate the activity coefficients, from Debye–Hückel limiting law applicable for very dilute electrolyte solutions ( $I \leq 0.01$ ) to Pitzer equations working nicely up to several molal concentrations.<sup>51, 52, 54</sup> Here, the activity coefficient of water solvent is taken to be one as we are dealing with ionic strengths less than 2 molal.<sup>39, 50</sup> The activity coefficients of other species may also be adequately estimated using Truesdell-Jones (TJ) equation applicable up to ionic strength around 2 molals<sup>54-56</sup>

$$\log_{10} \gamma_i = \frac{-Az_i^2 \sqrt{I}}{1 + a_i B \sqrt{I}} + b_i I + \log_{10}(x_{H_2O}) \quad (6)$$

where  $I = \frac{1}{2} \sum_{i=1}^{NS} m_i z_i^2$  is the molal ionic strength of aqueous solution, A and B are Debye–Hückel constants characteristic of the solvent (water in this case) at pressure and temperature of interest, and  $a_i$  and  $b_i$  are ion-specific fitting parameters.<sup>55</sup> The values of fit parameters for many aqueous species can be found in Refs. <sup>55</sup> and <sup>56</sup>. The missing parameters for the current system were estimated by fitting the TJ model to x-based activity coefficients calculated by OLI Studio software (version 9.2, OLI Systems, Inc.) working based on a speciation-based mixed-solvent electrolyte activity coefficient model (MSE).<sup>57</sup> The parameter values used in the activity coefficient calculations are included in the second, third, and fourth columns of input matrix

| Species name | NS | NC     | DA    | A    | B  | T | bi | zi | zi | zi     | zi | zi | zi | zi | zi | zi | zi | zi | zi | zi |
|--------------|----|--------|-------|------|----|---|----|----|----|--------|----|----|----|----|----|----|----|----|----|----|
| H2O          | 15 | 0.3114 | 0     | 0    | 0  | 0 | 0  | 0  | 0  | 0      | 0  | 0  | 0  | 0  | 0  | 0  | 0  | 0  | 0  | 0  |
| H+           | 5  | 0.3288 | 4.78  | 0.24 | 1  | 0 | 0  | 0  | 0  | 9.85   | -1 | -1 | 0  | 0  | 0  | 0  | 0  | 0  | 0  | 0  |
| OH-          | 0  | 0      | 10.65 | 0.21 | -1 | 1 | 0  | 0  | 0  | 13.1   | -1 | 0  | 0  | 0  | 0  | 0  | 0  | 0  | 0  | 0  |
| Ca+2         | 0  | 0      | 4.86  | 0.15 | 2  | 0 | 1  | 0  | 0  | 2.083  | 0  | 0  | 0  | 0  | 1  | 1  | 1  | -1 | -1 | -1 |
| H2SiO4       | 0  | 0      | 4.5   | 0.06 | -1 | 4 | 0  | 1  | 0  | 0.91   | 0  | -1 | 0  | 0  | 0  | 0  | 0  | 0  | 0  | 0  |
| Na+          | 0  | 0      | 4.32  | 0.06 | 1  | 0 | 0  | 0  | 1  | -1.23  | 0  | 0  | 0  | -1 | 1  | 0  | 0  | 0  | 0  | 0  |
| NO3-         | 0  | 0      | 3.58  | 0    | -1 | 3 | 0  | 0  | 0  | -0.42  | 0  | 0  | 0  | 0  | 1  | 0  | 1  | 0  | 0  | 0  |
| NaHCO3       | 0  | 0      | 0     | 0.08 | 0  | 3 | 0  | 0  | 1  | 1.258  | 0  | 0  | 0  | -1 | 0  | 0  | 0  | 0  | 0  | 0  |
| CaHCO3+      | 0  | 0      | 3.93  | 0.06 | 1  | 3 | 1  | 0  | 0  | 1.4749 | 0  | 0  | 0  | 0  | 0  | 0  | -1 | 0  | 0  | 0  |
| H2SiO4       | 0  | 0      | 0     | 0.05 | 0  | 4 | 0  | 1  | 0  | 0      | 0  | 1  | 0  | 0  | 0  | 0  | 0  | 0  | 0  | 0  |
| H2SiO4-2     | 0  | 0      | 3.74  | 0    | -2 | 4 | 0  | 1  | 0  | 0      | 0  | 0  | -1 | 0  | 0  | 0  | 0  | 0  | -1 | -1 |
| CaOH+        | 0  | 0      | 3.95  | 0.06 | 1  | 1 | 1  | 0  | 0  | 0      | 0  | 0  | 0  | 0  | -1 | 0  | 0  | 0  | 0  | 0  |
| CaHSiO3+     | 0  | 0      | 3.22  | 0.01 | 1  | 3 | 1  | 1  | 0  | 0      | 0  | 0  | 0  | 0  | 0  | 0  | 0  | 1  | 0  | 0  |
| CaH2SiO4     | 0  | 0      | 0     | 0.05 | 0  | 4 | 1  | 1  | 0  | 0      | 0  | 0  | 0  | 0  | 0  | 0  | 0  | 0  | 0  | 1  |
| NaHSiO3      | 0  | 0      | 0     | 0.05 | 0  | 3 | 0  | 1  | 1  | 0      | 0  | 0  | 0  | 1  | 0  | 0  | 0  | 0  | 0  | 0  |

Fig. 3. Spreadsheet containing the input parameters for aqueous speciation calculation.

As Zondervan mentions providing the analytical Jacobian for the equation set would enhance the efficiency of Newton-Raphson method.<sup>58</sup> Therefore, the partial derivatives of all equations with respect to each species is calculated analytically:

$$\frac{\partial \Psi_1}{\partial n_i} = z_i; i = 1, \dots, NS \quad (7)$$

$$\frac{\partial \Psi_j}{\partial n_i} = b_{e,i}; j = 2, \dots, NC + 1; e = j - 1; i = 1, \dots, NS \quad (8)$$

$$\frac{\partial \Psi_j}{\partial n_i} = \frac{v_{k,i}}{\ln(10) m_i} + \sum_{l=1}^{NS} v_{k,l} \left( \frac{-A z_i^2 z_l^2}{4\sqrt{I}(1 + a_l B \sqrt{I})^2} + \frac{b_l z_l^2}{2} \right); \quad (9)$$

$$j = NC + 2, \dots, NS; k = j - NC - 1; i = 1, \dots, NS$$

Traditionally, there are three major problems with Newton-Raphson method. First, at some iterations the Jacobian matrix may be singular and therefore, the direction vector is not defined. In some other cases, calculating the exact Newton step may be computationally expensive. Second, the initial guess should be close enough to the final solution so as to avoid erratic trajectories. Third, in spite of employing some remedy to correct the erratic behavior of Newton step the rate of convergence might still be extremely slow if we start iteration very far from the



final solution. The latter is particularly the case in higher dimensions (e.g., 15 dimensions corresponding to NS species in our problem).<sup>53, 58</sup> In order to cope with Jacobian singularity and erratic direction issues (first two problems above), we adopt the trust-region dogleg algorithm implemented in the **fsolve** function of MATLAB.<sup>59</sup> The algorithm is more robust, even compared to reduced-step Newton methods, when starting far from the solution or in case of having singular/nearly singular Jacobian matrix because it simultaneously changes the step direction and its magnitude to find an acceptable reduction of function norm.<sup>60</sup>

As we mentioned earlier, in spite of being more robust, **fsolve** may still not be efficient enough if we start far from the final solution, particularly for high-dimensional problems. In other words, a large number of iterations and/or function evaluations may be necessary (e.g., > 400 iterations and > 100×"number of variables" function evaluations being default values in MATLAB). To overcome this problem, Crerar used the curve crawler technique described by Acton.<sup>53, 61</sup> In this approach, the system of equations is down-scaled to less than 10 equations by removing some of the components and their associated species. The down-scaled equation set is then solved to find an equilibrium speciation. After that, the omitted components and their associated species are added one by one in small amounts so that the concentrations of the down-scaled species are not altered significantly. The amount of small component addition is used to calculate the concentration of its dependent species appearing with this increment of new component. With these new concentrations used as an initial guess the expanded system will be equilibrated. The former small addition of components and re-calculation of equilibrium for the expanded system is repeated until all the omitted components are completely added retrieving the initial full system. All these initial calculations shall be done with ideal solution assumption (unit activity coefficients for all species). Otherwise, suitable activity coefficient could be embedded in the iterative procedure above once a first initial guess is calculated. However, in practice the change in activity coefficient from one iteration to the next might be very large that the process diverges. As a remedy Crerar suggested fractional change of activity coefficient.<sup>61</sup>

Inspired by the approach of Crerar explained in the previous paragraph, we developed a simpler and more efficient scheme to generate a good initial guess for full nonlinear equation set. To make the explanation more straightforward and comprehensive, we will describe the scheme using the C-S-H precipitation system of interest as an example. The aqueous species considered in the current study along with corresponding TJ parameters. Here, we have 15 species, the equilibrium amounts of which are unknown, made up by of 5 components (O, Ca, Si, Na, and N). Having a charge balance and 5 component balance equations, NS-NC-1 = 9 independent LMAs are needed to complete the set of equations. The mass action equations considered in this work. The equilibrium constants are extracted from OLI software database. Having NS independent equations in NS molar amounts the steps below should be followed in order to calculate the equilibrium speciation for the system of interest:

- (1) Choose NC+1 species out of the total NS species in the system including water solvent,  $H^+$  or  $OH^-$  (depending on a former knowledge about whether the system is more acidic or basic, respectively), and NC+1-2 other species each representing a separate component. It is advised to choose these latter species in a manner that they are (among) the most abundant species bearing the relevant component (the reason behind the former will be explained shortly). These NC species will be referred to as *master* species, hereafter. For C-S-H precipitation system, we are working under basic conditions ( $OH^-$  in favor of  $H^+$  as a master species). Additionally, it sounds reasonable to choose  $Ca^{2+}$ ,  $H_3SiO_4^-$ ,  $Na^+$ ,  $NO_3^-$  as master species to represent Ca, Si, Na, and N.

- (2) Solve for the molar abundances of master species using only linear charge and component balance equations. This task can be easily achieved using matrix left division (\) in MATLAB. Once we have the molar abundances for water (solvent) and the rest of master species, we can calculate their molalities as well.
- (3) Assuming unit activity coefficients for all species employ LMAs to get an initial estimation of molalities for other NS-NC species (secondary species). One can discriminate two types of mass action equations. The first class consists of equations having only one unknown secondary species (LMAs 1 and 4 to 8). The rest of LMAs depend on more than one unknown secondary species (in this example the rest of LMAs depend on two secondary species; yet, in more complex systems there might be LMAs with a larger number of secondary species). Having the former in mind, LMAs with the least number of unknown secondary species will be solved sequentially to estimate some initial guess for these unknown molal concentrations. Convert the estimated molalities back into mole amounts.
- (4) At this step, we will check the quality of our initial guess generated so far by examining the residuals of linear component balance equations for all components except for O. If the maximum absolute relative residual is less than a tolerance, then the initial guess could be passed to full Newton-Raphson-based method. Otherwise, if for any component the residual is larger/smaller than the tolerance/minus tolerance, the guess for the molar abundance of corresponding master species will be reduced/increased by a little amount  $(1 \mp \text{fractional step size}) \times n_i$ . Charge balance will then be applied to calculate the mole amount of OH<sup>-</sup>. It is worth noting that the mole amount of water solvent calculated from step (2) is already the same order of magnitude as its equilibrium amount since we are dealing with rather dilute (Ionic strength < 2 mol.kg<sup>-1</sup>) solutions where most of oxygen (component O) is in water. As a result, no further correction will be made to H<sub>2</sub>O molar amount. Except for that, the new mole amounts of master species will be passed to step (3) to calculate new guesses for secondary species. Once a new set of values are generated for all molar amounts, its quality will be checked again as described earlier this step. The procedure will be repeated until a suitable initial guess is reached.
- (5) The molar amounts generated by the iterative process above (steps (2-4)) will be used as an initial guess to solve the full system of equations.

For a faster and more robust convergence of the full Newton-Raphson solution, the tolerances in the iterative process above are set so that the initial guesses have almost the same order of magnitude ( $\pm 3$  orders of magnitude) as equilibrium amounts.<sup>61</sup> Numerical experiments suggested that having the relative absolute residuals for component balances in a domain with radius 10 would result in an initial guess within a range of three orders of magnitude about the final solution:

$$\max_{e=3,\dots,NC+1} \left| \frac{\sum_{i=1}^{NS} b_{e,i} n_i^{\text{guess}}}{B_e} \right| < 10 \quad (10)$$

To prevent large oscillations around a suitable initial guess, the molar amounts of master species are adjusted by a fractional step size of 0.1 in case that any of the conditions are violated. Such a value is small enough to mimic a curve-crawling behavior toward the suitable initial guess yet still big enough to prevent excessively slow marching. Numerical experiments with the above iteration parameters showed that a desirable initial guess ( $\pm 3$  orders of magnitude as the final solution) is generally achieved in less than 50 iterations. Overall, the code calculates the equilibrium molar amounts in less than 0.7 s when run on an HP laptop with Intel® Core™ i5-4310M CPU @ 2.70GHz 2.70 GHz processor and 8.00 GB RAM.

As Messac affirms proper scaling is an inevitable step prior to solving an optimization problem particularly when independent variables (or the “design variables”) lie over a wide range.<sup>62</sup> Without proper scaling the optimization code may not converge or stops prematurely at a poor design variable, oftentimes without the coder realizing that this is the case. Even in convergent situations scaling enhances rate of convergence.<sup>62</sup> As it was discussed in the previous paragraph, the generated initial guess lies within a three-orders of magnitude range of the final solution. Therefore, all the design variables can be scaled using

$$\alpha_i^S = \frac{1}{n_i^0}; n_i^{\text{sclaed}} = n_i \times \alpha_i^S \quad (11)$$

with  $\alpha_i^S$  and  $n_i^{\text{sclaed}}$  being the scale factor and scaled mole amounts, respectively. This way, the optimization function (**fsolve**) will receive some scaled initial guess (with all variables lying around  $\pm 1 \times 1000$ ) and returns scaled final solution, which can be unscaled in a reverse manner.

The simulation results for C-S-H precipitation experiments described in Section above over a period of 20 hours, using OLI Studio software (with solid and vapor phases turned off) and our aqueous speciation code (called aqEQBRM). Both pH and molal ionic strength values are predicted with excellent accuracy when compared to OLI output as reference small differences due to using different activity coefficient models as discussed in Thomsen et al.<sup>63</sup>). The differences in predicted pH values are generally less than 0.1 pH units which is in the acceptable range of discrepancy between experimentally measured and calculated values.<sup>64-66</sup> . It depicts supersaturation ratios for both portlandite and C-S-H (different solid solutions models) using OLI (markers) and aqEQBRM (lines). Once again, there is an excellent match between aqEQBRM and OLI, with the small discrepancies attributable to different activity coefficient models (TJ for aqEQBRM and MSE for OLI).<sup>63</sup> Analogous to our experimental observation (no portlandite precipitating out of solution), for all C-S-H models the supersaturation ratio with respect to portlandite is smaller than that of C-S-H. The difference in C-S-H supersaturation ratio calculated based on different solid solution models could be ascribed to discrepancy in C-S-H models being calibrated using various experimental data sets. Such discrepancy is anticipated to be around 0.2-0.6 pK units in solubility product.<sup>1</sup> Simple hand calculation shows that the former is equivalent to supersaturation discrepancies by a factor of  $\sim 1.2-1.7$  for  $K_{sp} \approx 10^{-7}$ . Comparing the value shown reveals that the former is in fact consistent with C-S-H supersaturation ratios having an upper bound correspondent to Kersten’s model and a lower bound correspondent to Carey and Litchner’s model (assuming the intermediate Berner’s model represents the mean values).

#### IV. Implementation in PBE and coupling to Mass balance equation.

We insert the corresponding physicochemical expressions for different phenomena by replacing primary and secondary nucleation rates in the equation, we will arrive at the following expression for the discontinuous jumps signifying discrete events<sup>21</sup>

$$\overline{h_k} = (L_I)^k \times J_I(t) + (L_{II})^k \times J_{II}(t) \quad (12)$$

in order to express the growth expression in moment-transformed PBE in terms of QMOM approximation

$$k \int_0^\infty n(t, L) G_L L^{k-1} dL \approx k \sum_{i=1}^N w_i(t) G(L_i(t)) (L_i(t))^{k-1}; k = 0, 1, \dots, 2N - 1 \quad (13)$$

Combining Eqs. (12), (13) and knowing no C-S-H is in the feed

$$\frac{dm_k}{dt} + m_k \frac{d(\ln V)}{dt} = k \sum_{i=1}^N w_i(t) G(L_i(t)) (L_i(t))^{k-1} + (L_I)^k \times J_I(t) + (L_{II})^k \times J_{II}(t) \quad (14)$$

for  $k = 1, 2, \dots, 2N - 1$  denoting  $2N$  ordinary differential equations (ODEs) representing the first  $2N$  moment-transformed PBE equations in a QMOM closed form. The above equations have to be solved simultaneously with mass balance equations. These mass balance equations track the time evolution of elemental abundances in aqueous solution that is passed at every times-step into the speciation code. For the C-S-H system of interest, there are 4 elemental balance equations that have to be considered (O, Ca, Si, and Na; the overall amount of nitrogen in solution is constant as no N-containing compound is being introduced into the aqueous solution nor leaving it):

$$\frac{d}{dt} n_{O, Sol} = Q_1 C_O - v_O \frac{dn_{C-S-H}}{dt} \quad (15)$$

$$\frac{d}{dt} n_{Ca, Sol} = -v_{Ca} \frac{dn_{C-S-H}}{dt} \quad (16)$$

$$\frac{d}{dt} n_{Si, Sol} = Q_1 C_{Si} - v_{Si} \frac{dn_{C-S-H}}{dt} \quad (17)$$

$$\frac{d}{dt} n_{Na, Sol} = Q_1 C_{Na} \quad (18)$$

where  $n_{X, Sol}$  denotes the molar amount of element X in solution having a molar concentration  $C_X$  ( $\text{mol.m}^{-3}$ ) in the inlet stream with flow rate  $Q_1(\text{m}^3)$ , and contributing  $v_X$  moles in one mole C-S-H precipitated from solution. Additionally,

$$\begin{aligned} \frac{dn_{C-S-H}}{dt} &= k_V \rho_{solid} V \\ &\times \left( 3 \sum_{i=1}^N w_i(t) G(L_i(t)) (L_i(t))^2 + (L_I)^3 \times J_I(t) + (L_{II})^3 \times J_{II}(t) \right) \end{aligned} \quad (19)$$

is the overall rate of C-S-H precipitation due to nucleation and growth processes ( $\text{mol.s}^{-1}$ ). As per system specifications  $C_O$ ,  $C_{Si}$ , and  $C_{Na}$  are  $55.4842$ ,  $0.0090 \times 10^{-3}$ , and  $0.1172 \times 10^{-3} \text{ mol.m}^{-3}$ , respectively. Also, according to Kersten's model being used to model C-S-H solid phase thermodynamics,  $v_O$ ,  $v_{Ca}$ ,  $v_{Si}$  are  $7/2$ ,  $1$ , and  $1/2$ , respectively.<sup>36</sup>

## V. Optimization of kinetics parameters

Knowing all the kinetic parameters, solution of the PBE set, written for three quadrature nodes, coupled to mass balance equations give the temporal evolution of different elements in solution as well as solid C-S-H formed. Having unknown parameters one can develop an optimization scheme which varies these parameters to give a best fit to experimental data. In the current work, MATLAB's nonlinear least-squares solver (**lsqnonlin**) is employed for this purpose. Proper bounds were chosen to facilitate the convergence of the optimization function (Table 5). Once again, scaling is a key for reliable execution; therefore, the objective function and also all the design variables were scaled using proper scale factors to bring the values in the order of unity (Table 5).<sup>62</sup> The options for **lsqnonlin** function were 1000 maximum iterations, function and design variable tolerances of  $10^{-3}$ , and 600 maximum function evaluations. When run on an HP Intel® Core™ i5-4310M CPU @ 2.70GHz 2.7 GHz laptop with 8.00 GB RAM, the overall kinetic parameter estimation problem required  $\sim 45$  minutes to converge with the experimental data at  $2 \text{ mL.min}^{-1}$  inlet flow rate as the fitting points. The goodness of fit is quantitatively appraised by the coefficient of determination (R-squared) and maximum absolute residual (the biggest discrepancy between calculated and measured  $\text{Ca}^{2+}$  mole amounts). The former is defined as<sup>58</sup>

$$R^2 = 1 - \frac{\sum (n_{\text{Ca,experiment}} - n_{\text{Ca,calculated}})^2}{\sum (n_{\text{Ca,experiment}} - \bar{n}_{\text{Ca,experiment}})^2} \quad (20)$$

where  $n_{\text{Ca,experiment}}$  and  $n_{\text{Ca,calculated}}$  are the experimentally measured and calculated  $\text{Ca}^{2+}$  mole amount, respectively, and  $\bar{n}_{\text{Ca,experiment}}$  is the mean of observed data.

Table 1. Bounds for unknown kinetic parameters.

| Kinetic parameter | $\gamma \text{ (J.m}^{-2}\text{)}$ | $\frac{\sigma}{\gamma}$ | $x_A$ | $D \text{ (m}^2.\text{s}^{-1}\text{)}$ | $K_G$      | $g$ |
|-------------------|------------------------------------|-------------------------|-------|--|------------|-----|
| Lower bound       | 0.01                               | 0                       | 0     | $10^{-11}$                             | $10^{-13}$ | 1   |
| Upper bound       | 0.15                               | 2                       | 1     | $10^{-9}$                              | $10^{-7}$  | 3   |
| Scale factor      | 10                                 | 1                       | 1     | $10^{-9}$                              | $10^{-9}$  | 1   |

## VI. PSD of primary and secondary particles

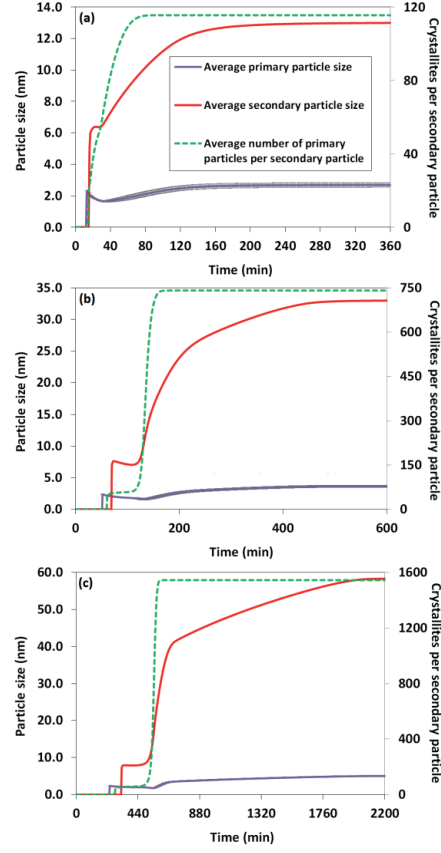


Fig. 4. Number-averaged primary (crystallite) and secondary particle size and the average number of crystallites per secondary particle as a function of time for 2 (a), 0.50 (b), and 0.11 mL.min<sup>-1</sup> (c) inlet flow rates; the standard deviation of crystallite size is shown as gray error bars around the respective graph.

Table 2. Equilibrium size-properties of precipitated C-S-H particles at different inlet flow rates.

| Inlet flow rate (mL.min <sup>-1</sup> ) | Number (volume) averaged crystallite size (nm) <sup>a</sup> | Standard deviation (crystallite; nm) <sup>b</sup> | Coefficient of variation (crystallite) <sup>b</sup> | Mean secondary particle size (nm) <sup>c</sup> | Average number of crystallites per secondary particle <sup>d</sup> |
|---|---|---|---|--|--|
| <b>2.0</b>                              | 2.7 (2.7)   | ± 0.16  | 0.06  | 13.0   | 116  |
| <b>0.5</b>                              | 3.6 (3.7)   | ± 0.19  | 0.05  | 33.0   | 741  |
| <b>0.11</b>                             | 5.0 (5.1)   | ± 0.39  | 0.08  | 58.3   | 1544   |

<sup>a</sup> Number-averaged primary particle (crystallite) size:  $\overline{L}_{1,0} = \frac{m_1}{m_0}$

Volume-averaged primary particle size:  $\overline{L}_{4,3} = \frac{m_4}{m_3}$  (from Ref. 104)

<sup>b</sup> Volume-based coefficient of variation and standard deviation:  $SD = CV \times \overline{L}_{4,3}$ ;  $CV = \sqrt{\frac{m_5 m_3}{m_4^2} - 1}$  (from Ref. 104)

<sup>c</sup> Mean secondary particle size =  $\sqrt[3]{\frac{6n_{C-S-H}}{\pi\rho_{solid} \times \int_0^{t_{end}} J_1 V dt}}$

$$^d \text{ Average number of crystallite per secondary particle} = \frac{m_0}{\int_0^{t_{\text{end}}} J_1 V dt}$$

## VII. References

- (1) Kulik, D. A., Improving the structural consistency of CSH solid solution thermodynamic models. *Cement and Concrete Research* **2011**, 41, (5), 477-495.
- (2) Taylor, H., Cement chemistry. **1997**.
- (3) Lothenbach, B.; Nonat, A., Calcium silicate hydrates: Solid and liquid phase composition. *Cement and Concrete Research* **2015**, 78, 57-70.
- (4) Pellenq, R. J.-M.; Kushima, A.; Shahsavari, R.; Van Vliet, K. J.; Buehler, M. J.; Yip, S.; Ulm, F.-J., A realistic molecular model of cement hydrates. *Proceedings of the National Academy of Sciences* **2009**, 106, (38), 16102-16107.
- (5) Bauchy, M.; Qomi, M. A.; Ulm, F.-J.; Pellenq, R.-M., Order and disorder in calcium-silicate-hydrate. *The Journal of chemical physics* **2014**, 140, (21), 214503.
- (6) Dolado, J. S.; Griebel, M.; Hamaekers, J.; Heber, F., The nano-branched structure of cementitious calcium-silicate-hydrate gel. *Journal of Materials Chemistry* **2011**, 21, (12), 4445-4449.
- (7) Dolado, J. S.; Van Breugel, K., Recent advances in modeling for cementitious materials. *Cement and concrete research* **2011**, 41, (7), 711-726.
- (8) Jennings, H. M., Refinements to colloid model of CSH in cement: CM-II. *Cement and Concrete Research* **2008**, 38, (3), 275-289.
- (9) Bentz, D. P.; Quenard, D. A.; Baroghel-Bouny, V.; Garboczi, E. J.; Jennings, H. M., Modelling drying shrinkage of cement paste and mortar Part 1. Structural models from nanometres to millimetres. *Materials and Structures* **1995**, 28, (8), 450-458.
- (10) Morales-Florez, V.; Brunet, F., Structural models of random packing of spheres extended to bricks: simulation of the nanoporous calcium silicate hydrates. *Molecular Simulation* **2009**, 35, (12-13), 1001-1006.
- (11) Gonzalez-Teresa, R.; Morales-Florez, V.; Manzano, H.; Dolado, J. S., Structural models of randomly packed Tobermorite-like spherical particles: A simple computational approach. *Materiales de construccion* **2010**, 60, (298), 7-15.
- (12) Chandler, M.; Peters, J.; Pelessone, D., Modeling nanoindentation of calcium silicate hydrate. *Transportation Research Record: Journal of the Transportation Research Board* **2010**, (2142), 67-74.
- (13) Mazumdar, T.; Mazumder, S.; Sen, D., Temporal evolution of mesoscopic structure of some non-Euclidean systems using a Monte Carlo model. *Physical Review B* **2011**, 83, (10), 104302.
- (14) Masoero, E.; Del Gado, E.; Pellenq, R.-M.; Ulm, F.-J.; Yip, S., Nanostructure and nanomechanics of cement: polydisperse colloidal packing. *Physical review letters* **2012**, 109, (15), 155503.
- (15) Yu, Z.; Lau, D., Nano-and mesoscale modeling of cement matrix. *Nanoscale research letters* **2015**, 10, (1), 1-6.
- (16) Lau, D.; Yu, Z.; Buyukozturk, O. In *Mesoscale modeling of cement matrix using the concept of building block*, MRS Proceedings, 2015; Cambridge Univ Press: 2015; pp mrsf14-1759-xx03-07.
- (17) Yu, Z.; Zhou, A.; Lau, D., Mesoscopic packing of disk-like building blocks in calcium silicate hydrate. *Scientific Reports* **2016**, 6.
- (18) Constantinides, G.; Ulm, F.-J., The nanogranular nature of C-S-H. *Journal of the Mechanics and Physics of Solids* **2007**, 55, (1), 64-90.
- (19) Testino, A.; Buscaglia, M. T.; Buscaglia, V.; Viviani, M.; Bottino, C.; Nanni, P., Kinetics and mechanism of aqueous chemical synthesis of BaTiO<sub>3</sub> particles. *Chemistry of materials* **2004**, 16, (8), 1536-1543.
- (20) Testino, A.; Buscaglia, V.; Buscaglia, M. T.; Viviani, M.; Nanni, P., Kinetic modeling of aqueous and hydrothermal synthesis of barium titanate (BaTiO<sub>3</sub>). *Chemistry of materials* **2005**, 17, (21), 5346-5356.
- (21) Schroeder, B.; Harris, D.; Smith, S.; Lignell, D., Theoretical framework for multiple-polymorph particle precipitation in highly supersaturated systems. *Crystal Growth & Design* **2014**, 14, (4), 1756-1770.
- (22) Marchisio, D. L.; Fox, R. O., *Computational models for polydisperse particulate and multiphase systems*. ed.; Cambridge University Press: 2013.
- (23) Randolph, A. D.; Larson, M. A., *Theory of Particulate Processes 2e: Analysis and Techniques of Continuous Crystallization*. ed.; Elsevier: 2012.
- (24) McGraw, R., Description of aerosol dynamics by the quadrature method of moments. *Aerosol Science and Technology* **1997**, 27, (2), 255-265.
- (25) Marchisio, D. L.; Piktura, J. T.; Fox, R. O.; Vigil, R. D.; Barresi, A. A., Quadrature method of moments for population-balance equations. *AIChE Journal* **2003**, 49, (5), 1266-1276.
- (26) Gautschi, W., *Orthogonal polynomials: computation and approximation*. ed.; Oxford University Press on Demand: 2004.



- (27) Gordon, R. G., Error bounds in equilibrium statistical mechanics. *Journal of Mathematical Physics* **1968**, 9, (5), 655-663.
- (28) Sack, R.; Donovan, A., An algorithm for Gaussian quadrature given modified moments. *Numerische Mathematik* **1971**, 18, (5), 465-478.
- (29) Wheeler, J. C., Modified moments and Gaussian quadratures. *Rocky Mountain Journal of Mathematics* **1974**, 4, (2), 287-296.
- (30) Hanhoun, M.; Montastruc, L.; Azzaro-Pantel, C.; Biscans, B.; Frèche, M.; Pibouleau, L., Simultaneous determination of nucleation and crystal growth kinetics of struvite using a thermodynamic modeling approach. *Chemical engineering journal* **2013**, 215, 903-912.
- (31) Galbraith, S.; Schneider, P., Modelling and simulation of inorganic precipitation with nucleation, crystal growth and aggregation: a new approach to an old method. *Chemical Engineering Journal* **2014**, 240, 124-132.
- (32) Zhu, Z.; Peng, Y.; Hatton, T. A.; Samrane, K.; Myerson, A. S.; Braatz, R. D., Crystallization of Calcium Sulphate During Phosphoric Acid Production: Modeling Particle Shape and Size Distribution. *Procedia Engineering* **2016**, 138, 390-402.
- (33) Lothenbach, B., Thermodynamic equilibrium calculations in cementitious systems. *Materials and Structures* **2010**, 43, (10), 1413-1433.
- (34) Berner, U., Modelling the incongruent dissolution of hydrated cement minerals. *Radiochimica Acta* **1988**, 44, (2), 387-394.
- (35) Berner, U., Evolution of pore water chemistry during degradation of cement in a radioactive waste repository environment. *Waste Management* **1992**, 12, (2), 201-219.
- (36) Kersten, M., Aqueous solubility diagrams for cementitious waste stabilization systems. 1. The CSH solid-solution system. *Environmental science & technology* **1996**, 30, (7), 2286-2293.
- (37) Carey, J.; Lichtner, P., Calcium silicate hydrate (CSH) solid solution model applied to cement degradation using the continuum reactive transport model FLOTRAN. *Transport properties and concrete quality: Materials Science of Concrete* **2007**, 73, 106.
- (38) Rahman, M. M.; Nagasaki, S.; Tanaka, S., A model for dissolution of CaO-SiO<sub>2</sub>-H<sub>2</sub>O gel at Ca/Si > 1. *Cement and concrete research* **1999**, 29, (7), 1091-1097.
- (39) Kulik, D. A.; Kersten, M., Aqueous Solubility Diagrams for Cementitious Waste Stabilization Systems: II, End-Member Stoichiometries of Ideal Calcium Silicate Hydrate Solid Solutions. *Journal of the American Ceramic Society* **2001**, 84, (12), 3017-3026.
- (40) Soler, J. M., *Thermodynamic description of the solubility of CSH gels in hydrated Portland cement*. ed.; Posiva Oy: 2007.
- (41) Prieto, M., Thermodynamics of solid solution-aqueous solution systems. *Reviews in Mineralogy and Geochemistry* **2009**, 70, (1), 47-85.
- (42) Thorstenson, D. C.; Plummer, L. N., Equilibrium criteria for two-component solids reacting with fixed composition in an aqueous phase; example, the magnesian calcites. *American Journal of Science* **1977**, 277, (9), 1203-1223.
- (43) Prieto, M.; Putnis, A.; Fernández-Díaz, L.; López-Andrés, S., Metastability in diffusing-reacting systems. *Journal of Crystal Growth* **1994**, 142, (1-2), 225-235.
- (44) Putnis, A.; Prieto, M.; Fernandez-Díaz, L., Fluid supersaturation and crystallization in porous media. *GEOLOGICAL MAGAZINE-LONDON-* **1995**, 132, (1), 1-1.
- (45) Pina, C.; Putnis, A., The kinetics of nucleation of solid solutions from aqueous solutions: a new model for calculating non-equilibrium distribution coefficients. *Geochimica et cosmochimica acta* **2002**, 66, (2), 185-192.
- (46) Pina, C.; Putnis, A.; Astilleros, J., The growth mechanisms of solid solutions crystallising from aqueous solutions. *Chemical geology* **2004**, 204, (1), 145-161.
- (47) Söhnel, O.; Garside, J., *Precipitation: basic principles and industrial applications*. ed.; Butterworth-Heinemann: 1992.
- (48) VanBriesen, J. M.; Small, M.; Weber, C.; Wilson, J., Modelling Chemical Speciation: Thermodynamics, Kinetics and Uncertainty. *Modelling of Pollutants in Complex Environmental Systems* **2010**, 2, 135.
- (49) Rubin, J., Transport of reacting solutes in porous media: Relation between mathematical nature of problem formulation and chemical nature of reactions. *Water resources research* **1983**, 19, (5), 1231-1252.
- (50) Kulik, D. A.; Wagner, T.; Dmytrieva, S. V.; Kosakowski, G.; Hingerl, F. F.; Chudnenko, K. V.; Berner, U. R., GEM-Selektor geochemical modeling package: revised algorithm and GEMS3K numerical kernel for coupled simulation codes. *Computational Geosciences* **2013**, 17, (1), 1-24.
- (51) Anderson, G. M.; Crerar, D. A., *Thermodynamics in geochemistry: the equilibrium model*. ed.; Oxford University Press on Demand: 1993.
- (52) Anderson, G. M., *Thermodynamics of natural systems*. ed.; Cambridge University Press: 2009.
- (53) Acton, F. S., *Numerical methods that work*. ed.; Maa: 1990.
- (54) Langmuir, D., *Aqueous environmental geochemistry*. ed.; 1997.

- (55) Truesdell, A. H.; Jones, B. F., WATEQ, a computer program for calculating chemical equilibria of natural waters. *J. Res. US Geol. Surv* **1974**, 2, (2), 233-248.
- (56) Parkhurst, D. L. In *Ion-association models and mean activity coefficients of various salts*, ACS symposium series, 1990; Oxford University Press: 1990; pp 30-43.
- (57) Wang, P.; Anderko, A.; Young, R. D., A speciation-based model for mixed-solvent electrolyte systems. *Fluid Phase Equilibria* **2002**, 203, (1), 141-176.
- (58) Zondervan, E., *A Numerical Primer for the Chemical Engineer*. ed.; CRC Press: 2014.
- (59) Powell, M. J. *A FORTRAN subroutine for solving systems of nonlinear algebraic equations*; Atomic Energy Research Establishment, Harwell (England): 1968.
- (60) Beers, K. J., *Numerical methods for chemical engineering: applications in Matlab*. ed.; Cambridge University Press: 2006.
- (61) Crerar, D. A., A method for computing multicomponent chemical equilibria based on equilibrium constants. *Geochimica et Cosmochimica Acta* **1975**, 39, (10), 1375-1384.
- (62) Messac, A., *Optimization in Practice with MATLAB®: For Engineering Students and Professionals*. ed.; Cambridge University Press: 2015.
- (63) Lin, Y.; Kate, A. t.; Mooijer, M.; Delgado, J.; Fosbøl, P. L.; Thomsen, K., Comparison of activity coefficient models for electrolyte systems. *AIChE journal* **2010**, 56, (5), 1334-1351.
- (64) Schmitz, G., The uncertainty of pH. *J. Chem. Educ* **1994**, 71, (2), 117.
- (65) Meinrath, G.; Spitzer, P., Uncertainties in determination of pH. *Microchimica acta* **2000**, 135, (3-4), 155-168.
- (66) Leito, I.; Strauss, L.; Koort, E.; Pihl, V., Estimation of uncertainty in routine pH measurement. *Accreditation and quality assurance* **2002**, 7, (6), 242-249.
- (67) De Yoreo, J. J.; Vekilov, P. G., Principles of crystal nucleation and growth. *Reviews in mineralogy and geochemistry* **2003**, 54, (1), 57-93.
- (68) Mersmann, A., *Crystallization technology handbook*. ed.; CRC Press: 2001.
- (69) Mersmann, A.; Bartosch, K., How to predict the metastable zone width. *Journal of crystal growth* **1998**, 183, (1), 240-250.
- (70) Nielsen, A. E., *Kinetics of precipitation*. ed.; Pergamon Press Oxford: 1964; Vol. 350.
- (71) Thomas, J. J.; Jennings, H. M.; Allen, A. J., Relationships between Composition and Density of Tobermorite, Jennite, and Nanoscale CaO– SiO<sub>2</sub>– H<sub>2</sub>O. *The Journal of Physical Chemistry C* **2010**, 114, (17), 7594-7601.
- (72) Garrault-Gauffinet, S.; Nonat, A., Experimental investigation of calcium silicate hydrate (CSH) nucleation. *Journal of crystal growth* **1999**, 200, (3), 565-574.
- (73) Dirksen, J.; Ring, T., Fundamentals of crystallization: kinetic effects on particle size distributions and morphology. *Chemical Engineering Science* **1991**, 46, (10), 2389-2427.
- (74) Nonat, A., The structure and stoichiometry of CSH. *Cement and Concrete Research* **2004**, 34, (9), 1521-1528.
- (75) Mullin, J. W., *Crystallization*. ed.; Butterworth-Heinemann: 2001.
- (76) Lewis, A.; Seckler, M.; Kramer, H.; Van Rosmalen, G., *Industrial Crystallization: Fundamentals and Applications*. ed.; Cambridge University Press: 2015.
- (77) Garside, J., The concept of effectiveness factors in crystal growth. *Chemical Engineering Science* **1971**, 26, (9), 1425-1431.
- (78) Ntafalias, E.; Koutsoukos, P., Spontaneous precipitation of calcium silicate hydrate in aqueous solutions. *Crystal Research and Technology* **2010**, 45, (1), 39-47.
- (79) Richardson, I., The calcium silicate hydrates. *Cement and concrete research* **2008**, 38, (2), 137-158.
- (80) Gauffinet, S.; Finot, É.; Lesniewska, E.; Nonat, A., Direct observation of the growth of calcium silicate hydrate on alite and silica surfaces by atomic force microscopy. *Comptes Rendus de l'Academie des Sciences Series IIA Earth and Planetary Science* **1998**, 4, (327), 231-236.
- (81) Pellenq, R.-M.; Lequeux, N.; Van Damme, H., Engineering the bonding scheme in C–S–H: The ionic-covalent framework. *Cement and Concrete Research* **2008**, 38, (2), 159-174.
- (82) Söhnel, O., Electrolyte crystal-aqueous solution interfacial tensions from crystallization data. *Journal of Crystal Growth* **1982**, 57, (1), 101-108.
- (83) Bullard, J. W.; Scherer, G. W.; Thomas, J. J., Time dependent driving forces and the kinetics of tricalcium silicate hydration. *Cement and Concrete Research* **2015**, 74, 26-34.
- (84) Greenberg, S.; Chang, T.; Anderson, E., Investigation of colloidal hydrated calcium silicates. I. Solubility products. *The Journal of Physical Chemistry* **1960**, 64, (9), 1151-1157.
- (85) Richardson, I.; Groves, G., Models for the composition and structure of calcium silicate hydrate (C S H) gel in hardened tricalcium silicate pastes. *cement and concrete research* **1992**, 22, (6), 1001-1010.

- (86) Maggion, R.; Bonnamy, S.; Levitz, P.; Van Damme, H., A scaling model of the microstructural evolution in C3S/CSH pastes. In *The Modelling of Microstructure and its Potential for Studying Transport Properties and Durability*, Springer: 1996; pp 137-155.
- (87) Xu, Z.; Viehland, D., Observation of a mesostructure in calcium silicate hydrate gels of portland cement. *Physical review letters* **1996**, 77, (5), 952.
- (88) Richardson, I., The nature of the hydration products in hardened cement pastes. *Cement and Concrete Composites* **2000**, 22, (2), 97-113.
- (89) Lesko, S.; Lesniewska, E.; Nonat, A.; Mutin, J.-C.; Goudonnet, J.-P., Investigation by atomic force microscopy of forces at the origin of cement cohesion. *Ultramicroscopy* **2001**, 86, (1), 11-21.
- (90) Gauffinet, S.; Finot, É.; Lesniewska, E.; Nonat, A., Observation directe de la croissance d'hydrosilicate de calcium sur des surfaces d'alite et de silice par microscopie à force atomique. *Comptes Rendus de l'Académie des Sciences-Series IIA-Earth and Planetary Science* **1998**, 327, (4), 231-236.
- (91) Sounart, T. L.; Liu, J.; Voigt, J. A.; Huo, M.; Spoerke, E. D.; McKenzie, B., Secondary nucleation and growth of ZnO. *Journal of the American Chemical Society* **2007**, 129, (51), 15786-15793.
- (92) Fang, J.; Du, S.; Lebedkin, S.; Li, Z.; Kruk, R.; Kappes, M.; Hahn, H., Gold mesostructures with tailored surface topography and their self-assembly arrays for surface-enhanced Raman spectroscopy. *Nano letters* **2010**, 10, (12), 5006-5013.
- (93) Liu, J.; Chen, X.; Wang, W.; Song, B.; Huang, Q., Secondary facet-selective nucleation and growth: highly oriented straight SnO<sub>2</sub> nanowire arrays on primary microrods. *Crystal Growth and Design* **2009**, 9, (4), 1757-1761.
- (94) Myint, A. A.; Lee, H. W.; Seo, B.; Son, W.-S.; Yoon, J.; Yoon, T. J.; Park, H. J.; Yu, J.; Yoon, J.; Lee, Y.-W., One pot synthesis of environmentally friendly lignin nanoparticles with compressed liquid carbon dioxide as an antisolvent. *Green Chemistry* **2016**, 18, (7), 2129-2146.
- (95) Kern, R.; Le Lay, G.; Métois, J. J., In *Current Topics in Materials Science*, Kaldis, E., Ed. North-Holland: Amsterdam, Netherlands, 1979; Vol. 3, p 135.
- (96) Marchisio, D. L., On the use of bi-variate population balance equations for modelling barium titanate nanoparticle precipitation. *Chemical Engineering Science* **2009**, 64, (4), 697-708.
- (97) Eble, A.; Mersmann, A. In *Interaction of kinetics governing the precipitation of nanoparticles*, Proceedings of the 14th International Symposium on Industrial Crystallization, Cambridge, 1999; 1999.
- (98) Donnet, M.; Bowen, P.; Lemaître, J., A thermodynamic solution model for calcium carbonate: Towards an understanding of multi-equilibria precipitation pathways. *Journal of colloid and interface science* **2009**, 340, (2), 218-224.
- (99) Pellenq, R.-M.; Caillol, J.; Delville, A., Electrostatic attraction between two charged surfaces: A (N, V, T) Monte Carlo simulation. *The Journal of Physical Chemistry B* **1997**, 101, (42), 8584-8594.
- (100) Neubauer, C.; Jennings, H. M., The use of digital images to determine deformation throughout a microstructure Part II Application to cement paste. *Journal of materials science* **2000**, 35, (22), 5751-5765.
- (101) Powers, T., The thermodynamics of volume change and creep. *Matériaux et Construction* **1968**, 1, (6), 487-507.
- (102) Skinner, L.; Chae, S.; Benmore, C.; Wenk, H.; Monteiro, P., Nanostructure of calcium silicate hydrates in cements. *Physical Review Letters* **2010**, 104, (19), 195502.
- (103) Carino, A.; Testino, A.; Andalibi, M. R.; Pilger, F.; Bowen, P.; Ludwig, C., Thermodynamic-Kinetic precipitation modelling. A case study: amorphous calcium carbonate (ACC) precipitation pathway. *Submitted* **2017**.
- (104) Chianese, A.; Kramer, H. J., *Industrial crystallization process monitoring and control*. ed.; John Wiley & Sons: 2012.
- (105) Jennings, H. M., A model for the microstructure of calcium silicate hydrate in cement paste. *Cement and Concrete Research* **2000**, 30, (1), 101-116.



## ABHISHEK KUMAR

S @: [abhishek.kumar.epfl@gmail.com](mailto:abhishek.kumar.epfl@gmail.com)  
 in: [ch.linkedin.com/in/kumar12](https://ch.linkedin.com/in/kumar12)

### Education

- PhD – Material Science & Engineering, EPFL Lausanne, Switzerland 2013-2017
- Master – Master de recherché, Process & Environment and Biotechnology Ecole Centrale Paris, France 2010-2012
- Bachelor – Chemical Engineering Indian Institute of Technology (IIT) Guwahati. 2006-2010

### Technical Experiences

- Master Thesis: Group of Catalytic Reaction Engineering (GGRC), EPFL Lausanne March- Sept, 2012
- Laboratoire d'Energétique Industrielle (LENI), EPFL, Lausanne, Switzerland May-July 2011
- Kinetics study of Alumina inclusion in steel, Arcelor-Mittal, Paris Jan –April, 2011
- Industrial Pharmaceutical Lab, University of BASEL, Switzerland May-July, 2009
- Precious Metal Processing – Vedanta Group, Mumabi, India June-August, 2008
- Chemistry Intern – National Thermal Power corporation, Delhi, India June-August, 2007

### Managerial Experiences

- President, YUVA – Indian association at EPFL, Lausanne. <http://yuva.epfl.ch/> 2014- 2015
- Founder – NGO – Computer education: [www.aviral.org](http://www.aviral.org) 2016
- Founder – Nanogence – Tech startup, EPFL Lausanne 2017
- External Relationship manager, FORUM EPFL, [www.forum.epfl.ch](http://www.forum.epfl.ch) 2015
- Member of Senate, IIT, Guwahati [www.iitg.ac.in](http://www.iitg.ac.in) 2006-2010

### Awards

- Winner European Venture Program: [Link](#) 2016
- Finalist and winner at AIT venture program 2016
- Finalist (ongoing) – Masschallenge, Switzerland 2017
- Innogrant winner, EPFL Lausanne 2017
- Enable grant winner, EPFL Lausanne 2017
- ERASMUS MUNDUS merit Scholarship student for doing Master at Paris, by EU 2010-2012
- Silver medalist in National level Computer Olympiad 2001

### Computer and technical skills

- Scientific Equipment: SEM/TEM/Particle Size/ BET/ TGA/XRD/ICP/XRF/FTIR/Zeta Potential
- Programming languages: Languages: C/C++, Visual C, Java , HTML
- Packages: MATLAB, Polymath, Stats-graphic, Mathematica, MS Office,
- Operating Systems: Win XP/2000, Linux, and Vista, Macintosh

### Sports

- Six time successful Half Marathon runner (<http://www.20km.ch/>) – 2012- 2017
- Played University Level Cricket for 5 years

### Personal Information

- Nationality: Indian, Permit B – Switzerland
- Languages: French (B1-B2), English (Professional), Hindi (Maternal), Spanish (notions).



ABHISHEK KUMAR

 @: [abhishek.kumar.epfl@gmail.com](mailto:abhishek.kumar.epfl@gmail.com)

 : [ch.linkedin.com/in/kumar12](https://ch.linkedin.com/in/kumar12)

## List of Publications

- 
- PhD studies: 2 conference / 5 Journal (1 published – 4 to be submitted)
  - Kumar A, et.al; ***“Controlled synthesis and characterization of homogeneous Calcium Silicate Hydrates phase with high Calcium to Silicate ratio”***, CCR, to be submitted
  - Kumar A, et.al; ***“The Atomic-Level Structure of Cementitious Calcium Silicate Hydrate”***, JPCC, accepted on the cover page of JPCC
  - Kumar A, et.al; ***“Cementitious Calcium silicate hydrates formation pathways and insights into alite hydration control”***, CCR, to be submitted
  - Kumar A, et.al; ***“Initial observations: Effect of the presence of divalent ions ( $Ba^{2+}$ ,  $Mg^{2+}$ ,  $Zn^{2+}$ ) on the morphology of precipitating calcium silicate”***, Conference Article.
  - Kumar A, et.al; ***“Simplistic model for growth of Calcium Silicate Hydrates from solution”***, PCCP, to be submitted
  - Kumar A, et.al; ***“Synthesis of nanostructured Calcium silicate hydrates”***, nanotech conference, 2014 Washington.
  - Kumar A, et.al; ***“Synthesis of higher ratio Calcium silicate hydrates”***, ICCI conference, 2015 Beijing.
- Other studies: 1 journal conference
- Patents: 3 from PhD studies.

